Behaviour of Cylindrical and Doubly-Curved Shell Roofs Under Earthquake

Shadi Ostovari Dailamani

A thesis submitted in partial fulfillment

of the requirements for the degree of

Doctor of Philosophy

of the

University College London.

Department of Civil, Environmental and Geomatic Engineering

University College London

2010

I, Shadi Ostovari Dailamani confirm that the work presented in this thesis is my own. Where information has been derived from other sources, I confirm that this has been indicated in the thesis.

Abstract

There are indications that thin shells are once again becoming a popular option for roofs covering large column free spaces. Relative to other structural forms there is relatively little analysis of their dynamic response. Especially in seismically active regions, this paucity of analyses could be of considerable significance. This research reports a verification study based upon two independent methods: a finite element solution and a newly developed analytical method. For typical cylindrical shell roofs these methods have been used to determine the spectra of natural vibration modes, displacements, accelerations and stress resultants of the shell under the action of the vertical motions of a selected earthquake. The comparisons showed the FE and analytical results to be in practically excellent agreement.

The study of the numbers of modes required for accurate prediction of displacement, acceleration, and stress response for a specific geometry of shell showed that unlike ordinary buildings, in roof shells there is a need to include substantial number of modes for a converged result.

Of the limited past investigations on how thin shell roofs respond to earthquakes, attention has been restricted to consideration of just the out-of-plane modes, with the contributions from the in-plane modes usually neglected. The importance of the inclusion of in-plane modes for a cylindrical shell subject to the vertical component of a selected earthquake loading showed that these modes can potentially have a major impact on the predicted levels of in-plane deformation and the associated membrane stresses, and therefore depending on the type of earthquake should be included for reliable estimates of earthquake response.

The assessment of the relative importance of the horizontal and vertical components of

earthquakes showed that vertical components result in higher accelerations and stresses compared to the horizontal components.

In the past investigations of how thin shell roofs respond to earthquakes, attention has been largely restricted to linear analysis, with contributions from pre-loading usually neglected. The independent approaches using finite element solution and a newly developed analytical method indicate that inclusion of self-weight and additional superimposed loading can significantly reduce the predicted natural frequencies. Consequently inclusion of pre-loading is shown to have a major influence on the levels of deformations and the associated membrane stresses. It is concluded that performing a modal analysis in which the effects of pre-loading are ignored could lead to serious underestimation of responses for large roof shells under earthquake loading. Furthermore a nonlinear snap buckling analysis showed that the snap buckling loads are much lower than the classical critical loads in cylindrical roof shell, which suggest a need for a complete nonlinear analysis for the cases of shell with pre-loading close to snap buckling loads.

The final section of the present research compares the frequencies and linear responses of a doubly curved shell with a cylindrical shell. The results showed that the frequencies of a doubly curved shell are higher than a cylindrical shell. The increase in the natural frequencies resulted in much lower displacements and stress resultant responses in the doubly curved shell.

Acknowledgements

I would like to express my sincere gratitude to my supervisor, Prof James G A Croll, for giving me the invaluable opportunity to carry out my PhD thesis under his world-class supervision. I would like to thank him for his patience and thorough supervision throughout my study, continuous valuable meetings, teaching me so many things about the subject in his unique and insightful way of teaching and reviewing my thesis. I will never forget his kindness, lessons that I learnt from him in the subject of shell structures and dynamics of structures. I am also grateful for his help to find funding to support my study. This thesis would have not been possible without him and it is an honor for me to be his student. I am certainly in his debt for all his supports.

I would also like to thank Ove Arup Partnership for funding this PhD. Special thank to Mr John Lyle for introducing me to the company and Mr. Michael Willford for making the financial support possible and giving me the opportunity to work in Advance Technology Group (ATG) under his excellent supervision. I learned so many things about earthquake engineering and nonlinear dynamics from him and other colleagues in Arup. I will never forget the friendly environment in Ove Arup. I am especially grateful to Dr Damian Grant for his support and guidance during my work in Arup. I learned many things from him and also would like to thank him for valuable discussions about my thesis.

Special thank to my second supervisor, Dr Tiziana Rossetto, for great discussions, her continuous supports and helps in different ways during my study at UCL.

I would like to show my gratitude to Dr Richard Bassett for his encouragement during my study and for reviewing and commenting on my thesis.

I would like to thank graduate school who provided me with the funding to present

three of my papers in conferences in USA and Greece. Especial thanks to Ms Ann Macdonald from the Graduate School for her supports, when I needed. Also many thanks to the Department of Civil Engineering, University College London for financially supporting me to present three papers in conferences, especially Prof. Nick Tyler who supported the applications.

Special thanks to Funds for Women Graduates (FfWG) for their generous foundation grant in my last year of PhD. Furthermore, I am grateful to my parents and my parents in law for their constant support and encouragement while they missed us for not being with them. Finally my deepest gratitude to my husband, Hooman Shayani, for accepting to come to UK to do a PhD and also for being a source of inspiration and his continues encouragement and support throughout my study that made my PhD study a pleasant experience.

Contents

List of Figures

List of Tables

Chapter 1

Introduction and Literature Review

1.1 Introduction

Shells are amongst the most efficient of natures' structures in terms of the strength-to-weight ratio. As a result, shell structures have also been exploited in different areas of science and technology. Among the various types of behaviour of shells, the dynamic response is one of the most complex and in areas of high seismicity the one likely to exert a controlling influence on design. In the context of the ship industry, it is very important for designers to consider, in the thin skin design, the dynamic loads resulting from wave shocks especially in large ships. History has witnessed many ships sinking as a result of ignoring these dynamic forces in the design process. In off-shore steel structure design, the dynamic response of the shell-like components to wind or wave forces plays an important role, which if left uncontrolled can lead to fatigue fractures with disastrous consequences, as tragically highlighted in the collapse of the Alexandra Kielland offshore platform in 1980 [2]. Aircraft shell components are also vulnerable to these forms of failure, which makes it vital in the aerospace industry to go through comprehensive and expensive dynamic testing processes. Apart from applications in marine, mechanical, and aerospace engineering, shells have much wider applications in civil engineering. In this context, storage tanks, cooling towers, containment structures, tunnels, and roofs are clear examples of shell structures that can experience potentially damaging dynamic responses.

The importance of roof shells lies in their unique characteristics. First of all, they

stand-out in terms of their high levels of load carrying capacity due to their shape. They are also very efficient structures in terms of their weight-to-area ratios so that they can be used to span large areas. This characteristic has been recognized in Japan and large span roofs are widely used to shelter people after earthquakes. In other parts of the world their deployment in the form of fabric shells for sheltering people after earthquake is also important. They can also be very elegant structures and landmarks of the structural engineering capability. They are often symbols of collaboration between architects, engineers and constructors. Many roof shells, built in different parts of the world, indicate simultaneous cooperation of architects and engineers. For example, in the roof shells designed by Isler (Switzerland), Candela (Mexico), and Nervi (Italy) [3]. The years between the 1920s to the early 1960s are considered the golden age of concrete shell construction in terms of number and variety of shells being built. Since then fewer concrete shells have been built and fewer technical papers were published on their analysis and design methods. This decline was largely due to the difficulties of construction of concrete shells and some serious collapses [4] [5]. But as will be explained later, roof shells are not limited to concrete roof shell and specifically the traditional way of construction of concrete shells.

By introducing new materials and innovative ways of construction the roof shell is again being recognized and increasingly adopted as an efficient means of covering large spaces. It is therefore surprising to find so few past studies seeking to understand how thin shell roof structures will respond to earthquake loading.

Despite the numerous past research efforts to understand the free vibrations of shells (see the comprehensive reviews [1][6]), which are briefly explained in section 1.5 and summarized in chapter 2 along with a critical review of the development of shell theory, there appears to be very little published on the earthquake response of shell roofs. The details of the previous research on the dynamic analysis of roof shells under earthquake loading are discussed in section 1.6. From the limited past studies it is difficult to draw general conclusions, indicating a need for rather more systematic investigations of the parameters most likely to effect the earthquake response of shells. However, any new

contribution to the existing literature needs to be cross-checked to ensure its validity and numerical accuracy. The little work that has been published in the area of dynamics of shells does not appear to be cross-checked to ensure the validity and accuracy of results. Moreover, because some of the important parameters controlling the behaviour were not previously reported [7], it is not possible to directly use these results as means of validating any new analysis. For this reason, there is a need for an independently validated analysis approach. Currently, dynamic analyses of shell structures are often performed using finite element (FE) programmes. But effective use of FE programmes should be based upon a sound understanding of shell theories, and an appreciation of the mechanics of shells as well as an insight into the basic concept of the analysis method. There are unconfirmed reports of poor designs having been produced as a result of insufficient understanding of these subtleties. Using analytical methods to verify the FE programme on simpler examples is an effective way to prevent possible errors from occurring when analysing more complicated problems.

There are also many behavioural aspects of roof shells that might affect their earthquake an dynamic response, which have been neglected in the past research. The relative importance of the membrane and bending stiffness in controlling natural modes is one of these behavioural aspects. Changing the stiffness by changing the dimension of the shell can change the natural frequencies and can be used towards an optimized design. The number of modes needed to provide adequate representation of the earthquake response has also not previously been looked at in detail. Much research has dealt with some aspects of the behaviour of the shell only by considering one or two modes or having not performed a convergence study [8], and in some cases by considering Rayleigh damping with a constant damping ratio for the two lowest modes, which consequently undermined the contribution of higher modes [9]. Whether the modes that are dominated by in-plane deformations can be important and how the importance of various modes is determined by the nature of the earthquake as well as the shell are other examples of the aspects of behaviour that have not been fully investigated before.

1.2 History of construction of roof shells

The early applications of shell structures in the context of civil engineering were for the roofing of cathedrals and temples. The Pantheon constructed in 126AD is the oldest standing domed structure in Rome, with a horizontal diameter of the interior circle as 43.3 m. Hagia Sophia in Istanbul, built nearly 1500 years ago, is another example of an ancient dome structure. The main dome was completely destroyed as a result of an earthquake in 558. However, it was rebuilt in 562 with a diameter of 31.24 meters and with 55.6 meters height from floor level. In more recent times, the development of reinforced concrete and improvement of the understanding of structural mechanics has led to construction of many roof shells around the world. Having a high compressive strength, reinforced concrete is a suitable material choice for shells whose main stresses are due to compression. Construction of a 16 meter diameter reinforced concrete shell having 30 mm thickness in 1922 in Germany, Jena can be named as the beginning of the new era of construction of thin concrete roof shells. This structure was designed by Walter Bauersfield of the Zeiss firm in collaboration with Dischinger [10]. Tedesko introduced their design approach and construction technique to the U.S, who in 1936 Tedesko designed the first large scale thin roof shell in the form of a barrel vault shell with $222\ ft$ ($71\ m$) span, $343\ ft$ ($104\ m$) length and $3.5\ in$ ($8.8\ cm$) thickness for an ice hockey arena in Harshley [11]. Tedesko's efforts to bring thin roof shell to the United States also lead to two major innovations in the design and construction of thin shells. They are the wide-spanning, short barrel shells, and the rib-less shells [10].

The years between 1920 to the early 1960s can be considered the golden age of the concrete shell [12]. An early example of a smooth reinforced concrete dome for the Novosibirsk theatre building constructed in 1934 consisted of a cupola with spherical radius of 30 m, plan diameter of $56\ m$, with a thickness of $8\ cm$. The $16\ mm$ thick hyperbolic paraboloid reinforced concrete roof shell of Cosmic Ray Pavilion in Mexico City designed by Candela and built in 1951 [13] set new boundaries for slenderness, while the Los Manantailes restaurant shell in Mexico City, completed in 1958 by Candela as an eight-sided groined vault composed of four intersecting hyperbolic

paraboloid saddles [14], provided an indication of the new architectural possibilities. Pier Luigi Nervi's $59\ m$ domed Sports Palace constructed in 1956-1957 for the 1960 Rome olympic [15]; St. Luis Air Terminal designed by Minoru Yamasaki in 1951 with a $37\ m$ span and 114-$216\ mm$ thickness was roofed by intersecting cylindrical shells with ribs at edges and the groins [13]; the MIT Auditorium in Boston, a spherical shell with $49\ m$ span and $89\ mm$ thickness designed by Eero Saarinen and completed in 1955 by Amman and Whitney Engineers [13]; the exhibition hall in Paris designed by Esquillan and completed in 1958, an equilateral triangle in its plan with $218\ m$ side span and a rise of $48\ m$ [13]; and a warehouse roof in Tcherepovets developed in 1962 as a reinforced concrete dome with $160\ m$ span and $65\ m$ rise, are all examples of many reinforced concrete roof shells inaugurated in different parts of the world in 1960's.

During these years a number of designers such as Pier Luigi Nervi, Eduardo Torrja, Vasilii Vlassov, and Felix Candela introduced new design theories and construction techniques while experimenting with different forms of shell. During this time many shell theories were also proposed to better define the behaviour of shell structures. It was during this period that many landmark shells of double curvature were constructed around the world.

Thin concrete roof shells lost their popularity by the late 60's. Since then fewer roof shells were constructed and fewer technical papers were published. In a survey by a group of engineers, architects, and people working in the construction sector in United States, the reasons cited for the loss of interest in the once so popular thin roof shells highlighted the cost of construction as being the main reason. Mention was also made that roof shells are very sensitive to small variation in geometry. Small errors in thickness and reinforcing steel placement can cause significant effects on internal forces and stability. Therefore expert labour is needed for construction of thin reinforced concrete shells [12]. However in many developing countries the labour costs are likely to be low. So building thin concrete roof shells, making the best use of possibly costly material is still economic.

It should be noted that people who believe that thin concrete roof shells have lost

their popularities in United States refer to the traditional way of constructing concrete thin roof shells [12]. However, the introduction of new materials or new methods of construction, which will be discussed in the next section, suggests that the adoption of thin shell could be reawakened. In fact there are signs that more and more shells are being constructed around the world making use of new developments in construction [12] [13].

1.3 Current situation of roof shells

As previously mentioned, the new era of thin concrete shell started in Germany with the construction of Zeiss planetarium in 1922, although thin roof shell construction was declined in its country of origin due to the collapse of an airplane hangar in Cottbus, Germany in early 1934 due to the creep in the concrete [10], during the same time as construction of thin shells gained acceptance in the United State and flourished.

The construction of thin roof shell continued in 70's in some parts of the world; a circus building having $72\ m$ diameter constructed in a highly active seismic zone in Bishkek and Ashkhabad as two precast reinforced concrete folded truncated cone shells, connected to each other by a spacer ring [16]; a $42 \times 42\ m$ design for sport halls and market roofs constructed in Moscow and other cities in 70's making repetitive use of 3×6 m cylindrical panels; construction of large span reinforced concrete shells of the positive Gaussian curvature with spans $100\ m$ and more in Tchelyabinsk and Minsk; construction of a precast large-span roofs of bus depots in Saint Petersburg in the 70's in the form of multi-wave shells with $96\ m$ spans; and the construction of multipurpose sport hall "Druzhba" and Danilovsky roofed market in Moscow in late 70's and early 80's with the use of spatial composite roofs by combining individual segments having different geometrical surfaces are examples of shell built in Russia [16]. However the latter roof shell was collapsed in 2006 as reported in the news.

In recent years, development of new construction methods have made the use of roof shells once again a feasible proposition. This implies that traditional concrete thin shells are fading out while new materials and technologies for constructing shells are rapidly emerging. Three methods, namely Bini's system, Monolithic Dome, and mod-

ular systems are among the new developments in construction of roof shells.

Dante Bini's system is one example of air-inflated formwork systems [17]. In this system reinforcement and concrete are placed over a fabric on the ground. The fabric is then inflated to create the shell form. This method became increasingly popular due to its economy, simplicity, speed of construction, and minimal use of material. Shells constructed by this method are used as bulk storage containers, roofing for supermarkets, swimming pools and tennis courts. Using this method it is reported that 1000 shells have been built world-wide during 1966 to 1986 [17][12].

Another system was developed by David and Barry South in late 70's and early 80's, and is now known as Monolithic Dome [12]. In this system an airform made of PVC coated nylon or polyestern fabric is inflated to determine the shape and size of the finished building. Then a thickness of polyurethane foam is sprayed over the inside of the inflated airform, which expands to thirty times of its original size. The foam is waterproof and gives the required stiffness to support the weight of reinforcing steel placed on the inside. Shotcrete is then sprayed to cover the foam and embeds the rebar. Using this method, it is common to construct domes with spans between 30 to 60 m and it is currently feasible for spans up to 300 m [12]. This form of shell has been constructed in 30 countries around the world and in 2001 their Texas based company shipped 150 airforms [12].

The modular system is another method currently very popular for constructing shells in the U.S. It consists of the modular structural steel forms that are bolted on site. Since the forms and reinforcement are able to carry the weight of shotcrete before it hardens using form work is unnecessary and the cost of construction is significantly reduced [12].

The thin concrete roof shell designed by Heinz Isler in Europe shows that they are as popular as before, with 2 to 12 roof shell constructed per year [12]. His work was often based on finding the form of shell defined by inverted hanging models. The hanging models were made of freely hanging fabric, which was first soaked in a wet cement

mix or resin. While the fabric is freely suspended from its corners the resin hardens. The solid shell model which is now in pure tension is then turned upside, giving the shell a pure compression state. After the form finding he went through the structural analysis and found the layout of reinforcement and support details before constructing the actual shell. Isler's shells have proved to be strong, aesthetic and durable.

In recent years the application of spatial reinforced concrete roofs has attracted a lot of attention due to their economic use of material, and the ability to spanning large column-free spaces [16]. Shugaev discusses the current situation of spatial structures and roof shells emphasizing the increasing use of constructing reinforced concrete roof shells and the necessity for further developments in this field. He argues that the recent development of reinforced concrete spatial roofs in Russia was due to increasing use of precast structures assembled on site. He then gives some examples of roof shells increasingly being built in Russia such as: short and long cylindrical roofs with spans of 18-36 m; shells in the form of hyperbolic paraboloids and positive Gaussian curvature shallow shells with spans of 18-$40\ m$; domes and suspended roofs with spans up to 100 m [16].

In this regard it is also worth mentioning the recent developments in construction of lattice roof shells in China. Liu, while mentioning the great progress of development of spatial structures in China, reported 15 large spatial structures recently completed in China around the year 2005, including some lattice roof shells [18]. The National grand theatre is a half-ellipsoid steel latticed shell, with a length of $212.3\ m$ in west-east axis and $143.46\ m$ in north-south axis with a total height of $46\ m$. The interior structure includes an opera hall, a music hall, a theatre hall, and a public hall.

A further two lattice shell structures are an exhibition hall and a hotspring bath center located in Jiuzhai paradise, an international conference and vacation center. The exhibition hall is a single-layer lattice elliptic paraboloid shell structure, with a long axis of $44\ m$ and short axis of $33\ m$ and height of $22\ m$. The structure of the hot spring bath center is also an elliptic paraboloid lattice shell, with a length of $150\ m$ in the long axis and $65\ m$ in the short axis and a height of $24\ m$. The structure is constructed

in the form of arch frames along the long axis and rectangle pipe purlins along the short axis. Liu also believes there would be significant growth in the construction of spatial structure before 2010 [18]. It is noteworthy to mention China is located in a highly active seismic zone indicating that special attention should be given towards the seismic consideration in the design of these structures.

1.4 Damage to shell structures due to earthquake

Although there has been a plethora of research on the response of the structures to earthquakes, there is still a dearth of information concerning the response of roof shell systems to earthquake ground motions. Investigations of the damage to structures indicate that a lot of shell structures such as oil storage tanks, silos and large span roof shells have experienced considerable damages during past earthquakes. Zama et al. [19] reported damage to 30 tanks excited by long duration ground motion during the Tokachi-oki earthquake (M=8.0). This earthquake happened on 26 September 2003 in Tomakomai, in northern of Japan, with the damage occurring at a 225km distance from the epicenter. Koketsu et al. [20] and Sezen et al. [21] have also reported similar damage to oil storage tanks during the 1999 Kocaeli earthquake in Turkey. Damage was generally reported to be caused by liquid sloshing, excited by long period ground motions. Low frequency ground motions are most likely to be experienced in long duration earthquakes. Long period waves can cause damage at greater distances. Moreover, long period ground motions can cause more severe damage to large-scale structures as a result of their natural frequencies being closer to the low frequency spectrum of earthquakes having long durations. Sinking of 6 floating roofs of the tanks during the Tokachi-oki earthquake [19] and more than 100 during Kocaeli earthquake [21] have also been reported as being the result of sloshing. This damage suggests there is insufficient understanding of the behaviour of shell structures in earthquakes. Cooling towers and stacks are other industrial structures that are vulnerable to severe earthquakes. Widespread damage to cooling towers and stacks have been reported during the Kocaeli earthquake [21]. Two reinforced concrete heater stacks designed according to ACI 307 (ACI 1969), were destroyed during that earthquake. Kilic and

Sezen [22] have analysed these two stacks and found that the damage was because of the coincidence of the location of the reinforcing-bar splices and the region the most extreme earthquake induced flexural loading. Silos have also been damaged during past earthquakes. Kawaguchi [23] has reported that 12 circular cylindrical steel silos, used for wheat storage, each having $7.2\ m$ diameter with $4.5\ mm$ wall thickness at the top and $14\ mm$ at the bottom, were heavily damaged by buckling collapse during the 1995 Hyogoken-Nanbu earthquake (M=7.2) in Japan. The increasing tendency to use shells in silos, tanks, stacks and many other structures, demands full understanding of the interaction between their geometric form and the seismic responses. There is currently little guidance as to how to prevent such catastrophic failures under earthquake loading.

As explained earlier there is also an increasing movement toward utilizing shells in large span roofs. An analytical or even intuitive understanding of the response of shell roofs to earthquake forces is essential, where these structures are adopted in seismically active regions. The collapse of such large structures in earthquake prone areas could be very serious. Kawaguchi [23] in his survey of damages to large roof structures caused during the Hyogoken-Nanbu earthquake, reported collapse of a roof of an elementary school gymnasium, as well as a public gymnasium roof. The elementary school gymnasium had $18.5 \times 40.5\ m$ plan dimensions. The roof was comprised of repetitive units of pre-cast cylindrical shells with a total number of 16 along the longer dimension in plan. The cylindrical shells had been anchored at the top of walls. During the earthquake the anchors broke and caused the collapse. The Public gymnasium also had the same roofing systems covering a space of $29.5 \times 38.5\ m$. The cylindrical shells were anchored to the tops of columns. During the earthquake the anchors broke off and all cylindrical shells fell to the floor. The collapse illustrates the poor design of connections and consequently the need for a more complete understanding of the induced forces in shell structure due to earthquake loading. However, during this earthquake damages to roof structures were relatively minor in comparison with other structures and many of them could serve as a refuge place for the people who lost their homes.
Serious damages to a lattice frame roof of a high school gymnasium built on top floor

of a reiforced concrete structure was also reported during the Hyogoken-Nanbu earthquake [23], [24]. The roof itself was a relatively stiff truss vault structure with welded pipe members. During the earthquake the roof was damaged as a consequence of rotational motion of the roof and collapse of the columns due to an uneven arrangement of seismic bearing walls and their columns.

Saka and Taniguchi [24] reported a number of double layer latticed shell severely damaged during earthquake because of the failure of anchor bolts at the roller bearing supports and inelastic buckling of members close to supports in cases where roof covered open areas between two buildings. They indicated that the relation between their roofing or supporting systems and the direction of ground motion might affect the extent of damage to roof shells. They also suggested that adequacy of in-plane stiffness for spatial roofs, balance of stiffness between roof and supports, and finally the effect of unbalanced levels of supports should be investigated in future studies of spatial roofs. Saka and Taniguchin's studies [24] on collapses of cylindrical roof shells and lattice frames indicate that suitable design of bearings of large roof structures is essential in hazardous areas. This cannot be made possible without having a clear insight into the characteristics of induced forces in shell structures due to earthquake.

Later in another survey investigating the damage to public halls in Nagaoka city after Niigata-Chuetsu earthquake in October 2004, Kawaguchi reported no significant structural damage [25]. He suggested this could have been due to Niigata-Chuetsu area including Nagoaka city being located in a heavy snow area, so the structures were generally stronger than usual structures and consequently were less vulnerable to earthquake. Distance from epicenter was the second reason Kawaguchi cited for these roof shells not suffering any significant structural damage. However, he reported the collapse of non-structural parts of the roof, which detracted from their functionality. The functionality of these halls is very important since they are usually converted to shelters for people who lost their houses after earthquakes.

In this regard Tatemichi and Kato [26] also agreed with other researchers that shell and spatial structures are not only to protect people and facilities during earthquake

but also in many cases they should serve as shelters after earthquake for people who lost their homes. However, from the experience of recent earthquakes in Japan they suggest roof shells could not fulfil their purpose due to both structural damage and non structural damages such as the shedding of the ceiling materials, finishing materials and lighting equipments. For instance, they reported that about 50% of the gymnasiums existing in the Great Hanshin area could not serve as shelters due to both structural and non-structural damage during the 1995 Hyogoken-Nanbu earthquake.
Also many spatial structures suffered from the damages to non-structural members during the 2001 Geiyo earthquake and the 2003 Tokachi-Oki earthquake [26].

1.5 Previous research on natural frequency of shells

Unlike most ordinary buildings for which the fundamental frequency tends to correspond with the mode having the largest wavelength, in shell structures the lowest frequency can occur in mode of shorter wavelengths. Many factors such as geometry, thickness, material, and initial imperfection can easily change the fundamental modes. They can also change the behaviour of the shell from being completely bending to being completely membrane. This shows the importance of these controlling factors in the design, especially in optimization problems. It implies how we can tune these factors in order to get the desired behaviour under external loadings. A suitable design is not possible without having a deep insight into the natural frequencies of shells.

1.5.1 Different methods for finding natural frequencies

Leissa in his survey introduced three methods for obtaining equations of motions [1]. First method was the standard one which applied Newton's laws by summing the forces and moments acting on a shell element of thickness h. Second method was based on deriving the equation of motion of an infinitesimal element of the three dimensional theory of elasticity and integrating it over the shell thickness to obtain the equations of motion for a shell element. Third method was based upon a variational approach. The differential equations are the most common method for finding equations of motion that have been used by researchers over the past years. Leissa in his book has summarized various studies on the derivation of various differential sets of equations

according to different shell theories before 1970. Differential equations of motion derived by Arnold-Warbuton, Goldenveizer and Novozhilov, Houghton and Johns, Epstein, and Kennard were among the most common sets of equations later adopted by other researchers in the analysis of shells. Arnold and Warburton [27], [28] used the Lagrange equations to find the equations of motion. They considered Timoshenko type strain-displacement equations, and made some assumption during solving the Lagrange equation which yielded the equations of Goldenveizer and Novozhilov [1]. Houghton and Johns [29] made some simplification on the Goldenveizer and Novozhilov equations by neglecting the nondimensional thickness parameter $h^2/12R^2$ with respect to unity. Epstein [30] derived the equations of shell theory from three dimensional elasticity theory. His equations were then derived and specialized to circular cylindrical shells by Kennard [31], [32].

Qatu has reviewed recent papers (1989-2000) on dynamic behaviour of shells [6]. He categorized various papers into four groupings. A first grouping dealt with the shell theories which were used by the researchers in their analysis, such as thin and thick shell theories, shallow and deep shell theories, linear and nonlinear shell theories. In the second grouping, papers were classified according to the different shell geometries, such as cylindrical, spherical, and conical shell. A third grouping of the papers was based on the method of analysis adopted, such as exact methods, Ritz method, and FE method. A fourth grouping was based on the complicating effects such as large deformation, interaction problems, and initial stresses. Most of the research reviewed by Qatu dealt with the free vibration problems of shells and only a few considered the response of shells under loadings such as: parametric vibration of cylindrical shell under combined static and periodic axial loading [33]; behaviour of cylindrical and spherical shells under internal explosion [34] [35]; and thermal effects on the dynamic behaviour of conical shell [6].

Souza and Croll (1980) in their comprehensive work on the analysis of orthotropic spherical shells derived the equation of motion for this form of shell using a finite difference method and investigated the variations of flexural and extensional orthotropic

stiffness properties in various modes. They systematically examined the contribution of various shell stiffness to the strain energy in each mode in order to accurately approximate frequency spectra for dynamic design process using the modified form of Rayleigh's method [36]. They have also performed physical experiments on spherical shells allowing comparison with theoretical predictions, which illustrated how the level of excitation energy can affect the characteristic responses. This influence of non-linear interaction was also investigated earlier for a simple system of two degrees of freedom by Croll [37]. It was shown that for low levels of excitation energy, classical thin shell theory can provide an accurate frequency spectrum. However, for larger excitations the effects of geometric non-linear modal interactions should be included in the vibration analysis [38]. The results of previous research illustrate the need of a complete understanding of linear and non-linear analysis for the case of cylindrical and doubly curved shells, which can have large deformations under earthquake. This will be investigated in this research. It might lead us to realizing the necessity of using non-linear shell theory in earthquake design of shell structures, as well as clarifying the nature of the non-linear modal coupling.

1.5.2 Free vibrations of single and doubly curved shallow shells

An early attempt for free vibration analysis of single-curved shallow shells was undertaken by Vlasov [39]. An extensive literature is available on the free vibration of single-curved shallow shells and is summarized by Qatu [40] and Liew et al [41]. The literature on the free vibration of spherical shallow shells is also extensive. It started with the work of Lamb in 1882 [42]. Most of the free vibration studies on the doubly-curved shell before 1970's are related to spherical shells; these are summarized by Liessa [43]. This concentration on spherical shells is mainly because of two reasons: firstly, the relative mathematical simplicity of equations in comparison with more general doubly-curved shells; and, secondly, the widespread use of this type of shell. However, free vibration of doubly curved shallow shells having curvilinear planform, has received relatively little attention compared to related work carried on cylindrical shells. It is mainly due to the difficulty in considering the curvatures in two

perpendicular directions and satisfying the in-plane and out-of-plane boundary conditions. The literature related to free vibration of doubly curved shells through the early 70's was summarized by Leissa [43]. In 1970 a computational study using doubly curved finite elements of triangular shape was performed by Cowper et al [44]. Olsen and Lindberg [45] continued the study and performed a free vibration analysis for shallow shells by developing an arbitrary doubly curved shallow element, which included variation of thickness. Their element incorporated a complete quadratic polynomial for the normal displacement and complete cubic for the tangential displacements [45]. However the tangential inertias were neglected. In chapter 8 the effect of neglecting tangential inertia on the resulting natural frequencies will be investigated. The resulting natural frequencies using their method were in good agreement with the analytical solutions and experimental results. Later, Liew and Lim [46] investigated free vibration of doubly curved shallow shells with a rectangular planform, where they investigated the effect of different boundary conditions on shells with positive (elliptic paraboloid) and negative Gaussian curvature (hyperbolic paraboloidal). They verified the resulting frequencies using their approach with available literature and experimental result. New results were also reported for shells with various ranges of aspect ratio, curvature ratio and shallowness. Free vibration of doubly curved shallow shells were analyzed by Chaudhuri and Kabir [47], [48], Chakravorty et al [49], Singh and Kumar [50], Narita et al [51]. The most recent literatures related to free vibration of doubly-curved shells are reviewed by Qatu [6], [52], Liew and Lim [41], and Alhazza [53]. However, there are only a small number of publications that have dealt with the forced vibration of doubly curved shells.

1.6 Previous research on response of roof shells to earthquake

As mentioned earlier thin roof shells are once again being recognized and increasingly adopted as efficient means of covering large spaces. It is surprising to see so little research has been performed on the behaviour of roof shells under earthquake loading.

Jiashen and Lei are among the first who studied the behaviour of shells under earthquake loading using Fourier series (1991) [54]. It was in 1995 that the effects of initial stresses on the vibration behaviour of shell like roofs were investigated by Yamada [55][56]. These studies were inspired by many roof shells in deep snow regions of Japan, which are also located in seismically active regions. In an earlier paper Yamada proposed a method to estimate the frequencies of shell by taking into account the initial stresses [57]. This was done by the assumption that the lowest frequency approximately occurred at the same mode as static critical buckling mode. Although the minimum frequency does not always occur at the same mode as the static critical buckling mode, they argued that this idealisation provided a good estimate for an approximate analysis method. Using this method they showed that as the ratio of pre-loading to critical load increases the frequency decreases. The roof shell was then excited by a sinusoidal external force and the maximum displacements for frequencies up to 3 Hz were derived for a perfect shell with two different ratios of pre-loading to critical load and compared with the displacement results using FE method. The resulting displacements were in good agreement with the results using FE method however the increase in the ratios of pre-loading to critical load did not necessarily result in a higher displacement response. The displacement was then derived for a shell considering the effect of reduction in membrane stiffness corresponding to one of its mode caused by imperfections on linear steady state response using the same sinusoidal loading. The result using the reduced stiffness method gave an upper conservative estimate for design in comparison with the full stiffness modelling [56]. In this research [55]-[57] shell was subjected to external force with a frequency up to 3 Hz. However, it is expected that if the shell was subjected to earthquake loading having wider frequency content the results would reveal more information on the behaviour of shells which have wide ranges of natural frequencies. This would allow better understanding of the behaviour of each mode in response to initial stresses during a typical earthquake loading. The dynamic response to periodic loading was also not compared for the cases of neglecting and including initial stresses.

In another paper Yamada reported the results of his investigation on vibration behaviour

of single-layer latticed cylindrical roofs, where he modelled a lattice shell using the continuum analogy [8]. The structure was then subjected to a vertical sinusoidal excitation, while the effects of in-plane inertia were neglected. He concluded that latticed shells can be effectively modelled using an orthotropic continuum analogy method. He also concluded that an increase in pre-motion loading would cause a decrease in frequency and an increase in maximum amplitude of dynamic deflection component. He also showed that using the reduced stiffness method would result in a higher response spectrum and would give upper conservative estimate for design. In his later research Yamada and his colleagues [9] investigated the seismic response behaviour of single layer latticed shell. They investigated the fundamental earthquake response behaviour of this kind of structure using a FE method. This showed that there was a direct correlation between strain energy and axial force responses. However, there was not any relation between acceleration and axial forces. They proposed an equivalent static load modelling for seismic design. The distribution of the seismic loading was modelled based on the distribution of the strain energy response. They showed that the resulting axial force using the equivalent static load is in good agreement with the resulting axial force using a dynamic analysis. However it seems that only a few modes have been considered in the analysis. Moreover they have considered Rayliegh damping equal to 2% damping ratio for the first two modes with the lowest frequency in the rank order. This causes the damping to increase as a proportion of critical damping for the modes outside the range between the two selected modes. This selection of modes (the first two modes with lowest frequencies) itself eliminates the contribution of modes with higher frequencies. These assumptions undermine the effects of these modes with higher frequencies, which could potentially have a significant effect on the response. The effect of modes with higher frequencies will be shown later in this research. Also bending moment resultants were not looked at in Yamada's study [9]. As will be demonstrated in the present study, earthquake loading can cause high bending moment stresses in shells, which cannot be overlooked.

In another paper Yamada et al derived the equivalent static seismic load based on the distribution of displacement for a simply supported cylindrical shell [58]. Using equiv-

alent static loading and taking advantage of an equivalent continuum shell analogy they found the maximum displacement and forces of a latticed roof shell subjected to earthquake loading, which gave reasonably conservative results in comparison with the results obtained from the dynamic analysis yet a simple seismic design. However only a few modes were considered in the study and they claimed the influence of the high frequency vibration modes did not become predominant. But as it will be discussed in future chapters many modes should be included in the analysis of roof shells to find a converged response and higher modes could influence the results significantly, especially bending moment results.

In 1995, Kobe, a modern city was struck by $M = 7.2$ earthquake that caused serious and widespread damages to buildings, and infrastructure. However, shell and space frames of gymnasiums and school were not seriously affected and could serve as shelters for those who lost their homes. In an attempt to assess the maximum responses and check the efficiency of roof shells, Kuneida in 1997 investigated the response of cylindrical roofs subjected to Kobe earthquake conditions [7]. He mentioned that there was no seismic code available for the design of space structures that were built in Japan and those space structures that were built did not always follow the seismic code for buildings. He also investigated the response of domes to earthquake but as there were no domes constructed in Hanshin district, where the earthquake happened, he preferred to investigate their responses subjected to an earthquake with the same pattern as Kobe but with a maximum acceleration of 1/8 of the acceleration magnitude of Kobe earthquake. He scaled down the acceleration of Kobe earthquake to be equal to the maximum acceleration of another earthquake that he had considered in a previous study, in order to compare the responses of domes under these two earthquakes. Kuneida derived the maximum responses of cylindrical roof shells and domes with different geometries and material properties. However, in order to reduce the computing time he modelled them as a continuous shell. The results of the investigation showed the stresses in cylindrical shells became very large especially for in-plane shear stresses when subjected to the horizontal component of the earthquake. Other stresses were also significant for both horizontal and vertical earthquakes. Nonetheless despite the very

large stresses induced in the shell modelled by Kuneida the cylindrical roof shell in the area of earthquake were not seriously damaged. The stress responses of the domes were much less than the cylindrical shell. However, as previously mentioned domes were subjected to an earthquake with the maximum acceleration much less than Kobe earthquake, so it was not possible to compare the level of stresses in domes with the cylindrical shells. Although Kuneida did not implement any modal combination rule to estimate the maximum responses but he suggested that the square root of the sum of squares (SRSS) estimation of the maximum response might not be valid for roof shell. The reason would be because of the closeness of natural frequencies in shells. Unfortunately as the geometry and material properties were not reported in his paper it was not possible to undertake comparative studies with Kuneida's reported results.

In 2004 Chen et al [59] investigated the dynamics characteristics of single-layer cylindrical lattice shells. They indicated that although there are extensive theoretical and experimental investigations on the stability of lattice cylindrical shell there is insufficient research dealing with the dynamic characteristic and seismic responses of lattice shells, especially for single-layer lattice shells. They suggested that there are insufficient guidelines for earthquake resistant design of cylindrical lattice shells. However they did not use the continuum shell analogy, and they modelled individual members of the lattice shell as three-dimensional beam elements. They continued their study by finding the effects of structural parameters such as rise to span ratio, damping, and ratio of length to span, on the responses of lattice shell members to earthquake loading using a direct integration method. However their study is limited to the effect of these ratios on natural frequencies and internal axial forces. They used Rayleigh damping in which a damping ratio equal to 2% for the mode with minimum and maximum frequency was considered, which means lower damping for the modes in between. Then they checked the effect of different damping ratios of 1%, 3%, 4%, and 5% for modes with lowest and highest frequencies using Rayleigh damping equation. The results showed a 25% and 15% decrease in the vertical and horizontal seismic induced internal axial forces in members, as a result of an increase in damping ratio from 1% to

5%. Using Rayleigh damping and allocating a constant damping ratio for the first and last modes, increases the participation of modes with higher frequency. It is because using the Rayleigh damping model creates lower damping ratios than the allocated damping ratios of the two selected modes for all modes between these two selected modes, while it produces higher damping ratios for any modes having frequencies outside the range of frequencies of these two modes. As the two selected modes in their study corresponds to modes having lowest and highest frequencies, so all modes have lower damping ratios than these two modes. However with a different damping model or with a different selection of modes instead of just the first and last modes, many of these modes correspond to modes with higher frequencies might have higher damping ratios, which consequently would produce insignificant results. They do not appear to have investigated the effects of different damping models such as considering a constant damping ratio for all modes. They did show that the rise to span ratio had a significant effect on the seismic responses of a cylindrical lattice shells. For a large rise to span ratio the response to horizontal earthquakes was higher than to vertical earthquakes, and vice versa when this ratio decreased. They also suggested that as the natural frequencies of lattice shell were close to each other, higher numbers of modes should be considered in the dynamic response analysis. However, they did not give any advice on the required number of modes for a converged response.

In an earlier paper, Chen et al [60] analyzed the dynamic response of single layer reticulated shells under earthquake loading considering both material and geometric nonlinearities. In this analysis the members of the reticulated shell were modelled by nonlinear three-dimensional beam elements. The elements had six degrees of freedom at each node, which could transmit an axial force, two bending moments, two shear forces and a torque. Then they used the finite element method, in which a nonlinear three-dimensional beam element was employed. As an example they considered a single-layer reticulated spherical shell. They performed a nonlinear analysis taking into account both material and geometric nonlinearities and compared the results with a linear dynamic responses that were found for the first 20 modes in rank order. The results of the comparative study showed for strong earthquake linear analysis under-

estimated the axial forces and nodal displacement. They have not however reported any results for the bending moments. In 2003 Shizhao et al [61] performed a numerical study on the free vibration properties and dynamic response of single layer latticed cylindrical shell with pin joint supports to horizontal and vertical component of earthquake. They modelled latticed shell as space frame with the rigid connections between joints and did not use the equivalent shell section. They mentioned the seismic design code for latticed shell is not available in China, suggesting that it is due to the complex behaviour of this kind of structure. Based on their opinion, understanding the behaviour of latticed shell demands a huge calculation and research effort. They studied the effect of rise-span ratio, length-span ratio, surface load, and member sizes on natural frequencies and concluded single layer latticed cylindrical shell have a very closely distributed natural frequencies as it is also shown in the present research. They also showed the decrease in rise-span ratio caused an increase in natural frequencies, and by increasing length-span ratio more mode shapes exhibit vertical vibration along the longitudinal direction. This is an obvious conclusion, because with increasing the length in longitudinal direction more half-waves can be created in that direction. The effect of the increase in surface load was treated as an increase in the mass of the structure in their study, which reduces the natural frequencies. A complete investigation on the effect of surface load will be presented in Chapter 5. It was shown that the increase in member sizes increases the frequencies as a result of increase in structure overall stiffness. Their investigation was continued by finding the effect of above mentioned ratios on the axial and bending stresses in members of latticed shell when subjected to vertical and horizontal earthquake and also the bending and axial stresses due to static load equal to gravity applied in vertical and horizontal directions. They considered three earthquakes, two real and one artificial earthquake. However they did not mention how many modes they have considered in the time history modal analysis. They concluded that higher stresses in shell members are produced when subjected to horizontal earthquake in comparison with when it is subjected to vertical earthquake, which as will be shown in the present research it is not always true. Finally using the relation between dynamic and static stresses in members they proposed a factor

to convert bending and axial stresses produced as a result of a static loading equal to gravity load to dynamic stresses resulting from earthquake for different rise to span ratios. However, their study is based on considering only three earthquake loads, but as will be discussed in this research the stress responses of shells are very dependent on the natural frequencies of shell and frequency content of the earthquake. This makes it difficult to propose a reliable factor to relate the stress responses due to static load to stresses resulting from earthquake loading. They suggested the reason for finding a factor to relate the static stresses to dynamic stresses was because the complete quadratic combination (CQC) method can not be used in such complicated structures and time history analysis method requires a lot of computing time and skillful engineers. However, they have not presented any result indicating that CQC method gives wrong estimation of results. The reliability of the modal combination methods such as square-root-of-sum-of-squares (SRSS) and CQC will be investigated in Chapter 6.

In 1997 Kato et al [62] investigated the dynamic response behaviour of single layer reticular domes subjected to only horizontal component of earthquake. They found equivalent static seismic forces applied to domes. Their proposed equivalent static seismic force coefficients were different for high rise domes having half open angle greater than 60 degree with the one for low rise domes having half open angle less than 60 degree. It was because in low rise domes more modes were participating in the total response. However, they did not use the equivalent continuum shell analogy. Members were assumed to be rigidly connected at the nodes. Three elasto-plastic hinges were also placed at two ends and one in the middle to simulate the plasticity of members when over stressed. In a later contribution, Kato et al investigated the effects of spatially nonuniform ground motions on space structure [63]. In this research a gable cylindrical steel structure was used for which the effect of phase shift effect was investigated along two lines supports. The earthquake was considered uniform along each line. A new average response spectrum was proposed for this case for which they modelled the earthquake as a combination of two parts. In the first part, a uniform acceleration equal to the average of the acceleration at each line was applied to the

supports in the same direction. While in the second part, acceleration equal to half of the difference between the acceleration at each line was applied at each line in the opposite direction. The investigation showed that the internal forces generated in some members increased when the wave passage effect was included. It should be noted that their method is only applicable to systems with linear elastic behaviour and it is unable to take into account the structural nonlinearities.

In 2005, Tatemichi and Kato reported the damages to roof shells during recent earthquakes [26]. They indicated that seismic performance requirements were not currently available in the Japanese technical standards for the serviceability and ultimate levels of response of spatial structures to earthquakes. In the light of the recent damages to spatial and shell roofs and also the uniqueness of shell and spatial structures, both in respect to structural behaviour and their performance requirement especially after earthquake for sheltering people, they proposed a method for presenting the seismic performance of these classes of structure. They proposed that the performance targets should be taken into account in the level of functionality expected from structures. For example, certain criteria should be included in the design process for the case of spatial structures if they are expected to remain completely functional after earthquake as refuges for people. One of these criteria is the stress level that should remain less than the allowable stress for ground motion with a return period of 475 years. However, they recognized that further investigation is needed to define these design criteria [26].

1.7 Objectives and scope of the thesis

Despite the growing popularity of thin shells as efficient solutions for covering large column-free spaces, there is a surprising scarcity of analysis looking at their response to dynamic loads. Especially in seismically active regions, this paucity of analysis could be of considerable significance. Having reviewed past works concerning some aspects of shell structures and identified the problems in the dynamic behaviour of shells under earthquake loading the main object of the present research is to investigate a number of seemingly neglected aspects of the dynamic behaviour of roof shells. These aspects could affect the response of roof shells under earthquake loading and consequently im-

pact upon their design. However, much of the work also applies to the response under other dynamic loading conditions, particularly the detailed studies related to modes and frequencies.

To ensure an adequate theoretical basis for this study, a verification study is provided using two independent methods of analysis - a finite element solution and a newly developed analytical method. For typical cylindrical shell roofs these methods are used to determine the spectra of natural vibration modes. A second verification involved the prediction of the displacement and acceleration responses of the shell under the action of the vertical motions of a typical earthquake, again using both the analytical and FE methods.

Of practical importance are the numbers of modes required for accurate prediction of displacement, acceleration, and stress responses for a specific geometry of shell. Using a typical study in which the number of rank order modes is gradually increased allows investigation the convergence patterns for displacement and acceleration responses.

This study also explores the participation of the modes in the stress response as well as displacement and acceleration responses and gives some recommendation on the required number of modes in design.

Of the limited past investigations on how thin shell roofs respond to earthquakes, attention has been restricted to consideration of just the out-of-plane modes, with the contributions from the in-plane modes usually neglected. In this research the importance of the inclusion of in-plane modes for a cylindrical shell subject to vertical and horizontal components of typical earthquake loading is also investigated.

Moreover, this research assesses the relative importance of the horizontal and vertical components of one earthquake on the responses of shell. It should be mentioned that the chosen earthquake has a high ratio of vertical to the horizontal component, which can occur in near-field events with specific characteristics. Therefore the relative importance of the horizontal to the vertical components of earthquakes are valid for near-field earthquakes.

In the limited previous studies of how thin shell roofs respond to earthquakes, attention has been largely restricted to linear analysis, with contributions from pre-loading usu-

ally neglected. The present research analyses the effects of pre-loading on the natural vibration spectra, again using two independent methods of analysis - a finite element solution and a newly developed analytical method. In the finite element modelling, vibrations are determined about a geometrically nonlinear primary equilibrium path, while the analytical method is based on a membrane idealization of this primary state. The analytical method adopts an explicit solution using Love-Timoshenko strain-displacement relationships and employs a Lagrangian approach to derivation of equations of motion. These independent approaches allow assessment of the reliability of analysis and more conveniently allow questions such as what are the effects of inclusion of self-weight and additional superimposed loading on the predicted natural frequencies. Another section of this research assesses the importance of the inclusion of pre-loading on the displacement, acceleration, and stress responses of a set of cylindrical roof shells, having different geometries, when subject to the vertical motions of a typical earthquake. Again to provide independent confirmation of predictions, results from both the analytical and FE methods are reported. A final section compares the levels of response to earthquake for cylindrical and doubly curved shells.

Initially, Chapter 1 gives a history of roof shells and outlines the importance of roof shells in the infrastructure of a society. It looks at the problems involved in the construction of roof shells, and provides an indication of past attempts to determine the dynamic response of roof shells.

The theoretical background for complete cylindrical shells is reviewed in Chapter 2. Included are the basic assumptions necessary to develop analytical solutions based on the thin shell theory and the criteria used for defining shells and shallow shells. In addition, Chapter 2 discusses a brief development of different shell theories and compares the resulting frequencies calculated using these shell theories; an appropriate shell theory formulated as differential equations of equilibrium is then selected for the current research. Furthermore, the background to the total potential energy of equilibrium state is established. It is based on the principal of stationary of total potential energy. It states that in a particular configuration, a structure can be in equilibrium only when the total potential energy is stationary. As a result, the individual energy components can be

expressed in terms of stresses and strains.

Having established the theoretical background, it is then possible to derive the analytical solution for the dynamic analysis of open cylindrical shells in Chapter 3. This chapter explains the analytical method based on the superposition of modes for the case of an open cylindrical roof shell under earthquake loading. It also compares the resulting frequencies with those previously reported in the literature. The newly developed analytical method allows the investigation of the extent to which the shell response is influenced by factors such as: the importance of different modes in the response; the adequate number of modes for a converged displacement/acceleration and stress resultant response; the relative importance of vertical and horizontal earthquake through a parametric study; the importance of including in-plane inertia in response.

It was earlier noted that the parameters controlling the response of roof shells to earthquake were incompletely reported. This means it is not possible to directly compare the result of the analytical method with them. As an alternative check on reliability Chapter 4 compares the results of the analytical solutions in Chapter 3 with results found using a FE method; ABAQUS, a commercially available FE programme, is used for this purpose. With the use of ABAQUS, frequency results and the earthquake responses of cylindrical shells are compared.

Investigation of the dynamic behaviour of roof shells continues in Chapter 5 with a study of the importance of including pre-loading such as self-weight and snow in the resulting frequency spectrum and consequently the earthquake response.

Chapter 6 then addresses the accuracy of modal combination rules for estimating the critical dynamic response conditions for roof shells. In particular, two modal combination rules, SRSS and CQC methods are considered.

Chapter 7 deals with the verification of the results of Chapter 5 using FE method. Having derived the linear response of cylindrical roof shells under earthquake loading, Chapter 7 concludes with an investigation of the nonlinear dynamic analysis of roof shells under earthquake loading.

Among the few studies on the response of roof shells to earthquake most relate to cylindrical shells. Chapter 8 develops the equations for the response of doubly curved shells

to earthquakes. This allows investigation of the effect of introducing a curvature in another direction on the behaviour of shell responses such as, maximum displacement and stress responses. Furthermore, Chapter 8 compares the required number of modes for a converged result for a doubly curved shell in comparison with a cylindrical shell. And finally, Chapter 9 presents the conclusion of the present study and suggests some areas for the future study.

Chapter 2

Analytical Modelling of Complete Cylindrical Shell

This chapter outlines a number of simplified forms of the basic equations of shell theory. It starts with a brief history of early attempts towards the development of shell theories.

The aim of this chapter is to compare the natural frequencies of shells found using the selected shell theory in the present research with the other available data in the literature. The shell theories, discussed in this chapter are all based on the Love's approximation and adopt the differential equation formulation for deformation of the middle surface for shells. The material is considered to be linearly elastic, isotropic, and homogeneous, and the equations are derived on the basis of small deformation, yielding to linear equations.

2.1 Shell theories

Before the Renaissance design of structures was largely based on experience, it then replaced by experiment. In 1660, Hook proposed the first equation, nowadays known as the elasticity equation, relating the linear relationship between forces and deformation.

In 1816, the first attempt to investigate general theory of plate was made by Germaine [64] [53]. She was the first who developed linear isotropic plate theory. However her

equations contained some errors, which Lagrange noticed and corrected. A further attempt to find the theory of plate was made by Poisson. He assumed that plates consist of particles with molecular forces in between them. He then found the equilibrium equation for plates with the assumption that all particles are distributed in the middle plane of the plate [65].

In this regard Navier must be credited with finding the first satisfactory theory of bending of plates. Like Poisson he assumed that plates consist of molecules but he distributed them through the thickness and assumed during bending their displacements are parallel to the middle plane of the plate and proportional to the distance from that plane.

In 1850 Kirchhoff [65] published his important paper on the theory of plates. At the beginning of his paper he mentioned the first attempts to obtain the differential equation of plate by Sophie Germain and Lagrange's correction of her mistake. He also discussed the shortfalls of Poisson's theory. But he did not mention Navier's differential equations for bending of plates. His theory was based on two assumptions, first that each line initially perpendicular to the middle plane remains straight during bending and remain normal to the middle surface and, secondly, neglect of any stretching during small deflection in the middle plane of a plate under lateral loading.

In 1874, Aron derived five equations in curvilinear coordinates, based on general theory of elasticity. He showed that his equations would reduce to those of the equations for plates [66][53] for zero curvatures. However, the interaction between the effects of membrane and bending remained one of the difficulties in the theory of shells. In 1881, Lord Rayleigh [67] [68] was investigating the natural frequencies of bells. His professional interest in church bells led him to the conclusion that the deformation would be inextensional for a thin hemisphere bowl. Then he developed a solution for finding natural frequency, in which the membrane strain energy was neglected. In 1888 Love showed that for thin shells the dominant effect is that due to membrane action rather than bending [69]. He then derived the equations governing the behaviour of thin elastic shells based on Kirchhof's assumptions.

Development of thin shell theory continued into 20^{th} century. The equations of Love can be considered as the basis for the development of shell theories for vibration of continuous structures with small thickness such as those of Galerkin [70], [71]. Galerkin developed a method to find shell equations from the general theory of elasticity [70]. His method was used by many researchers such as Lur'ye [72], Valsov [39], [73], Novozhilov [74], Vorovich [75], Mushtari [76], [77], Gol'denveiser [78], [79]. Many shell theories developed were based on Love-Kirchhof assumption such as the derivation of three simultaneous partial differential equations in terms of in-plane and out-of-plane displacements by Flugge [80]. He did not ignore the ratio of thickness to the smallest radius of curvature in his equations. In the early 20^{th} century, Donnell developed a theory simpler than Flugge's theory. In his theory, in-plane and out-of-plane displacements appeared in uncoupled form and the equations were easier to solve than those of Flugge. In 1956, Knowles and Reissner [81] generalized the equations based on Love-Kirchhoff assumptions. They adopted an arbitrary orthogonal coordinate system in the middle surface of shell. Green and Zerna [1] enhanced the simplification by adopting non-orthogonal coordinate curves in the middle surface. In 1959, Sanders [82] improved the shell theory based on Love- Kirchhoff assumptions. Then during 1960's, Novozhilov [83] formulated the general theory of shells. His theory involved eighth-order equations. However, Koiter showed that Novozhilov's equation did not adequately describe the axisymmetric deformation of a helicoidal shell [1]. Later, Sanders and Budiansky (1963) derived a first order linear shell theory [84]. They used general tensor notations in terms of an arbitrary coordinate system for the middle surface. This method, later known as Sanders-Koiter equations, provided the first equations which finally resolved the essential conditions of consistency and accuracy. In 1967, Sanders achieved a complex transformation by avoiding any approximation in the equilibrium and compatibility equations or any other relations except for the constitutive equations. However, his method might not be accurate for all classes of shell [1].

Thereafter, various strain-displacement equations have been introduced by researchers to improve the general thin shell theory and some specialised theories for specific geometries of shells. Each of them made some assumptions in the real behaviour of shell elements. There have also been considerable discussions on whether or not the differences between these shell theories are significant. Many of shell theories use common equations and some of them are duplications of another. An excellent summary of research on the vibration aspects of thin shells before 1970 was completed by Leissa [1], where he has included more than 1000 references and categorized and compared the developed shell theories. Among all different theories proposed by different researchers the ones chosen and categorized by Leissa [1] are used in this study for comparison of the resulting frequencies. He categorized them into the theories proposed by

- Byrne [85], Flugge [86], Goldenveizer [78], Lur'ye [72], Novozhilov [87]
- Love [88], and Timoshenko [89]
- Reissner [90], Naghdi [1], and Berry [91]
- Vlasov [73][92]
- Sanders [82]
- Donnell [93], and Mushtari

All these theories are all based on Love's first approximation.

Love made four assumptions in the classical theory of small displacements of thin shells, which later became the basis of many shell theories. His first assumption considers the thickness of the shell, h, to be small in comparison to other dimensions such as the radius of curvature, R. This assumption allows the higher powers of h/R to be neglected in comparison to unity. The second assumption assumes strains and displacements to be very small. Therefore, the higher order terms in the strain-displacement relations can be neglected compared to first order term. This allows all calculation to

be performed about to the original shape of the shell and the differential equations to be linear. Since the thickness of the shell is very small, third assumptions considers the transverse stresses normal to the middle surface of the shell to be very small in comparison to the in-plane stresses. Hence the normal stresses, σ_z, are negligible. The Fourth assumption forces normals to the undeformed middle surface of the shell to remain normal to the deformed surface of the shell. This assumption is also known as Kirchhoff hypothesis. Use of the Love's assumption (Kirchhoff hypothesis) restricts the in-plane displacements u and v to vary linearly through the thickness. As a consequence of the fourth assumption, often referred to as the Kirchhoff's hypothesis the following relations should be satisfied.

$$\begin{aligned} \gamma_{\alpha z} &= 0 \quad (a) \\ \gamma_{\beta z} &= 0 \quad (b) \\ \epsilon_z &= 0 \quad (c) \end{aligned} \tag{2.1}$$

where (α, β) are a set of orthogonal in-plane coordinates, $\gamma_{\alpha z}$ and $\gamma_{\beta z}$ are the in-plane shear strains, and ϵ_z is the normal strain. Using the Hooke's Law the transverse shear stresses would also vanish

$$\sigma_{\alpha z} = \sigma_{\beta z} = 0. \tag{2.2}$$

However eqn (2.2) raises some contradictions since shear stresses and their integrals are used to find the transverse shear forces needed for equilibrium. These contradictions will be discussed in Section 2.2.

A complete discussion on the selected thin shell theories and the force and moment resultant based on these theories can be found in Reference [1]. The differences between these theories are largely due to the simplifying assumptions. In order to compare the equations of motion based on these theories, Leissa introduced the Donnell-Mushtari [43] theory, in which the contribution of bending shears, q_x, and q_y, to the equilibrium in the tangential directions were ignored. Then he introduced a modifying factor operator, which transforms the Donnell-Mushtari operator to form another shell theory and summarized different shell theories such as, Love-Timoshenko [88], [89], simplified Goldenveizer-Novozhilov [78], [87], Flugge-Byrne-Lur'ye [86], [85], [72], Biezeno-

Grammel, Reissner-Naghdi-Berry [90], [91], Sanders [82], Vlasov [73], [92], Epstein-Kennard [30], [31], and Kennard simplified [32]. The equations of motion based on these various theories, which are presented in 2.4.3, were extensively used by other researchers in recent years. The resulting natural frequencies based on these theories, calculated by Leissa, are presented in Section 2.5.1, and compared with the resulting frequency parameter based on the theory chosen for the present study.

Although most parts of Leissa's review were related to circular cylindrical shells, having different boundary conditions, variable thickness, effect of added mass and other complicating factors, it also dealt with different types of shells such as conical, spherical, ellipsoidal, and paraboloidal plus a section on the nonlinear complicating factor.

A more recent review on the development of research in vibration of shallow shells and specifically laminated composite shallow shells was published by Qatu in 1992 [40]. In 1997 Liew and Lim [41] undertook another survey, which completed the work of Leissa and Qatu by covering the literature from 1970 to 1997 with coverage of the Love-Kirchhoff, first-order, and higher order shallow shell theories. It also covered the three-dimensional elasticity analysis of thick shells. Later in 2002 Qatu reviewed 606 articles on shell theories and free vibration of shells [6]. He categorized them in terms of different shell theories such as thin, thick, 3D, nonlinear; different geometries such as cylindrical, conical, spherical; various analysis methods such as exact, Ritz, finite elements; and different complicating effects such as imperfection, elastic support, interaction with fluids. It is worthy to mention that the focus of the present research is on thin and shallow shells having single and double curvatures.

2.1.1 Thin shell theory

Shells are mostly categorized by their thickness. If the shell thickness is less than $1/20$ of the wavelength of the deformation, it can be classified as a thin shell. As explained earlier, shear deformations and rotary inertia are negligible in thin shells. Depending on various assumptions made in deriving the strain-displacement relations, stress-strain relations, and equilibrium equations, various shell theories have been developed. A short description of these theories is discussed earlier in this section. However, a more

complete discussion of different thin shell theories are available in [1]. It is shown that most thin shell theories yield similar results [1]. The only exceptions are theories based on the Donnell-Mushtari approximation, which are only valid for shallow shells.

2.1.2 Shallow shell theory

Another important factor in categorizing shells is the shallowness of the shell. When the rise of the shell is less than $1/5$ of the smallest planform dimension it is considered as shallow shell. Shallow shell theory was originally derived by Donnell and Mushtari for isotropic material. Shallow shells can be thin or thick single or doubly curved shells. Shallow shell equations can be derived from the equations of doubly curved shells by replacing the curvilinear coordinates with the Cartesian coordinates for shell with rectangular planform, and polar coordinates for shells with circular planform. The literature on shallow shell vibration research is reviewed by Qatu (1992) [94] and Liew and Lim (1997) [41]. In the present study, the doubly curved shells are considered to be shallow. For shallow shell it is assumed that the curvature of the shell and its variation are very small over the whole surface. This allows the actual lengths measured over the surface to be considered as their projections. Moreover, the in-plane forces are measured to be the principal forces.

2.2 Stress and moment stress resultants for shell element

A complete relationships between strains and displacements using different shell theories based on Love's first approximation are presented in [1]. Using Hook's law, the relationships between stresses and strains can be defined. The resulting stresses are then derived by integrating the stresses over the shell thickness. The resultants of the integrals are called "stress resultants" and "moment stress resultants" in the present research. The stress and moment stress resultants have dimensions of force per unit length and moment per unit length, respectively.

As mentioned above Hook's law is assumed as the constitutive law, so the material considered should be linearly elastic. For a three-dimensional element the Hook's law

is written as

$$\begin{aligned}
\epsilon_\alpha &= \frac{1}{E}[\sigma_\alpha - \nu(\sigma_\beta + \sigma_z)] \\
\epsilon_\beta &= \frac{1}{E}[\sigma_\beta - \nu(\sigma_z + \sigma_\alpha)] \\
\epsilon_z &= \frac{1}{E}[\sigma_z - \nu(\sigma_\alpha + \sigma_\beta)] \\
\gamma_{\alpha\beta} &= \frac{2(1+\nu)}{E}\sigma_{\alpha\beta} \\
\gamma_{\alpha z} &= \frac{2(1+\nu)}{E}\sigma_{\alpha z} \\
\gamma_{\beta z} &= \frac{2(1+\nu)}{E}\sigma_{\beta z}
\end{aligned} \tag{2.3}$$

in which σ_α, and σ_β are the normal stresses, $\sigma_{\alpha\beta}$, and $\sigma_{\beta\alpha}$ are the in-plane shear stresses on respectively the α, and β constant faces, $\sigma_{\alpha z}$, and $\sigma_{\beta z}$ are the transverse shear stresses (Fig 2.1), E is the modulus of elasticity, and ν is the Poisson's ratio.

The moment equilibrium of a typical infinitesimal element result in $\sigma_{\alpha\beta} = \sigma_{\beta\alpha}$, and Kirchhoff hypothesis, puts constrains on the strains $\epsilon_z = \gamma_{\alpha z} = \gamma_{\beta z} = 0$, which together with eqn (2.3) leads to $\sigma_{\alpha z} = \sigma_{\beta z} = 0$, and $\sigma_z = \nu(\sigma_\alpha + \sigma_\beta)$.

However, it is worth noting that there are some contradictions between the assumptions. One arises from Love's third assumption, which considers the transverse normal stress, σ_z, to be negligibly small, whereas assuming $\epsilon_z = 0$ leads to $\sigma_z = \nu(\sigma_\alpha + \sigma_\beta)$. Another contradiction is that despite considering $\gamma_{\alpha z} = \gamma_{\beta z} = 0$, $\sigma_{\alpha z}$, and $\sigma_{\beta z}$ are non-zero terms, since their integrals must supply the transverse shear forces needed for equilibrium, however they are negligibly small in comparison with σ_α, σ_β, and $\sigma_{\alpha\beta}$ [43].

Retaining the assumption that σ_z is negligibly small reduces eqn (2.3) to

$$\begin{aligned}
\epsilon_\alpha &= \frac{1}{E}[\sigma_\alpha - \nu\sigma_\beta] \\
\epsilon_\beta &= \frac{1}{E}[\sigma_\beta - \nu\sigma_\alpha] \\
\gamma_{\alpha\beta} &= \frac{2(1+\nu)}{E}\sigma_{\alpha\beta}
\end{aligned} \tag{2.4}$$

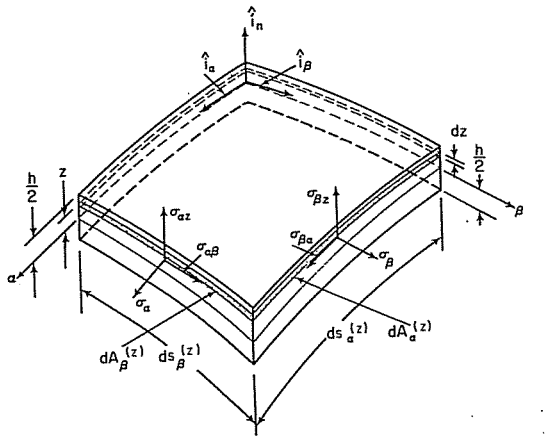

Figure 2.1: Positive directions of stress in shell (Figure taken from [1])

which gives

$$\begin{aligned}\sigma_\alpha &= \frac{E}{1-\nu^2}(\epsilon_\alpha + \nu\epsilon_\beta)\\ \sigma_\beta &= \frac{E}{1-\nu^2}(\epsilon_\beta + \nu\epsilon_\alpha)\\ \sigma_{\alpha\beta} &= \frac{E}{2(1+\nu)}\gamma_{\alpha\beta}\end{aligned} \tag{2.5}$$

Now, the stress resultants acting on faces in Fig 2.1 can be developed from integrating the stresses acting on each face over the thickness of the shell (Figs 2.2, 2.3). For example the stress resultants acting on a face perpendicular to axis α is equal to the multiplication of arc length of the intercepts of the surface, $ds^z_\beta = B(1 + z/R_\beta)d\beta$, by the stress. So the equivalent stress resultant, N_α, is given by integrating $\sigma_\alpha ds^z_\beta$ over the thickness of the shell and dividing by $B\ d\beta$, which has the unit of force per unit length of the middle surface. The stress resultants acting on the face perpendicular to α axis (Fig 2.2) can be presented as

$$\begin{Bmatrix} N_\alpha \\ N_{\alpha\beta} \\ Q_\alpha \end{Bmatrix} = \int_{-h/2}^{h/2} \begin{Bmatrix} \sigma_\alpha \\ \sigma_{\alpha\beta} \\ \sigma_{\alpha z} \end{Bmatrix} \left(1 + \frac{z}{R_\beta}\right)\ dz \tag{2.6}$$

Similarly, the stress resultants on the face perpendicular to the β-axis (Fig 2.2) are

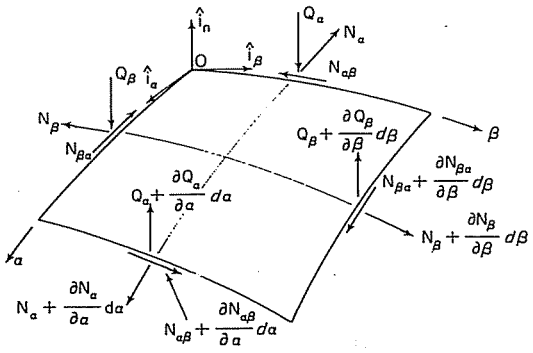

Figure 2.2: Positive directions of membrane stress resultants in shell coordinates (Figure taken from [1])

$$\begin{Bmatrix} N_\beta \\ N_{\beta\alpha} \\ Q_\beta \end{Bmatrix} = \int_{-h/2}^{h/2} \begin{Bmatrix} \sigma_\beta \\ \sigma_{\beta\alpha} \\ \sigma_{\beta z} \end{Bmatrix} \left(1 + \frac{z}{R_\alpha}\right) \, dz \tag{2.7}$$

The moment stress resultants on an α constant face about the tangential and normal axes (Fig 2.3) are respectively presented as

$$\begin{Bmatrix} M_\alpha \\ M_{\alpha\beta} \end{Bmatrix} = \int_{-h/2}^{h/2} \begin{Bmatrix} \sigma_\alpha \\ \sigma_{\alpha\beta} \end{Bmatrix} \left(1 + \frac{z}{R_\beta}\right) \, z \, dz \tag{2.8}$$

and similarly on the β constant face (Fig 2.3)

$$\begin{Bmatrix} M_\beta \\ M_{\beta\alpha} \end{Bmatrix} = \int_{-h/2}^{h/2} \begin{Bmatrix} \sigma_\beta \\ \sigma_{\beta\alpha} \end{Bmatrix} \left(1 + \frac{z}{R_\alpha}\right) \, z \, dz \tag{2.9}$$

It might be noticed that although $\sigma_{\alpha\beta} = \sigma_{\beta\alpha}$, in eqns (2.6) to (2.9), $N_{\alpha\beta} \neq N_{\beta\alpha}$ and $M_{\alpha\beta} \neq M_{\beta\alpha}$ unless $R_\alpha = R_\beta$.

The equations of stress and moment stress resultants found by different researchers can be found in [1]. The next section presents the strain-stress equation chosen for this study for a complete cylindrical shell and the corresponding stress and moment stress resultants.

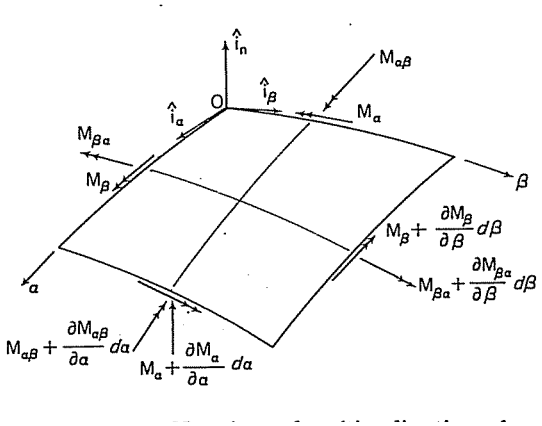

Figure 2.3: Positive directions of moment resultants in shell coordinates (Figure taken from [1])

2.3 Compatibility and constitutive relationships for a thin circular shell

Previous sections introduced the strain-stress relationships and equations for stress and moment stress resultants for shells having arbitrary double curvature. This section specializes the strain-displacement and consequently stress-displacement for cylinders. The shell theory initially chosen for a complete cylindrical shell is based on Love-Timoshenko strain-displacement equations. In subsequent sections these shell equations will be compared with those based upon the assumptions of other researchers. The coordinates used for the cylindrical shell are x, y, and z representing axial, circumferential and radial directions respectively, as shown in Fig 2.4. As mentioned earlier, according to Love's first approximation higher powers of z/R or h/R are neglected in comparison with unity. The strain-displacement relations are derived based on the Love-Timoshenko equations as explained in [1]. The displacement vector is $\{u, v, w\}$, in which u, v, w are the orthogonal components of the displacement in x, y, and radial directions respectively.

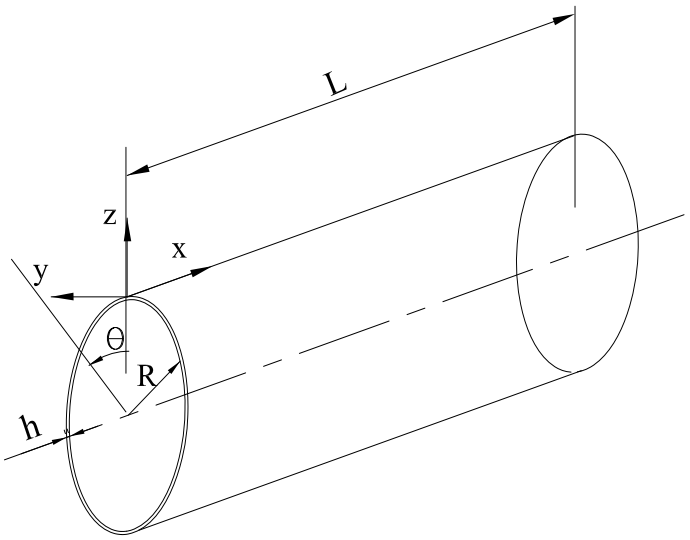

Figure 2.4: Circular cylindrical shell coordinate system

The total strains at a distance z from the middle surface are given by

$$\begin{aligned} \epsilon_x &= \epsilon'_x + z\chi_x \\ \epsilon_y &= \epsilon'_y + z\chi_y \\ \gamma_{xy} &= \gamma'_{xy} + 2z\chi_{xy} \end{aligned} \tag{2.10}$$

and the strains and changes in curvature at mid-surface are

$$\begin{aligned} \epsilon'_x &= \frac{\partial u}{\partial x} \\ \epsilon'_y &= \frac{\partial v}{\partial y} + \frac{w}{R} \\ \gamma'_{xy} &= \frac{\partial u}{\partial y} + \frac{\partial v}{\partial x} \\ \chi_x &= -\frac{\partial^2 w}{\partial x^2} \\ \chi_y &= -\frac{\partial^2 w}{\partial y^2} + \frac{1}{R}\frac{\partial v}{\partial y} \\ \chi_{xy} &= -\frac{\partial^2 w}{\partial x \partial y} + \frac{1}{R}\frac{\partial v}{\partial x} \end{aligned} \tag{2.11}$$

in which ϵ'_x and ϵ'_y are the strains in x, and y direction; χ_x and χ_y are the changes of the curvature in x, and y directions; ϵ_{xy}, and χ_{xy} are the shear strain and twist at mid-surface respectively.

In this initial derivation stress and moment stress resultant equations are also derived

based on Love-Timoshenko theory, which has the greatest simplifications by neglecting z/R_i $(i = \alpha,\ \beta)$ in comparison with unity. For thin shells this simplification will be shown to be reasonable and does not lead to significant error. As explained earlier, theories based on Love-Timoshenko assumptions consider $\epsilon_x = \gamma_{xz} = \gamma_{yz} = 0$ and σ_z to be negligibly small, together with neglecting z/R_i in comparison with unity.
Using Kirchhoff hypothesis and Love's third assumption in Hooke's law, the stress-strain relationships reduce to a plane stress representation in which

$$\begin{aligned}
\sigma_x &= \frac{E}{1-\nu^2}(\epsilon_x + \nu\epsilon_y) \\
\sigma_y &= \frac{E}{1-\nu^2}(\epsilon_y + \nu\epsilon_x) \\
\sigma_{xy} &= \frac{E}{2(1+\nu)}\gamma_{xy}
\end{aligned} \tag{2.12}$$

Consequently, the membrane and bending stress resultants can be derived as

$$\begin{aligned}
N_x &= \int_{-\frac{h}{2}}^{+\frac{h}{2}} \sigma_x(1-\frac{z}{R_y})dz = K(\epsilon'_x + \nu\epsilon'_y) \\
N_y &= \int_{-\frac{h}{2}}^{+\frac{h}{2}} \sigma_y(1-\frac{z}{R_x})dz = K(\epsilon'_y + \nu\epsilon'_x) \\
N_{xy} = N_{yx} &= \int_{-\frac{h}{2}}^{+\frac{h}{2}} \sigma_{xy}(1-\frac{z}{R_y})dz = \frac{K(1-\nu)}{2}\gamma'_{xy} \\
M_x &= \int_{-\frac{h}{2}}^{+\frac{h}{2}} \sigma_x z(1-\frac{z}{R_y})dz = D(\chi_x + \nu\chi_y) \\
M_y &= \int_{-\frac{h}{2}}^{+\frac{h}{2}} \sigma_y z(1-\frac{z}{R_x})dz = D(\chi_y + \nu\chi_x) \\
M_{xy} &= \int_{-\frac{h}{2}}^{+\frac{h}{2}} \sigma_{xy} z(1-\frac{z}{R_y})dz = D(1-\nu)\chi_{xy}
\end{aligned} \tag{2.13}$$

in which $K = \frac{Eh}{1-\nu^2}$ is the extensional stiffness, $D = \frac{Eh^3}{12(1-\nu^2)}$ is the flexural stiffness, E modulus of elasticity, and ν the poisson's ratio. The relationship between membrane

and bending stress resultants and displacement can be written in the form of

$$
\begin{aligned}
N_x &= K(\frac{\partial u}{\partial x} + \nu\frac{\partial v}{\partial y} + \nu\frac{w}{R}) \\
N_y &= K(\frac{\partial v}{\partial y} + \frac{w}{R} + \nu\frac{\partial u}{\partial x}) \\
N_{xy} = N_{yx} &= \frac{K(1-\nu)}{2}(\frac{\partial u}{\partial y} + \frac{\partial v}{\partial x}) \\
M_x &= D(-\frac{\partial^2 w}{\partial x^2} - \nu\frac{\partial^2 w}{\partial y^2} + \frac{\nu}{R}\frac{\partial v}{\partial y}) \\
M_y &= D(-\frac{\partial^2 w}{\partial y^2} + \frac{1}{R}\frac{\partial v}{\partial y} - \nu\frac{\partial^2 w}{\partial x^2}) \\
M_{xy} = M_{yx} &= D(1-\nu)(-\frac{\partial^2 w}{\partial x \partial y} + \frac{1}{R}\frac{\partial v}{\partial x})
\end{aligned}
\tag{2.14}
$$

2.4 Equations of motion for free vibrations of a thin circular cylindrical shell

Two methods are adopted in this section to find the equation of motion for thin circular cylindrical shells. The first method is based on Newton's laws by writing the equilibrium equation for force and moment acting on a shell element. The second method is based on the variational method, using the Lagrange equations. It should be noted that based on the simplifications during the derivation of equations of motion, the governing equation could be different from one another. Both methods follow the Love-Timoshenko theory. For simplicity, the equations of motion are first derived for the static case and then extended by including the inertial term using d'Alambert 's principle.

The rest of the section deals with the comparison between the governing equations of motion with other commonly used equations based on different theories previously proposed for modelling the vibrational behaviour of circular cylindrical shells.

2.4.1 Equation of equilibrium

The equation of equilibrium is written for a shell element of thickness h. The internal and external forces and moments are shown in Fig 3.2 and 3.3. The external force per unit area is shown as $\vec{P}= P_x\ \vec{i}\ + P_y\ \vec{j}\ + P_z\ \vec{k}$. The equilibrium equation using

Newton's laws can be written as

$$\begin{aligned}
\sum F_x &= \frac{\partial N_x}{\partial x} + \frac{\partial N_{yx}}{\partial y} + P_x = 0 && (a)\\
\sum F_y &= \frac{\partial N_y}{\partial y} + \frac{\partial N_{xy}}{\partial x} + q_y(\frac{1}{R}) + P_y = 0 && (b)\\
\sum F_z &= \frac{\partial q_x}{\partial x} + \frac{\partial q_y}{\partial y} - (\frac{N_y}{R}) + P_z = 0 && (c)\\
\sum M_{xx} &= \frac{\partial M_y}{\partial y} + \frac{\partial M_{xy}}{\partial x} - q_y = 0 && (d)\\
\sum M_{yy} &= \frac{\partial M_x}{\partial x} + \frac{\partial M_{yx}}{\partial y} - q_x = 0 && (e)
\end{aligned} \tag{2.15}$$

This study follows the simplification of Love, Timoshenko, and Reissner, using the approximation of $N_{xy} = N_{yx}$ and $M_{xy} = M_{yx}$, to reduce the number of equations and unknowns. However, Donnell Mushtari's simplification, which is based on neglecting the term containing q_y in the y direction, is not applied.

The five equilibriums equations in (2.15) are then reduced to three equations by deriving the shear forces q_x, and q_y from eqns (2.15) (d), (e) in terms of M_y, M_{xy}, M_x and replacing them in eqns (2.15) (b), (c). The force and moments in the equilibrium eqn (2.15) are then substituted by the stress-displacement eqn (2.14) as

$$K(\frac{\partial^2 u}{\partial x^2} + \frac{1+\nu}{2}\frac{\partial^2 v}{\partial x \partial y} + \frac{1-\nu}{2}\frac{\partial^2 u}{\partial y^2} + \frac{\nu}{R}\frac{\partial w}{\partial x}) + P_x = 0$$

$$\begin{aligned}
&K(\frac{\partial^2 v}{\partial y^2} + \frac{1-\nu}{2}\frac{\partial^2 v}{\partial x^2} + \frac{1+\nu}{2}\frac{\partial^2 u}{\partial x \partial y} + \frac{1}{R}\frac{\partial w}{\partial y}) +\\
&\frac{D}{R}(-\frac{\partial^3 w}{\partial y^3} + \frac{1}{R}\frac{\partial^2 v}{\partial y^2} - \frac{\partial^3 w}{\partial x^2 \partial y} + \frac{1-\nu}{R}\frac{\partial^2 v}{\partial x^2} + P_y = 0
\end{aligned} \tag{2.16}$$

$$\begin{aligned}
&-\frac{K}{R}(\frac{\partial v}{\partial y} + \frac{w}{R} + \nu\frac{\partial u}{\partial x}) + D(-\frac{\partial^4 w}{\partial x^4} - 2\frac{\partial^4 w}{\partial x^2 \partial y^2} -\\
&\frac{\partial^4 w}{\partial y^4} + \frac{2-\nu}{R}\frac{\partial^3 v}{\partial x^2 \partial y} + \frac{1}{R}\frac{\partial^3 v}{\partial y^3}) + P_z = 0
\end{aligned}$$

Time, t, appears in the equations of motion through the inertia terms in the equations. For free vibration case, body forces, P_x, P_y, and P_z are replaced by inertia terms

$$\begin{aligned} P_x &= -\rho h \frac{\partial^2 u}{\partial t^2} \\ P_y &= -\rho h \frac{\partial^2 v}{\partial t^2} \\ P_z &= -\rho h \frac{\partial^2 w}{\partial t^2} \end{aligned} \tag{2.17}$$

in which ρ is mass density per unit volume, h is shell thickness, and t is time. The above equation of motion (2.16) can be written in matrix form;

$$\begin{bmatrix} \Gamma_{11} & \Gamma_{12} & \Gamma_{13} \\ \Gamma_{21} & \Gamma_{22} & \Gamma_{23} \\ \Gamma_{31} & \Gamma_{32} & \Gamma_{33} \end{bmatrix} \cdot \begin{Bmatrix} u \\ v \\ w \end{Bmatrix} = \begin{Bmatrix} 0 \\ 0 \\ 0 \end{Bmatrix} \tag{2.18}$$

where

$$\begin{aligned} \Gamma_{11} &= \frac{\partial^2}{\partial x^2} + \frac{(1-\nu)}{2}\frac{\partial^2}{\partial y^2} - \frac{\rho(1-\nu^2)}{E}\frac{\partial^2}{\partial t^2} \\ \Gamma_{12} &= \frac{(\nu+1)}{2}\frac{\partial^2}{\partial x \partial y} \\ \Gamma_{13} &= \frac{\nu}{R}\frac{\partial}{\partial x} \\ \Gamma_{21} &= \frac{(\nu+1)}{2}\frac{\partial^2}{\partial x \partial y} \\ \Gamma_{22} &= \frac{\partial^2}{\partial y^2} + \frac{(1-\nu)}{2}\frac{\partial^2}{\partial x^2} + \frac{h^2}{12R^2}(\frac{\partial^2}{\partial y^2} + (1-\nu)\frac{\partial^2}{\partial x^2}) - \frac{\rho(1-\nu^2)}{E}\frac{\partial^2}{\partial t^2} \\ \Gamma_{23} &= \frac{1}{R}\frac{\partial}{\partial y} + \frac{h^2}{12R}[-\frac{\partial^3}{\partial y^3} - \frac{\partial^3}{\partial x^2 \partial y}] \\ \Gamma_{31} &= \frac{\nu}{R}\frac{\partial}{\partial x} \\ \Gamma_{32} &= \frac{1}{R}\frac{\partial}{\partial y} - \frac{h^2}{12R}((2-\nu)\frac{\partial^3}{\partial x^2 \partial y} + \frac{\partial^3}{\partial y^3}) \\ \Gamma_{33} &= \frac{1}{R^2} + \frac{h^2}{12}(\frac{\partial^2}{\partial x^2} + \frac{\partial^2}{\partial y^2})^2 + \frac{\rho(1-\nu^2)}{E}\frac{\partial^2}{\partial t^2} \end{aligned} \tag{2.19}$$

2.4.2 Equations of motions based on variational method

One of the variational principles is Hamilton's principle

$$\delta \int_{t_2}^{t_1} (U - T) dt = 0 \tag{2.20}$$

It means the variation of the time integral, between given time limits, of the difference between the kinetic (T) and potential (U) energies must vanish. The equations of motion for a shell undergoing a free vibratory motion, where the damping is neglected, are derived by Euler-Lagrange equations

$$\begin{aligned} -\frac{\partial}{\partial x}\frac{\partial L}{\partial u_x} - \frac{\partial}{\partial y}\frac{\partial L}{\partial u_y} - \frac{\partial}{\partial t}\frac{\partial L}{\partial \dot{u}} = 0 \\ -\frac{\partial}{\partial x}\frac{\partial L}{\partial v_x} - \frac{\partial}{\partial y}\frac{\partial L}{\partial v_y} - \frac{\partial}{\partial t}\frac{\partial L}{\partial \dot{v}} = 0 \\ \frac{\partial L}{\partial w} + \frac{\partial^2}{\partial x^2}\frac{\partial L}{\partial w_{xx}} + \frac{\partial^2}{\partial y^2}\frac{\partial L}{\partial w_{yy}} + \frac{\partial^2}{\partial x \partial y}\frac{\partial L}{\partial w_{xy}} - \frac{\partial}{\partial t}\frac{\partial L}{\partial \dot{w}} = 0 \end{aligned} \tag{2.21}$$

where, $()_x = \frac{\partial}{\partial x}$, $()_y = \frac{\partial}{\partial y}$, and $\dot{()} = \frac{\partial}{\partial t}$, $L = U - T$ is the Lagrangian. The strain energy for a shell undergoing a total displacement (U, V, W) about an unloaded and unreformed state, may be written as constituent parts

$$U = \frac{1}{2}\int_{-\frac{h}{2}}^{+\frac{h}{2}}\int_0^L\int_0^{R\phi}[\sigma_x\epsilon_x + \sigma_y\epsilon_y + \sigma_{xy}\gamma_{xy}]dxdydz \tag{2.22}$$

Using eqn (2.10)-(2.14) and integrating over the shell thickness the total potential energy can be written in terms of its bending and membrane stress resultant as

$$\begin{aligned} U = \underbrace{\frac{1}{2}\int_0^L\int_0^{\phi}(M_x\chi_x + M_\theta\chi_\theta + 2M_{x\theta}\chi_{x\theta})R\,\mathrm{d}\theta\,\mathrm{d}x}_{Contribution\ from\ bending\ energy} \\ + \underbrace{\frac{1}{2}\int_0^L\int_0^{\phi}(N_xE_x + N_\theta E_\theta + 2N_{\theta x}E_{\theta x})R\mathrm{d}\theta\,\mathrm{d}x}_{Contribution\ from\ membrane\ energy} \end{aligned} \tag{2.23}$$

The total displacement is presented in terms of the incremental displacements (u, v, w) about a fundamental displacement state (U^F, V^F, W^F), so that

$$\begin{aligned} U &= U^F + u \\ V &= V^F + v \\ W &= W^F + w \end{aligned} \tag{2.24}$$

Likewise, the total stresses (M_x, M_θ, $M_{x\theta}$, N_x, N_θ, $N_{x\theta}$) and strains (E_x, E_θ, $E_{x\theta}$) in eqn (2.23) are then written in terms of their associated fundamental and incremental

stresses and strains as

$$\begin{aligned} N_x &= N_x^F + n_x \\ N_\theta &= N_\theta^F + n_\theta \\ N_{x\theta} &= N_{x\theta}^F + n_{x\theta} \end{aligned} \tag{2.25}$$

$$\begin{aligned} E_x &= E_x^F + \epsilon_x \\ E_\theta &= E_\theta^F + \epsilon_\theta \\ E_{x\theta} &= E_{x\theta}^F + \epsilon_{x\theta} \end{aligned}$$

$$\begin{aligned} M_x &= M_x^F + m_x \\ M_\theta &= M_\theta^F + m_\theta \\ M_{x\theta} &= M_{x\theta}^F + m_{x\theta} \end{aligned} \tag{2.26}$$

$$\begin{aligned} X_x &= X_x^F + \chi_x \\ X_\theta &= X_\theta^F + \chi_\theta \\ X_{x\theta} &= X_{x\theta}^F + \chi_{x\theta} \end{aligned}$$

As pre-loading is not taken into account in this chapter, the fundamental displacement states, fundamental stresses and strains are considered to be zero ($U^F = 0,\ V^F = 0,\ W^F = 0,\ N_x^F = 0,\ N_\theta^F = 0,\ N_{x\theta}^F = 0,\ M_x^F = 0,\ M_\theta^F = 0,\ M_{x\theta}^F = 0,\ E_x^F = 0,\ E_\theta^F = 0,\ E_{x\theta}^F = 0,\ X_x^F = 0,\ X_\theta^F = 0,\ X_{x\theta}^F = 0$). However as it will be seen in Chapter 5, the fundamental displacements, stresses, and strains should be included in the derivation of the equations of motion for the case of pre-loaded roof shell.

With the kinetic energy, T, defined as

$$T = \frac{1}{2}\rho h \int_0^L \int_0^{R\phi} [\dot{u}^2 + \dot{v}^2 + \dot{w}^2] dx dy \tag{2.27}$$

making use of the eqns (2.22), (2.27) and employing the strain-displacement relations of eqn (2.10) to (2.12), the Euler-Lagrange equations (2.21) will be simplified to the

differential equation of motions

$$S_x(u,v,w) + \rho \times h\frac{\partial^2 u}{\partial t^2} = 0$$

$$S_y(u,v,w) + \rho \times h\frac{\partial^2 v}{\partial t^2} = 0 \tag{2.28}$$

$$S_z(u,v,w) + \rho \times h\frac{\partial^2 w}{\partial t^2} = 0$$

where $S_x(u,v,w)$, $S_y(u,v,w)$, and $S_z(u,v,w)$ are the static equations of equilibrium for cylindrical shell in the form of

$$S_x(u,v,w) = -K(\frac{\partial^2 u}{\partial x^2} + \frac{1+\nu}{2}\frac{\partial^2 v}{\partial x \partial y} + \frac{1-\nu}{2}\frac{\partial^2 u}{\partial y^2} + \frac{\nu}{R}\frac{\partial w}{\partial x})$$

$$\begin{aligned} S_y(u,v,w) = &-K(\frac{\partial^2 v}{\partial y^2} + \frac{1-\nu}{2}\frac{\partial^2 v}{\partial x^2} + \frac{1+\nu}{2}\frac{\partial^2 u}{\partial x \partial y} + \frac{1}{R}\frac{\partial w}{\partial y}) - \\ &\frac{D}{R}(-\frac{\partial^3 w}{\partial y^3} - (2-\nu)\frac{\partial^3 w}{\partial x^2 \partial y} + \frac{1}{R}\frac{\partial^2 v}{\partial y^2} + \frac{2(1-\nu)}{R}\frac{\partial^2 v}{\partial x^2}) \end{aligned} \tag{2.29}$$

$$S_z(u,v,w) = \frac{K}{R}(\nu\frac{\partial u}{\partial x} + \frac{\partial v}{\partial y} + \frac{w}{R}) + D(\nabla^4 w - \frac{1}{R}\frac{\partial^3 v}{\partial y^3} - \frac{(2-\nu)}{R}\frac{\partial^3 v}{\partial x^2 \partial y})$$

in which, $\nabla^4 w = \frac{\partial^4 w}{\partial x^4} + 2\frac{\partial^4 w}{\partial x^2 \partial y^2} + \frac{\partial^4 w}{\partial y^4}$. The above equation of motion can be written in matrix form as in eqn (2.18); in which,

$$\begin{aligned} \Gamma_{11} &= \frac{\partial^2}{\partial x^2} + \frac{1-\nu}{2}\frac{\partial^2}{\partial y^2} - \frac{\rho(1-\nu^2)}{E}\frac{\partial^2}{\partial t^2} \\ \Gamma_{12} &= \frac{\nu+1}{2}\frac{\partial^2}{\partial x \partial y} \\ \Gamma_{13} &= \frac{\nu}{R}\frac{\partial}{\partial x} \\ \Gamma_{21} &= \frac{\nu+1}{2}\frac{\partial^2}{\partial x \partial y} \\ \Gamma_{22} &= \frac{\partial^2}{\partial y^2} + \frac{1-\nu}{2}\frac{\partial^2}{\partial x^2} + \frac{h^2}{12R^2}(\frac{\partial^2}{\partial y^2} + 2(1-\nu)\frac{\partial^2}{\partial x^2}) - \frac{\rho(1-\nu^2)}{E}\frac{\partial^2}{\partial t^2} \\ \Gamma_{23} &= \frac{1}{R}\frac{\partial}{\partial y} - \frac{h^2}{12R}(\frac{\partial^3}{\partial y^3} + (2-\nu)\frac{\partial^3}{\partial x^2 \partial y}) \\ \Gamma_{31} &= \frac{\nu}{R}\frac{\partial}{\partial x} \\ \Gamma_{32} &= \frac{1}{R}\frac{\partial}{\partial y} - \frac{h^2}{12R}(\frac{\partial^3}{\partial y^3} + (2-\nu)\frac{\partial^3}{\partial x^2 \partial y}) \\ \Gamma_{33} &= \frac{1}{R^2} + \frac{h^2}{12}(\frac{\partial^2}{\partial x^2} + \frac{\partial^2}{\partial y^2})^2 + \frac{\rho(1-\nu^2)}{E}\frac{\partial^2}{\partial t^2} \end{aligned} \tag{2.30}$$

2.4.3 Comparison of the equation of motion based on various shell theories

The formulation of various selected shell theories are explained in [1] for an arbitrary double curvature shell element. This section summarizes the difference between some of these shell theories in modelling the free vibrations of circular cylindrical shells. Considering equation of free vibration motion (2.18) as

$$[\Gamma]\{u_i\} = \{0\} \tag{2.31}$$

In order to facilitate the comparison of equation of motions based on different shell theories Liessa presented $[\Gamma]$ as the sum of two operators; the differential operator according to the Donnell-Mushtari theory, $[\Gamma_{D-M}]$, with the most simplification, which ignores q_x, and q_y in the tangential direction (in eqn (2.15)b)and the modifying operator, $[\Gamma_{MOD}]$, the operator which converts Donnell-Mushtari theory to other shell theories.

$$[\Gamma] = [\Gamma_{D-M}] + k\,[\Gamma_{MOD}] \tag{2.32}$$

in which $k = h^2/12R^2$ is very small for thin shells.

The following equations, reported by Leissa, summarize the Donnell-Mushtari operator together with the operator converting Donnell-Mushtari to other shell theories [1].

$$[\Gamma_{D-M}] = \begin{bmatrix} \frac{\partial^2}{\partial x^2} + \frac{1-\nu}{2}\frac{\partial^2}{\partial y^2} & \frac{\nu+1}{2}\frac{\partial^2}{\partial x \partial y} & \frac{\nu}{R}\frac{\partial}{\partial x} \\ -\frac{\rho(1-\nu^2)}{E}\frac{\partial^2}{\partial t^2} & & \\ \frac{\nu+1}{2}\frac{\partial^2}{\partial x \partial y} & \frac{\partial^2}{\partial y^2} + \frac{1-\nu}{2}\frac{\partial^2}{\partial x^2} + & \frac{1}{R}\frac{\partial}{\partial y} \\ & -\frac{\rho(1-\nu^2)}{E}\frac{\partial^2}{\partial t^2} & \\ \frac{\nu}{R}\frac{\partial}{\partial x} & \frac{1}{R}\frac{\partial}{\partial y} & \frac{1}{R^2} + \frac{h^2}{12}\left(\frac{\partial^2}{\partial x^2} + \frac{\partial^2}{\partial y^2}\right)^2 \\ & & +\frac{\rho(1-\nu^2)}{E}\frac{\partial^2}{\partial t^2} \end{bmatrix} \tag{2.33}$$

Love-Timoshenko

$$[\Gamma_{MOD}] = \begin{bmatrix} 0 & 0 & 0 \\ 0 & \frac{\partial^2}{\partial y^2} + (1-\nu)\frac{\partial^2}{\partial x^2} & -R\frac{\partial^3}{\partial x^2 \partial y} - R\frac{\partial^3}{\partial y^3} \\ 0 & -(2-\nu)R\frac{\partial^3}{\partial x^2 \partial y} - R\frac{\partial^3}{\partial y^3} & 0 \end{bmatrix} \tag{2.34}$$

Goldenveizer-Novozhilov and Arnold-Warburton

$$[\Gamma_{MOD}] = \begin{bmatrix} 0 & 0 & 0 \\ 0 & \frac{\partial^2}{\partial y^2} + 2(1-\nu)\frac{\partial^2}{\partial x^2} & -(2-\nu)R\frac{\partial^3}{\partial x^2 \partial y} - R\frac{\partial^3}{\partial y^3} \\ 0 & -(2-\nu)R\frac{\partial^3}{\partial x^2 \partial y} - R\frac{\partial^3}{\partial y^3} & 0 \end{bmatrix} \tag{2.35}$$

Houghton-Johns (Simplified Godenveizer-Novozhilov)

$$[\Gamma_{MOD}] = \begin{bmatrix} 0 & 0 & 0 \\ 0 & 0 & -(2-\nu)R\frac{\partial^3}{\partial x^2 \partial y} - R\frac{\partial^3}{\partial y^3} \\ 0 & -(2-\nu)R\frac{\partial^3}{\partial x^2 \partial y} - R\frac{\partial^3}{\partial y^3} & 0 \end{bmatrix} \tag{2.36}$$

Flugge-Byrne-Lur'ye

$$[\Gamma_{MOD}] = \begin{bmatrix} \frac{(1-\nu)}{2} & 0 & -R\frac{\partial^3}{\partial x^3} + \frac{R(1-\nu)}{2}\frac{\partial^3}{\partial x \partial y^2} \\ 0 & \frac{3(1-\nu)}{2}\frac{\partial^2}{\partial x^2} & -\frac{(3-\nu)}{2}R\frac{\partial^3}{\partial x^2 \partial y} \\ -R\frac{\partial^3}{\partial x^3} + \frac{R(1-\nu)}{2}\frac{\partial^3}{\partial x \partial y^2} & -\frac{(3-\nu)R}{2}\frac{\partial^3}{\partial x^2 \partial y} & \frac{1}{R^2} + 2\frac{\partial^2}{\partial y^2} \end{bmatrix} \tag{2.37}$$

Reissner-Naghdi-Berry

$$[\Gamma_{MOD}] = \begin{bmatrix} 0 & 0 & 0 \\ 0 & \frac{\partial^2}{\partial y^2} + \frac{(1-\nu)}{2}\frac{\partial^2}{\partial x^2} & -R\frac{\partial^3}{\partial x^2 \partial y} - R\frac{\partial^3}{\partial y^3} \\ 0 & -R\frac{\partial^3}{\partial x^2 \partial y} - R\frac{\partial^3}{\partial y^3} & 0 \end{bmatrix} \tag{2.38}$$

Sanders

$$[\Gamma_{MOD}] = \begin{bmatrix} \frac{(1-\nu)}{8}\frac{\partial^2}{\partial y^2} & -\frac{3(1-\nu)}{8}\frac{\partial^2}{\partial x \partial y} & \frac{(1-\nu)R}{2}\frac{\partial^3}{\partial x \partial y^2} \\ -\frac{3(1-\nu)}{8}\frac{\partial^2}{\partial x \partial y} & \frac{9(1-\nu)}{8}\frac{\partial^2}{\partial x^2} + \frac{\partial^2}{\partial y^2} & -\frac{(3-\nu)R}{2}\frac{\partial^3}{\partial x^2 \partial y} - R\frac{\partial^3}{\partial y^3} \\ \frac{(1-\nu)R}{2}\frac{\partial^3}{\partial x \partial y^2} & -\frac{(3-\nu)R}{2}\frac{\partial^3}{\partial x^2 \partial y} - R\frac{\partial^3}{\partial y^3} & 0 \end{bmatrix} \quad (2.39)$$

By comparing the governing equations of motion in this study, it is noticed that derivation of equation of motion based on the equilibrium equation (2.18) and (2.19) result in the ones based on Love and Timoshenko eqn (2.34), while the Euler-Lagrange equation (2.30) lead to the ones based on Goldenveizer-Novozhilov and Arnold-Warburton equations (2.35). The latter equations of motion, based on Lagrange equation, are used in Section 2.5.1 to compare the frequency parameters for a circular cylindrical shell with the frequency parameters reported by Liessa [1] based on the shell theories discussed in this section.

2.5 Free vibration of simply supported circular cylindrical shell

So far the equations governing the motion of shell are complete except for the boundary conditions. The simply supported boundary condition at both ends are considered for the case of this study. The boundary conditions for a circular cylindrical shell with simply supported boundary conditions at both ends are exactly satisfied by displacement function in the form of

$$\begin{aligned} u(x,y,t) &= \bar{u}_{ij}\cos(\frac{j\pi x}{L})\cos(i\theta)\sin\omega t \\ v(x,y,t) &= \bar{v}_{ij}\sin(\frac{j\pi x}{L})\sin(i\theta)\sin\omega t \\ w(x,y,t) &= \bar{w}_{ij}\sin(\frac{j\pi x}{L})\cos(i\theta)\sin\omega t \end{aligned} \quad (2.40)$$

in which $\bar{u}_{ij}$, $\bar{v}_{ij}$, and $\bar{w}_{ij}$ are non-dimensional coefficients. Substituting eqn (2.40) in the equation of motion of eqn (2.28)-(2.30) results in

$$\begin{bmatrix} \lambda^2 + \frac{1-\nu}{2} i\lambda - \Delta & -\frac{1+\nu}{2} & -\nu\lambda \\ -\frac{1+\nu}{2} i\lambda & i^2 + \frac{1-\nu}{2}\lambda^2 + k[i^2 & i + ki[i^2 + (2-\nu)\lambda^2] \\ & +2(1-\nu)\lambda^2] - \Delta & \\ -\nu\lambda & i + ki[i^2 + (2-\nu)\lambda^2] & 1 + k(\lambda^2 + i^2)^2 - \Delta \end{bmatrix} \cdot \begin{Bmatrix} \bar{u} \\ \bar{v} \\ \bar{w} \end{Bmatrix} = \begin{Bmatrix} 0 \\ 0 \\ 0 \end{Bmatrix} \tag{2.41}$$

in which $\lambda = \frac{j\pi R}{L}$ (j is the number of half-waves in longitudinal direction), $k = \frac{h^2}{12R^2}$, and $\Delta = \frac{\rho R^2(1-\nu^2)}{E}\omega^2$ ($\omega = 2\pi f$ and f is the natural frequency) is a non-dimensional frequency parameter.

2.5.1 Verification study

A Matlab programme was written to compare and verify the natural frequencies based on Euler-Lagrange equation predicted in this study with the frequencies of shells reported in the literature [43] based on different shell theories. As mentioned earlier, the governing equation of motion using Lagrange method, eqn (2.41), yielded to the ones based on Goldenveizer-Novozhilov and Arnold-Warburton. The comparison study is performed through two examples. The first example compares the governing fundamental non-dimensional frequency based on eqn (2.41) with the ones derived based on three dimensional elastic theory as explained in [43]. The results are presented in Table 2.1. The numbers shown in parenthesis are based on three dimensional theory of elasticity as reported in [43]. The results are given for four circumferential wave numbers ($i = 1, 2, 3, 4$), for four value of length/radius ratios ($\frac{L}{jR} = 1, 4, 20, 100$), two radius/thickness ratios ($\frac{R}{h} = 20, 500$), and $\nu = 0.3$. The term L/jR implies that a shell having a particular L/R ratio will have the same natural frequencies as a shell having twice the length and twice the number of axial half-waves. The results are in good agreement with the results based on three dimensional elasticity theory especially for thinner shells, which are for practical purposes identical.

In a second example, the frequency parameters based on eqn (2.41) and the reported

R/h	i	L/jR			
		1	4	20	100
20	1	0.856414 (0.85766)	0.257011 (0.25696)	0.0161063 (0.016103)	0.000665031 (0.00066489)
	2	0.675486 (0.67639)	0.121249 (0.1212)	0.0392332 (0.039271)	0.0347711 (0.038728)
	3	0.539294 (0.54045)	0.129881 (0.1302)	0.109477 (0.10981)	0.109186 (0.10952)
	4	0.492343 (0.49495)	0.219098 (0.22044)	0.209008 (0.21028)	0.208711 (0.20998)
500	1	0.844952 (0.84495)	0.256883 (0.25688)	0.0161011 (0.016101)	0.002664824 (0.00266482)
	2	0.652148 (0.65215)	0.112689 (0.11269)	0.00545243 (0.005453)	0.00156235 (0.0015637)
	3	0.481028 (0.48103)	0.0580087 (0.058009)	0.00503724 (0.0050415)	0.00438626 (0.0043833)
	4	0.354118 (0.35412)	0.0353927 (0.035393)	0.00853409 (0.0085338)	0.00840299 (0.0084024)

Table 2.1: Comparison of frequency parameter, $\Delta^{0.5}$ for circular cylindrical shells obtained from present theory (unbracketed) and three-dimensional theory (bracketed), $\nu = 0.3$

frequency parameters in [43] based on different shell theories shown in Section 2.4 are presented. Only the frequency parameter based on eqn (2.41) is calculated and presented as research result in Tables 2.2 and 2.3. As explained earlier in the present research, eqn (2.41) is found based on Euler-Lagrange formula. Other frequency parameters are based on different shell theories as explained in Section 2.4, which are calculated and reported by Leissa [1]. The results in Tables 2.2 and 2.3 are calculated and reported by Leissa for shells with infinite lengths based on different shell theories

[1] by neglecting the term $\lambda = \frac{j\pi R}{L}$. In addition, he has neglected the term k^2 in finding in-plane and out-of-plane frequencies based on all theories mentioned in 2.4.

However, in the present study the frequency parameters are found for $L/R = 100$ and k^2 is not neglected. Eqn (2.41) will have three roots for fixed values of i, and j. So a shell having a given geometry may vibrate in any of the three distinct modes, each having the same circumferential and longitudinal waves, and each having its own frequency. In Tables 2.2 and 2.3 the frequency parameters associated with the three vibration modes are presented. These modes can be classified as radial, longitudinal, and circumferential. The lowest frequency parameter is usually associated with a motion that is primary radial. The radial modes are referred to as out-of-plane modes in this study, for which w_{ij} is maximum. The longitudinal modes for which u_{ij} is maximum and the circumferential modes with the maximum v_{ij} are referred to as in-plane modes. The frequency parameters are derived for two different radius/thickness ratios of $R/h = 20$, and $R/h = 500$ and for circumferential half waves equal to $i = 1, 2, 3, 4$.

The results presented in Tables 2.2 and 2.3 show that for $i = 1$ there are considerable differences between different shell theories.

For $i \geq 2$ the resulting frequencies in Tables 2.2 and 2.3 are in agreement except for those of Donnell-Mushtari and Flugge.

Except for the aforementioned two theories, there is little difference between the resulting natural frequencies based on different shell theories. The differences also decreases as R/h increases. This is because for the thinner shells the value of $k = \frac{h^2}{12R^2}$ tends to zero, so results of most theories converge to those of Donnell-Mushtari.

There are also some differences between the radial frequency parameters using the method in the present study and other shell theories for $i = 1$. Even though in the present study the equation of motion using the Lagrange method yielded to those based on Goldenveizer-Novozhilov, as explained earlier, but the frequency parameters for $i = 1$ is not identical. This could be caused by two simplifications; considering shell having infinite length and ignoring the term k^2 that Leissa considered in deriving the frequency parameter.

Shell theory	i	$\Delta^{0.5}$		
		Axial modes	Radial modes	Circumferential modes
Donnell-Mushtari	1	0.591608	1.02062×10^{-2}	1.41425
Love-Timoshenko	1	0.591608	1.47648×10^{-4}	1.30676
Goldenveizer-Novozhilov	1	0.591608	1.476×10^{-4}	1.30676
Flugge	1	0.591608	1.25×10^{-2}	1.30657
Reissner-Naghdi-Berry	1	0.591608	1.47648×10^{-4}	1.30676
Sanders	1	0.591623	1.47648×10^{-4}	1.30657
Research result	1	0.592359	6.65×10^{-4}	1.41453
Donnell-Mushtari	2	1.18322	5.16417×10^{-2}	2.23622
Love-Timoshenko	2	1.18322	3.87307×10^{-2}	2.23666
Goldenveizer-Novozhilov	2	1.18322	3.87307×10^{-2}	2.23622
Flugge	2	1.18322	5.47755×10^{-2}	2.23614
Reissner-Naghdi-Berry	2	1.18322	3.87307×10^{-2}	2.23666
Sanders	2	1.18325	3.87307×10^{-2}	2.23666
Research result	2	1.18347	3.87×10^{-2}	2.23683
Donnell-Mushtari	3	1.77482	0.123256	3.16254
Love-Timoshenko	3	1.77482	0.109548	3.16334
Goldenveizer-Novozhilov	3	1.77482	0.109548	3.16334
Flugge	3	1.77482	0.126637	3.16301
Reissner-Naghdi-Berry	3	1.77482	0.109548	3.16334
Sanders	3	1.77487	0.109548	3.16334
Research result	3	1.77496	0.110000	3.16354
Donnell-Mushtari	4	2.36643	0.224118	4.12348
Love-Timoshenko	4	2.36643	0.21007	4.12463
Goldenveizer-Novozhilov	4	2.36643	0.21007	4.12463
Flugge	4	2.36643	0.227600	4.12482
Reissner-Naghdi-Berry	4	2.36643	0.210077	4.12483
Sanders	4	2.36650	0.210077	4.12483
Research result	4	2.36652	0.21000	4.1247

Table 2.2: Frequency parameter for circular cylindrical shells of infinite length, $\nu = 0.3$, $R/h = 20$

Shell theory	i	$\Delta^{0.5}$		
		Axial modes	Radial modes	Circumferential modes
Donnell-Mushtari	1	0.59161	4.08166×10^{-4}	1.41421
Love-Timoshenko	1	0.59161	0.541195	1.41421
Goldenveizer-Novozhilov	1	0.59161	0.541195	1.41421
Flugge	1	0.59161	0.541196	1.41421
Reissner-Naghdi-Berry	1	0.59161	0.541195	1.41421
Sanders	1	0.59161	0.54195	1.41421
Research result	1	0.59166	6.65×10^{-4}	1.41421
Donnell-Mushtari	2	1.18322	2.06553×10^{-2}	2.23607
Love-Timoshenko	2	1.18322	1.54919×10^{-3}	2.23607
Goldenveizer-Novozhilov	2	1.18322	1.549×10^{-3}	2.23607
Flugge	2	1.18322	2.19075×10^{-3}	2.23607
Reissner-Naghdi-Berry	2	1.18322	1.54919×10^{-3}	2.23607
Sanders	2	1.18322	1.54919×10^{-3}	2.23607
Research result	2	1.18322	1.55×10^{-3}	2.23609
Donnell-Mushtari	3	1.77482	4.92926×10^{-3}	3.16228
Love-Timoshenko	3	1.77482	4.38155×10^{-3}	3.16228
Goldenveizer-Novozhilov	3	1.77482	4.382×10^{-3}	3.16228
Flugge	3	1.77482	4.42416×10^{-3}	3.16228
Reissner-Naghdi-Berry	3	1.77482	4.38155×10^{-3}	3.16228
Sanders	3	1.77482	4.38155×10^{-3}	3.16228
Research result	3	1.77482	4.38×10^{-3}	3.16228
Donnell-Mushtari	4	2.36643	8.96144×10^{-3}	4.12311
Love-Timoshenko	4	2.36643	8.40119×10^{-3}	4.12311
Goldenveizer-Novozhilov	4	2.36643	8.40119×10^{-3}	4.12311
Flugge	4	2.36643	7.92069×10^{-3}	4.12482
Reissner-Naghdi-Berry	4	2.36643	8.40119×10^{-3}	4.12311
Sanders	4	2.36643	8.40119×10^{-3}	4.12311
Research result	4	2.36643	8.40×10^{-3}	4.12311

Table 2.3: Frequency parameter for circular cylindrical shells, $\nu = 0.3$, $R/h = 500$

2.6 Energy content of cylindrical shells

In order to better understand the behaviour of cylinders and the nature of each mode a study is performed to investigate the energy contribution of each mode of a cylinder. Fig 2.5 presents the contribution of bending and membrane energy (as explained in eqn (2.23)) in the modes for each frequency and non-dimensional frequency for a shell with $R = 104.8\ m$, $L = R$, $\rho = 4140.5\ kg/m^3$, $E = 91 \times 10^9\ N/m^2$, $\nu = 0.3$ for two thicknesses of $h = R/500$ (Fig 2.5(a),(b)) and $h = R/20$ (2.5(c),(d)). It is observed that the minimum frequency represents a form of optimum in which the high bending energy at short wavelength (high value of i) is played off against the high membrane energy for long wavelength (low value of i). It is also noticed that the resistance is dominated by membrane energy at long wavelengths (low value of i), while it is dominated by bending energy at short wavelengths (hight value of i). Fig 2.5(a),(c) shows that a thicker shell has more contribution of bending energy towards the total energy so the contribution of terms depending on $h^2/12R^2$ become more significant, so for thicker shell the reliability of different shell theories depend upon the extent to which bending and membrane energy are important. As it was shown in Section 2.4 the difference between the various selected shell theories were in considering bending energies. Tables 2.2 and 2.3 showed that frequency parameter based on all theories converged in thinner shells. It was because there is little contribution from bending energies for the selected longer wavelengths ($i = 1, 2, 3, 4$) in a thinner shell ($R/h = 500$) however for a thicker shell ($R/h = 20$) the contribution of bending energy becomes higher than membrane energies in modes with longer wavelengths.

2.7 Effect of in-plane modes in out-of-plane Frequency

Neglect of in-plane inertia (circumferential and axial) involves neglection of Δ in the second and third row in the eqn (2.41). This reduces the equation to a first order equation and simplifies the calculation. But it is important to check how neglecting the in-plane inertia will affect the governing out-of-plane natural frequencies. In order to investigate the effects of in-plane inertia in out-of-plane frequency, 8 cases of shells with different length/radius and thickness/radius ratios are chosen for which the non-

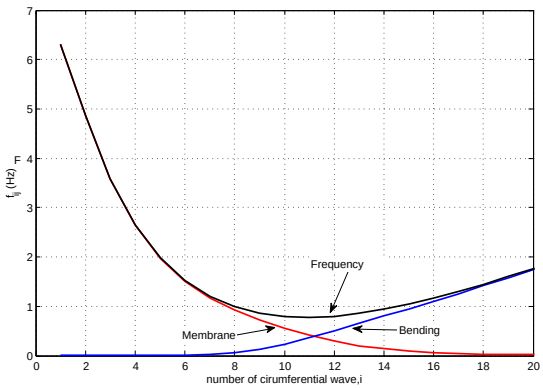

(a) Frequency, $R/h = 500$

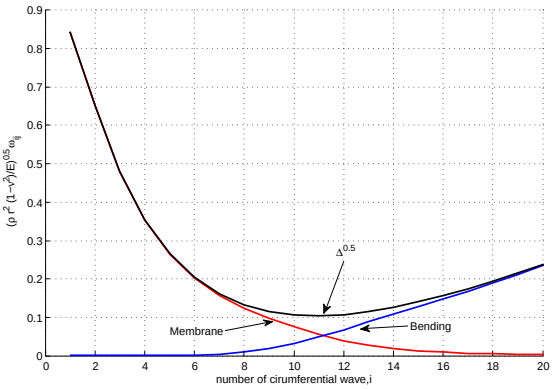

(b) $\Delta^{0.5}$, $R/h = 500$

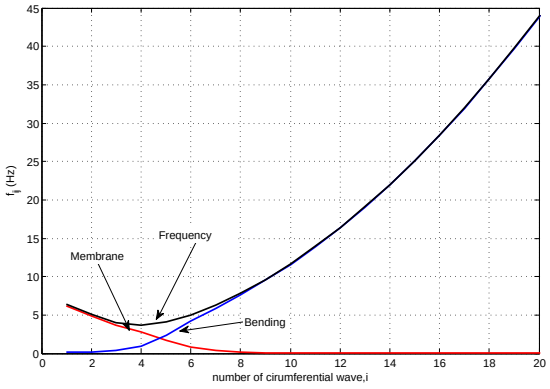

(c) Frequency, $R/h = 20$

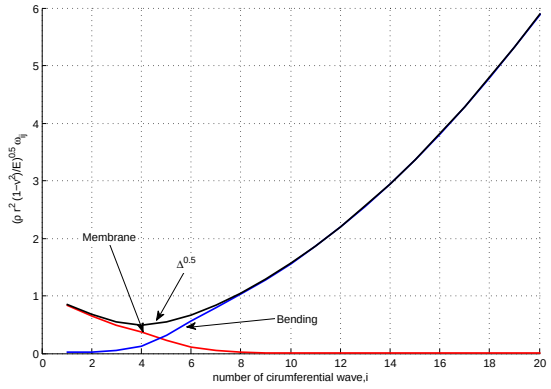

(d) $\Delta^{0.5}$, $R/h = 20$

Figure 2.5: Variation of the frequency parameter of circular cylindrical shell

dimensional frequency parameters are derived by including and neglecting in-plane inertia; the results are summarized in Fig 2.6.

It is noticed that neglecting in-plane inertia does not significantly affect cases of Fig 2.6(a),(b),(e). It is only in the modes corresponding to $(i, j) = (1, 1)$ as can be seen in Fig 2.6(c),(d),(f), that in-plane inertia changes the frequency parameter. For example, neglecting the in-plane inertia for a shell having $L/jR = 4$, $R/h = 500$ (Fig 2.6(d)) increases the frequency parameter corresponding to mode $(i, j) = (1, 1)$ by 46%.

Examining Table 2.4, which presents the eigenvectors corresponding to the shell having $L/jR = 4$, $R/h = 500$, reveals that the deformation for the first root, corresponding to the out-of-plane mode, of mode $(1, 1)$ is a combination of axial and circumferential deformation with a significant contribution from circumferential deformation ($\bar{v} = 0.7031 > \bar{w} = 0.6888$). It is for this reason that neglecting the in-plane modes corresponding to $\bar{v}$ has such a significant change on the resulting out-of-plane natural frequency. The contribution of circumferential deformation reduces as the circumferential wave number, i, increases and the deformation will be mainly radial. This means the effect of in-plane inertia becomes gradually insignificant with the increase in i. Table 2.4 and Fig 2.6 show that neglecting the in-plane inertia in modes having a high contribution from in-plane eigen-vector such as $(i, j) = (1, 1)$ would significantly change the resulting out-of-plane frequencies.

As the fundamental mode (the mode having the lowest frequency) significantly contributes to the response of structures to external loadings, it is important to mention that for the cases of the shells in Fig 2.6 neglect of in-plane inertia does not appreciably change the fundamental frequency parameter, and does not reduce the accuracy of fundamental frequency. Neglect of the in-plane inertia also does not change the frequencies for modes in which bending energy is dominant, such as modes corresponding to $i > 3$ in Fig 2.6(c). This is due to the fact that modes with bending energy are dominated by out-of-plane deformations. In these modes $\bar{u}$, and $\bar{v}$ are very small in comparison to $\bar{w}$ (Table 2.4), so neglect of Δ in second and third rows in eqn (2.41) has little effect on the natural frequencies of these modes, as illustrated in Fig 2.6(e).

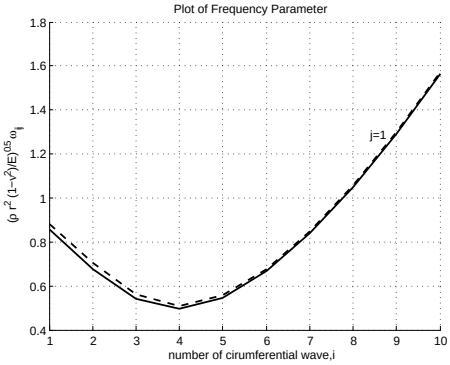

(a) $L/R = 1$,$R/h = 20$

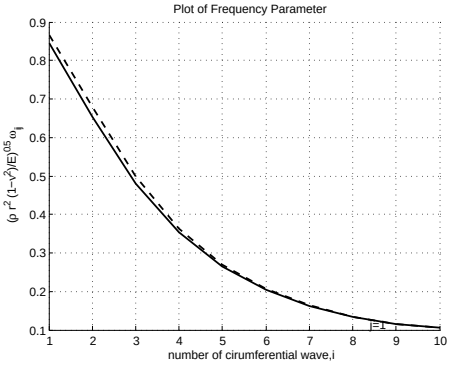

(b) $L/R = 1$,$R/h = 500$

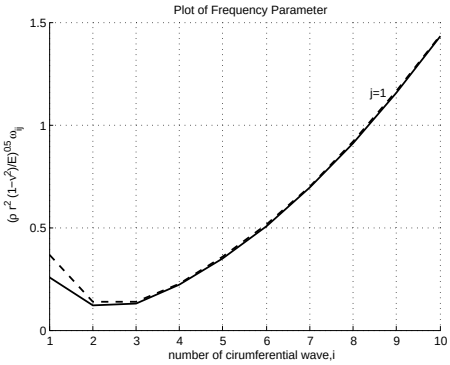

(c) $L/R = 4$,$R/h = 20$

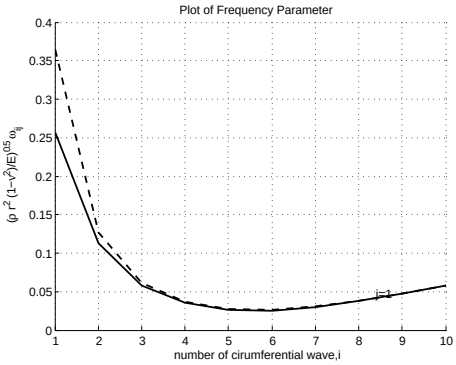

(d) $L/R = 4$,$R/h = 500$

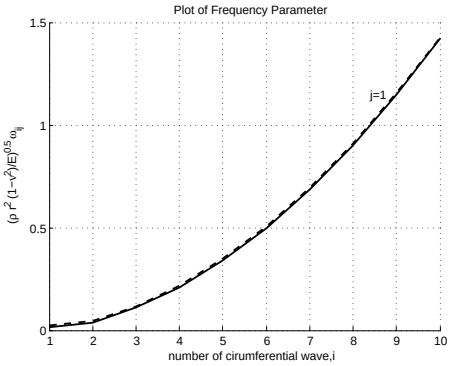

(e) $L/R = 20$,$R/h = 20$

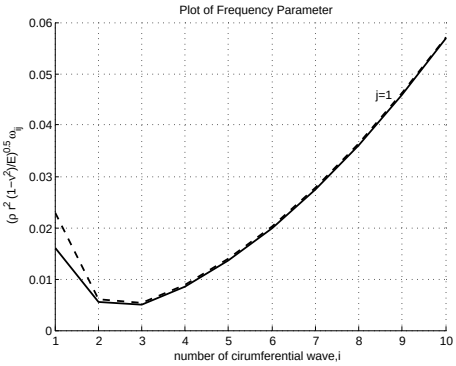

(f) $L/R = 20$,$R/h = 500$

Figure 2.6: Comparing parametric frequency of circular cylindrical shell including and neglecting in-plane inertia (dashed lines represent the parametric frequencies when the in-plane inertia is neglected)

	$l/jR = 4$ and $R/h = 500$								
	1st root			2nd root			3rd root		
i	$\bar{u}$	$\bar{v}$	$\bar{w}$	$\bar{u}$	$\bar{v}$	$\bar{w}$	$\bar{u}$	$\bar{v}$	$\bar{w}$
1	0.1767	0.7031	-0.6888	0.9754	-0.0314	0.2181	-0.1317	0.7104	0.6914
2	0.0662	0.4486	-0.8913	0.9913	0.0719	0.1098	-0.1134	0.8908	0.4399
3	-0.0323	-0.3169	0.9479	0.9955	0.0743	0.0587	-0.089	0.9455	0.3131
4	-0.0188	-0.2429	0.9699	0.9973	0.0647	0.0355	-0.0714	0.9679	0.241
5	-0.0122	-0.1963	0.9805	0.9982	0.0555	0.0235	-0.059	0.979	0.1953
6	-0.0086	-0.1645	0.9863	0.9987	0.048	0.0167	-0.0501	0.9852	0.1639
7	-0.0063	-0.1415	0.9899	0.999	0.0421	0.0124	-0.0434	0.989	0.1411
8	-0.0049	-0.1241	0.9923	0.9993	0.0374	0.0096	-0.0383	0.9916	0.1238
9	-0.0038	-0.1105	0.9939	0.9994	0.0336	0.0076	-0.0342	0.9933	0.1103
10	-0.0031	-0.0995	0.995	0.9995	0.0305	0.0062	-0.0309	0.9946	0.0994

Table 2.4: Eigen-modes for circular cylindrical shells; $\nu = 0.3$, $L/jR = 4$ and $R/h = 500$

2.7.1 Natural frequency of cylindrical shell

In Section 2.5.1 the governing natural frequencies found by using different shell theories were compared for the selected numbers of half-waves in axial and circumferential directions. For some cases of shells presented in Tables 2.1, 2.2, and 2.3, the fundamental frequency occurred within the presented circumferential half waves, such as that occurring at $i = 2$ for the shell having $R/h = 200$, and $L/R = 4$ in Table 2.1. For others, the fundamental frequency is seen to occur at higher circumferential half-wave numbers. However, in the previous section no attempt was made to define the fundamental natural frequencies.

For the case of beams, the fundamental natural frequency corresponds to the mode with the longest wave-length. Finding the successive natural frequencies are also simple as they are spaced in terms of i^2, as the frequency for a simply supported beam is derived using $\omega_i^2 = \frac{EI}{m}(\frac{i\pi}{L})^4$.

For two dimensional problems such as plates, the variation of natural frequencies is in proportion with the variation of $(\frac{i}{a})^2 + (\frac{j}{b})^2$, where a, b are the rectangle half-width

in two directions. It is because the natural frequencies for simply supported plates are derived using $\omega_{ij} = \sqrt{\frac{D}{\rho h}}\pi[(\frac{i}{a})^2 + (\frac{j}{b})^2]$, where D is the bending stiffness of plate. However, the behaviour of shells are not as simple as one and two dimensional structures like beams and plates that have no curvature. To find the response of shells to excitations it is necessary to know both the fundamental natural frequency and the spacing of the frequencies. It is for this reason that a study is performed to investigate the variations of the frequency parameter of cylindrical shells with different geometries as presented in Fig 2.7, and 2.8. However, this chapter does not investigate the importance of fundamental modes or other modes in the response of shell to earthquake loading. This section only investigates the variation of frequency parameters for different ratios of length/radius. A complete discussion of the importance of each mode in the response of shell to earthquakes will be presented in chapter 3.

Using Fig 2.7 and 2.8 the fundamental natural frequency can be easily found for shells with different ratios of $\frac{L}{jR}$. For example, for a shell having $R/h = 500$ the fundamental frequency occurs at $i = 5$ for $\frac{L}{jR} = 5$. The frequency content of this shell can also be easily derived using Fig 2.7. The range of changes in non-dimensional frequency parameter for this shell is between 0.02 and 0.2. The ranges of natural frequency are then conveniently derived for a specific material from the non-dimensional frequency parameter.

Fig 2.7 and 2.8 show that as the ratio of length to radius increases, the fundamental frequency occurs in lower modes corresponding to longer circumferential wavelengths. Moreover when the ratio of length to radius increases the frequency parameter decreases and after a certain ratio it remains effectively constant. For example, as $\frac{L}{jR}$ increases in Fig 2.7(a) the frequency parameter corresponding to $i = 3$ decreases until around $\frac{L}{jR} = 20$, and then remains constant. It is noticed that the convergence of the frequency parameter depends on the radius to thickness ratio of the shell. The frequency parameter at each mode reaches a lower plateau faster for thicker shells having $R/h = 20$ (Fig 2.8) than for very thin shells having $R/h = 500$ (Fig 2.7).

The horizontal axis is presented in terms of L/jR, which includes the term j defining the axial half-wave number; this makes it possible to find the frequency parameters corresponding to shorter axial wavelengths. For example, for a shell with $L/R = 20$ (Fig 2.8) the frequency parameters of mode $(i, j) = (3, 1)$ is equal to 0.005. However, for the same ratio of L/R the frequency parameter for $(i, j) = (3, 20)$ is equal to 0.5. It is indicating that for a fixed number of circumferential half-waves, the frequency parameter increases with an increase in the number of axial half-waves, j. Also the fundamental frequency always appears to occur at $j = 1$, but for different values of i depending on the ratio of L/R. For lower values of L/R the fundamental frequency occurs at larger values of i.

2.8 Summary of the chapter

Chapter 2 discusses a brief history of shell theories. It then explains Love's first approximation, which is the basis of many shell theories. However the relationship between strain and displacement and stress and moment stress resultant for various shell theories based on Love's first approximation are explained in [1]. It then finds the compatibility and constitutive relationship for a circular cylindrical shell based on Love-Timoshenko theory. The equation of motion for a circular cylindrical shell is found using two methods of equilibrium and the Euler-Lagrange method. The derived equation of motion is then compared with the reported equations of motion based on different shell theories [1], and realized that the one found using the Euler-Lagrange method is the same as the one based on Goldenveizer-Novozhilov theory. The frequency parameters derived using the Euler-Lagrange method for a circular cylindrical shell of infinite length and two thickness to radius ratios of $R/h = 20$, and $R/h = 500$ is then compared with the reported frequency parameters based on different shell theories by Leissa [1]. The comparison showed that the in-plane modes had practically the same frequency parameters based on all shell theories. However, the out-of-plane frequency parameter was not the same. But they were in better agreement for the thinner shells. The frequency parameters derived in this study based on Euler-Lagrange method were also compared with the ones based on three-dimensional theory of elasticity, which showed they were

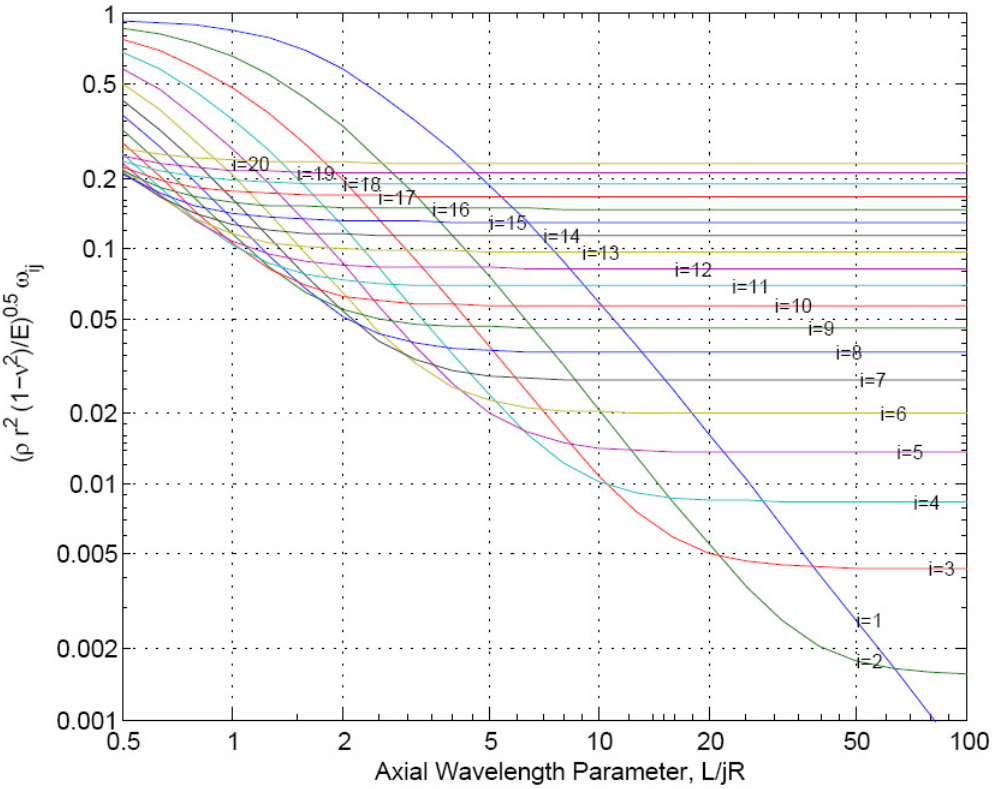

(a) 1st Root

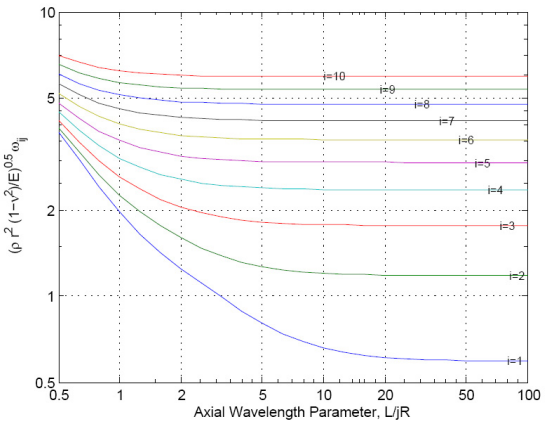

(b) 2nd Root

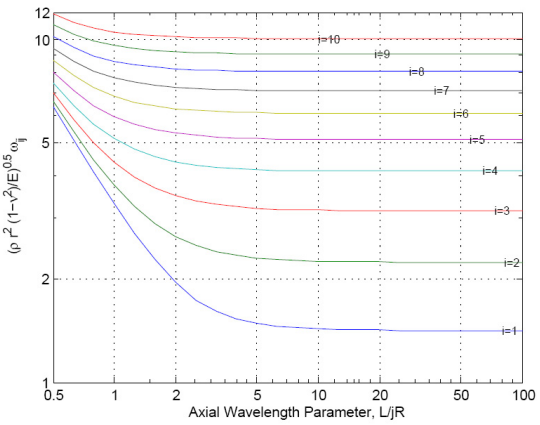

(c) 3rd Root

Figure 2.7: Variation of the frequency parameter of circular cylindrical shell for shell with $R/h = 500$

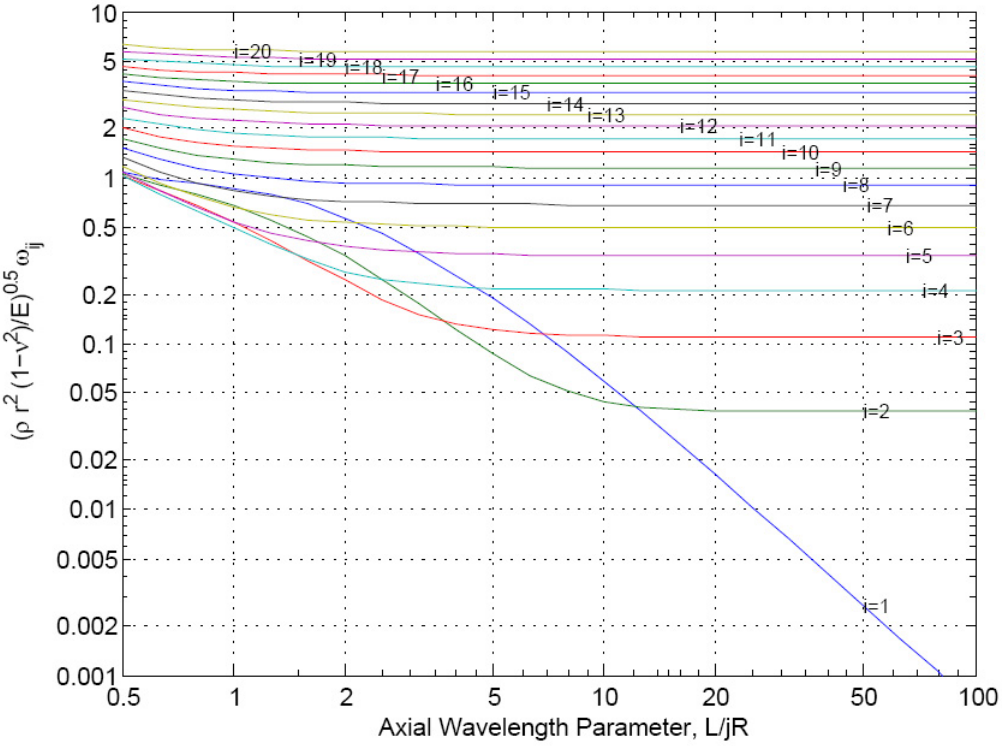

(a) 1st Root

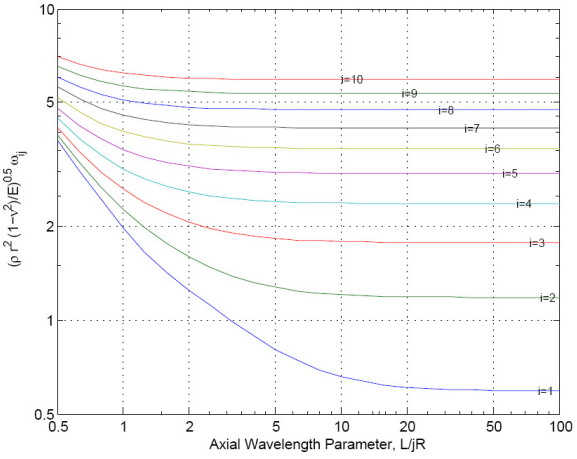

(b) 2nd Root

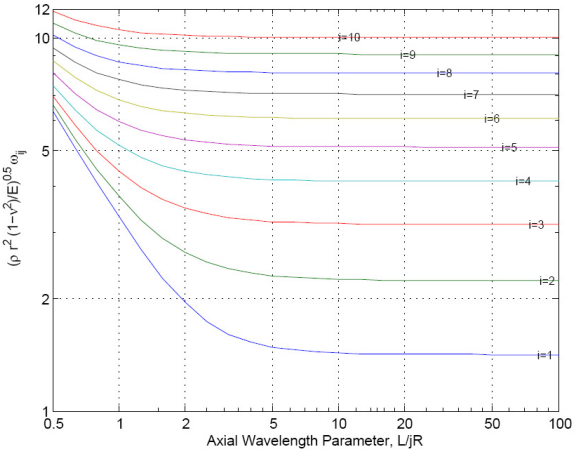

(c) 3rd Root

Figure 2.8: Variation of the frequency parameter of circular cylindrical shell for shell with $R/h = 20$

identical for practical purposes. Subsequently, the equation of motion derived using the Euler-Lagrange method based on Love-Timoshenko theory is used for the rest of the present research.

The study on the energy content of different modes in cylindrical shell showed that the contribution of bending energy toward the total energy is higher in thicker shells. In thinner shells the bending energy only contribute in modes with shorter wavelengths (higher i).

Investigation of the in-plane inertia showed that inclusion of in-plane inertia affected only long wavelength modes for which the membrane energy is most important. The deformation of modes with long wavelength is a combination of out-of-plane and in-plane deformation. It was shown that neglecting the in-plane inertia increased the frequency parameters by 46%. The changes in frequency content of shells could be very important in the context of response of shells to earthquake and could lead to underestimation of the responses of the shell. The next chapter investigates the earthquake response of open cylindrical shell and factors influencing the response.

Chapter 3

Analytical Modelling of Cylindrical Shell Roof subjected to earthquake loading

3.1 Introduction

As explained in chapter 1, there appears to be insufficient research available on the dynamic responses of roof shells to earthquake loadings. The purpose of this chapter is to investigate different aspects of the behaviour of roof shells under earthquake loading to ensure all necessary aspects of behaviour influencing the response are included in the analysis of roof shells.

The dynamic analysis of structures is usually performed using FE methods. But using FE programmes should be based on a sound understanding of shell theories. Moreover it should ideally be verified with other means such as experiments or analytical approaches. In this research the response of cylindrical roof shells under earthquake loading is investigated using an analytical approach. The analytical approach allows investigation of different aspects of behaviour of roof shells, as will be explained in the following sections, which are not easy to explore using a general purpose FE programme. The analytical approach described in the following is developed for a number of purposes. First, it will be used to provide confidence in the use of FE programmes. Second, it will be used to check a number of potentially important questions that have

not so far been fully answered. For example, is it legitimate to use the same number of modes for the convergence of stresses as it is for displacements? What are the influences of including in-plane inertia in deriving the out-of-plane frequencies. Third, the analytical method is used to systematically examine the importance of the contribution of each of the natural modes to the total dynamic response. Fourth, and of particular importance in the present study, is consideration of the relative contributions to the total response of the in-plane modes compared with the more conventional restriction to just the out-of-plane modes. How these in-plane and out-of-plane modes interact, will be shown to influence the response of shell structures for one ground motion. Finally, the analytical method will be used to assess the relative importance of vertical and horizontal components of earthquake motion in the displacement, acceleration, and stress responses of the shell.

The analytical formulation is solved using a specially prepared Matlab program. This calculates the natural frequencies of roof shells through an eigenvalue analysis. It then calculates the displacement and acceleration as well as stress responses of the isotropic open cylindrical shell with constant damping ratio subjected to earthquake loading. Using the dynamic modal analysis facility the accuracy of the analytical solutions is verified using ABAQUS, a commercially available FE program. The same relations of strain-displacement and equations of motion as in chapter 2 are used for the open cylindrical roof shell. But the equations of motion should be modified for the relevant boundary conditions for open cylindrical shells. In addition to finding the natural frequencies of shells in this chapter the programme is also extended to include the earthquake excitation in the equation of motion.

3.2 Analytical modelling

An analytical model is developed for a thin, open cylindrical shell, of radius of curvature R, longitudinal length $L_x = L$, thickness h, and opening angle ϕ as shown in Fig 3.1. Material is taken to be linearly elastic, and the damping ratio is taken to

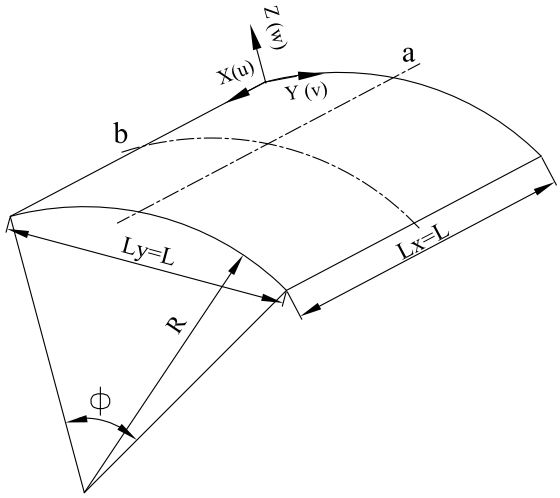

Figure 3.1: Geometry of shell

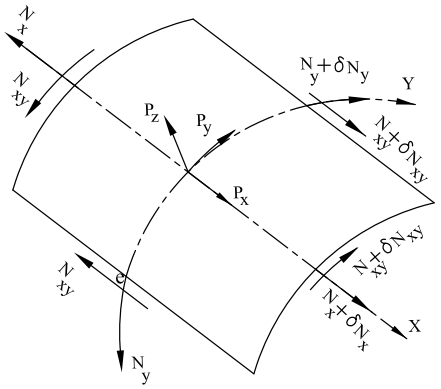

Figure 3.2: Membrane stress resultants

be constant in all modes. The strain-displacement relationships are derived using the equations of Love and Timoshenko [1]; with strains at a distance z from the middle surface and the corresponding membrane and bending strains at mid-surface as presented in eqns (2.10) and (2.11), respectively. The stress-strain relationships, the membrane and bending stress resultants (Fig 3.2 and 3.3) are the same as in eqns (2.12) and (2.14), respectively. For a shell undergoing a free vibration, the equations of motion are derived based on Euler-Lagrange equation and the resulting equations are the same as in eqn (2.18) with the eigenvectors as eqn (2.30). However, for the extraction of the natural frequencies the equations satisfying the conditions of simply support boundary condition for an open cylindrical shell is different to those of complete cylindrical shells. The next section derives the equation of motion for open cylindrical shells with

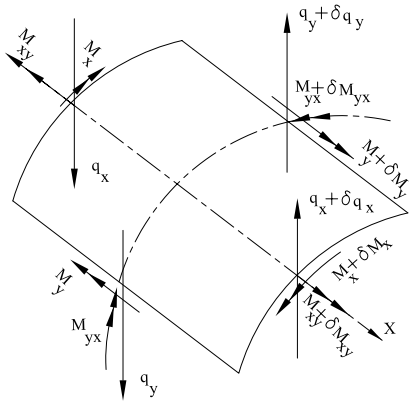

Figure 3.3: Bending stress resultants

simply support boundary conditions.

3.2.1 Natural frequency extraction

In deriving the analytical solutions based upon the above mentioned equations an exact solution for the natural vibration modes for a shell having simple support boundaries, may be taken in the form of double trigonometric series

$$\begin{aligned} u(x,y,t) &= \sum_i \sum_j u_{ij}(x,y) q_{ij}(t) \\ v(x,y,t) &= \sum_i \sum_j v_{ij}(x,y) q_{ij}(t) \\ w(x,y,t) &= \sum_i \sum_j w_{ij}(x,y) q_{ij}(t) \end{aligned} \tag{3.1}$$

where

$$\begin{aligned} u_{ij}(x,y) &= \overline{u}_{ij} cos\frac{j\pi x}{L} sin\frac{i\pi y}{R\phi} \\ v_{ij}(x,y) &= \overline{v}_{ij} sin\frac{j\pi x}{L} cos\frac{i\pi y}{R\phi} \\ w_{ij}(x,y) &= \overline{w}_{ij} sin\frac{j\pi x}{L} sin\frac{i\pi y}{R\phi} \end{aligned} \tag{3.2}$$

Each mode of this series satisfies the conditions of simple support boundaries, namely

$$\begin{aligned} v = w = 0, \;\; N_x = M_x = 0 \quad at \;\; x = 0, \; L \\ u = w = 0, \quad N_y = M_y = 0 \quad at \;\; y = 0, \; R\,\phi \end{aligned} \tag{3.3}$$

In the modal forms of eqn (3.1), (i, j) represent the number of half waves in the circumferential and longitudinal directions, respectively and $\overline{u}_{ij}$, $\overline{v}_{ij}$, and $\overline{w}_{ij}$ are the normalized coefficients determined by solving the eigenvalue problem. The generalized response, used for solving the eigenvalue problem, is taken as $q_{ij}(t) = \sin(\omega_{ij}t + \theta_{ij})$. This equation is on the basis of the assumption that free-vibration motion is harmonic. In this expression ω_{ij} is the natural radial frequency corresponding with the mode (i, j) and θ is the phase angle. Use of eqn (3.1) allows eqn (2.28) to be represented as an eigen value problem (eqn (3.4)), in which the eigen values are associated with the natural frequencies, ω_{ij}, and the eigen modes with amplitudes $\overline{u}_{ij}$, $\overline{v}_{ij}$, and $\overline{w}_{ij}$

$$\begin{bmatrix} k_{11} & k_{12} & k_{13} \\ k_{21} & k_{22} & k_{23} \\ k_{31} & k_{32} & k_{33} \end{bmatrix} \cdot \begin{Bmatrix} \bar{u}_{ij} \\ \bar{v}_{ij} \\ \bar{w}_{ij} \end{Bmatrix} = \begin{Bmatrix} 0 \\ 0 \\ 0 \end{Bmatrix} \tag{3.4}$$

where the stiffness terms, k_{ij}, can be written as

$$\begin{aligned}
k_{11} &= \lambda^2 + \frac{(1-\nu)}{2}\frac{i^2\pi^2}{\phi^2} - \Delta_{ij} \\
k_{12} &= k_{21} = \frac{\nu+1}{2}\lambda i\frac{\pi}{\phi} \\
k_{13} &= -k_{31} = \nu\lambda \\
k_{22} &= \frac{1-\nu}{2}\lambda^2 + (\frac{i\pi}{\phi})^2 k\left\{2(1-\nu)\lambda^2 + (\frac{i\pi}{\phi})^2\right\} - \Delta_{ij} \\
k_{23} &= k_{32} = -i\frac{\pi}{\phi} - k\left\{(2-\nu)\lambda^2\frac{i\pi}{\phi} + (\frac{i\pi}{\phi})^3\right\} \\
k_{33} &= 1 + k\left(\lambda^2 + (i\frac{i\pi}{\phi})^2\right)^2 - \Delta_{ij}
\end{aligned} \tag{3.5}$$

In these expressions, $\lambda = \frac{j\pi R}{L}$, $k = \frac{h^2}{12R^2}$, and $\Delta_{ij} = \frac{\rho(1-\nu^2)R^2}{E}(\omega_{ij})^2$ is a non-dimensionalized form of frequency. The resulting eigenvalue problem has been solved to extract frequencies for varying (i, j) with modal normalization based upon

$$\sqrt{(\overline{u}_{ij})^2 + (\overline{v}_{ij})^2 + (\overline{w}_{ij})^2} = 1 \tag{3.6}$$

Once the mode shapes and natural frequencies of the open cylindrical shell have been obtained, the dynamic response of the structure can be computed from the mode super-

position analysis.

3.2.2 Verification of natural frequencies

The analytically derived natural frequencies have been verified by comparing them with the results reported by Kuneida *et al.*[95]. A simply supported panel having $R/h = 500$, $L_y/L_x = 0.5$, and $\phi = \pi/2$ was chosen by Kuneida, who employed an analytical method similar to that used in the present study for extracting the eigenvalues. He reported the eigenvalues for a total of 18 circumferential half waves and 9 axial half waves in modes both symmetric and antisymmetric about lines aa and bb in Fig 3.1. The results from the present analytical method were identical to those presented by Kuneida [95] and are presented in Tables 3.1 and 3.2.

	i								
j	1	3	5	7	9	11	13	15	17
1	0.1992	0.0374	0.0587	0.1132	0.1869	0.2793	0.3901	0.5195	0.6673
2	0.4886	0.1155	0.0745	0.1175	0.1896	0.2816	0.3923	0.5216	0.6694
3	0.6772	0.2231	0.1139	0.1291	0.1951	0.2858	0.3961	0.5253	0.6730
4	0.7805	0.3349	0.1706	0.1512	0.2050	0.2923	0.4017	0.5305	0.6781
5	0.8377	0.4370	0.2357	0.1833	0.2201	0.3018	0.4093	0.5374	0.6848
6	0.8715	0.5244	0.3033	0.2233	0.2408	0.3145	0.4191	0.5462	0.6930
7	0.8930	0.5965	0.3693	0.2681	0.2669	0.3307	0.4314	0.5568	0.7030
8	0.9076	0.6553	0.4315	0.3154	0.2974	0.3505	0.4462	0.5695	0.7147
9	0.9180	0.7030	0.4887	0.3634	0.3313	0.3736	0.4635	0.5842	0.7281

Table 3.1: Eigen value $\Delta^{0.5}$ for $R/h = 500$, $L_y/L_x = 0.5$, $\phi = \pi/2$ (symmetric modes about line aa in Fig 3.1)

Table 3.1 and 3.2 show that for a given axial wavelength j the minimum frequency occurs at a characteristic circumferential wavelength, i_{min}, for example for $j = 1$, $i_{min} = 3$; for $j = 2$, $i_{min} = 5$; $j = 3$, $i_{min} = 6$. This shows it could be either a symmetric or antisymmetric mode.

	i								
j	2	4	6	8	10	12	14	16	18
1	0.0667	0.0409	0.0834	0.1477	0.2308	0.3324	0.4525	0.5911	0.7481
2	0.2179	0.0781	0.0907	0.1508	0.2332	0.3346	0.4547	0.5932	0.7502
3	0.3807	0.1461	0.1117	0.1583	0.2378	0.3386	0.4584	0.5968	0.7538
4	0.5173	0.2279	0.1479	0.1723	0.2455	0.3445	0.4637	0.6020	0.7589
5	0.6207	0.3125	0.1951	0.1938	0.2570	0.3528	0.4709	0.6087	0.7655
6	0.6962	0.3930	0.2486	0.2226	0.2728	0.3637	0.4801	0.6172	0.7736
7	0.7513	0.4661	0.3044	0.2570	0.2929	0.3775	0.4914	0.6274	0.7834
8	0.7920	0.5307	0.3601	0.2955	0.3171	0.3943	0.5048	0.6395	0.7948
9	0.8227	0.5868	0.4139	0.3365	0.3449	0.4139	0.5206	0.6535	0.8079

Table 3.2: Eigen value $\Delta^{0.5}$ for $R/h = 500$, $L_y/L_x = 0.5$, $\phi = \pi/2$ (anti-symmetric modes about line aa in Fig 3.1)

For $i < i_{min}$ the energy of resistance has high contribution from membrane energy, while for $i > i_{min}$ the resistance is increasingly dominated by bending energy. This will be discussed in section 3.2.3.

In a second study, the natural frequencies obtained using the analytical method were compared with results obtained using the ABAQUS FE programme. The analysis was again performed on an isotropic open cylindrical shell with simply supports at four edges as indicated by eqn (3.3). Shell geometry and material property ratios for this study were $\phi = \pi/3,\ \frac{L_y}{L_x} = 1,\ \frac{R}{h} = 500,\ B = \frac{\rho h R}{E} = 10^{-6}\ s^2,\ \nu = 0.3$, with the exact value of $R = 104.8m$, $L_x = 104.8m$, $\Phi = \pi/3$, $h = 104.8/500$, $\rho = 4140.5kg/m^3$, $E = 91 \times 10^9 N/m^2$. Convergence of the 10 lowest natural frequencies, using the FE method, was found to be adequate using a 30×30 mesh. A complete discussion on the convergence of the frequency results with mesh size will be presented in section 4.3.2. But it is worth mentioning that ABAQUS derived frequencies are ranked from the mode having the lowest frequency and then in ascending order for the requested number of frequencies. Each mode has characteristic circumferential and axial wave

numbers corresponding with values of i and j, which can be found by observing the deformed shapes of the shell in each mode. However in the analytical method, the frequencies are extracted for the requested numbers of i and j.

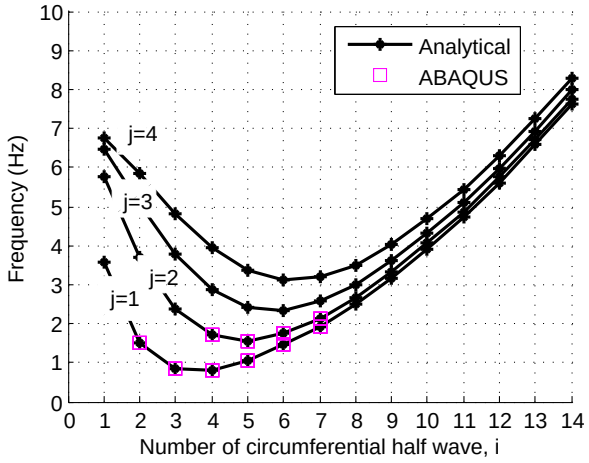

Figure 3.4: Comparison of analytical and ABAQUS natural frequency for a shell having $\phi = \pi/3,\ \frac{L_y}{L_x} = 1,\ \frac{R}{h} = 500,\ B = \frac{\rho h R}{E} = 10^{-6}\ s^2,\ \nu = 0.3$

In the extraction of natural frequencies, similar to the analytical method, ABAQUS normalizes the displacement. The normalizing in ABAQUS is such that the largest displacement entry in each eigen vector of $\bar{u}_{ij}, \bar{v}_{ij}, \bar{w}_{ij}$ is equal to unity. But in the analytical method the normalization method is adopted based on $\sqrt{\bar{u}_{ij}^2 + \bar{v}_{ij}^2 + \bar{w}_{ij}^2}$ being equal to 1.

Fig 3.5 shows the mode shapes corresponding to some selected modes for the shell in Fig 3.4.

The FE predictions are compared with the present analytical results in Fig 3.4 and both FE and analytical method exhibit the same deformation. The very close agreement between the resulting natural frequencies using the analytical and FE method provides further confidence in the extension of these methods to predict the response of shells when subject to earthquakes.

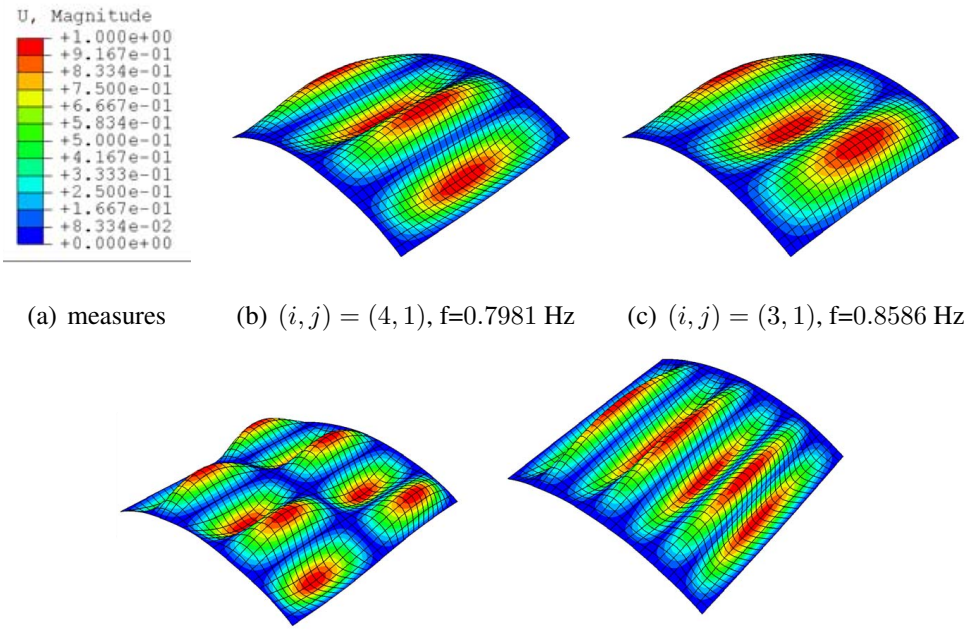

(a) measures (b) $(i,j)=(4,1)$, f=0.7981 Hz (c) $(i,j)=(3,1)$, f=0.8586 Hz

(d) $(i,j)=(5,2)$, f=1.5505 Hz (e) $(i,j)=(7,1)$, f=1.9418 Hz

Figure 3.5: Frequency and deformed shape of some selected modes for a shell with $R/h = 500$, $\phi = \pi/3$, $\rho hR/E = 10^{-6}\ s^2$, $\rho = 4140.5\ kg/m^3$, $E = 9.1 \times 10^{10}$, $R = 104.8\ m$

3.2.3 Energy content of each mode

In order to understand the nature of each mode, the energy content of each mode for the shell reported in Fig 3.4 are investigated. This shell has the same radius, length and material properties as the complete cylindrical shell in Fig 2.5(a) but it is an open cylindrical shell with open angle equal to $\pi/3$.

Fig 3.6(a) shows the frequency with the separate contributions from membrane and bending energy to the frequency (as is shown in eqn (2.23)) identified for each mode. Comparing with the energy contribution of each mode for the complete cylindrical shell in Fig 2.5(a), it can be seen that the contribution of membrane energy to the frequency corresponding to each value of i decreases. At the same time in open cylindrical shell the contribution of modes having bending energy increases in comparison to complete cylindrical shell. Comparing the two Figs 3.6(a) and 2.5 shows that the frequency of modes dominated by membrane energy decreases in open cylindrical shell in comparison to the complete cylindrical shell such as modes with $i = 1, 2$.

In the open cylindrical shell in Fig 3.6 the contribution of membrane energy reaches a negligible proportion at circumferential half-wave number, i, equal to 6, in comparison with the membrane energy in the complete cylindrical shell reaching the same proportion at $i = 18$ in Fig 2.5; both having the same wavelength. This shows that for open cylindrical shell with $\Phi = \pi/3$ the frequency for mode i would correspond with that of $3i$ in the complete cylinder. For example, the modes with $i = 6$ in Fig 2.5 have the same frequency as modes with $i = 2$ in Fig 3.6(a) as they have the same wavelength. This indicates that the modes having the same wavelength have exactly the same frequency and equal contribution from bending and membrane energy.

Fig 3.6(b) provides a break down of the contributions of different energy component to the total energy for modes having $j = 1$. Curves labelled (N_x, N_y, N_{xy}) indicate the contributions derived from the membrane energy associated with the axial, circumferential and shear actions. Curves labelled with (M_x, M_y, M_{xy}) indicate the contribution derived from the bending energy associated with the axial, circumferential and shear actions (as is shown in eqn (2.23)).
For this shell, the contribution of membrane energy is dominated by N_x and N_{xy}. N_x becomes more important at the minimum frequency. However the bending energy is dominated by M_y with the insignificant contribution from M_x and M_{xy}.

3.2.4 In-plane modes

In section 2.7 the effects on out-of-plane frequencies by neglecting in-plane inertia in the equations of motion were investigated. The results showed that for those geometries where the contribution of $\bar{u}_{ij}$ or $\bar{v}_{ij}$ were significant in comparison to $\bar{w}_{ij}$ such as mode $(i, j) = (1, 1)$ for which $\bar{v}_{ij} > \bar{w}_{ij}$ in Table 2.4 the neglect of in-plane inertia substantially changed the corresponding out-of-plane frequency for this mode (Fig 2.6(d)).

In this section, the effects of in-plane inertia on out-of-plane frequencies are first investigated for the selected shell with geometry and material property as in Fig 3.4.

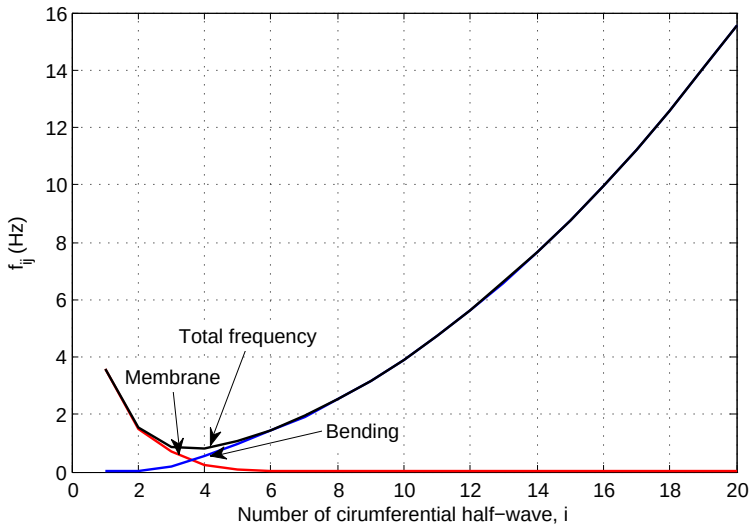

(a) Frequency

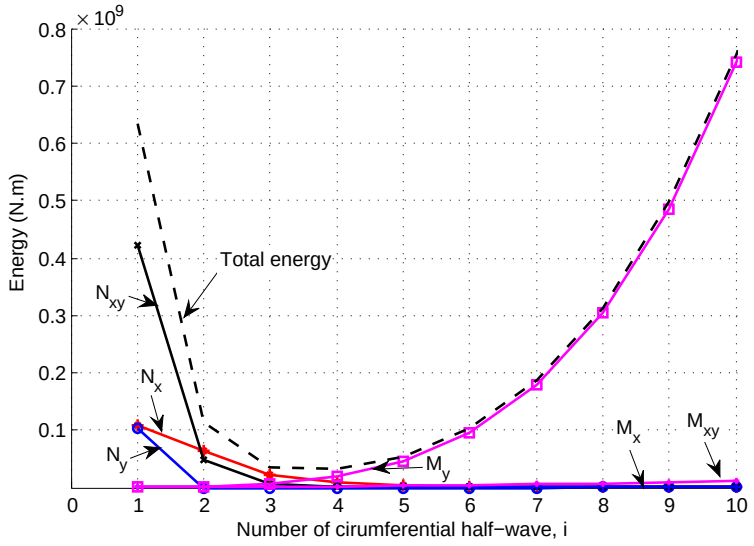

(b) Energy

Figure 3.6: Frequency and energy contribution for a shell with $R/h = 500$, $\phi = \pi/3$, $\rho hR/E = 10^{-6}\ s^2$, and $j = 1$ ($\rho = 4140.5\ kg/m^3$, $E = 9.1 \times 10^{10}\ N/m^2$, $R = 104.8\ m$)

Table 3.3 presents the out-of-plane frequency and corresponding eigenvector in mode $j = 1$ for this shell (when in-plane inertia is included), and the out-of-plane frequencies resulting from neglect of in-plane inertia. As can be seen in Table 3.3 the changes in frequencies are generally insignificant with maximum error equal to 3.7% corresponding to mode $(1, 1)$. The reason for the insignificant changes in frequencies is because the value of $\bar{u}_{ij}$ and $\bar{v}_{ij}$ are generally at least one order of magnitude less than $\bar{w}_{ij}$. It

i	f (Hz) (Including in-plane inertia)	$\bar{u}$	$\bar{v}$	$\bar{w}$	f (Hz) (Ignoring in-plane inertia)	$\%$ error
1	3.5891	-0.0556	0.2642	0.9629	3.7236	3.7
2	1.5205	-0.0488	0.1651	0.9851	1.5435	1.5
3	0.8586	-0.0295	0.1123	0.9932	0.8644	0.67
4	0.7981	-0.0187	0.0842	0.9963	0.8011	0.38
5	1.0483	-0.0126	0.0672	0.9977	1.0507	0.23
6	1.4468	-0.0090	0.0559	0.9984	1.4492	0.17
7	1.9418	-0.0068	0.0479	0.9988	1.9441	0.12
8	2.5200	-0.0052	0.0418	0.9991	2.5223	0.09
9	3.1777	-0.0042	0.0372	0.9993	3.1799	0.07
10	3.9137	-0.0034	0.0334	0.9994	3.9159	0.06

Table 3.3: Eigen-vector and comparison of out-of-plane frequency for open cylindrical shell in Fig 3.4 for including and neglecting in-plane inertia, $j = 1$

is observed that the importance of in-plane inertia increases in modes such as $(1, 1)$ and $(2, 1)$ where the circumferential displacement $\bar{v}_{ij}$ is significant. As mentioned in section 2.7, when $\bar{u}_{ij}$ or $\bar{v}_{ij}$ are significant, it is likely that the membrane energy will be significant. Table 3.3 shows that the in-plane inertia can be neglected in extraction of out-of-plane frequencies for this specific shell. However, in this chapter a large number of shells with different geometry and material properties are investigated for which the effect of in-plane inertia might not be insignificant. In order to prevent the checking procedure for the importance of in-plane inertia for each case of shell, the in-plane inertia is included in all analyses reported in this research.

The use of in-plane inertia is not limited to its effect on the out-of-plane frequency. It is also possible that the in-plane frequencies corresponding to these in-plane inertia terms and their corresponding eigenvectors could influence the responses of shell to earthquake. Although these in-plane frequencies have generally been neglected in the dynamic analysis of shell in earlier research studies [57] [8] [95] [7], it is important to

check the influence of these modes on the displacement and stress responses. If they significantly influence the responses of shells this should influence the approach to the analysis of roof shells to earthquakes. However, as the dynamic analysis of roof shell has not yet been explained, this section only presents the frequencies corresponding to in-plane and out-of-plane modes and their influence on the response will be presented later in section 3.9.

Fig 3.7 shows the out-of-plane and in-plane frequencies for the shell with geometry and material properties as in Fig 3.4. Most of the in-plane frequencies in Fig 3.7(b),(c) are not in the range of earthquake frequencies. However, there are a few modes in which the in-plane frequencies are in the range of earthquake frequencies, such as modes $(1,1)$, $(1,2)$, $(1,3)$, $(2,1)$, $(2,2)$ corresponding to the in-plane frequencies in circumferential direction (Fig 3.7(b)) and mode $(i,j) = (1,1)$ in axial direction (Fig 3.7(c)). These modes could potentially have significant participation in the displacement and stress responses of a shell to earthquake; this aspect will be investigated in section 3.9.

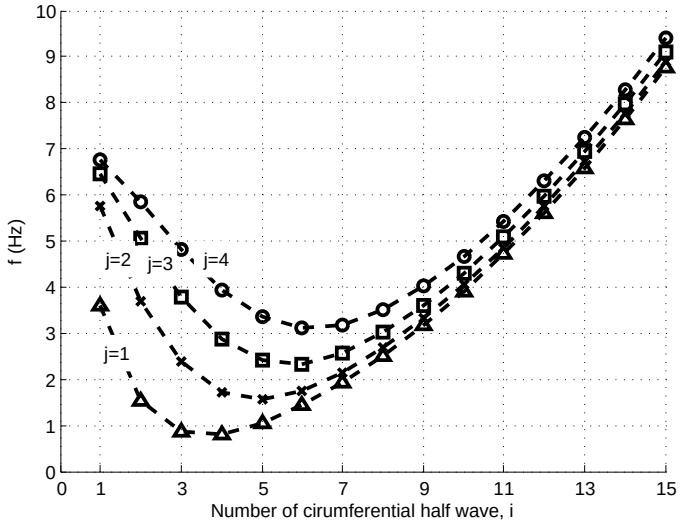

(a) out-of-plane mode ($\bar{w}_{ij}$ dominates)

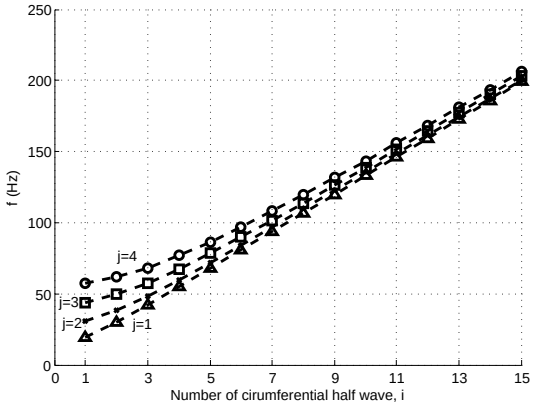

(b) in-plane mode ($\bar{v}_{ij}$ dominates)

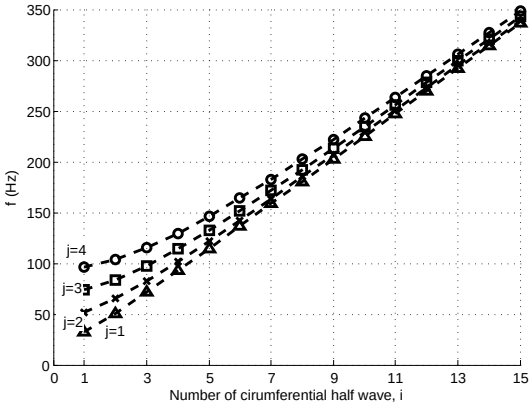

(c) in-plane mode ($\bar{u}_{ij}$ dominates)

Figure 3.7: In-plane and out-of-plane natural frequencies for a shell with $\phi = \pi/3,\ \frac{L_y}{L_x} = 1,\ \frac{R}{h} = 500,\ B = \frac{\rho h R}{E} = 10^{-6}\ s^2,\ \nu = 0.3$

3.3 Modal response

Considering the simplest model of a Single Degree of Freedom (SDOF) system undergoing an external force of $P(t)$, each of the physical properties such as mass, stiffness and energy loss mechanism is concentrated in the rigid block as in Fig 3.8. The block

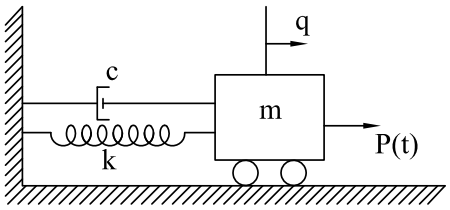

Figure 3.8: Mass spring damper system

is constrained by rollers so it can only translate in the single displacement coordinate system, $q(t)$. The system resistance to the external force is provided by the inertia force $f_I(t)$, spring force, $f_S(t)$, and damping force $f_D(t)$. The equation of motion is derived by the equilibrium of these forces as

$$f_I(t) + f_D(t) + f_S(t) = P(t) \tag{3.7}$$

where the inertia force is $f_I(t) = m\ddot{q}(t)$ according to d'Alembert's principle, the damping force is $f_D(t) = c\dot{q}(t)$ considering a viscous damping, and $f_S(t) = kq(t)$ is the elastic force. Replacing the inertia force, damping force and elastic force in eqn (3.7), the equation of motion for the SDOF in Fig 3.8 becomes

$$m\ddot{q}(t) + c\dot{q}(t) + kq(t) = P(t) \tag{3.8}$$

However the analysis of a more complicated system such as roof shell needs more complicated idealization. The displacement of a Multi Degree of Freedom (MDOF) system with N degrees of freedom can be modelled by N components in vector $\mathbf{X}$ as explained by Clough and Penzien [96]. Consider the equation of motion for a MDOF system, including all degrees of freedom as

$$\mathbf{m}\ddot{\mathbf{X}}(t) + \mathbf{c}\dot{\mathbf{X}}(t) + \mathbf{k}\mathbf{X}(t) = P(t) \tag{3.9}$$

where **m**, **c**, **k** are mass, damping and stiffness matrices.

The displacement for any modal component $X_r(t)$, can be written as the product of the

mode shape vector ϕ_r, and the modal amplitude $q_r(t)$.

$$X_r(t) = \Phi_r q_r(t) \tag{3.10}$$

provided the mode shape vector satisfies the boundary conditions. The total displacement vector, $\mathbf{X}(t)$, can then be defined as the sum of all modal vectors, in which each modal vector is obtained by the product of the mode shape vector and the modal amplitudes

$$\mathbf{X}(t) = \Phi_1 q_1(t) + \Phi_2 q_2(t) + \ldots + \Phi_N q_N(t) = \sum_{r=1}^{N} \Phi_r q_r(t) \tag{3.11}$$

Matrix $\mathbf{X}(t)$ can be expressed in matrix form as

$$\mathbf{X} = \mathbf{\Phi q} \tag{3.12}$$

in which the $\mathbf{\Phi}$ mode shape matrix consists of N independent modal vector $\mathbf{\Phi} = [\Phi_1\ \Phi_2\ \ldots\ \Phi_N]$, which make it a nonsingular matrix so it is invertible. This matrix transforms the generalized coordinate system, $\mathbf{q}$, to the geometric coordinate vector, $\mathbf{X}$. Comparing the above procedure with the frequency extraction method in section 3.2.1 the matrices and vectors notation can be introduced in the context of section 3.2.1 for the case of roof shells.

The total displacement vector $\mathbf{X}(t)$ is comprised of u, v, w in eqn (3.1) as

$$\mathbf{X}(t) = \begin{bmatrix} u(x,y,t) \\ v(x,y,t) \\ w(x,y,t) \end{bmatrix} \tag{3.13}$$

Each independent modal vector, ϕ_r, in the mode shape matrix $\mathbf{\Phi}$ is equal to a vector of u_{ij}, v_{ij}, w_{ij} in eqn (3.2), which can be presented as

$$\phi_{\mathbf{r}} = \begin{bmatrix} \overline{u}_{ij} cos\frac{j\pi x}{L} sin\frac{i\pi y}{R\phi} \\ \overline{v}_{ij} sin\frac{j\pi x}{L} cos\frac{i\pi y}{R\phi} \\ \overline{w}_{ij} sin\frac{j\pi x}{L} sin\frac{i\pi y}{R\phi} \end{bmatrix} \tag{3.14}$$

The orthogonality of normal modes, which will be explained later, allows simplification of the equations of motion of the multi-degree-of-freedom system of eqn (3.9). Substituting eqn (3.11) in eqn (3.9) and pre-multiplying by the transpose of the $n\ th$ mode shape vector, Φ_n^T, gives

$$\sum_{r=1}^{N} \Phi_n^T \mathbf{m} \Phi_r \ddot{q}_r(t) + \sum_{r=1}^{N} \Phi_n^T \mathbf{c} \Phi_r \dot{q}_r(t) + \sum_{r=1}^{N} \Phi_n^T \mathbf{k} \Phi_r q_r(t) = \Phi_n^T P(t) \tag{3.15}$$

If the three terms in the left hand side of eqn (3.15) are expanded as in eqn (3.11), the orthogonality of mode shape implies that $\phi_n^T m \phi_r = 0$, $\phi_n^T k \phi_r = 0$, $\phi_n^T c \phi_r = 0$, for $\omega_n \neq \omega_r$. This means all terms except the $n\ th$ will vanish in eqn (3.15) allowing it to be written as

$$\Phi_n^T \mathbf{m} \Phi_n \ddot{q}_r(t) + \Phi_n^T \mathbf{c} \Phi_n \dot{q}_r(t) + \Phi_n^T \mathbf{k} \Phi_n q_r(t) = \Phi_n^T P(t) \tag{3.16}$$

Using the following symbols

$$\begin{aligned} M_n &= \Phi_n^T \mathbf{m} \Phi_n \\ K_n &= \Phi_n^T \mathbf{k} \Phi_n \\ C_n &= \Phi_n^T \mathbf{c} \Phi_n \\ P_n(t) &= \Phi_n^T P(t) \end{aligned} \tag{3.17}$$

in which M_n, K_n, C_n, and P_n are often referred to as generalized mass, generalized stiffness, modal coordinate viscous damping, and generalized load for mode n, respectively, eqn (3.16) can be written as

$$M_n \ddot{q}_n(t) + C_n \dot{q}_n + K_n q_n = P_n(t) \tag{3.18}$$

If the damping is neglected and there is no external force, eqn (3.9) would take the form of

$$\mathbf{m} \ddot{\mathbf{X}}(t) + \mathbf{k} \mathbf{X}(t) = 0 \tag{3.19}$$

Using eqn (3.12), eqn (3.19) can be written as

$$\mathbf{m} \phi \ddot{\mathbf{q}}(t) + \mathbf{k} \phi \mathbf{q}(t) = 0 \tag{3.20}$$

This equation is equivalent to eqn (2.28). Substituting the harmonic expression of $q_{ij}(t) = \sin(\omega_{ij}t + \theta_{ij})$ as explained in section 3.2.1 gives

$$-\omega_{ij}^2 \mathbf{m}\phi \sin(\omega_{ij}t + \theta_{ij}) + \mathbf{k}\phi \sin(\omega_{ij}t + \theta_{ij}) = 0 \tag{3.21}$$

which can be simplifies as

$$[-\omega_{ij}^2 \mathbf{m} + \mathbf{k}]\phi = 0 \tag{3.22}$$

Eqn (3.22) is equivalent to the eigen value problem of eqn (3.4). The nontrivial solution of eqn (3.22) is possible only when the determinate of $\left\|-\omega_{ij}^2 \mathbf{m} + \mathbf{k}\right\| = 0$

Once the mode shapes and natural frequencies of the open cylindrical shell have been obtained from the eigenvalue problem of eqn (3.4), the dynamic response of the structure in each mode can be computed using the method that will be described in section 3.4. This dynamic response is in the generalized coordinate system, q_r. As explained earlier in this section, by multiplying ϕ_r by q_r the displacement modal component $X_r(t)$ would be derived. The total displacement time history response is then found by the sum of all modal responses as in eqn (3.11).

3.3.1 Orthogonality of modes

The orthogonality conditions are satisfied when

$$\begin{aligned} \Phi_n^T \mathbf{m} \Phi_r &= 0 \\ \Phi_n^T \mathbf{k} \Phi_r &= 0 \end{aligned} \tag{3.23}$$

for the values of $\omega_n \neq \omega_r$ [97]. The orthogonality of modes in other words eqn (3.23) can be proven as follows: The relation between the stiffness and mass for the n^{th} mode can be derived from the equation of motion for a system in free vibration, eqn (3.22), as

$$\mathbf{k}\phi_n = \omega_n^2 \mathbf{m}\phi_n \tag{3.24}$$

premultiplying eqn (3.24) by ϕ_r^T, the following equation will be derived

$$\phi_r^T \mathbf{k}\phi_n = \omega_n^2 \phi_r^T \mathbf{m}\phi_n \tag{3.25}$$

Similarly the relation between stiffness and mass for the r^{th} mode satisfies

$$\mathbf{k}\phi_r = \omega_r^2 \mathbf{m}\phi_r \tag{3.26}$$

premultiplying eqn (3.26) by ϕ_n^T, the following equation will be derived

$$\phi_n^T \mathbf{k}\phi_r = \omega_r^2 \phi_n^T \mathbf{m}\phi_r \tag{3.27}$$

in which the rule of transposing matrix product can be observed because of the symmetry of $\mathbf{k}$ and $\mathbf{m}$. Transposing both side of eqn (3.25) gives

$$\phi_n^T \mathbf{k}\phi_r = \omega_n^2 \phi_n^T \mathbf{m}\phi_r \tag{3.28}$$

which upon subtraction of (3.27) gives

$$(\omega_n^2 - \omega_r^2)\phi_n^T \mathbf{m}\phi_r = 0 \tag{3.29}$$

Hence, when the frequencies of the two modes are not the same, eqn (3.29) gives the first orthogonality condition of eqn (3.23).
The second orthogonality condition is now clear by applying first equation of eqn (3.23) into eqn (3.28) , which gives

$$\phi_n^T \mathbf{k}\phi_r = 0 \qquad \omega_n \neq \omega_r \tag{3.30}$$

so both the orthogonality conditions of eqn (3.23) are true when $\omega_n^2 \neq \omega_r^2$.
Because of the orthogonality of modes the square matrices in eqn (3.15) are diagonal

$$\begin{aligned} \mathbf{K} &\equiv \Phi^T k \Phi \\ \mathbf{M} &\equiv \Phi^T m \Phi \end{aligned} \tag{3.31}$$

where the diagonal elements are

$$\begin{aligned} K_n &= \Phi_n^T \mathbf{k} \Phi_n \\ M_n &= \Phi_n^T \mathbf{m} \Phi_n \end{aligned} \tag{3.32}$$

The diagonal term of $\mathbf{K}$ and $\mathbf{M}$ are related by

$$K_n = \omega_n^2 M_n \tag{3.33}$$

3.3.2 Confirmation of earthquake dynamic response

Once the mode shapes and natural frequencies of the undamped open cylindrical shell undergoing a free vibration have been obtained, the dynamic response of the damped structure subjected to a forced vibration can be computed from the mode superposition analysis. The dynamic equation of motion for a forced damped system in the x, y, and z directions may be written in the form

$$\begin{aligned} F_x(u,v,w) &= S_x(u,v,w) + c.\frac{\partial u}{\partial t} + \rho.h.\frac{\partial^2 u}{\partial t^2} - P_x(t) = 0 \\ F_y(u,v,w) &= S_y(u,v,w) + c.\frac{\partial v}{\partial t} + \rho.h.\frac{\partial^2 v}{\partial t^2} - P_y(t) = 0 \\ F_z(u,v,w) &= S_z(u,v,w) + c.\frac{\partial w}{\partial t} + \rho.h.\frac{\partial^2 w}{\partial t^2} - P_z(t) = 0 \end{aligned} \tag{3.34}$$

where c is the damping. In the present study the earthquake loading is considered to be an external force which is modeled in terms of modal forces using a Fourier series representation of equivalent body forces ($P_x(t)$, $P_y(t)$, $P_z(t)$), and $S_x(u,v,w)$, $S_y(u,v,w)$, and $S_z(u,v,w)$ are static equation of equilibrium for cylindrical shell as in eqn (2.29).

The derivation of the equations governing the vibrations of open cylindrical shells follows the method used by Yamada [8]. To obtain the corresponding equations of motion in modal form the following procedure is considered. If eqn (3.34) are satisfied then any weighted combination

$$\begin{aligned} \int_0^L \int_0^{R\phi} (F_x(u,v,w,t).u(x,y,t) + F_y(u,v,w,t).v(x,y,t) \\ + F_z(u,v,w,t).w(x,y,t))\, dx\, dy = 0 \end{aligned} \tag{3.35}$$

must also be satisfied. Substitution of eqns (3.1), and (3.34) into eqn (3.35) and taking the orthogonal properties of normal modes into account allows eqn (3.35) to be

rewritten as

$$\int_0^L \int_0^{R\phi} (S_x(u,v,w)u_{ij}q_{ij}(t) + c.\frac{\partial q_{ij}(t)}{\partial t}u_{ij}^2 + \rho.h.\frac{\partial^2 q_{ij}(t)}{\partial t^2}u_{ij}^2 - P_x(t)u_{ij}$$
$$+S_y(u,v,w)v_{ij}q_{ij}(t) + c.\frac{\partial q_{ij}(t)}{\partial t}v_{ij}^2 + \rho.h.\frac{\partial^2 q_{ij}(t)}{\partial t^2}u_{ij}^2 - P_y(t)v_{ij} \quad (3.36)$$
$$+ S_z(u,v,w)w_{ij}q_{ij}(t) + c.\frac{\partial q_{ij}(t)}{\partial t}w_{ij}^2 + \rho.h.\frac{\partial^2 q_{ij}(t)}{\partial t^2}w_{ij}^2 - P_z(t)w_{ij})dx\,dy = 0$$

For undamped free vibration $c = 0$ and $P_x(t) = P_y(t) = P_z(t) = 0$ and considering a periodic free vibration as $q_{ij}(t) = \sin(\omega_{ij}t + \theta_{ij})$ as explained in Section 3.2.1, allows eqn (3.36) to be written

$$\int_0^L \int_0^{R\phi} (S_x(u,v,w)u_{ij} + S_y(u,v,w)v_{ij} + S_z(u,v,w)w_{ij}) \sin(\omega_{ij}t + \theta_{ij})dx\,dy$$
$$= \int_0^L \int_0^{R\phi} [\omega_{ij}^2\rho h(u_{ij}^2 + v_{ij}^2 + w_{ij}^2)] \sin(\omega_{ij}t + \theta_{ij})dx\,dy \quad (3.37)$$

canceling $\sin(\omega_{ij}t + \theta_{ij})$ from both sides of eqn (3.37) it will take the form

$$\int_0^L \int_0^{R\phi} (S_x(u,v,w)u_{ij} + S_y(u,v,w)v_{ij} + S_z(u,v,w)w_{ij})dx\,dy =$$
$$\int_0^L \int_0^{R\phi} [\omega_{ij}^2\rho h(u_{ij}^2 + v_{ij}^2 + w_{ij}^2)]dx\,dy \quad (3.38)$$

in which the modal mass, M_{ij}, is represented as

$$M_{ij} = \rho.h \int_0^L \int_0^{R\phi} (u_{ij}^2 + v_{ij}^2 + w_{ij}^2)dx\,dy \quad (3.39)$$

Replacing u_{ij}, v_{ij}, and w_{ij} with eqn (3.2) and making use of the modal normalization introduced in eqn (3.6), eqn (3.39) is simplified to

$$M_{ij} = \rho.h\frac{LR\phi}{4} \quad (3.40)$$

As it can be seen a uniform distribution of mass in the open cylindrical shell results in a generalized modal mass, M_{ij}, which is constant in all modes.

So the equation of motion for undamped free vibration motion will be

$$\int_0^L \int_0^{R\phi} (S_x(u,v,w)u_{ij} + S_y(u,v,w)v_{ij} + S_z(u,v,w)w_{ij})dx\,dy = M_{ij}\omega_{ij}^2 \quad (3.41)$$

Now, for the damped forced vibration system, substitution of eqns (3.41) and (3.39) into eqn (3.36) results in

$$\omega_{ij}^2 M_{ij}q_{ij} + \frac{c}{\rho h}M_{ij}\frac{\partial q_{ij}}{\partial t} + M_{ij}\frac{\partial^2 q_{ij}}{\partial t^2} \quad (3.42)$$
$$= \int_0^L \int_0^{R\phi} (P_x(t)u_{ij} + P_y(t)v_{ij} + P_z(t)w_{ij})dx\,dy$$

allowing the modal amplitudes of the shell response to be determined from

$$\frac{\partial^2 q_{ij}}{\partial t^2} + 2\zeta_{ij}\omega_{ij}\frac{\partial q_{ij}}{\partial t} + \omega_{ij}^2 q_{ij} = \frac{P_{ij}}{M_{ij}} \tag{3.43}$$

where, $\zeta_{ij} = \frac{c}{2\omega_{ij}\rho h}$, is the modal damping ratio, and the modal force is taken as

$$P_{ij}(t) = \int_0^L \int_0^{R\phi} (P_x(t)u_{ij} + P_y(t)v_{ij} + P_z(t)w_{ij})dx\,dy \tag{3.44}$$

However, a full discussion on deriving the modal force will be presented in section 3.3.3. In the absence of precise empirical information on modal damping, the modal damping ratio (the ratio of damping to the critical damping in each mode) is considered constant in all modes, which implies c varies in proportion to ω_{ij}. This means modes with higher frequencies have higher damping forces. However, it should be noted that using different damping models would result in different damping forces. For example, if Rayleigh damping model was chosen, depending on the selection of the two modes with a constant damping ratio, the damping ratio corresponding to other modes could be higher or lower than the chosen constant damping ratio in the present research. Therefore, the participation of modes with higher frequencies could be higher or lower than their present participation.

Eqn (3.43) represents a set of uncoupled equations, which can be solved individually for each of the (i, j) modes using a method that will be described in section 3.4. Once the modal responses $q_{ij}(t)$ have been determined they can be substituted in eqn (3.1) to find the displacement time history responses for different locations on the roof shell. Shell stresses and strains are determined from eqns (2.11), (2.12), and (2.14) and the acceleration time history responses are obtained from

$$\begin{aligned}
\ddot{u}(x, y, t) &= \sum_i \sum_j u_{ij}\ddot{q}_{ij}(t) \\
\ddot{v}(x, y, t) &= \sum_i \sum_j v_{ij}\ddot{q}_{ij}(t) \\
\ddot{w}(x, y, t) &= \sum_i \sum_j w_{ij}\ddot{q}_{ij}(t)
\end{aligned} \tag{3.45}$$

The stress resultant of eqn (2.14) take the form of

$$N_x = \frac{Eh}{1-\nu^2}\sum_i\sum_j(-\bar{u}_{ij}\frac{j\pi}{l} - \nu\frac{i\pi}{R\phi}\bar{v}_{ij} + \frac{\nu}{R}\bar{w}_{ij})\sin\frac{j\pi x}{l}\sin\frac{i\pi y}{R\phi}q_{ij}(t)$$

$$N_y = \frac{Eh}{1-\nu^2}\sum_i\sum_j(-\nu\bar{u}_{ij}\frac{j\pi}{l} - \frac{i\pi}{R\phi}\bar{v}_{ij} + \frac{1}{R}\bar{w}_{ij})\sin\frac{j\pi x}{l}\sin\frac{i\pi y}{R\phi}q_{ij}(t)$$

$$N_{xy} = N_{yx} = \frac{Eh}{2(1+\nu)}\sum_i\sum_j(\frac{i\pi}{R\phi}\bar{u}_{ij} + \frac{j\pi}{l}\bar{v}_{ij})\cos\frac{j\pi x}{l}\cos\frac{i\pi y}{R\phi}q_{ij}(t)$$

$$M_x = \frac{Eh^3}{12(1-\nu^2)}\sum_i\sum_j((\frac{j\pi}{l})^2\bar{w}_{ij} + \nu(\frac{i\pi}{R\phi})^2\bar{w}_{ij} - \frac{\nu}{R^2}\frac{i\pi}{\phi}\bar{v}_{ij})\sin\frac{j\pi x}{l}\sin\frac{i\pi y}{R\phi}q_{ij}(t) \tag{3.46}$$

$$M_y = \frac{Eh^3}{12(1-\nu^2)}\sum_i\sum_j((\nu\frac{j\pi}{l})^2\bar{w}_{ij} + (\frac{i\pi}{R\phi})^2\bar{w}_{ij} - \frac{1}{R^2}\frac{i\pi}{\phi}\bar{v}_{ij})\sin\frac{j\pi x}{l}\sin\frac{i\pi y}{R\phi}q_{ij}(t)$$

$$M_{xy} = M_{yx} = -\frac{Eh^3}{12(1+\nu)}\sum_i\sum_j(-\frac{i\pi}{R\phi}\frac{j\pi}{l}\bar{w}_{ij} + \frac{1}{R}\frac{j\pi}{l}\bar{v}_{ij})\cos\frac{i\pi y}{R\phi}q_{ij}(t)$$

3.3.3 Modal force

In modal analysis, external force should also be applied in terms of its modal components of eqn (3.44). For uniform vertical earthquake motions (synchronised at each support) the earthquake loading will be symmetric, and hence only the odd modes will contribute to the total response of the shell. (P_y, P_z) represent the exact body forces which are approximated by (P'_y, P'_z), where (P'_y, P'_z) are the Fourier series; ie

$$P_z \approx P'_z = \sum_{i=1,3,5,\ldots}\sum_{j=1,3,5,\ldots} P_{z_{ij}}\sin\frac{j\pi x}{L}\sin\frac{i\pi y}{R\phi} \tag{3.47}$$

$$P_y \approx P'_y = \sum_{i=1,3,5,\ldots}\sum_{j=1,3,5,\ldots} P_{y_{ij}}\sin\frac{j\pi x}{L}\cos\frac{i\pi y}{R\phi} \tag{3.48}$$

For the normal to the shell, define

$$e^2 = (P_z - P'_z)^2 \tag{3.49}$$

where e is the error between exact force P_z and the approximate force P'_z. Taking the integral of the square of the error

$$E = \int_0^L\int_0^{R\phi} e^2 dx\,dy = \int_0^L\int_0^{R\phi}(P_z - P'_z)^2 dx\,dy = \int_0^L\int_0^{R\phi}(P_z - \sum_j\sum_i P_{z_{ij}}\sin\frac{j\pi x}{L}sin\frac{i\pi y}{R\phi})^2 dx\,dy \tag{3.50}$$

then a least square error minimization requires

$$\frac{\partial E}{\partial P_{zij}} = 0 \tag{3.51}$$

for which the Fourier coefficient is given by

$$P_{zij} = \frac{\int_0^L \int_0^{R\phi} P_z \sin\frac{j\pi x}{L} \sin\frac{i\pi y}{R\phi} dx\, dy}{\int_0^L \int_0^{R\phi} \sin^2\frac{j\pi x}{L} \sin^2\frac{i\pi y}{R\phi} dx\, dy} \tag{3.52}$$

Through a similar process the circumferential modal force is

$$P_{y_{ij}} = \frac{\int_0^L \int_0^{R\phi} P_y \sin\frac{j\pi x}{L} \cos\frac{i\pi y}{R\phi} dx\, dy}{\int_0^L \int_0^{R\phi} \sin^2\frac{j\pi x}{L} \cos^2\frac{i\pi y}{R\phi} dx\, dy} \tag{3.53}$$

When the shell supports are subject to a synchronized vertical acceleration $a_{gv}(t)$, the time dependent body forces are

$$P_z = \overline{P} cos(-\frac{\phi}{2} + \frac{y}{R}) \tag{3.54}$$

$$P_y = \overline{P} sin(-\frac{\phi}{2} + \frac{y}{R}) \tag{3.55}$$

where $\overline{P} = \rho h a_{gv}(t)$. Substituting eqn (3.54) in eqn (3.52), allow eqn (3.48) to be written

$$P_z \approx \sum_{i=1,3,5,\ldots} \sum_{j=1,3,5,\ldots} \frac{\int_0^L \int_0^{R\phi} \overline{P} cos(-\frac{\phi}{2} + \frac{y}{R}) sin\frac{j\pi x}{L} sin\frac{i\pi y}{R\phi} dx\, dy}{\int_0^L \int_0^{R\phi} sin^2\frac{j\pi x}{L} sin^2\frac{i\pi y}{R\phi} dx\, dy} sin\frac{j\pi x}{L} sin\frac{i\pi y}{R\phi} \tag{3.56}$$

The same procedure is used to find P_y in the form

$$P_y \approx \sum_{i=2,4,6,\ldots} \sum_{j} \frac{\int_0^L \int_0^{R\phi} \overline{P} sin(-\frac{\phi}{2} + \frac{y}{R}) sin\frac{j\pi x}{L} cos\frac{i\pi y}{R\phi} dx\, dy}{\int_0^L \int_0^{R\phi} sin^2\frac{j\pi x}{L} cos^2\frac{i\pi y}{R\phi} dx\, dy} sin\frac{j\pi x}{L} cos\frac{i\pi y}{R\phi} \tag{3.57}$$

which upon substitution of eqns (3.1), (3.56) and (3.57) into eqn (3.44), permits the modal force to be represented as

$$P_{ij}(t) = \rho h L R \phi a_{gv}(t) \frac{(-1 + cosi\pi)(-1 + cosj\pi)(\overline{w_{ij}} i\pi - \overline{v_{ij}}\phi)}{j\pi(i\pi - \phi)(i\pi + \phi)} cos\frac{\phi}{2} \tag{3.58}$$

The horizontal earthquake acting normal to the axis of the shell, is derived using the procedure similar to that outlined for the vertical component of the earthquake, except

that the horizontal load is antisymmetric and only the even harmonics i will be involved. Following a similar procedure to that for vertical earthquake the horizontal force the relationship between y, position on the shell surface, and force is

$$P_z = \overline{P} sin(-\frac{\phi}{2} + \frac{y}{R})$$
$$P_y = \overline{P} cos(-\frac{\phi}{2} + \frac{y}{R}) \tag{3.59}$$

where $\overline{P} = \rho h a_{gh}$, and a_{gh} is the horizontal ground acceleration. For the horizontal earthquake component modal force can be represented as

$$P_{ij}(t) = \rho h L R \phi a_{gh}(t) \frac{(1 + cosi\pi)(-1 + cosj\pi)(-\overline{w_{ij}} i\pi - \overline{v_{ij}}\phi)}{j\pi(-i\pi + \phi)(i\pi + \phi)} sin\frac{\phi}{2} \tag{3.60}$$

For a particular earthquake record $a_{gv}(t)$, $a_{gh}(t)$ the modal loads of eqns (3.58), (3.60) allow the modal displacement q_{ij} to be found from eqn (3.43).

3.4 Numerical evaluation of earthquake response

In order to solve the eqn of (3.43) a numerical approach using the time stepping methods for integration of differential equations is chosen. There are a huge number of numerical time-stepping methods for solving different forms of differential equations. Chopra in his book [97] presents the basic concepts underlying the mathematical developments, as well as aspects of accuracy, convergence, and stability problems of a few methods that are especially useful in dynamic response of SDOF systems. For the case of dynamic response of roof shells, a numerical method based on one of the time-stepping methods is needed to solve the differential eqn (3.43) or eqn (3.18).

As discussed in previous sections a MDOF system may be represented as the superposition of several SDOF systems. In all time stepping methods the differential equation of motion is conveniently solved numerically for each mode. Consider the generic form of eqn (3.43) for a specific mode. The equation can be represented as

$$m\ddot{q} + 2\zeta m\omega\dot{q} + \omega^2 mq = P \tag{3.61}$$

subjected to initial conditions of

$$q_0 = q(0)$$
$$\dot{q}_0 = \dot{q}(0) \tag{3.62}$$

The excitation force is presented by a set of discrete values $P_k = P(t_k)$, $k = 0\ to\ N$, with the time interval

$$\Delta t_k = t_{k+1} - t_k \tag{3.63}$$

taken to be constant and equal to $\mathbf{h}$. The response should be determined at each discrete time t_k. The displacement, velocity and acceleration responses at time k denoted as q_k, $\dot{q}_k$, and $\ddot{q}_k$ respectively. These values should satisfy the equilibrium eqn of (3.64) at time k.

$$m\ddot{q}_k + 2\zeta m\omega\dot{q}_k + \omega^2 m q_k = P \tag{3.64}$$

Using the selected numerical method enables the response to be derived at other time instants, where they all should satisfy eqn (3.64) at that time instant. However, knowing the initial conditions of eqn (3.62) is essential to start the procedure.

Stepping from time k to time $k+1$ is not an exact procedure and involves many approximations. Chopra [97] especially emphasizes the three requirements for numerical methods to be practically accurate as firstly by decreasing the time step the solution should converge to exact solutions; secondly the solution should be stable with the errors caused by round off errors; and third the result that should be convincingly close to the exact solution.

Among the various time-stepping numerical method a highly efficient method based on interpolation of excitation over each time interval is used to find the response of shell to earthquake [97]. The method of interpolation of excitation gives good result with short time intervals. Fig 3.9 shows the excitation force over the time interval t_k and t_{k+1}

$$P(\tau) = P_k + \frac{\Delta P_k}{\mathbf{h}}\tau \tag{3.65}$$

$$\Delta P_k = P_{k+1} - P_k \tag{3.66}$$

where the local time variable τ varies from 0 to $\mathbf{h}$.

For simplicity, the solution is first given for a system without damping, so in eqn (3.43) the second term is neglected. Then the solution will be expanded to cover the systems with damping. For a system without considering the damping, the equation of motion

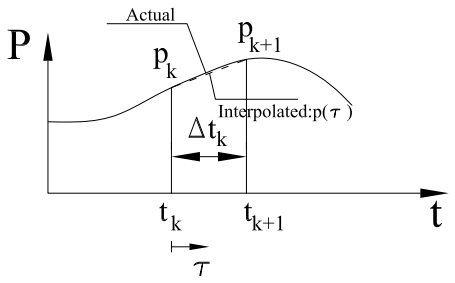

Figure 3.9: Interpolation of force

(3.61) is reduced to

$$m\ddot{q} + kq = p_k + \frac{\Delta p_k}{\mathbf{h}}\tau \tag{3.67}$$

The response of eqn (3.67) consists of three parts: first the free vibration response with the initial condition of q_k, and $\dot{q}_k$ at time $\tau = 0$ for the displacement and velocity respectively, which are the first and second term in the eqn (3.68); second the response to step force equal to P_k with zero initial conditions, which is the third term in eqn (3.68); and third, the response to ramp force $\frac{\Delta P_k}{\mathbf{h}}$ considering zero initial conditions, which is the fourth term in the following equation.

$$q(\tau) = q_k \cos\omega_n\tau + \frac{\dot{q}_k}{\omega_n}\sin\omega_n\tau + \frac{P_k}{k}(1-\cos\omega_n\tau) + \frac{\Delta p_i}{k}(\frac{\tau}{\mathbf{h}} - \frac{\sin\omega_n\tau}{\omega_n\mathbf{h}}) \tag{3.68}$$

and

$$\frac{\dot{q}(\tau)}{\omega_n} = -q_k\sin\omega_n\tau + \frac{\dot{q}_k}{\omega_n}\cos\omega_n\tau + \frac{p_k}{k}\sin\omega_n\tau + \frac{\Delta p_i}{k}\frac{1}{\omega_n\mathbf{h}}(1-\cos\omega_n\tau) \tag{3.69}$$

As the damping is neglected, ω_n represents the natural frequency of the SDOF system. These equations are evaluated at $\tau = \mathbf{h}$, which gives the displacement q_{k+1} and velocity $\dot{q}_{k+1}$ at time $k+1$, as

$$q_{k+1} = q_k\cos(\omega_n\mathbf{h}) + \frac{\dot{q}_k}{\omega_n}\sin(\omega_n\mathbf{h}) + \frac{p_k}{k}[1-\cos(\omega_n\mathbf{h})] + \frac{\Delta p_k}{k}\frac{1}{\omega_n\mathbf{h}}[\omega_n\mathbf{h} - \sin(\omega_n\mathbf{h})] \tag{3.70}$$

$$\frac{\dot{q}_{k+1}}{\omega_n} = -q_k\sin(\omega_n\mathbf{h}) + \frac{\dot{q}_k}{\omega_n}\cos(\omega_n\mathbf{h}) + \frac{p_k}{k}\sin(\omega_n\mathbf{h}) + \frac{\Delta p_k}{k}\frac{1}{\omega_n\mathbf{h}}[1-\cos(\omega_n\mathbf{h})] \tag{3.71}$$

In these equations k represents both the stiffness, and the index representing the interval number; the meanings should be clear from the context.

By substituting eqn (3.66), eqns (3.70) and (3.71) may be written as

$$q_{k+1} = Aq_k + B\dot{q}_k + Cp_k + Dp_{k+1} \tag{3.72}$$

$$\dot{q}_{k+1} = A^{'} q_k + B^{'} \dot{q}_k + C^{'} p_k + D^{'} p_{k+1} \tag{3.73}$$

The same procedure will be used for the system with damping of eqn (3.43). Repeating the above procedure for system with $\xi < 1$, A, B, C,..., $D^{'}$ are given as

$$\begin{aligned}
A &= e^{-\xi\omega_n \mathbf{h}} \left(\frac{\xi}{\sqrt{1-\xi^2}} \sin\omega_D \mathbf{h} + \cos\omega_D \mathbf{h} \right) \\
B &= e^{-\xi\omega_n \mathbf{h}} \left(\frac{1}{\omega_D} \sin\omega_D \mathbf{h} \right) \\
C &= \frac{1}{k} \left\{ \frac{2\xi}{\omega_n \mathbf{h}} + e^{-\xi\omega_n \mathbf{h}} \left[\left(\frac{1-2\xi^2}{\omega_D \mathbf{h}} - \frac{\xi}{\sqrt{1-\xi^2}} \right) \sin\omega_D \mathbf{h} - \left(1 + \frac{2\xi}{\omega_n \mathbf{h}} \right) \cos\omega_D \mathbf{h} \right] \right\} \\
D &= \frac{1}{k} \left[1 - \frac{2\xi}{\omega_n \mathbf{h}} + e^{-\xi\omega_n \mathbf{h}} \left(\frac{2\xi^2 - 1}{\omega_D \mathbf{h}} \sin\omega_D \mathbf{h} + \frac{2\xi}{\omega_n \mathbf{h}} \cos\omega_D \mathbf{h} \right) \right] \\
A^{'} &= -e^{-\xi\omega_n \mathbf{h}} \left(\frac{\omega_n}{\sqrt{1-\xi^2}} \sin\omega_D \mathbf{h} \right) \\
B^{'} &= e^{-\xi\omega_n \mathbf{h}} \left(\cos\omega_D \mathbf{h} - \frac{\xi}{\sqrt{1-\xi^2}} \sin\omega_D \mathbf{h} \right) \\
C^{'} &= \frac{1}{k} \left\{ -\frac{1}{\mathbf{h}} + e^{-\xi\omega_n \mathbf{h}} \left[\left(\frac{\omega_n}{\sqrt{1-\xi^2}} + \frac{\xi}{\mathbf{h}\sqrt{1-\xi^2}} \right) \sin\omega_D \mathbf{h} + \frac{1}{\mathbf{h}} \cos\omega_D \mathbf{h} \right] \right\} \\
D^{'} &= \frac{1}{k\mathbf{h}} \left[1 - e^{-\xi\omega_n \mathbf{h}} \left(\frac{\xi}{\sqrt{1-\xi^2}} \sin\omega_D \mathbf{h} + \cos\omega_D \mathbf{h} \right) \right]
\end{aligned} \tag{3.74}$$

in these equations, ξ is the damping ratio, $\omega_D = (1-\xi^2)^{0.5}\omega$ represents the damped frequency. As Chopra explained the approximation of the results only depends on h as the solutions are derived from the exact solution of the equation of motions. This semi-analytical, numerical procedure is especially accurate for the excitations over small time intervals such as earthquake loading. The method is presented for SDOF systems which can be extended to MDOF systems by use of the modal analysis. In this study, this method is extended for MDOF system by using the superposition of modal responses as explained in section 3.3.

3.5 Program set up

Input: $\rho, L, R, \nu, c, h, \Phi, E, a_g$

Output: $u(x,y,t)$, $v(x,y,t)$, $w(x,y,t)$, $\ddot{u}(x,y,t)$, $\ddot{v}(x,y,t)$, $\ddot{w}(x,y,t)$

foreach *mode* i, j *in set of desired modes* **do**

Solve eigenvalue problem of eqn (3.4) *for* $\Delta_1, \Delta_2, \Delta_3$;

$\Delta \leftarrow \min(\Delta_1, \Delta_2, \Delta_3)$ and store the corresponding eigenvector components $\overline{u}_{ij}$, $\overline{v}_{ij}$, $\overline{w}_{ij}$;

Calculate ω_{ij}^2 using eqn (3.4), and (3.5) ;

$K_{ij} \leftarrow \omega_{ij}^2 M_{ij}$, where M_{ij} is given by eqn (3.40) ;

Compute $q_{ij}(t)$ for all t over earthquake period using method based on interpolation of excitation in [97] section 5.2 page 167. ;

Compute acceleration $(\ddot{q}_{ij}(t) = \frac{\partial^2 q_{ij}}{\partial t^2})$ for all t over earthquake period;

end

foreach *point* (x,y) *on the shell surface* **do**

forall t *over earthquake period* **do**

$u(x,y,t), v(x,y,t), w(x,y,t) \leftarrow \mathbf{0}$;

$\ddot{u}(x,y,t), \ddot{v}(x,y,t), \ddot{w}(x,y,t) \leftarrow \mathbf{0}$;

end

foreach *mode* i, j *in set of desired modes* **do**

forall t *over earthquake period* **do**

$u(x,y,t) \leftarrow u(x,y,t) + u_{ij} \cdot q_{ij}(t)$

$v(x,y,t) \leftarrow v(x,y,t) + v_{ij} \cdot q_{ij}(t)$

$w(x,y,t) \leftarrow w(x,y,t) + w_{ij} \cdot q_{ij}(t)$

$\ddot{u}(x,y,t) \leftarrow \ddot{u}(x,y,t) + u_{ij} \cdot \ddot{q}_{ij}(t)$

$\ddot{v}(x,y,t) \leftarrow \ddot{v}(x,y,t) + v_{ij} \cdot \ddot{q}_{ij}(t)$

$\ddot{w}(x,y,t) \leftarrow \ddot{w}(x,y,t) + w_{ij} \cdot \ddot{q}_{ij}(t)$

end

end

end

Algorithm 1: The algorithm for calculating time history displacement and acceleration components of each point (x,y) over the period of earthquake.

The developed programme of Algorithm 1 is used to investigate different aspects of an open cylindrical shell under an earthquake as will be discussed through the rest of this chapter.

3.6 Earthquake ground motion

Landers earthquake measured on June 28^{th} 1992 at the Lucrene station with duration of 48.12 s is used for this study. The vertical component of Landers earthquake has a Peak Ground Acceleration (PGA) of 0.818 g as shown in Fig 3.10(a) with a 0.005 s time interval of recorded data. The frequency content of vertical component shown in Fig 3.10(b) indicates that most of the energy in the accelerogram is in the frequency range up to 45 Hz and the largest amplitude is at a frequency approximately 14 Hz. The reason for choosing this earthquake is because the earthquake has significant energy over a wide range of frequencies and especially around high frequencies. As the natural frequencies of cylindrical shell also have a wide range and includes modes with high frequency, the choice of this earthquake should help to investigate the possible contribution of the modes with high frequencies in the response. The displacement and acceleration response spectra are then derived and reported in Fig 3.10(c),(d) for a 5 $\%$ damped system subjected to the vertical component of Landers earthquake. The Response spectrum is an important tool in the earthquake analysis and design of structures unlike the frequency content of earthquake which gives information about energy of earthquake and frequency content of ground motion, the response spectrum presents the maximum response of structure to a given earthquake. The response spectrum describes the maximum response of a damped SDOF system at different frequencies or periods. As it can be seen from Fig 3.10(c) the displacement response spectrum reduces significantly for the frequencies above 2 Hz. However it has a high acceleration response spectrum (Fig 3.10(d)) for the frequencies up to and including 50 Hz. The acceleration time history, frequency content of the horizontal component of this earthquake is shown in Fig 3.11(a),(b). The displacement and acceleration response spectrum is also derived and presented in Fig 3.11(c),(d) for a 5 $\%$ damped system. The horizontal component has a $PGA = 0.789$ g and again the earthquake data is

available for every $0.005\ s$. The horizontal component of Landers earthquake also has a small displacement response spectrum for the frequencies higher than $2\ Hz$ but it has large acceleration response spectrum for frequencies up to $50\ Hz$. As can be seen, the Landers earthquake has a high ratio of vertical to horizontal peak ground acceleration, which make it a suitable choice to show the conditions that the vertical component of an earthquake can result in higher responses that the horizontal components of an earthquake. However, it should be noted that this earthquake is not a typical earthquake and such records can only happen in near-field events. By considering a constant damping ratio, the damping force in modes with higher frequencies increases proportionally with the frequency. However, as explained in Section 3.3, the damping ratio and consequently the damping force in each mode would be different if different damping models were used. Therefore, depending on the chosen model, the responses would converge either faster or slower than the present model.

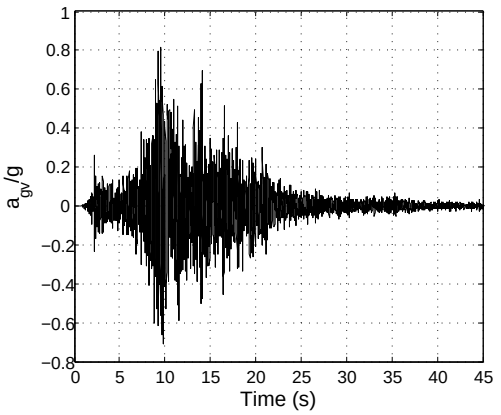

(a) Acceleration time history

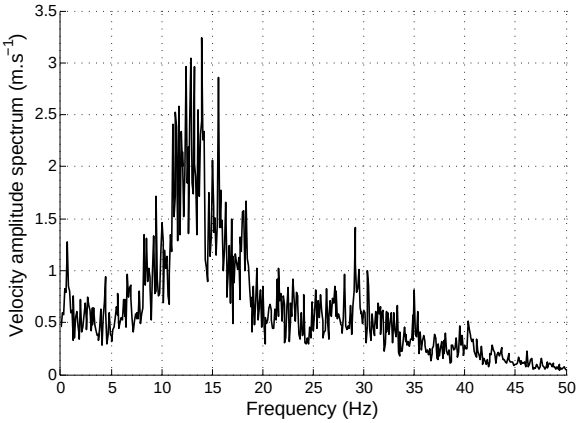

(b) Frequency content

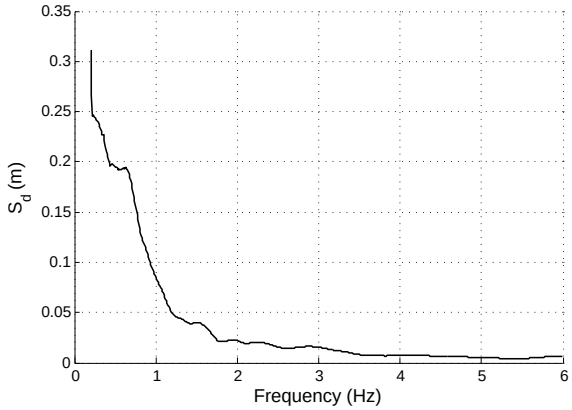

(c) Displacement response spectrum for 5 % damped system

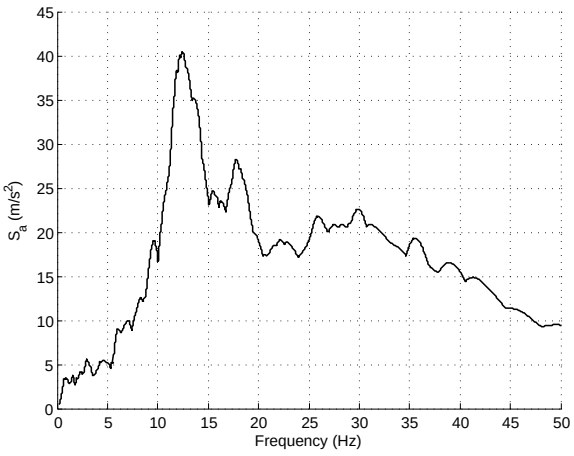

(d) Acceleration response spectrum for 5 % damped system

Figure 3.10: Vertical component of Landers earthquake

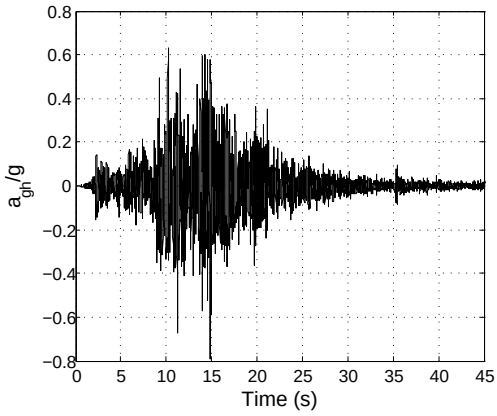

(a) Acceleration time history

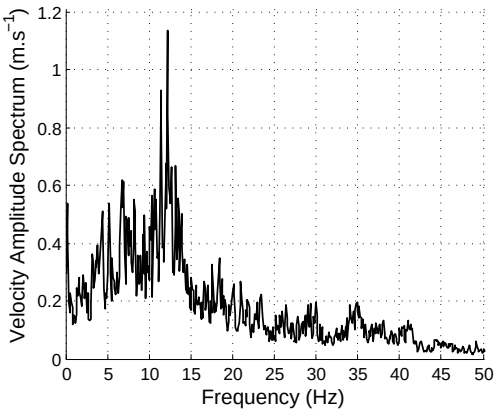

(b) Frequency content

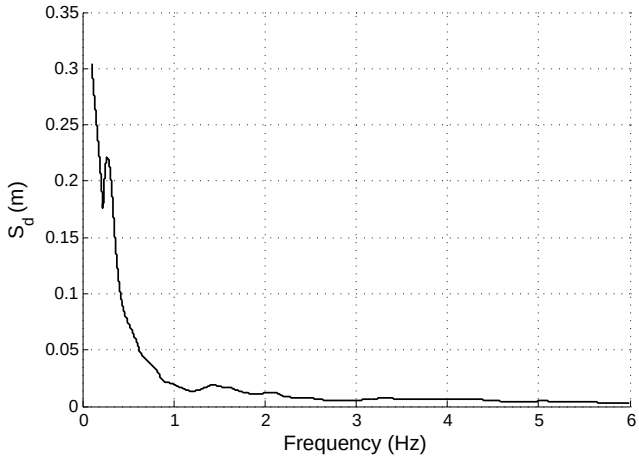

(c) Displacement response spectrum for 5 % damped system

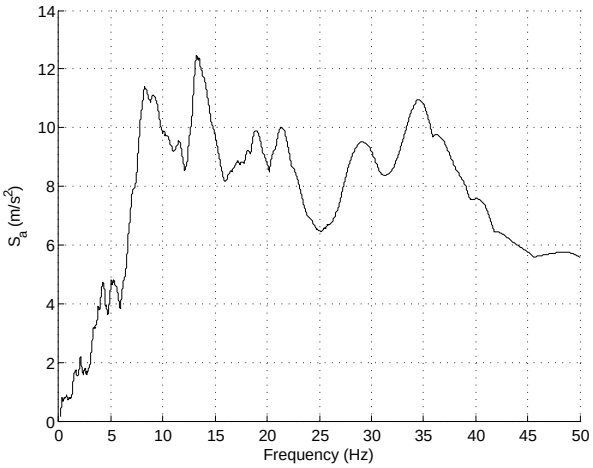

(d) Acceleration response spectrum for 5 % damped system

Figure 3.11: Horizontal component of Landers earthquake

3.7 Convergence of the shell responses to earthquake

The semi-analytical method using the time history modal analysis as explained in section 3.5 provides the facility to investigate some aspects of behaviour of roof shells to earthquake that can affect the responses. The investigation is performed for several cases of shells with different length/radius and different material property ratios defined as $B = \rho h R/E$. However, first a convergence study on displacement, acceleration, and stress resultants is performed for the shell with natural frequencies summarized in Fig 3.4, having $\phi = \pi/3$, $L_y/L_x = 1$, $R/h = 500$, $B = 1 \times 10^{-6}\ s^2$ undergoing the vertical component of Landers earthquake (Fig 3.10).

This analysis involved the use of the 10 modes having the lowest frequencies, which will also be used in section 4.4.3 to compare with the result using FE programme for the validation purposes. The analysis also takes into account different total numbers of axial and circumferential half-waves for a converged response as shown in Fig 3.12 for displacements and relative accelerations and Fig 3.13 for stress resultants. The responses are plotted along center-line bb. For convenience and in the absence of more precise estimation of damping, a constant damping ratio equivalent to 0.05 is considered for each mode.

Fig 3.12(a),(b) show that the displacements converge after including a total number of $(I, J) = (19, 1)$ modes, which is faster in comparison with the convergence of acceleration responses (3.12(c),(d)); I and J are the total number of circumferential and axial half wavelength. As it can be seen, radial acceleration almost converges after including a total number of 19 half-waves in both circumferential and axial directions ($(I, J) = (19, 19)$). The reason for the need for inclusion of more modes for acceleration in comparison to displacements is because of relative acceleration being obtained by multiplying ω^2 by displacements. Consequently, many of the modes having small displacement responses that correspond with modes having high frequencies, contribute to the acceleration response as a result of being multiplied by ω^2.

As Fig 3.12 and 3.13 only present the results along center line bb in order to know more about the distribution of response over the entire surface of shell another analysis

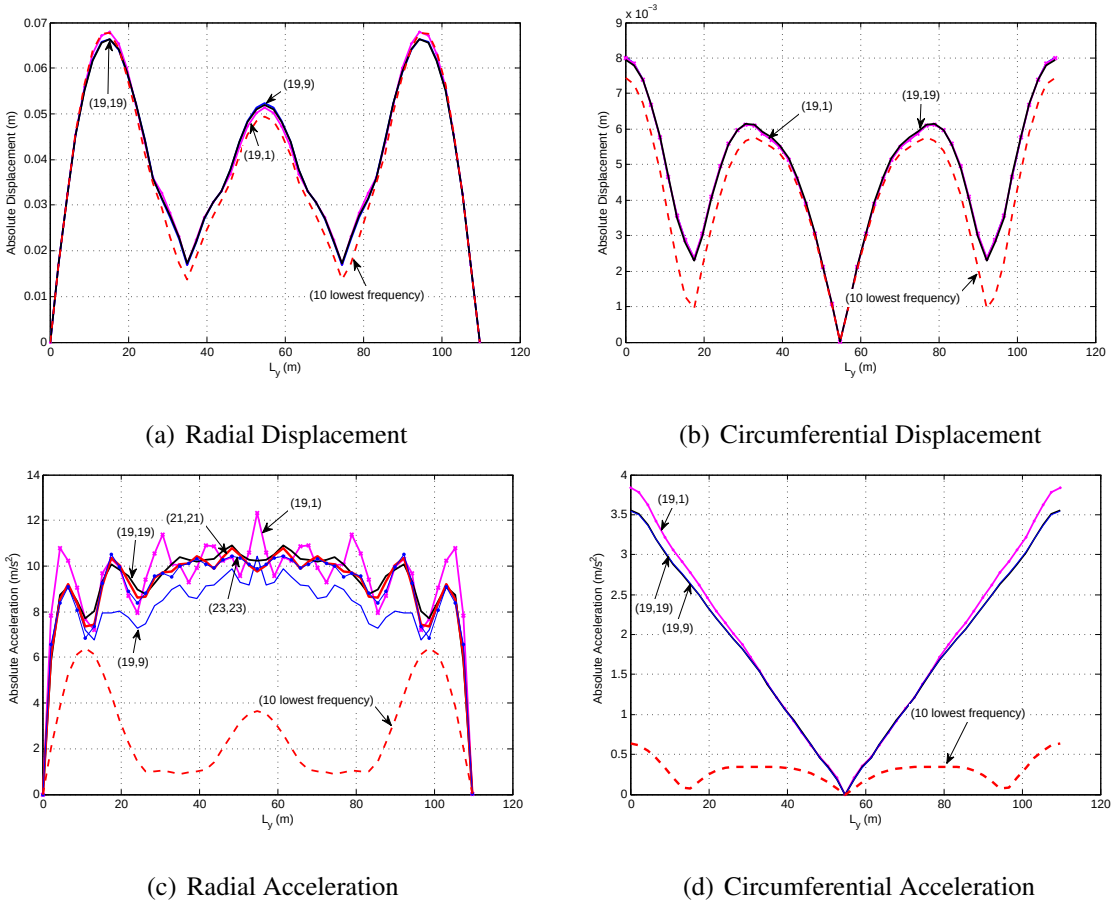

(a) Radial Displacement

(b) Circumferential Displacement

(c) Radial Acceleration

(d) Circumferential Acceleration

Figure 3.12: Convergence of maximum absolute displacement and acceleration along line (bb)

is performed, which finds the converged maximum displacements and relative accelerations with a total number of 19 half-waves in circumferential and axial directions over the time history of earthquake as shown in Fig 3.14 and 3.15. Fig 3.15 shows the maximum displacement and circumferential acceleration occur along center line *bb*. However, higher radial acceleration are shown to be concentrated near the circumferential edges (Fig 3.14(b)) rather than center line *bb* (Fig 3.14(a)), where the maximum radial displacement occurs. This shows the maximum acceleration does not necessarily occur in the same location as the corresponding maximum displacement happens.

The stress resultants in Fig 3.13 also only converge with a total of 19 half-waves in both circumferential and axial directions ($(I, J) = (19, 19)$). This shows that, for a converged result, stresses also require higher numbers of modes than needed for displacement responses. It also shows modes with shorter wavelengths significantly

contribute to the total stress responses. This could be due to the first and second derivatives of u, v, and w in terms of x and y as found in eqn (2.14), which cause the involvement of first and second order of i and j in the stress and moment resultants. This, consequently, increase the importance of modes with shorter wavelengths in the stress response in comparison to displacement responses.

However, to highlight the importance of different modes in displacement and acceleration responses, a more detailed analysis of the contribution of each individual modes in the total response of displacement and stress will be discussed in section 3.8.

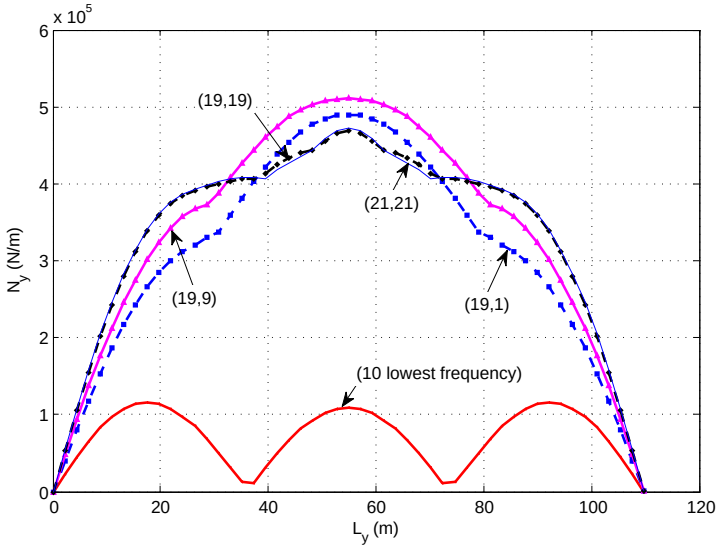

(a) N_y

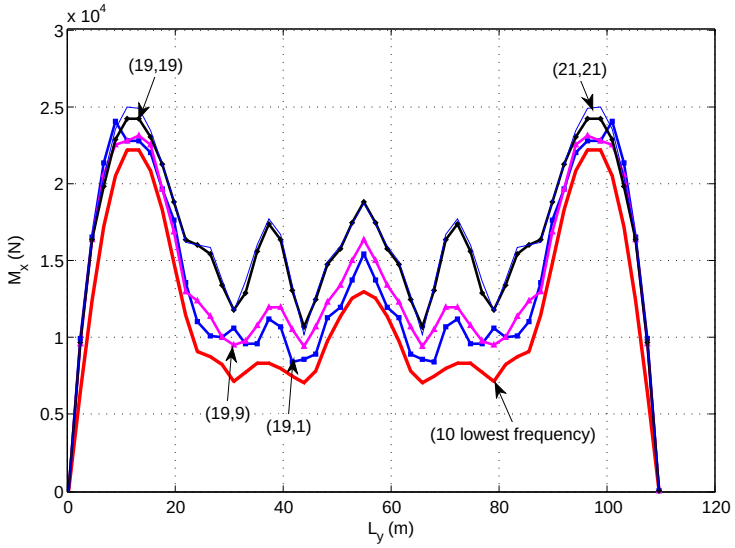

(b) M_x

Figure 3.13: Convergence of maximum absolute stress along line (bb)

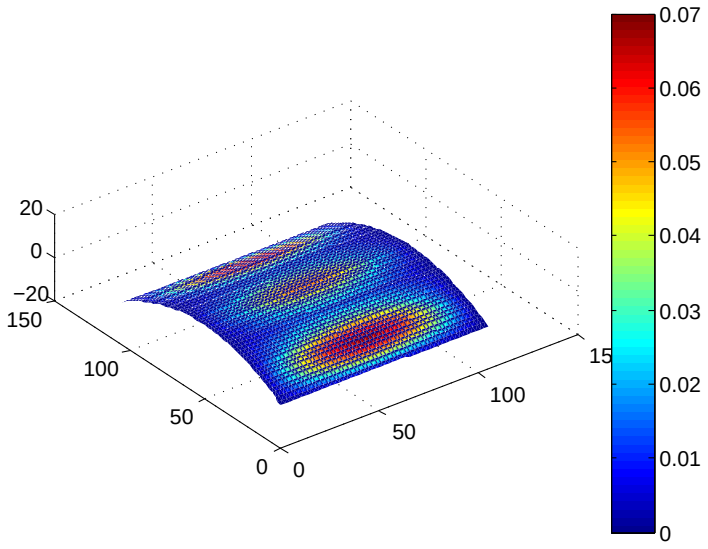

(a) Displacement

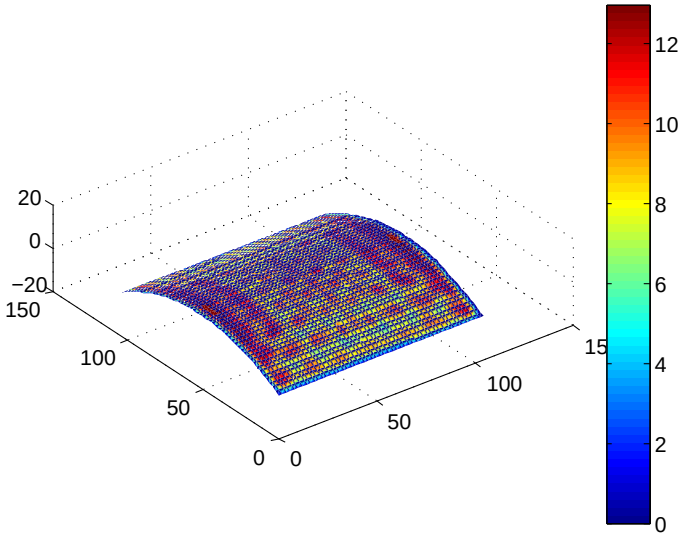

(b) Acceleration

Figure 3.14: Maximum absolute radial displacement and acceleration

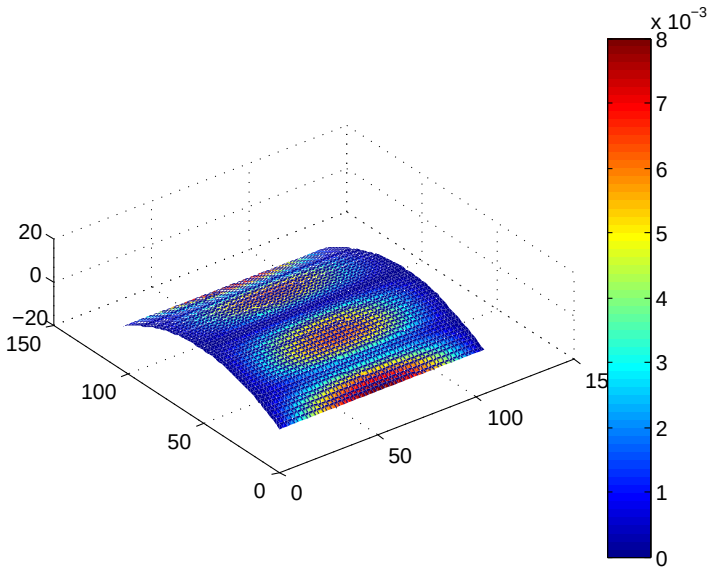

(a) Displacement

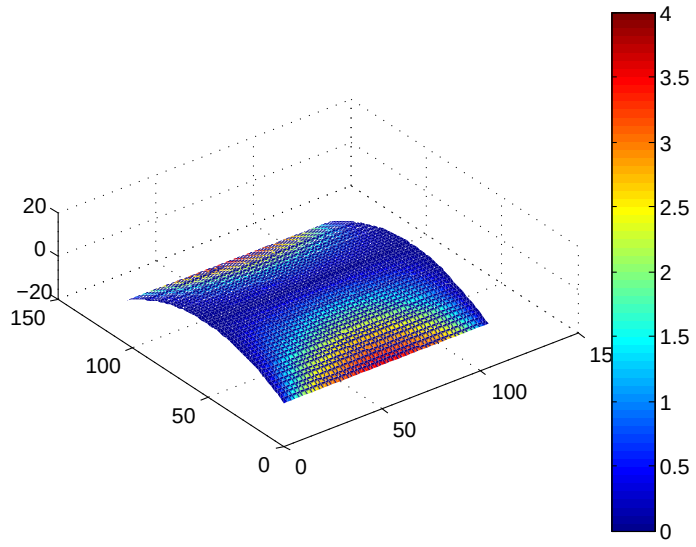

(b) Acceleration

Figure 3.15: Maximum absolute circumferential displacement and acceleration

3.8 Importance of different modes in the response

As shown in Fig 3.12, 3.13 a total number of 19 half waves in axial and circumferential directions should be included for adequate convergence of results. This section investigates the participation of different modes in the displacement response and their relationships with the modal participation in the stress resultants. The analysis is performed for the previously considered isotropic cylindrical shell in section 3.7 having $R = 104.8\ m,\ L_x = 104.8\ m,\ \phi = \pi/3,\ R/h = 500,\ \nu = 0.3,\ E = 9.1 \times 10^{10} N/m^2,\ \rho = 4150.5\ kg/m^3$; the natural frequencies for this shell are shown in Fig 3.4. For convenience, the modal damping ratio, ζ_{ij}, was again considered to be 0.05 for each mode. The time history modal analysis was carried out for the vertical component of the Landers earthquake as shown in Fig 3.10. The analysis was performed using modes having half-wave numbers $i = 1, 3, \cdots, 19$ and $j = 1, 3, \cdots, 19$. Using the semi-analytical method the contributions of the most significant modes in the displacement and stress responses of the shell, at the times of maximum response, are plotted in Fig 3.16(a) to (f) for the half-width across the center-line bb; as expected the response is symmetric about the center line aa.

It should be noted that the modal responses are not the maximum modal responses over the time history of the earthquake and over the entire surface of the shell. They only represent the modal responses at the time when the maximum total response occurs. The maximum total responses can also occur at different times and different locations over the surface of shell, as shown in Table 3.4. However, as most of the responses for this particular shell have their maxima along center-line bb, it was decided to plot the rest of responses along this line as well. Table 3.4 shows the maximum total displacements and stress resultants predicted using a total of 19 half-wave in the axial and the circumferential directions, together with the times when they occurred and their locations on the shell surface. The results of the analysis show that even though the maximum displacement may occur at a particular time and location, this would not necessarily relate to the most severe stresses.

Fig 3.16 shows that stresses have a very different modal participation. The nature of the modal participations in both the maximum displacement and by implication the

Response	Maximum total response	Time (s)	Location of maximum response
W	$0.0663\ m$	10.795	$(52.4142, 15.3687)$
V	$0.0079\ m$	10.86	$(52.414, 0)$
N_y	$7.8973 \times 10^5\ N.m^{-1}$	10.12	$(54.8881, 8.3863)$
N_x	$1.0494 \times 10^6\ N.m^{-1}$	10.855	$(52.4142, 92.212)$
N_{xy}	$9.348 \times 10^5\ N.m^{-1}$	10.64	$(0, 0)$
M_x	$2.5194 \times 10^4\ N.m$	10.66	$(58.7040, 8.7821)$
M_y	$6.5864 \times 10^4\ N.m$	10.665	$(52.4142, 100.9940)$
M_{xy}	$1.8188 \times 10^4\ N.m$	10.64	$(0, 0)$

Table 3.4: Location and time of the maximum stress resultants and displacements

stress response are strongly influenced by the relationship between the natural frequency spectrum of the shell and the spectral responses of the earthquake; this will be demonstrated in chapter 5. Therefore, depending on the relationship between the natural frequency spectrum and earthquake spectrum very different results could be expected.

As can be seen in Fig 3.16 for a shell having $L_y/L_x = 1$, $B = \rho hR/E = 1 \times 10^{-6}\ s^2$ the participations of different modes are not the same for displacements and stresses. The out-of-plane displacement is dominated by modes $(i, j) = (5, 1), (3, 1)$. Despite having a high modal loading in mode $(i, j) = (1, 1)$, the contribution of this mode toward the out-of-plane displacement is very small in comparison with its contribution to the in-plane displacements. This can be explained using the displacement response spectrum for this earthquake in Fig 3.10(c). The natural frequency of mode $(1, 1)$ is equal to $3.587\ Hz$, which corresponds to a small displacement response spectrum as can be seen in Fig 3.10(c).

The circumferential displacement responses (Fig 3.16(b)) are considerably lower than out-of-plane displacements. This is because of the circumferential displacements are derived by multiplying out-of-plane displacements by $\frac{\bar{v}}{\bar{w}}$, and $\bar{v}$ are significantly lower than $\bar{w}$ as it can be seen for some selected modes in Table 3.3. But mode $(i, j) = (1, 1)$

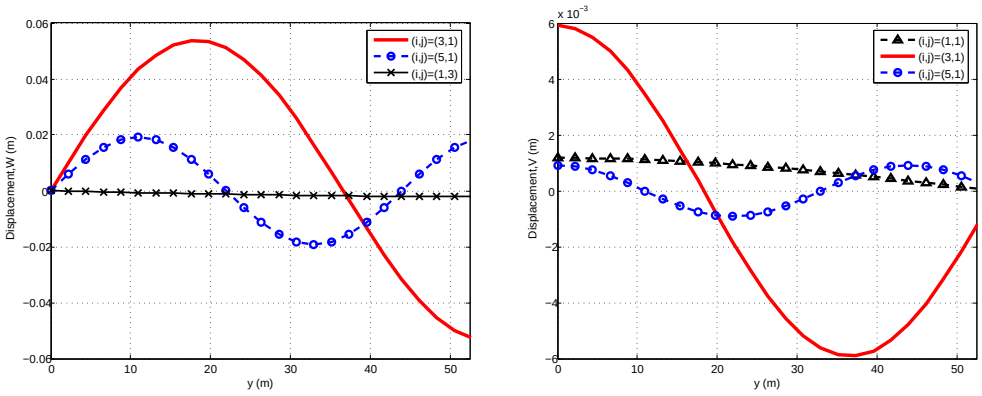

(a) Radial Displacement, W

(b) Circumferential Displacement,V

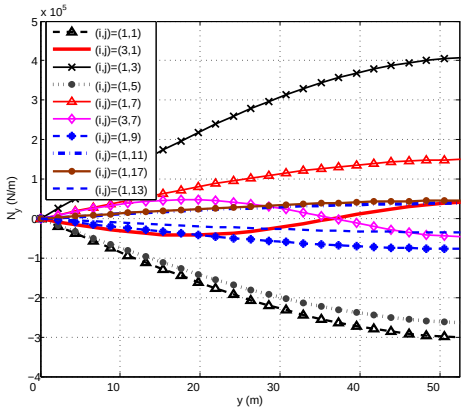

(c) N_y

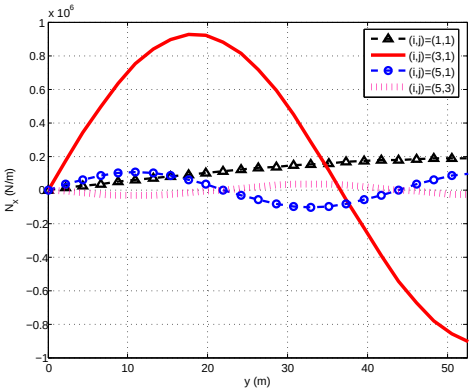

(d) N_x

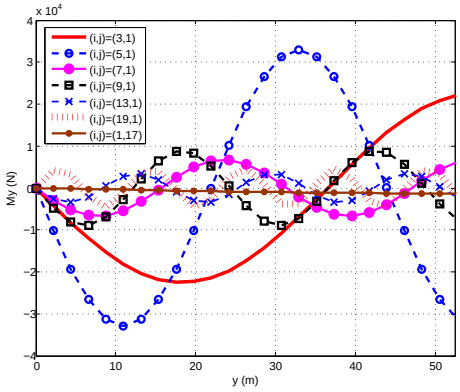

(e) M_y

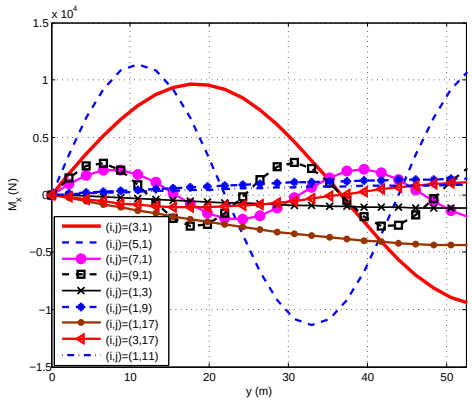

(f) M_x

Figure 3.16: Modal contribution of displacement, membrane and bending stress resultants at $x = L_x/2$, for cylindrical shell with $\phi = \pi/3$, $L_y/L_x = 1$, $B = 1 \times 10^{-6}\ s^2$, $R/h = 500$ subjected to Landers earthquake

is among the three modes having the most significant contribution to the circumferential displacement (Fig 3.16(b)). This is due to the radial displacement corresponding to mode $(1, 1)$ being quite insignificant in comparison with modes $(3, 1)$, $(5, 1)$,

$(1,3)$ in Fig 3.16(a) but when multiplied by $\frac{\bar{v}}{\bar{w}}$ as $\bar{v} = 0.2642$ corresponding to mode $(i,j) = (1,1)$ (Table 3.3) is higher than $\bar{v} = 0.1123$ corresponding to $(i,j) = (3,1)$ and $\bar{v} = 0.0672$ corresponding to mode $(5,1)$, this mode $((1,1))$ becomes more significant in the circumferential displacement.

In Fig 3.16(c) the importance of $(i,j) = (1,1)$ to the membrane stress resultant, N_y, is a reflection of the contribution of this mode to in-plane displacement, v, so it would be expected that ignoring mode $(i,j) = (1,1)$ would result in higher error for in-plane displacements (Fig 3.16(b)) than out-of-plane displacements (Fig 3.16(a)), and for membrane stress resultants (Fig 3.16(c),(d)) compared with bending stress resultants (Fig 3.16(e),(f)).

As Fig 3.4 shows, the modes having short wavelengths correspond with high frequencies, which consequently results in very small contributions to the out-of-plane displacements because of the small displacement spectrum for the Landers earthquake at these high frequencies as shown in Fig 3.10(c). In contrast, modes having short wavelengths in both the axial and circumferential directions make significant contributions to the membrane stresses of Fig 3.16(c) and particularly the bending stresses as illustrated in Fig 3.16(e),(f). This can be due to the fact that the modal contributions to stress resultants are not only dependent upon the modal participation factor and displacement response spectrum of earthquake, as will be explained in chapter 5, but also to the formulation of stress resultant itself. Looking at the equations for stress resultants (eqn (2.14)) shows that membrane stresses also depend on the value of i and j, while the bending stress resultants depend on i^2 and j^2, which consequently makes the contribution of shorter wavelengths, higher i and j, in membrane and bending stress resultants significant in comparison to displacements.

The frequencies and mode numbers corresponding to some selected modes having short wavelengths are shown in Table 3.5. All these modes correspond to high mode numbers in terms of the rank order, which clarifies the need for including about 300 modes for the convergence of bending stresses in FE programme ,which, unlike semi-

(i, j)	$f(hz)$	Mode number in terms of rank order
$(1, 11)$	8.761	136
$(1, 13)$	10.11	161
$(19, 1)$	14.03	241
$(1, 17)$	14.22	248
$(3, 17)$	14.41	253

Table 3.5: Short wavelength modes participating in stresses

analytical method used in this study, include modes in rank order starting from the mode having the lowest frequency; this will be further explained in section 4.5.

3.9 Effect of in-plane modes in the response of cylindrical shells

For each choice of wave number (i, j) there are 3 natural frequencies. In the past just the out-of-plane modes (those for which the out-of-plane deformation, w, dominates) have been considered in the earthquake response of shells [95], [8]. However, for each (i, j) there are two other modes within which one of the in-plane deformations (u, v) dominates. These are referred to here as in-plane modes. Although the in-plane modes generally correspond with frequencies an order of magnitude higher than equivalent out-of-plane modes, there may be circumstances in which these modes could conceivably play an important role in the earthquake response of the shell. In this section the effects of considering in-plane modes in the displacement, acceleration, and stress responses have been investigated. The analyses were performed for a range of shells with $R/h = 500$, $\phi = \pi/3$, $B = \rho\, R\, h/E$ between 0.5 to $2 \times 10^{-6}\ s^2$, and $L_y/L_x = 0.5,\ 1,\ 2$. Having derived the out-of-plane and in-plane natural frequencies the responses have been determined considering just the out-of-plane modes and compared with the responses when the effects of in-plane modes were also included.

Analyses of shells under the vertical components of earthquake showed that the changes in radial and circumferential displacements were insignificant when the in-plane modes

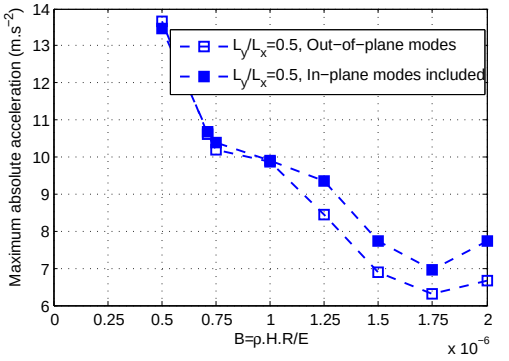

(a) Radial acceleration

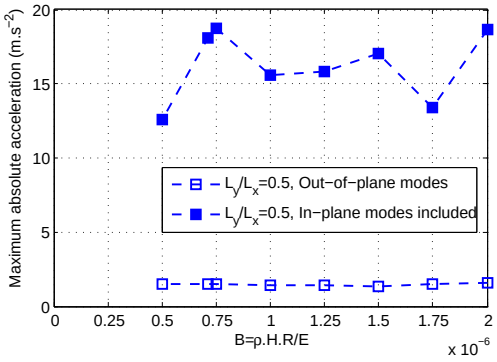

(b) Circumferential acceleration

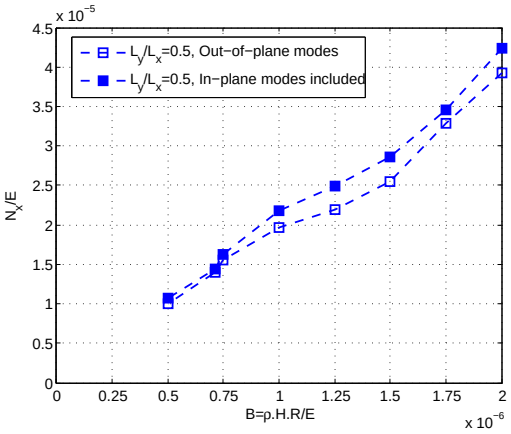

(c) N_x

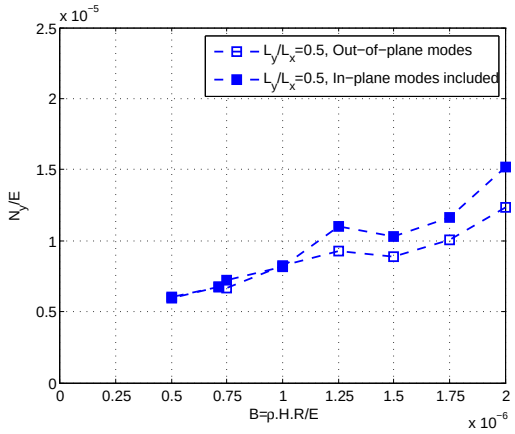

(d) N_y

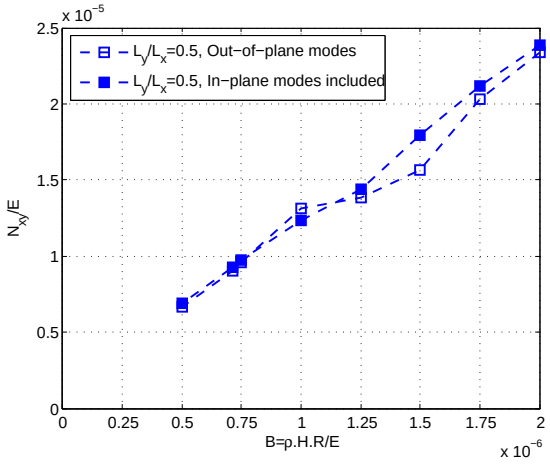

(e) N_{xy}

Figure 3.17: Acceleration, and membrane stress for vertical component of Landers earthquake, $L_y/L_x = 0.5$, $R/h = 500$, $\phi = \pi/3$

are neglected; so the displacements are not plotted in Figs 3.17-3.19. However neglecting the effects of in-plane modes can result in considerable differences, particularly

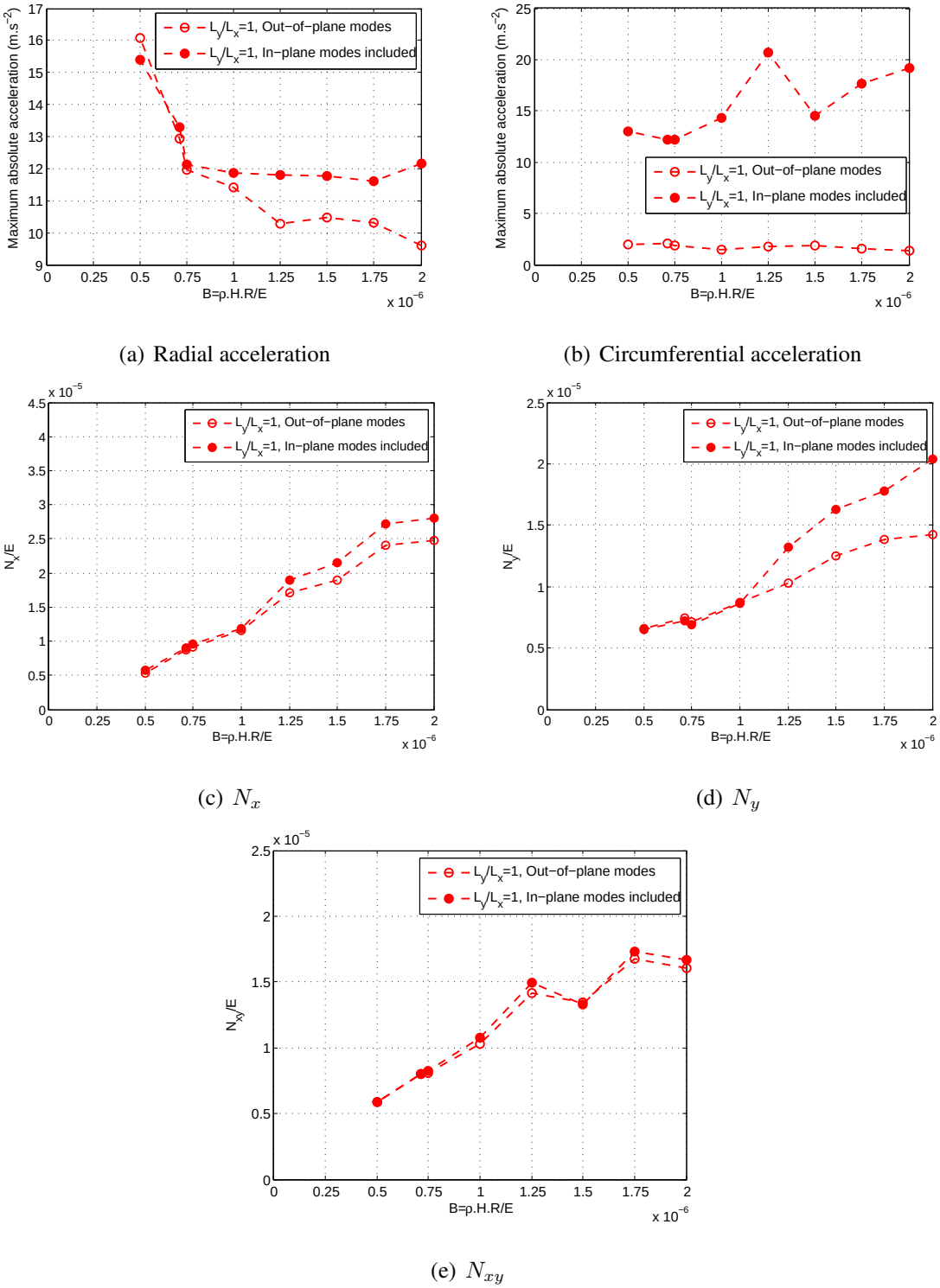

(a) Radial acceleration

(b) Circumferential acceleration

(c) N_x

(d) N_y

(e) N_{xy}

Figure 3.18: Acceleration, and membrane stress for vertical component of Landers earthquake, $L_y/L_x = 1$, $R/h = 500$, $\phi = \pi/3$

in the circumferential acceleration as shown in Figs 3.17(b), 3.18(b) and 3.19(b). The increase is different for each case of shell and also for the various responses. For

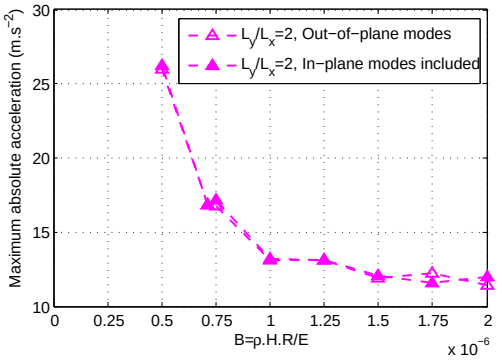

(a) Radial acceleration

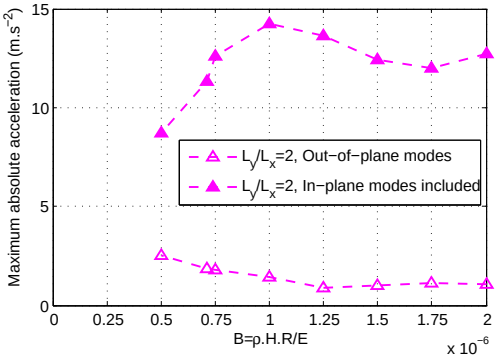

(b) Circumferential acceleration

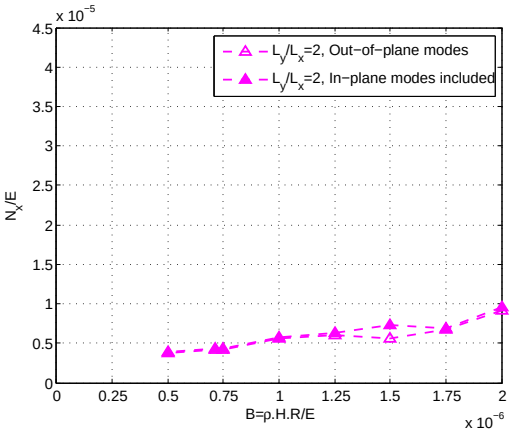

(c) N_x

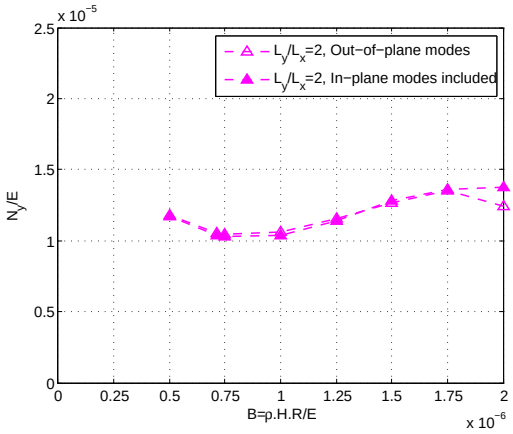

(d) N_y

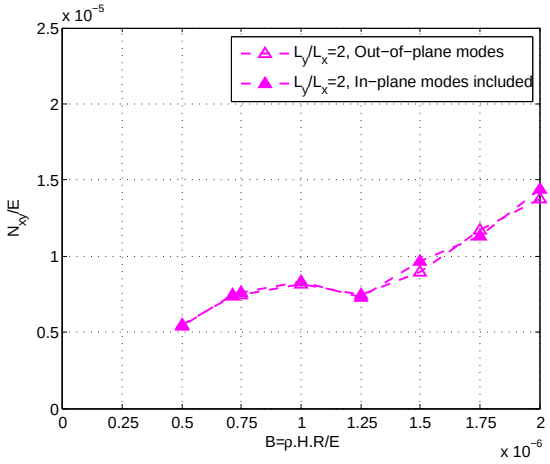

(e) N_{xy}

Figure 3.19: Acceleration, and membrane stress for vertical component of Landers earthquake, $L_y/L_x = 2$, $R/h = 500$, $\phi = \pi/3$

example, including in-plane modes increases circumferential acceleration very much more than radial acceleration. This is because, although the changes in both radial

Out-of-plane mode	In-plane mode	In-plane mode
$\bar{u}_1 = -0.0556$	$\bar{u}_2 = 0.7096$	$\bar{u}_3 = 0.7024$
$\bar{v}_1 = 0.2642$	$\bar{v}_2 = -0.6680$	$\bar{v}_3 = 0.6957$
$\bar{w}_1 = 0.9629$	$\bar{w}_2 = 0.2243$	$\bar{w}_3 = -0.1503$
$\omega_1^2 = 508.5453$	$\omega_2^2 = 15284$	$\omega_3^2 = 42392$
$f_1 = 3.5891$	$f_2 = 19.6763$	$f_3 = 32.7689$

Table 3.6: Eigenvalues, frequencies and ω^2 for a shell with $B = \rho hR/E = 1 \times 10^{-6}\ s^2$ and $L_y/L_x = 1$ considering only 1 circumferential and axial half-wave

and circumferential displacements are insignificant, the changes in circumferential displacement are higher than the radial displacement. Consequently, when the displacements are multiplied by the respective values of ω^2, to produce the corresponding accelerations, the circumferential acceleration responses will increase more than radial acceleration.

As a large number of modes (19 circumferential and axial half-waves) are included in the responses in Fig 3.17-3.19, it is not easy to explain the above discussion numerically. In order to show the validity of the above discussion and explain the huge difference in accelerations as a result of a small change in displacements, an analysis is performed for the shell with $B = \rho hR/E = 1 \times 10^{-6}\ s^2$, $L_y/L_x = 1$ in Fig 3.18(a)(b) for which only one circumferential and axial half-wave is included. The $\bar{u}$, $\bar{v}$, $\bar{w}$ corresponding to the out-of-plane and in-plane modes, the associated frequency and ω^2 are shown in Table 3.6.

The maximum displacement and acceleration with the assumption of including and neglecting in-plane modes are also presented in Table 3.7. As can be seen because $\bar{v}$ corresponding to in-plane modes are larger than $\bar{w}$, it will effect the circumferential displacement more than the radial displacement as shown in Table 3.7; changing circumferential displacement from $0.0027\ \ m$ to $0.0029\ \ m$, while changing radial displacement from $0.00986\ \ m$ to $0.00987\ \ m$. Consequently, even small changes in displacement will increase the acceleration significantly as it is multiplied by high value of ω^2 corresponding to in-plane modes; in this case multiplied by $\omega_2^2 = 15284$

In-plane modes neglected	In-plane modes included
$a_v = 1.3686\ m/s^2$	$a_v = 14.283\ m/s^2$
$v = 0.0027\ m$	$v = 0.0029\ m$
$a_w = 5.0516\ m/s^2$	$a_w = 6.4504\ m/s^2$
$w = 0.00986\ m$	$w = 0.00987\ m$

Table 3.7: Maximum absolute circumferential and radial displacement for a shell with $B = \rho hR/E = 1 \times 10^{-6}\ s^2$ and $L_y/L_x = 1$ considering just mode $(i, j) = (1, 1)$

	Time (s)	Location $(\frac{x}{L}, \frac{y}{R\phi})$
a_v	9.32	$(1/2, 1/50)$
v	10.36	$(1/2, 1/50)$
a_w	10.595	$(1/2, 1/2)$
w	10.35	$(1/2, 1/2)$

Table 3.8: Location and time of maximum absolute circumferential and radial displacement and acceleration for a shell with $B = \rho hR/E = 1 \times 10^{-6}\ s^2$ and $L_y/L_x = 1$ considering just mode $(i, j) = (1, 1)$

and $\omega_3^2 = 42392$ (Table 3.6).

To verify and better understand the result in Table 3.7, another analysis is performed using the Matlab programme. It should be noted that the maximum response corresponding to each of the three roots occurs at a different time and different location over the surface of the shell. To find the maximum responses in Table 3.7 the displacement and acceleration response corresponding to each of the three roots are derived at the time and location of the maximum response over the surface of the shell when all three roots are included. Table 3.8 shows the time when the maximum displacement and acceleration responses occur and their locations over the surface of the shell; the results are derived based on including all three roots of mode $(i, j) = (1, 1)$.

For $(i, j) = (1, 1)$ the displacements corresponding to each root is calculated according to eqn (3.1) and the accelerations are derived by multiplication by the corresponding ω^2 as defined in Table 3.6. As shown in Table 3.9 the maximum displacements and

	$w\ (m)$	$a_w = \omega^2 w$ $(m.s^{-2})$	$v\ (m)$	$a_v = \omega^2 v$ $(m.s^{-2})$
1st root	(0.0087)	-4.402	(-5.8094×10^{-4})	0.308
	0.00986		0.00256	
2nd root	(9.1315×10^{-5})	-1.3950	(-3.8489×10^{-4})	5.8830
	1.7748×10^{-6}		1.9597×10^{-4}	
3rd root	(1.7005×10^{-5})	-7.435	(-1.9050×10^{-4})	8.092
	7.9336×10^{-6}		1.0661×10^{-4}	
$\sum$	(0.00871)	-6.5405	(0.001156)	14.283
	0.00987		0.00286	

Table 3.9: Contribution of each of the three roots to the maximum absolute circumferential and radial displacement and acceleration for a shell with $B = \rho h R/E = 1 \times 10^{-6}\ s^2$ and $L_y/L_x = 1$ considering just mode $(i, j) = (1, 1)$

accelerations occur at various times according to Table 3.8. So in order to find the contribution of each root to the total accelerations, the displacements are also derived at the time when the maximum total acceleration occurs. The numbers shown without parenthesis in Table 3.9 are the contribution of each of the three roots to the total radial displacement at $t = 10.595\ s$ and their contributions to the total circumferential displacement at $t = 9.32\ s$; these are the times when the maximum radial and circumferential acceleration occur according to Table 3.8. However, the contribution of each root to the total maximum radial displacement ($w = 0.00987$) and maximum circumferential displacement ($v = 0.00286$) are also shown in Table 3.9 in parenthesis. These are found at the time when the maximum radial and circumferential displacements occurred according to Table 3.8; i.e. $t = 10.35\ s$ for radial displacement and $t = 10.36\ s$ for circumferential displacement.

Table 3.9 shows that although the displacements do not noticeably increase as a result of including the in-plane modes the corresponding accelerations increases significantly; the radial acceleration increases from $5.0516\ m.s^{-2}$ to $6.4504\ m.s^{-2}$ and circumferential acceleration increases from $1.3686\ m.s^{-2}$ to $14.283\ m.s^{-2}$. The changes in

circumferential acceleration is also higher than the radial acceleration. This is because $\bar{v}$ corresponding to the second and third roots are higher than $\bar{w}$ (Table 3.6), so when multiplied by corresponding ω^2 contributes more significantly to the circumferential acceleration.

In-plane modes make little difference to bending stresses just as they make little differences to radial displacements, since bending stresses are influenced by radial displacement. But as the membrane stresses are directly related to the in-plane displacements the in-plane modes would be important in their determination. Fig 3.18(d) shows that inclusion of the in-plane modes for a shell with $R/H = 500$, $\phi = \pi/3$, $B = \rho h R/E = 2 \times 10^{-6} s^2$, $L_y/L_x = 1$ results in almost 43% increase in N_y, and 13% in N_x (Fig 3.18(c)).

The changes in the responses are also different for various cases of shells. For example, as stated before in relation to Fig 3.18(d), N_y in creases by 43% as a result of including in-plane modes for the shell with $B = 2 \times 10^{-6}\ s^2$. However, it does not induce any significant change for the case of a shell having $B = 1 \times 10^{-6}\ s^2$. The rest of the responses in Fig 3.18 are also higher in a shell with $B = 2 \times 10^{-6}\ s^2$ than in a shell with $B = 1 \times 10^{-6}\ s^2$. In order to explain the reason, the natural frequencies of a shell with $B = 2 \times 10^{-6}\ s^2$ are plotted in Fig 3.20; these can be compared with the natural frequencies of a shell with $B = 1 \times 10^{-6}\ s^2$ in Fig 3.7.

The comparison shows that in Fig 3.20 the in-plane modes have considerably lower frequencies; many more in-plane modes have frequencies in the range of the frequencies of the earthquake (Fig 3.10), such as $f_{i,j} = f_{1,1} = 13.9\ Hz$, $f_{i,j} = f_{3,1} = 29.82\ Hz$, and $f_{i,j} = f_{1,3} = 30.93\ Hz$, in Fig 3.20(b) and $f_{i,j} = f_{1,1} = 23.1\ Hz$ in Fig 3.20(c).

Therefore, the extent of the effects of ignoring in-plane modes are strongly dependent upon the relationships between the earthquake frequency spectrum and natural frequencies of the shell. In that the in-plane modes have such an important influence on membrane stresses, earlier conclusions as to the numbers of modes required for an adequate FE analysis, or to meet code requirements need to be further emphasized.

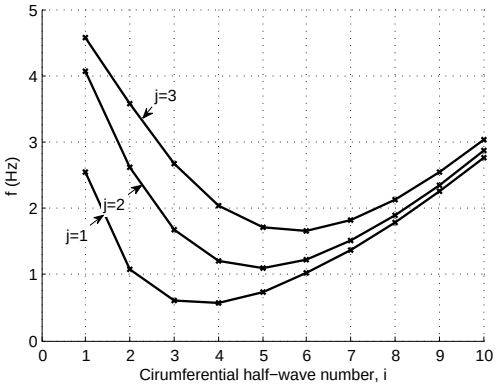

(a) out-of-plane mode

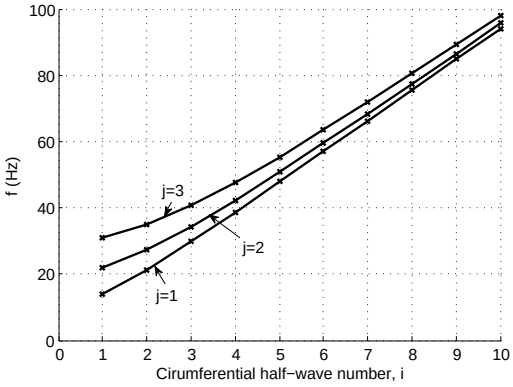

(b) in-plane mode

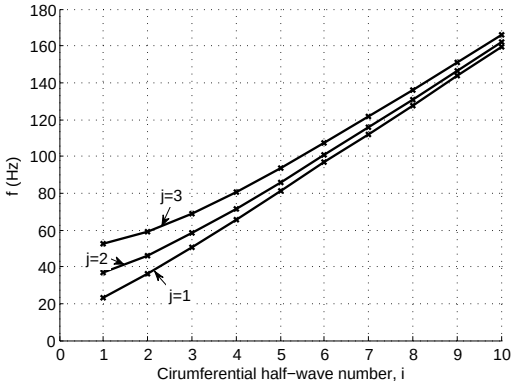

(c) in-plane mode

Figure 3.20: In-plane and out-of-plane natural frequencies for a shell with $B = 2 \times 10^{-6}\ s^2$, $L_y/L_x = 1$

3.10 Vertical and horizontal component of earthquake

The seismic analysis of structures is usually performed for horizontal component of earthquake with the vertical component of earthquake often neglected. In this research the response of shells under vertical components of earthquake is investigated. However, in order to highlight the conditions that the vertical component of earthquake could result in higher responses, Landers earthquake with a high vertical component compared to its horizontal component is chosen. It should be noted that the earthquakes with high vertical to horizontal components usually occur in near-field events. In order to find the relative importance of vertical and horizontal components of earthquakes the maximum acceleration and stress resultants of the same shells as discussed in section 3.9, are presented in Fig 3.21. The shells are subjected to the horizontal component of Landers earthquake as in Fig 3.11.

Only the out-of-plane modes are included with the contribution of in-plane modes neglected. However, in a separate study the importance of in-plane modes for shells in Fig 3.21 showed that including in-plane modes did not change the responses to the horizontal component of the Landers earthquake.

For simplicity of comparison, the maximum responses to vertical component of earthquake (Fig 3.17-3.19) are also added in Fig 3.21, in which the solid lines represent the responses of shells to vertical components of the Landers earthquake, while the dashed lines show the responses of shells to horizontal components of the Landers earthquake. Looking at Fig 3.21, it is clear that the vertical components of the Landers earthquake lead to significantly higher displacements, accelerations, and stresses compared with the horizontal component of the Landers earthquake. This can be explained by comparing the acceleration response spectrum in Fig 3.10(d), and 3.11(d), showing that at each specific frequency the acceleration response spectrum of vertical component of Landers earthquake is considerably higher than the horizontal component. So the response of each individual mode of the shell having these frequencies to the vertical component of the Landers earthquake is higher than the horizontal component of this earthquake. For example, for a mode having $f = 10\ Hz$, the acceleration response spectrum of the horizontal component of earthquake is $S_a = 10\ m/s^2$ (Fig 3.11(d)), which is less than the acceleration response spectrum of vertical component of earthquake equal to $S_a = 18\ m/s^2$ (Fig 3.10(d)). This study involved considering a total number of 19 half-waves in circumferential and axial directions so the sum of the responses of these modes to the vertical component of Landers earthquake would be higher than the responses when subjected to horizontal component of the Landers earthquake as shown in Fig 3.21.

Fig 3.21(c)-(e) show the stress resultants are also higher when shells are subjected to vertical component of earthquake. It is because the stress resultants are dependent to displacement response spectrum. Displacement response spectrum is shown to have higher responses to vertical component of Landers earthquake (Fig 3.10(c), Fig 3.11(c)). To better understand this, a shell with $B = 1 \times 10^{-6}\ s^2$ and $L_y/L_x = 1$ is chosen; Fig 3.21(c) shows the axial membrane stress resultant is higher when the

shell is subjected to vertical component of the Landers earthquake. According to Fig 3.16(d), the most contributing modes in axial membrane stress resultant for this shell are $(i, j) = (1, 1)$, $(3, 1)$, $(5, 1)$, and $(5, 3)$ with the corresponding frequencies as $f_{1,1} = 3.589\ Hz$, $f_{3,1} = 0.8586$, $f_{5,1} = 1.0483\ Hz$, $f_{5,3} = 2.5\ Hz$. Using Fig 3.10(c) and 3.11(c), the displacement response spectrum corresponding to mode $(1, 1)$, $(3, 1)$, $(5, 1)$, and $(5, 3)$ are equal to $0.015\ Hz$, $0.025\ Hz$, $0.07\ m$, and $0.12\ m$, respectively when subjected to vertical component of earthquake (Fig 3.10). They reduce to $0.015\ Hz$, $0.015\ Hz$, $0.02\ m$, and $0.04\ m$, respectively when subjected to horizontal component of earthquake. This explains the reason for the reduction in N_x when the shell is subjected to horizontal component of the Landers earthquake.

As previously mentioned (section 3.9), the responses are different for shells with various material properties. This results from the shells having different natural frequencies which as a consequence of the displacement response spectrum result in different responses. Fig 3.21 highlights the importance of consideration of the vertical component of earthquakes, in the design of this form of shell.

For the horizontal component of earthquake, the inclusion of in-plane modes generally has a negligible effect on the predicted results but as shown in section 3.9 can be significant for the vertical components. However, as can be seen from Fig 3.21, the responses to earthquake components are more significantly dependent on the shell geometry and material properties so that this conclusion may need to be reassessed for shells with different geometric and material parameters.

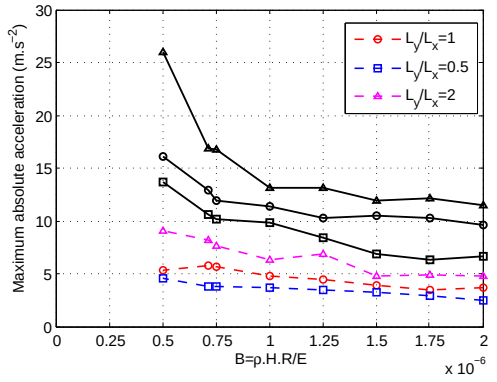

(a) Radial acceleration

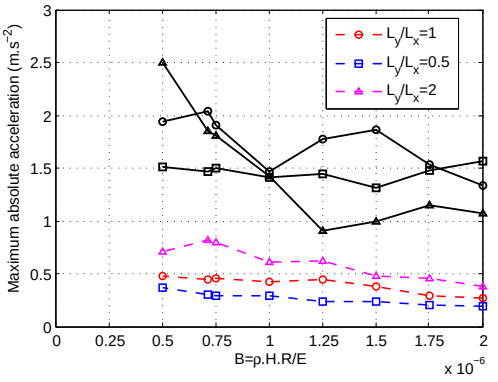

(b) Circumferential acceleration

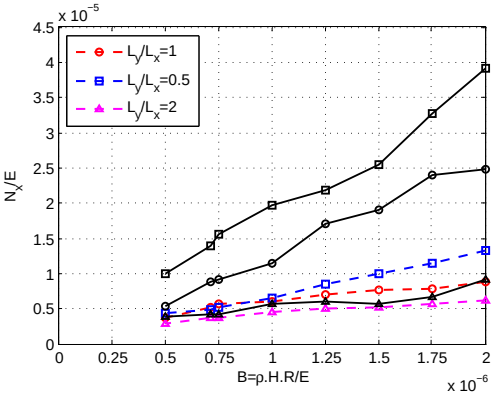

(c) N_x

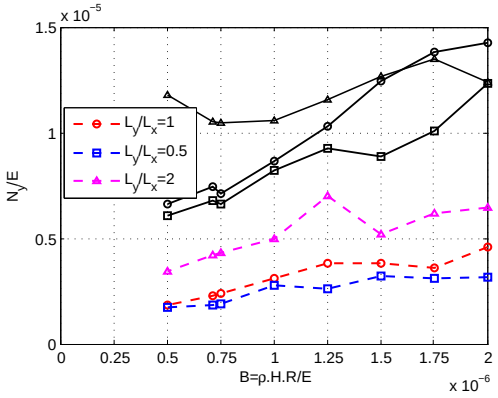

(d) N_y

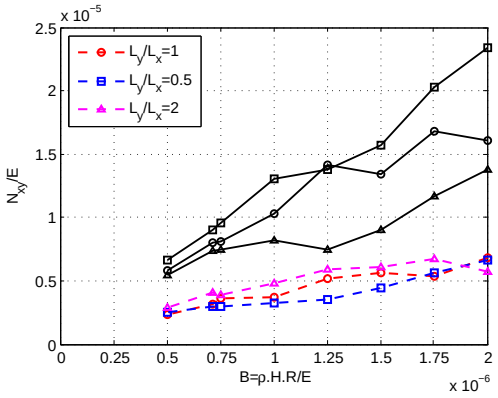

(e) N_{xy}

Figure 3.21: Comparison of maximum absolute acceleration and stress for horizontal and vertical components of Landers earthquake, $R/h = 500$, $\phi = \pi/3$ (Only out-of-plane modes are included). Solid lines represent the responses of shells to the vertical component of the Landers earthquake. Dashed lines represent the responses of shells to horizontal component of the Landers earthquake.

3.11 Summary

The dynamic equations of motion governing the linear elastic vibrations of open cylindrical shells with a constant damping ratio are developed and solved using an analytical method. The predicted natural frequencies are verified by comparison with past results [7]. For one earthquake loading, convergence studies on the number of modes required in the modal analysis suggest that a detailed analysis should be performed to ensure the adequacy in the numbers of modes considered for the response of the shell. A further study confirms that inclusion of the in-plane modes within the analysis of the seismic behaviour of cylindrical shell roofs can have substantial effects upon the predicted stresses, especially in the response to the vertical components of the earthquake. The results also confirm that the vertical components of earthquakes are likely to produce higher responses than those of the horizontal components.

In this chapter only the natural frequencies are verified with the available literature. However, the dynamic responses of shell to earthquake loading are also needed to be validated. In the next chapter these responses are compared with the results of a FE analysis to increase confidence in the use of either analytical or FE method. It also explains the method used in FE to extract the natural frequencies and find the responses of shell to earthquake loading. The required numbers of modes for an adequately converged response are also examined in the next chapter.

Chapter 4

Numerical Modelling of Cylindrical Shell Roof subjected to earthquake loading

As explained in chapter 3, there are limited studies on the dynamic response of roof shells subjected to earthquakes, which makes it difficult to draw general conclusions. It was indicated that there is a need for rather more systematic investigations of the parameters most likely to affect the earthquake response of shells. To fulfil this need an analytical method based on solution using Love-Timoshenko strain-displacement relationships and employing a Lagrangian approach to derivation of equations of motion was introduced in chapter 3. The response of roof shells to earthquake loading was also derived based on interpolation of the excitation method as explained in section 3.4. This method was then used to answer some practical questions about the dynamic behaviour of roof shells. However, to validate this new contribution to the existing literature there is a need for cross-checks to ensure its numerical accuracy.

Unfortunately, because some of the important parameters controlling behaviour were not reported in the available past research [7] [8], it was not possible to directly use these results as a mean of validating the present analysis. For this reason, the present work requires for an independently validated analysis approach. The dynamic analysis of shell structures is often performed by use of finite element (FE) programs. ABAQUS, a commercially available FE software package, is used for the purpose of

this research.

As mentioned earlier the analytical method was conveniently used to answer practical questions such as: the effect of in-plane modes in the response of the shell; participation of different modes in the displacement, acceleration and stress responses; and the comparison between the effects of horizontal and vertical components of earthquake on the response of the shells. While the FE is less convenient for such studies, it has the considerable advantage of allowing more complex shell problems to be analysed. But effective use of FE programs should be based upon a sound understanding of shell theories, and an appreciation of the mechanics of shells as well as an insight into the basic concept of the analysis method. The first part of this chapter starts with a brief discussion on the concept of FE; this is followed with the appropriate choice of element for this research, and explanation of the basis of different analysis used in this section.

Using analytical methods to verify the FE program on simpler examples is an effective way to prevent possible errors from occurring when analysing more complicated problems. Therefore, the second part of this chapter performs a comparison study of natural frequencies and associated modes resulting from the analytical and FE methods through linear numerical eigenvalue analysis. It is followed by comparisons of the induced displacements, accelerations and stresses in a shell subjected to an earthquake loading using modal dynamic analysis.

Finally, this chapter tackles the question of choosing sufficient numbers of modes in the context of dynamic analysis of roof shells for converged displacement, acceleration, and stress responses.

4.1 FE method

The concept of the finite element method, often regarded as being first proposed by Clough in 1957, is based on subdividing a structure into a finite number of elements that are connected by nodes, with the element behaviour approximating the exact solution. It is based on the satisfaction of three equations; stress-strain relationship within the element, displacement compatibility between adjacent elements, and force equilibrium

on an integral basis at a finite number of nodes within the structure. When properly formulated the response of a structure will converge as the mesh is refined.

In the finite element analysis, results, such as displacement, are evaluated at nodes and then interpolated over the element to find their values over the entire element. Satisfying the three essential equations over the entire structure involves solving a large number of algebraic equations which makes it impossible to solve manually. Therefore, there is a need for a FE program to carry out the analysis.

In this study ABAQUS has been chosen to perform the numerical analysis. This package is divided into: ABAQUS/Standard which is a general purpose finite element program, ABAQUS/Explicit, an explicit finite element program; ABAQUS/CAE, an interactive environment used to create the model, check the model for potential errors in the modelling, submit the analysis, monitor the job and evaluate the results; and finally ABAQUS/viewer, which contains the post-processing capabilities of the visualization mode.

ABAQUS consists of the model data and the history data. The model data defines a finite element model, such as elements, nodes, material properties, whilst the history data defines the changes in the model such as the response of the model after a loading. The analysis history is defined in ABAQUS by dividing the problem history into different steps, defining one analysis procedure in each step such as static stress analysis, dynamic stress analysis, eigenvalue buckling, along with the description of prescribed loads, boundary conditions, and requesting output for each step.

There are two kinds of steps in ABAQUS, general analysis steps and linear perturbation analysis steps. General analysis steps can be used to analyze linear or nonlinear response and can be included in an ABAQUS/Standard or ABAQUS/Explicit analysis. While linear perturbation steps, only available in ABAQUS/Standard, can be used only in the linear problems. It always considers the analysis to be linear about a state at the time when the linear analysis procedure is introduced. In other words ABAQUS/Standard treats a linear perturbation analysis as a linear perturbation about a pre-loaded, pre-deformed state. It allows the application of linear analysis techniques where the linear response depends on pre-loading or on the non-linear response history

of the model.

As all the analyses in this research are limited to linear perturbation analysis ABAQUS/Standard is chosen for this study. It has the ability to perform different procedures, which will be discussed in details in the relevant sections.

4.2 Element selection

First step in defining a particular structure in ABAQUS is to define the model data. As previously stated model data defines a finite element model which includes elements, nodes, elements properties and material definition. Choosing the right shell element is very important in the modelling process of a shell structure. The element library in ABAQUS has complete elements which can be used to build the model and be used for many types of analysis.

This research deals with different analysis procedures for the cylindrical shells such as: the linear analysis in this chapter; the analysis based on including pre-stressed loading, together with the buckling analysis in chapter 7; and finally the analysis of doubly curved shells in chapter 8. It is very important to select appropriate elements for these analyses to accurately capture the behaviour of the shell under certain loading conditions and for different analysis procedures. Among the different forms of shell elements available in ABAQUS library S8R5 is chosen for this study. S8R5 is a three-dimensional conventional thin shell element and is part of the conventional shell elements available in ABAQUS. The conventional shell elements can be used in three-dimensional or axisymmetric analysis. They can be used to model static and dynamic procedures. Some of the elements in this group include the effect of shear deformation and thickness change. These elements use thick shell theory for thick shells and as the thickness decreases any small transverse shear deformations are ignored and consequently converge to discrete Kirshhoff thin shell elements. Some other elements in this group are suitable for large strain analysis as they consider finite membrane strains and arbitrary large rotations. Although as stated earlier general purpose conventional shell elements provide accurate results for most applications, but some of the elements are especially designed for thick or thin shells for an enhanced performance.

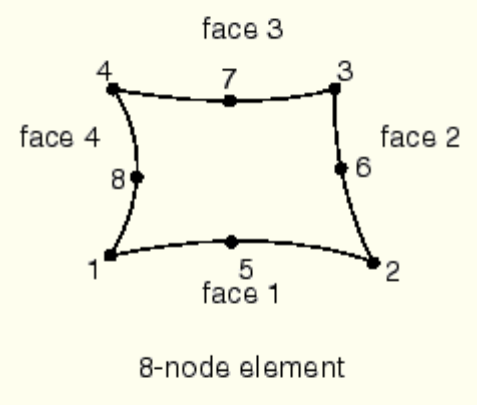

Figure 4.1: 8 node element, the figure is taken from ABAQUS/Standard manual

For example, when the ratio of thickness to smallest length on the surface of the shell is more than about $1/5$ the transverse shear flexibility becomes important and the second order integration is needed. In this case the shell is considered a thick shell and using an element especially design for thick shells can enhance the performance.

However, as for the case of this research the analyses are performed for thin shells for which the transverse shear flexibility is negligible and the shell theory is based on those of Kirchhoff hypothesis as described in section 2.1; so the three-dimensional conventional thin shell element is chosen. It is worth noting that there are two kinds of thin shells available in ABAQUS. The first group is the ones in which the Kirchhoff constraint is satisfied analytically and solve thin shells. This group of elements should only be used for thin shells. The second group is the ones in which the Kirchhoff constraints are satisfied numerically; it means they converge to thin shell theory as the thickness decreases.

S8R5, chosen for the analysis of cylindrical shells in this research, falls into the second group. It has the potential of modelling large rotations but only small strains. The changes in thickness are ignored in this element. Bending strain representations are based on those of Koiter-Sanders shell theory like all other shell elements in ABAQUS [98]. There is one node at each corner and one node at the middle of each side, as illustrated in Fig 4.1. It is a reduced integration element, which has four integration points located at the four corners shown in Fig 4.2 to form the element stiffness. Using the element with reduced integration usually reduces the running time, especially

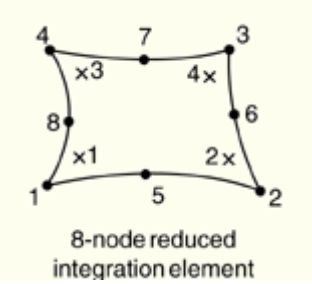

Figure 4.2: Integration points, the figure is taken from ABAQUS manual

in three dimensional problems. However, the mass matrix and distributed loadings are still integrated exactly. In this element there are five degrees of freedom at each node, three of which corresponds to the displacement components and two represents the rotation components about the surface tangents, which makes the calculation faster than the elements having six degrees of freedom at each mode. However, as explained in the ABAQUS manual [99] ABAQUS/Standard automatically considers three-global rotation components at each node when;

- "The model has kinematic boundary conditions applied to rotational degree of freedom,
- is used in a multi-constraint that has rotational degrees of freedom,
- is shared with a beam or a shell element that has six degrees of freedom at all nodes,
- is located on a line adjoining two shell surfaces with different surface normals,
- is loaded with moments." [99]

4.3 Extraction of natural frequency

Natural frequency extraction is a linear perturbation analysis, in which natural frequencies are extracted about the base state. The base state is the current state of the model at the end of the last analysis step. If the frequency extraction is the first step in the analysis, then the base state is determined from the initial conditions.

This analysis performs an eigenvalue extraction to calculate the natural frequencies and the corresponding mode shapes. In this section the analysis is performed using small-displacement assumptions, in which the elements are formulated in the original configuration, using the original nodal coordinates. However, if the geometric non-linearities is taken into account in the base state, as in chapter 5, the program would include initial stress and load stiffness effects due to pre-loads and initial conditions.

Natural frequencies are extracted by means of eigenvalue techniques. For an undamped finite element model it can be written as

$$(-\omega^2 M^{MN} + K^{MN})\phi^N = 0 \tag{4.1}$$

where, M^{MN} is the mass matrix, K^{MN} is the stiffness matrix, ϕ^N is the natural mode, ω the natural frequency, and M and N are degrees of freedom of the whole model. K^{MN} would always be positive for the cases where the geometric nonlinearities are not included in the analysis as in this chapter. However, the stiffness matrix may be either positive or negative if the initial stress effects due to geometric-nonlinearities are included in the analysis. The negative eigenvalues indicate instability in the model. The eigenvectors, ϕ^N, are normalized so that the maximum displacement in each vector is unity.

ABAQUS/Standard uses two methods, Lanczos and the subspace iteration eigenvalue extraction methods, to find the natural frequencies of the structure. Lanczos method is chosen in this study, because it is generally faster than the subspace method when a large number of eigen-modes is required [99]. Lanczos method is an iterative algorithm to find eigenvalues and eigenvectors of a square matrix. The details of the Lanczos method can be found in ABAQUS theory manual section $2.5.1$ [99].

4.3.1 Verification of natural frequencies

Using the FE method the natural frequencies are extracted for an isotropic open cylindrical shell with simple supports at four edges. This allows direct comparison with the analytical results using the methods described in chapter 3. A shell having geometry and material properties of $\phi = \pi/3$, $\frac{L_y}{L_x} = 1$, $\frac{R}{h} = 500$, $B = \frac{\rho h R}{E} = 10^{-6}\ s^2$, $\nu = 0.3$,

$\rho = 4140.5\ kg/m^3$, $E = 9.1 \times 10^{10}\ N/m^2$, $R = 104.8\ m$ (the same shell as in Fig 3.4) is chosen for this purpose, for which the 10 lowest frequencies are extracted after performing a convergence study leading to a 30×30 mesh. It should be noted that the choice of the number of mesh points has a great effect in the accuracy of the results, which will be explained in section 4.3.2 through a detailed convergence study. The verification study in section 3.2.2 Fig 3.4 showed the close agreement between the natural frequencies using analytical solutions based on equations of section 3.2.1 and the present FE predictions. This provides confidence in the extended use of these methods to predict the response of the shell when subject to earthquakes.

4.3.2 Mesh sizes

A refined mesh should be used in order to ensure sufficiently precise representation of the modes and consequently provide adequate accuracy in results. It is therefore necessary to carry out a mesh convergence study to find a suitable mesh size for the analyses. In this section the convergence study is performed for the natural frequencies of a shell with different numbers of mesh points and comparing the FE results with the analytical solution.

For the same shell as in Fig 3.4 the convergence study is carried out for the natural frequencies of a shell using 9 different mesh numbers, starting from a coarse mesh of 10 by 10 elements to a very fine mesh of 90 by 90 elements over the surface of the shell as shown in Fig 4.3.

As mentioned earlier, ABAQUS presents the frequency results in rank order starting from those of having the lowest frequencies. The number of half-waves in the axial and circumferential directions is found using the deformed shape of the associated eigenmode, found in the post-processing viewer feature of ABAQUS, as in Fig 4.4. Whereas in the analytical solution the frequencies are presented in terms of the i, and j, representing the circumferential and axial half-wave number, respectively; this makes it easy to find the frequency easily for the desired i, and j.

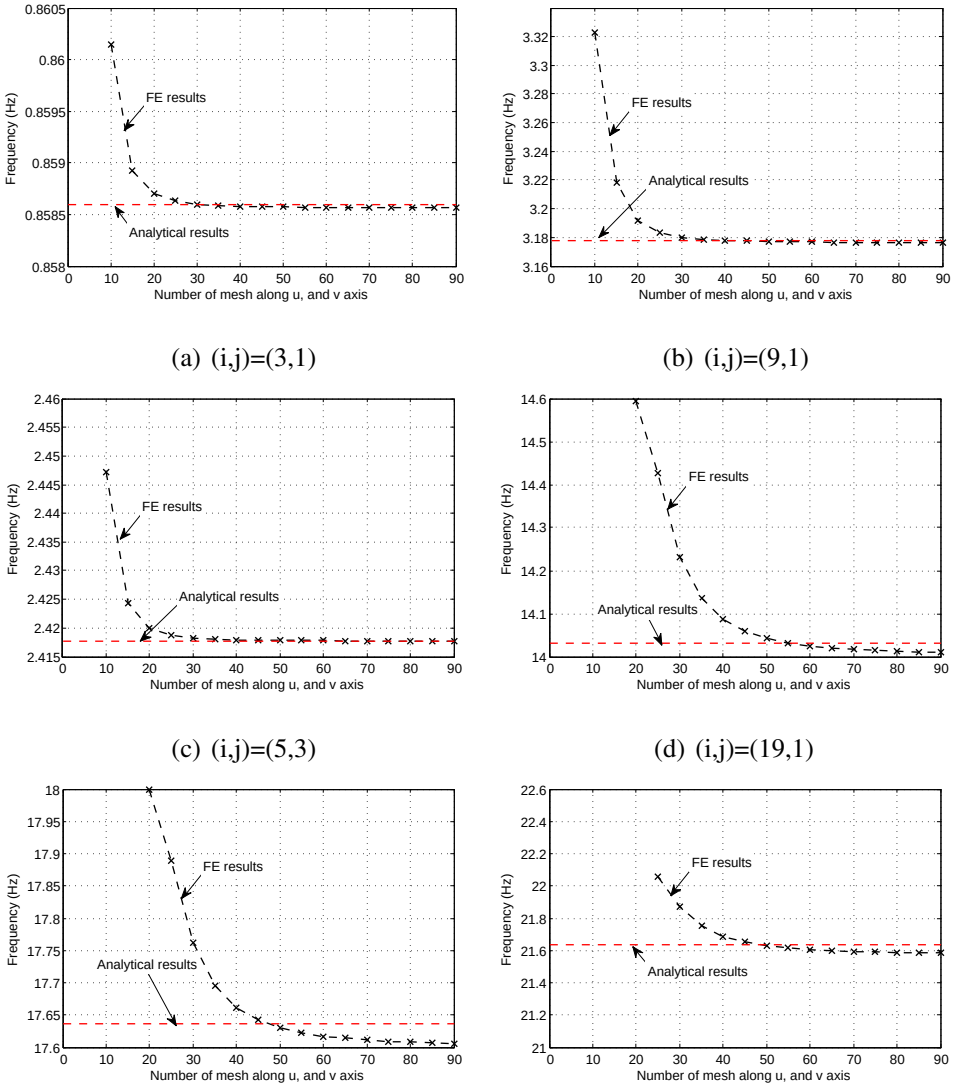

(a) (i,j)=(3,1)

(b) (i,j)=(9,1)

(c) (i,j)=(5,3)

(d) (i,j)=(19,1)

(e) (i,j)=(5,19)

(f) (i,j)=(7,21)

Figure 4.3: Convergence of frequency of some selected modes, for a shell with $R/h = 500$, $\phi = \pi/3$, $\rho hR/E = 10^{-6}\ s^2$, $\rho = 4140.5\ kg/m^3$, $E = 9.1 \times 10^{10}\ N/m^2$, $R = 104.8\ m$

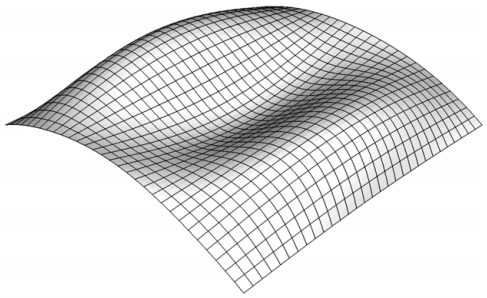

(a) $(i, j) = (3, 1)$, f=0.85860 Hz, mesh: 30×30

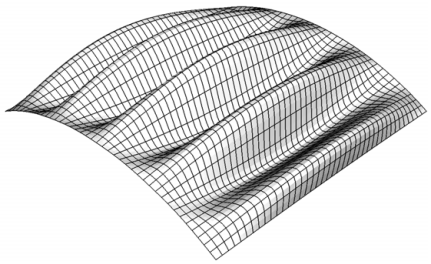

(b) $(i, j) = (9, 1)$, f=3.1779 Hz, mesh: 40×40

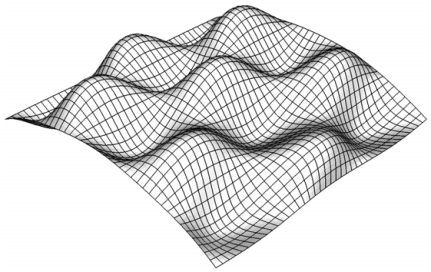

(c) $(i, j) = (5, 3)$, f=2.4179 Hz, mesh: 40×40

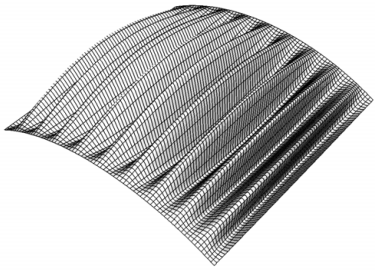

(d) $(i, j) = (19, 1)$, f=14.017 Hz, mesh: 70×70

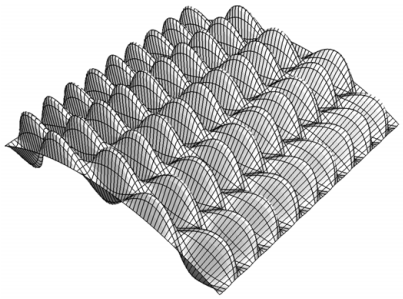

(e) $(i, j) = (5, 19)$, f=17.611 Hz, mesh: 70×70

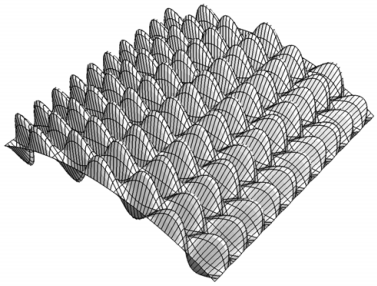

(f) $(i, j) = (7, 21)$, f=21.595 Hz, mesh: 70×70

Figure 4.4: Frequency and deformed shape of some selected modes for a shell with $R/h = 500$, $\phi = \pi/3$, $\rho h R/E = 10^{-6}\ s^2$, $\rho = 4140.5\ kg/m^3$, $E = 9.1 \times 10^{10}\ N/m^2$, $R = 104.8\ m$

The convergence study is performed by finding the natural frequencies for a selected number of modes having different axial and circumferential half-wave numbers and frequency range, as presented in Fig 4.3. The reason for choosing this wide range of half-wave numbers and frequency range is to investigate the required numbers of mesh for convergence of frequencies for modes having short and long wavelengths.

Fig 4.3 shows that modes having longer wavelength such as $(i, j) = (3, 1)$ and $(i, j) = (2, 3)$ converge with 30×30 mesh numbers. While modes having shorter wavelength such as $(i, j) = (19, 1)$, $(i, j) = (5, 19)$, $(i, j) = (7, 21)$ are shown to require a finer mesh of 70×70 for the frequency convergence.

It is noted that with a 30×30 mesh, frequency of mode $(i, j) = (3, 1)$ would converge to the exact results. However, a coarser mesh of 10 by 10 elements would result in a good approximation of governing frequencies with a 0.2% difference with the converged solution (Figs 4.3(a), 4.4(a)).

Similarly, with a coarser mesh of 15 by 15 elements and 10 by 10 elements, the frequency corresponding to modes $(i, j) = (5, 3)$ would have a 0.2% and 1.2% difference, respectively with the converged frequency resulting from using a finer mesh of 35 by 35 elements (Figs 4.3(c), 4.4(c)). The frequency of mode $(i, j) = (9, 1)$ using a 20 by 20 elements would also have 0.4% difference with the converged frequency resulting from using a finer mesh of 40 by 40 elements.

As stated earlier, modes having shorter wavelengths require a finer mesh. For example, modes $(i, j) = (19, 1)$ and $(i, j) = (5, 19)$ converge with 70×70 mesh number (Fig 4.3(d),(e),(f)). However, using a 40×40 mesh number for mode $(i, j) = (5, 19)$ would result a 0.11%, and 0.2% difference with the theoretical solution and with the converged frequency, respectively; A 40×40 mesh number also introduce 0.5% difference with the converged frequency for $(i, j) = (19, 1)$; and produce 0.3%, and 0.5% difference with the analytical solution and the converged results, respectively for mode $(i, j) = (7, 21)$.

From the above discussion it can be concluded that the frequencies would converge with a difference of less than 0.5% of the exact solution using a mesh number of double the number of half-waves.

The results in Fig 4.3 and 4.4 are governed by considering equal number of mesh in both axial and circumferential directions. However, the adequacy of the mesh number equal to double of half-wave number is needed to be verified for the modes having different number of half-waves in each axial and circumferential direction. For this purpose the frequency of mode $(i, j) = (5, 19)$ is derived using a 10×70 mesh number in circumferential and axial directions, respectively. The governing frequency is equal to $17.566\ Hz$ which has 0.2% difference with the frequency of this mode with a mesh of 70×70 as shown in Fig 4.4(e). However, as the rest of study deals with the combinations of different modes having different half-wave numbers in both axial and circumferential directions, equal mesh numbers are considered in both directions.

It is also noticed that the frequencies in Fig 4.3 do not always converge to the analytical results. However, the difference is very small. The reason for this difference is because the shell element in ABAQUS is based on Koiter-Sanders shell theory. Whereas in analytical solution the strain-displacement relationships are derived based on Love-Timoshenko. As explained in chapter 2 the frequencies based on different shell theories could differ from each other. However, as it can be seen the difference is negligible.

Using the discussion above implies, for a maximum half-wave number of $i = 7$ for the first 10 lowest frequencies (Fig 4.3), using a 15 by 15 element would result in a very small difference with the exact solution. However a 30 by 30 elements is used in the comparison study of frequencies and in the derivation of the responses of shell to earthquake loading in section 4.4.3.

4.4 Modal dynamic analysis

Modal dynamic analysis is a linear perturbation procedure, used to analyze the transient linear dynamic problems using the modal superposition method. It gives the response of the model subjected to an external time dependent loading as a function of time. This procedure derives the response of the requested numbers of the modes of the system. The characteristics of each mode, which includes the natural frequencies and eigenvectors, must first be extracted through a preceding frequency extraction procedure.

Modal amplitude of each mode is integrated through time, and then the total response is found by combination of these modal responses. This method produces accurate results for linear systems with adequate numbers of modes being selected, which is a small portion of the total modes of the finite element model. The reason for accuracy is because the integration operator used is exact when the external load varies in a piecewise linear manner with time. However, the choice of time increment should be consistent with the time increment of the external loading.

In ABAQUS the dynamic analysis can be performed using the *MODAL DYNAMIC command, and by defining the time increment and total duration of external force. As it is a linear analysis considering small displacements, the initial conditions are not carried over from the results of the preceding step, so initial displacement and velocity are assumed to be zero.

The participating modes in the modal analysis can be specified by the mode numbers individually or by requesting the modes belonging to specified frequency ranges using the *SELECT EIGENMODES command. However, if none of the above mentioned are selected, all modes extracted in the preceding eigenfrequency extraction step are automatically used in the modal superposition.

Damping is specified for modal analysis using the *MODAL DAMPING command. Different damping model can be defined in ABAUQS. The desired damping coefficient can be defined for a selected mode numbers or a range of frequencies. If the damping coefficients are defined for a range of frequencies then the damping coefficient for the modes having a frequency between those frequencies for which the damping coefficients are defined are found using the interpolation method. In this case the damping coefficient for the modes having the frequency outside the frequency range remain constant and equal to the predefined damping coefficient for the closest frequency. The damping coefficient can also be considered constant for the whole range of participating frequencies as it is assumed for this study.

4.4.1 Equation of modal dynamic analysis

As mentioned earlier the modal dynamic response provides time history analysis for linear problems. The external dynamic force is given as a function of time, assuming that the variation of the magnitude of the excitation within each increment is linear. The total response is based on the combination of responses of its participating modes, in which each mode can be considered as a single degree of freedom. Each uncouple one degree of freedom system, should satisfy the equilibrium equation at time t

$$\ddot{q} + 2\xi\omega\dot{q} + \omega^2 q = P_t = P_{t-\Delta t} + \frac{\Delta P}{\Delta t}\Delta t \tag{4.2}$$

where ξ is the critical damping ratio, q is the amplitude of the response in this mode, P is the magnitude of the modal loading, ΔP is the change in P over the time increment (Δt), and ω is the natural frequency, which is derived in the frequency extraction step. It is assumed that the excitation varies linearly within each time increment. ABAQUS [99] calculates the solution to this equation using

$$\begin{Bmatrix} q_{t+\Delta t} \\ \dot{q}_{t+\Delta t} \end{Bmatrix} = \begin{bmatrix} a_{11} & a_{12} \\ \\ a_{21} & a_{22} \end{bmatrix} \begin{Bmatrix} q_t \\ \dot{q}_t \end{Bmatrix} + \begin{bmatrix} b_{11} & b_{12} \\ \\ b_{21} & b_{22} \end{bmatrix} \begin{Bmatrix} P_t \\ P_{t+\Delta t} \end{Bmatrix} \tag{4.3}$$

where a_{ij}, b_{ij}, $i, j = 1, 2$ are constants, because at each time increment the loading only varies linearly. The solution is the sum of three parts: free vibration modes due to initial displacement and velocity; response to step force, P_i with zero initial conditions; and, response to ramp force, ΔP, with zero initial conditions. ABAQUS adopts the following method [99] to find the constants a_{ij}, b_{ij}, $i, j = 1, 2$ for problems with

damping ratio of less than the critical damping as in this research:

$$
\begin{aligned}
a_{11} &= exp(-\xi\omega\Delta t)\left(\xi\frac{\omega}{\bar{\omega}}\sin\bar{\omega}\Delta t+\cos\bar{\omega}\Delta t\right)\\
a_{12} &= exp(-\xi\omega\Delta t)\frac{1}{\bar{\omega}}\sin\bar{\omega}\Delta t\\
a_{21} &= -exp(-\xi\omega\Delta t)\frac{\omega}{\sqrt{1-\xi^2}}\sin\bar{\omega}\Delta t\\
a_{22} &= exp(-\xi\omega\Delta t)\left(\cos\bar{\omega}\Delta t-\frac{\xi\omega}{\bar{\omega}}\sin\bar{\omega}\Delta t\right)\\
b_{11} &= -exp(-\xi\omega\Delta t)\left\{\left(\frac{\xi}{\omega\bar{\omega}}+\frac{2\xi^2-1}{\omega^2\bar{\omega}\Delta t}\right)\sin\bar{\omega}\Delta t+\left(\frac{1}{\omega^2}+\frac{2\xi}{\omega^3\Delta t}\right)\cos\bar{\omega}\Delta t\right\}+\frac{2\xi}{\omega^3\Delta t}\\
b_{12} &= exp(-\xi\omega\Delta t)\left\{\frac{2\xi^2-1}{\omega^2\bar{\omega}\Delta t}\sin\bar{\omega}\Delta t+\frac{2\xi}{\omega^3\Delta t}\cos\omega\bar{\Delta t}\right\}+\frac{1}{\omega^2}-\frac{2\xi}{\omega^3\Delta t}\\
b_{21} &= -exp(-\xi\omega\Delta t)(\bar{\omega}\cos\bar{\omega}\Delta t-\xi\omega\sin\bar{\omega}\Delta t)\left(\frac{2\xi^2-1}{\omega^2\bar{\omega}\Delta t}+\frac{\xi}{\bar{\omega}\omega}\right)+\\
&\quad exp(-\xi\omega\Delta t)\left(\bar{\omega}\sin\bar{\omega}\Delta t+\xi\omega\cos\bar{\omega}\Delta t\right)\left(\frac{1}{\omega^2}+\frac{2\xi}{\omega^3\Delta t}\right)-\frac{1}{\omega^2\Delta t}\\
b_{22} &= exp(-\xi\omega\Delta t)(\bar{\omega}\cos\bar{\omega}\Delta t-\xi\omega\sin\bar{\omega}\Delta t)\frac{2\xi^2-1}{\bar{\omega}\omega^2\Delta t}-\\
&\quad exp(-\xi\omega\Delta t)(\bar{\omega}\sin\bar{\omega}\Delta t+\xi\omega\cos\bar{\omega}\Delta t)\frac{2\xi}{\omega^3\Delta t}+\frac{1}{\omega^2\Delta t}
\end{aligned}
\tag{4.4}
$$

Comparing the solution with the solution for the equilibrium of eqn (3.61) in chapter 3 shows both methods use the same procedure. Both use the method based on interpolation of excitation, which is a highly efficient numerical procedure for linear systems. As explained in chapter 3 this method finds the solution by interpolating the excitation over each time interval and develops the exact solution to the excitation.

In order to find an accurate representation of the excitation and response, the time interval should not exceed the earthquake time interval. Each mode extracted in the previous frequency step is treated as a SDOF system, for which the response to external loading is derived. The total response is then derived using superposition of the modal responses.

As explained earlier, the time integration is done in terms of amplitude of response in each mode. The response of the variables such as displacement (u), strain (ϵ), stress

(σ), and reaction (R) is then obtainable by summation

$$\begin{aligned} u &= \sum_{\alpha} \phi_\alpha q_\alpha \\ \epsilon &= \sum_{\alpha} \epsilon_\alpha q_\alpha \\ \sigma &= \sum_{\alpha} \sigma_\alpha q_\alpha \\ R &= \sum_{\alpha} R_\alpha q_\alpha \end{aligned} \tag{4.5}$$

where ϕ_α are the modes, ϵ_α are the modal strain amplitudes, σ_α are the modal stress amplitudes, and R_α are the modal reaction force amplitudes corresponding to each eigenvector α. The displacement, u, is equivalent to eqn (3.1) for the case of displacements in axial, circumferential and radial directions.

4.4.2 Earthquake excitation

In ABAQUS the earthquake excitation can be applied to the supports using the facility of the *BASE MOTION command. Base motion can be defined as displacement, velocity, or acceleration. However, in all these cases the input is converted into an acceleration time history. Because in this study a constant vertical component of earthquake is applied along all four edges of the shell, it can be considered as a distributed surface loading in the vertical direction. The distributed load, equal to $\rho \times h \times a_g$, where ρ is the density, h thickness, and a_g ground acceleration time history is applied as a surface load.

In ABAQUS $\rho \times h$ is introduced using the *DSLOAD command which is then multiplied by the ground acceleration time history defined using the *AMPLITUDE command.

4.4.3 Validation of predictions

The comparison of the 10 lowest frequencies of the shell in section 3.2.2 showed an excellent agreement between the FE and analytical methods. This section provides a comparison study for the displacement, acceleration, and stress responses of shells under earthquake loading when using the FE and analytical methods.

The agreement between the results using the FE and analytical methods gives confi-

dence in the use of either method to investigate the behaviour of shells under earthquake. It gives confidence in the convenient use of analytical method for simple examples like cylindrical shells with simply support boundary conditions to answer issues of practical importance such as those discussed in chapter 3. While it also gives confidence in the use of FE to investigate the response of shells for more complicated problems such as a more complicated boundary condition.

For this purpose the displacement and acceleration response of the shell having the geometry and material properties as in section 4.3.1, with natural frequencies summarized in Fig 3.4, undergoing the vertical component of Landers earthquake loading (Fig 3.10) have been derived using the analytical solution and compared with the results of a FE analysis. This comparison involved the use of the lowest 10 modes for both the analytical and FE method. While these limited numbers of modes are adequate to compare alternative methods, it should be noted that the results are not fully converged.

Both the analytical and FE methods are solved using the time history modal analysis. For convenience and in the absence of more precise estimation of damping, a constant damping ratio equivalent to 0.05 is considered for each mode. Maximum absolute displacement and acceleration responses of the shell over the earthquake duration are plotted in Fig 4.5 along the center-lines aa and bb (Fig 3.1). The comparison shows that FE and analytical results summarized in Fig 4.5 are in excellent agreement for the case of displacement and acceleration.

The comparison continues by comparing maximum absolute stress resultants over the time history of the earthquake plotted along the center-line bb as shown in Fig 4.6. The excellent agreement between the FE and analytical stress resultant gives confidence in use of either method for investigation on dynamic responses of cylindrical roof shell under earthquake loading.

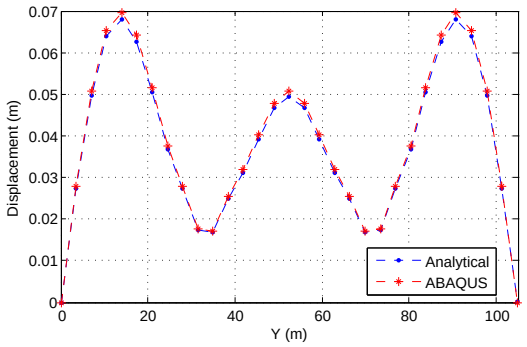

(a) Radial displacement-line bb

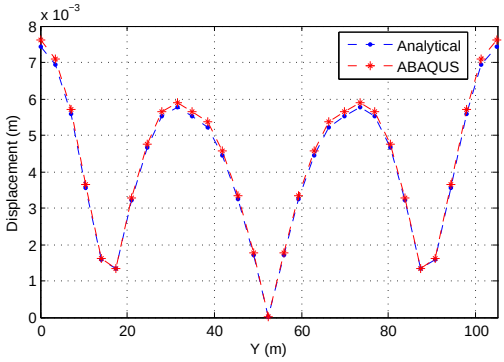

(b) Circumferential displacement-line bb

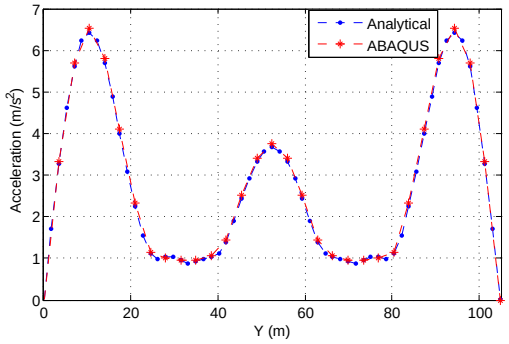

(c) Radial acceleration-line bb

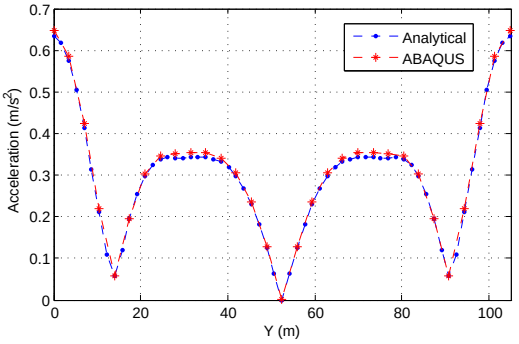

(d) Circumferential acceleration-line bb

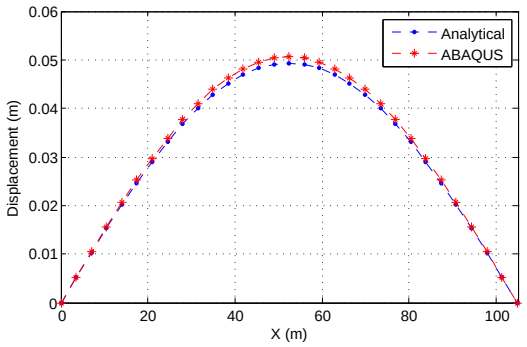

(e) Radial displacement-line aa

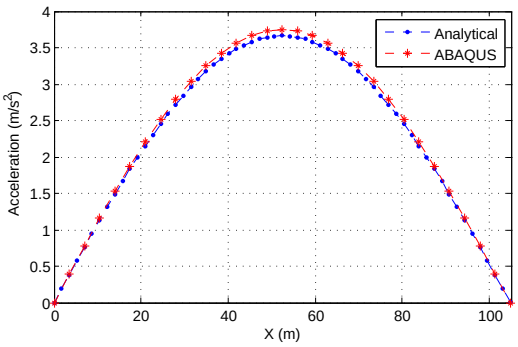

(f) Radial acceleration-line aa

Figure 4.5: Maximum absolute displacement and acceleration over the whole earthquake duration

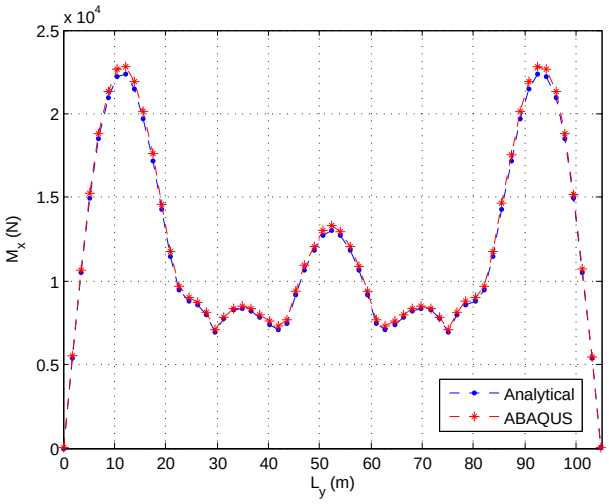

(a) M_x

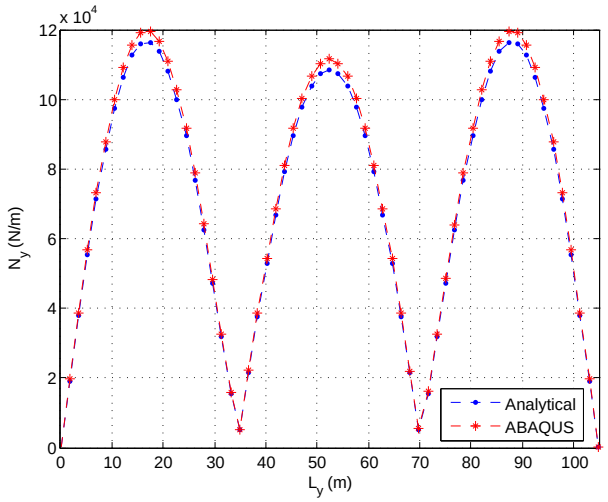

(b) N_y

Figure 4.6: Maximum absolute stress along line (bb) over the whole earthquake duration

4.5 Response convergence with mode numbers

Of practical importance are the numbers of modes required for accurate prediction of displacement, acceleration, stress, etc., for a specific geometry of shell. Fig 4.7 summarises the results of a study in which the predictions are plotted against the numbers of modes included in the analysis. Modes are included in rank order, starting from that of the lowest frequency. Shell geometry is again chosen as that adopted in section 4.3.1 with the natural frequency as summarized in Fig 3.4.

Using the convergence with mesh number study of frequencies in 4.3.2, a 60 by 60 mesh is considered for this study. Displacement and acceleration results appear to have converged when 20 modes are included. But as can be seen from Fig 4.7(a),(b) there is a jump in the displacement response when mode 25 is included, then showing no real change for increasing numbers of included modes. The reason for this jump is that mode 25 corresponds with mode $(i, j) = (1, 1)$ as in Fig 3.4, which has the highest contribution of modal force. Bending stresses, on the other hand, show different convergence behaviour, only converging after including about 300 modes (Fig 4.7(c),(d)). In order to explain the reason for requiring such a large number of modes in the analysis of stresses, the ratio of participating mass to the total effective mass of the structure is plotted against the number of modes in Fig 4.8 and compared with the requirement of Uniform Building Code (UBC), 1997 [100] and Eurocode 8 [101].

The UBC requires the number of modes in the modal analysis to be selected such that their participating mass is at least 90% of the total effective mass [100], [101]. Eurocode 8 demands either the participation of mass to be 90% of the total effective mass or inclusion of every mode with effective masses greater than 5% of the total mass. Although in the present case the participating mass reaches 90% of the total effective mass of the shell after 98 modes, as shown in Fig 4.8, and hence satisfies the requirement of the UBC and Eurocode 8, it is evident from Fig 4.7(c),(d) that this requirement may not be sufficient to ensure convergence of stresses. In the UBC code there is no mention of the participation of mass in the vertical direction for the case of the vertical loading. As is demonstrated in chapter 3, the vertical component of earthquakes is quite important in the response of roof shells. For this reason the UBC

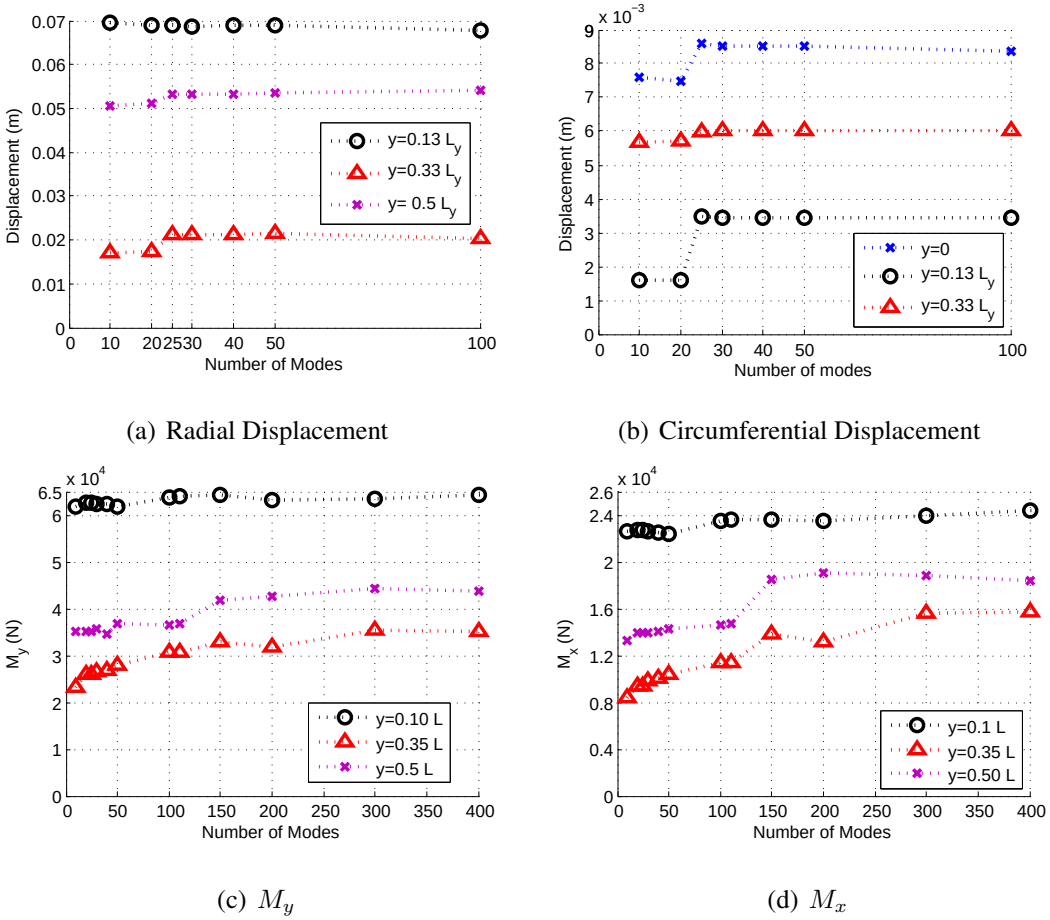

(a) Radial Displacement

(b) Circumferential Displacement

(c) M_y

(d) M_x

Figure 4.7: Convergence study of selected points along line b-b

code requirement should not be generalized to cover the case of shell roofs subject to the vertical components of earthquakes. Moreover, the slow rates of convergence of stresses, suggest that a similar analysis should be performed for the horizontal component of earthquakes.

The further reason for the jump in Fig 4.7(c),(d) is investigated through a detailed study on the importance of each mode in the response in section 3.8. It is suggestive that the consideration of 90% of effective mass is not enough for a converged result of cylindrical roof shell subjected to earthquake. However, as it can be seen in Fig 4.7(c),(d), the requirements of UBC and Eurocode 8 based on considering 98 modes for this case is satisfied for the maximum stress at $y = 0.1\ L$. Although it is not sufficient for the convergence of maximum stress at other locations such as $0.35\ L$ and $0.5\ L$. It can be concluded that if only the maximum response over the entire surface of shell is of interest, then the code requirements seem sufficient to accurately capture the converged

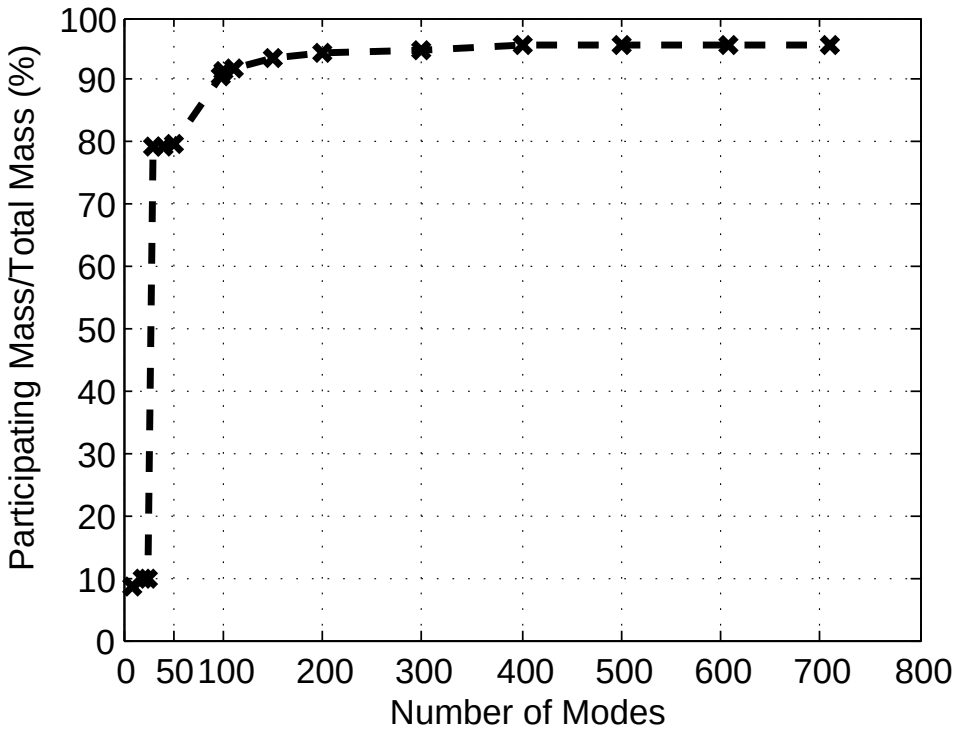

Figure 4.8: Ratio of participating mass to the total mass of the shell

result. This would be appropriate if the whole surface of shell is to be designed for a maximum response equivalent to the one at $0.1\ L$ for the case of this example.

However, if an optimal design, is based on the maximum stress responses at all locations of the shell surface, then it should be noted that the requirement of UBC and Eurocode 8 may no loner be sufficient. This is evident in that it is not sufficient to accurately capture the converged results for $0.35\ L$, and $0.5\ L$ in Fig 4.7(c),(d). It is then advisable to perform a complete convergence study to adequately include the participating modes in the response.

It should be noted that the above explanation is based on one shell with specific geometry. However, in order to confidently comment on the adequacy of the requirement of the code for the maximum response over the entire surface of shell a study for shells with different geometry and material properties should be performed.

Chapter 5

Effect of Pre-loading on the Dynamic Response of Cylindrical Shell Roof

5.1 Modelling effects of pre-loading

The total energy of a cylindrical roof shell of length L, radius R, thickness h, and open angle ϕ is derived in section 2.4.2 eqn (2.23). If the self weight and additional loading due to roof covering and snow loading is taken into account the potential energy due to pre-loading, $-\int_0^L \int_0^\phi PW \mathrm{d}R\theta \, \mathrm{d}x$, would be added to eqn (2.23).

Also the fundamental strains, stresses, and displacements may no longer be zero. The total energy is defined in terms of the fundamental and incremental states. As mentioned in section 2.4.2 the total displacement is presented in terms of the incremental displacements (u, v, w) about a fundamental displacement state (U^F, V^F, W^F) (eqn (2.25)).

For the purpose of this study it will be convenient to break the incremental membrane strains into their components that are linear $(\epsilon'_x, \epsilon'_\theta, \epsilon'_{x\theta})$, and quadratic $(\epsilon''_x, \epsilon''_\theta, \epsilon''_{x\theta})$ in terms of the incremental displacements as well as the associated membrane stresses $(n'_x, n'_\theta, n'_{x\theta})$ and $(n''_x, n''_\theta, n''_{x\theta})$ [102] derived from linear and quadratic strains. The total energy can now be expanded into terms that are independent, V_0, linear, V_1, and quadratic V_2 with respect to the incremental displacements, so that

$$V = V_0 + V_1 + V_2 \tag{5.1}$$

For the case of a roof shell subject to a uniform pressure loading and assumed to develop a pure membrane fundamental state, so that $N_x^F = 0$ and $N_{x\theta}^F = 0$, while N_θ^F, E_θ^F, E_x^F are non zero. The various energy components take the form

$$\begin{aligned}
V_0 &= \frac{1}{2}\int_0^L\int_0^\phi [N_\theta^F E_\theta^F] R\,\mathrm{d}\theta\,\mathrm{d}x + \int_0^L\int_0^\phi PW^F R\,\mathrm{d}\theta\,\mathrm{d}x \\
V_1 &= \frac{1}{2}\int_0^L\int_0^\phi [(N_\theta^F \epsilon'_\theta + n'_\theta E_\theta^F) + n'_x E_x^F] R\,\mathrm{d}\theta\,\mathrm{d}x + R\int_0^L\int_0^\phi Pw\mathrm{d}\theta\,\mathrm{d}x \\
V_2 &= \frac{1}{2}\int_0^L\int_0^\phi [m'_x\chi'_x + m'_\theta\chi'_\theta + 2m'_{x\theta}\chi'_{x\theta}] R\,\mathrm{d}\theta\,\mathrm{d}x + \\
&\quad \frac{1}{2}\int_0^L\int_0^\phi [n'_x\epsilon'_x + n'_\theta\epsilon'_\theta + 2n'_{x\theta}\epsilon'_{x\theta}] R\,\mathrm{d}\theta\,\mathrm{d}x \\
&\quad + \frac{1}{2}\int_0^L\int_0^\phi [(N_\theta^F\epsilon''_\theta + n''_\theta E_\theta^F) + (n''_x E_x^F)] R\,\mathrm{d}\theta\,\mathrm{d}x
\end{aligned} \tag{5.2}$$

Of present interest is the inclusion of components which have not been considered in the governing potential energy in chapter 2. In order to avoid overly repetitive calculations, only the additional integrals will be presented. The results will be subsequently added to eqn (2.23). In eqn (5.3) the first additional integral is related to the fundamental stress and strain in V_0, the second, third, and forth integrals represent the linear membrane stresses. The fifth integral depends upon the quadratic membrane strain displacement relations which should be seen as part of the non-linear membrane strain energy.

$$\begin{aligned}
V_{additional} &= \frac{1}{2}\int_0^L\int_0^\phi [N_\theta^F E_\theta^F] R\,\mathrm{d}\theta\,\mathrm{d}x + \int_0^L\int_0^\phi PW^F R\,\mathrm{d}\theta\,\mathrm{d}x \\
&\quad + \frac{1}{2}\int_0^L\int_0^\phi [(N_\theta^F \epsilon'_\theta + n'_\theta E_\theta^F) + n'_x E_x^F] R\,\mathrm{d}\theta\,\mathrm{d}x + \int_0^L\int_0^\phi PwR\mathrm{d}\theta\,\mathrm{d}x \\
&\quad + \frac{1}{2}\int_0^L\int_0^\phi [(N_\theta^F \epsilon''_\theta + n''_\theta E_\theta^F) + (n''_x E_x^F)] R\,\mathrm{d}\theta\,\mathrm{d}x
\end{aligned} \tag{5.3}$$

The full quadratic components of the strain-displacement relation

$$\begin{aligned}
\epsilon''_x &= \frac{1}{2}[(\frac{\partial v}{\partial x})^2 + (\frac{\partial w}{\partial x})^2] \\
\epsilon''_y &= \frac{1}{2}[(\frac{\partial u}{\partial y})^2 + (\frac{\partial w}{\partial y} + \frac{v}{R})^2]
\end{aligned} \tag{5.4}$$

will be approximated by the Donnell assumptions

$$\begin{aligned}
\epsilon''_x &= \frac{1}{2}[(\frac{\partial w}{\partial x})^2] \\
\epsilon''_y &= \frac{1}{2}[(\frac{\partial w}{\partial y})^2]
\end{aligned} \tag{5.5}$$

with the relevant quadratic stress components given by

$$\begin{aligned} n''_x &= K(\epsilon''_x + \nu\epsilon''_y) \\ n''_y &= K(\epsilon''_y + \nu\epsilon''_x) \end{aligned} \tag{5.6}$$

For the current pure pressure loading case

$$\begin{aligned} N^F_\theta &= -PR \\ N^F_x &= 0 \\ N^F_{x\theta} &= 0 \\ E^F_\theta &= \frac{1}{Eh} n^F_\theta = -\frac{PR}{Eh} \\ E^F_x &= \frac{1}{Eh}(-\nu n^F_\theta) = \frac{\nu PR}{Eh} \end{aligned} \tag{5.7}$$

where $P = P_s + P_w$ in which P_w is the wind loading, $P_s = P_{s1} + P_{s2}$ is the combination of self weight P_{s1}, and roof covering or snow loading P_{s2}. For a shallow shell P is accurately approximated to be applied in radial direction. Only the snow load and additional self weight load will have associated proportional mass. Eqn (5.5), (5.6), and loading condition eqn (5.7) when substituted into eqn (5.3) provides the additional strain energy terms.

The kinetic energy of eqn (2.27), only due to self-weight, can now be augmented to include the kinetic energy due to additional loading. The kinetic energy can now be written as the summation of the kinetic energies due to self-weight and additional loading.

$$T = \frac{1}{2}\frac{P_{s1}}{g}\int_0^L\int_0^\phi [\dot{u}^2+\dot{v}^2+\dot{w}^2]R\mathrm{d}\theta\ \mathrm{d}x + \underbrace{\frac{1}{2}\frac{P_{s2}}{g}\int_0^L\int_0^\phi [\dot{u}^2+\dot{v}^2+\dot{w}^2]R\,\mathrm{d}\theta\ \mathrm{d}x}_{T_{additional}} \tag{5.8}$$

The second integral, $T_{additional}$, in eqn (5.8) presents the kinetic energy due to the additional loading.

Substituting the additional strain and kinetic energy terms in the Lagrange equation of $L = V - T$, and then substituting L into the Euler-Lagrange eqn (2.21) leads to derivation of the additional terms $\frac{P_{s2}(1-\nu^2)}{E\,h\,g}\frac{\partial^2 w}{\partial t^2} + PR\frac{\partial^2 w}{\partial y^2}$ in the third equation of equilibrium

(2.28) in chapter 2, to give

$$K(\frac{\nu}{R}\frac{\partial u}{\partial x}+\frac{1}{R}\frac{\partial v}{\partial y}+\frac{w}{R^2})+D(\nabla^4 w+\frac{\nu-2}{R}\frac{\partial^3 v}{\partial x^2\partial y}-\frac{1}{R}\frac{\partial^3 v}{\partial y^3})+$$
$$(\frac{P_{s1}+P_{s2}}{g})\frac{\partial^2 w}{\partial t^2}+PR\frac{\partial^2 w}{\partial y^2}=0 \tag{5.9}$$

While, the first and second equation of equilibrium remain unchanged, only Γ_{33} of eqn (2.30) in the eigenvalue eqn of (2.18) will be affected to become

$$\Gamma_{33}=\frac{1}{R^2}+\frac{h^2}{12}(\frac{\partial^2}{\partial x^2}+\frac{\partial^2}{\partial y^2})^2+\frac{\frac{P_{s1}}{g}(1-\nu^2)}{Eh}\frac{\partial^2}{\partial t^2}+\underbrace{\frac{\frac{P_{s2}}{g}(1-\nu^2)}{Eh}\frac{\partial^2}{\partial t^2}+PR\frac{1-\nu^2}{Eh}\frac{\partial^2}{\partial y^2}}_{\text{additional term}} \tag{5.10}$$

Likewise in eqn (3.4), (3.5) only the stiffness terms, k_{33}, will be changed to

$$k_{33}=1+\beta(\lambda^2+(i\frac{i\pi}{\phi})^2)^2-\underbrace{\frac{PR(1-\nu^2)}{Eh}(\frac{i\pi}{\phi})^2}_{\text{additional term}}-\Delta_{ij} \tag{5.11}$$

in which

$$\Delta_{ij}=\frac{(\frac{P_{s1}}{g})(1-\nu^2)R^2}{Eh}(\omega_{ij})^2+\overbrace{\frac{(\frac{P_{s2}}{g})(1-\nu^2)R^2}{Eh}(\omega_{ij})^2}^{\text{additional term}} \tag{5.12}$$

$$\Delta_{ij}=\frac{(\rho h+\overbrace{\frac{P_{s2}}{g}}^{\text{additional term}})(1-\nu^2)R^2}{Eh}(\omega_{ij})^2 \tag{5.13}$$

The most significant changes in the eigenvalue problem comparing eqn (5.11) (including the effect of pre-loading) and eqn (3.4) and (3.5) (ignoring the effect of additional loading) can be summarised as:

- The additional added mass in Δ due to the imposed load P_{s2}
- Change in the stiffness term k_{33} with $-\frac{PR(1-\nu^2)}{Eh}(\frac{i\pi}{\phi})^2$ due to the pre-loading, P, which is the sum of self-weight, P_{s1}, snow, P_{s2}, and wind loading, P_w. However, in this research the effect of wind loading has not been considered.

Considering k_{33} in eqn (5.11) as a result of including pre-loading in eqn (3.4) and neglecting the in-plane inertia terms (eqn (3.4)) would represent a linear eigenvalue problem in which

$$\frac{PR(1-\nu^2)}{Eh}(\frac{i\pi}{\Phi})^2+\Delta_{ij}=C_{ij} \tag{5.14}$$

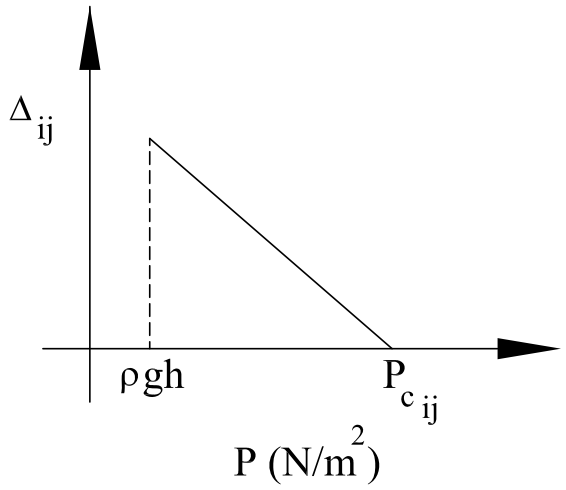

Figure 5.1: Relationship between P and Δ

where C_{ij} would be constant for a given mode.
Eqn (5.14) shows that there is a linear relation between Δ and P. An increase in P would result in a decrease in Δ as shown in Fig 5.1 for a typical mode.

As shown in section 3.2.4 the inclusion of in-plane inertia in the eigenvalue problem eqn (3.4) does not significantly change the resulting out-of-plane frequency. So eqn (5.14) gives a relatively good approximation of the out-of-plane frequencies. However, it should be noted that the numerical results of section 5.4 (Fig 5.6, 5.8, 5.10) are based upon the inclusion of in-plane inertia, which also confirms the linear relationship between Δ and preloading P. On the other hand eqn (5.14) indicates a nonlinear relation between ω^2 and P taking the form

$$\omega_{ij}^2 = \frac{C_{ij}Ehg}{P(1-\nu^2)R^2} - \frac{g}{R}(i\pi/\Phi)^2 \tag{5.15}$$

This nonlinear relationship is shown in Fig 5.2 for a typical mode for the cases where the self-weight is included. In section 5.4 the resulting frequency based on the neglect of self-weight is also reported, for which C_{ij} would be derived by neglecting the additional term in k_{33} in eqn (5.11). This is done to compare the resulting frequencies based on neglecting the pre-loading with the ones derived based on including the pre-loading in the analysis.

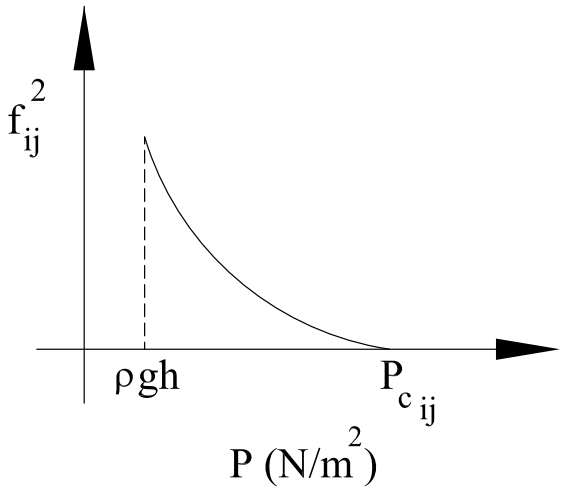

Figure 5.2: Relationship between P and f^2

5.2 Comparison between self-weight and critical buckling load

The governing displacement, acceleration, and stresses responses of the cylindrical shell in chapter 3 may no longer be valid when the pre-loading is taken into account as it will not satisfy one of the basic requirement of stability, where the self-weight should remain less than the buckling load. The classical critical load in mode (i, j) can be derived from the eigenvalue eqn (3.4) with k_{33} given by eqn (5.11) and the assumption that ω_{ij} and hence Δ_{ij} reaches to zero at the buckling load. Eqn (5.14) indicates this occurring when

$$P_{ij_c} = \frac{Eh}{R(1-\nu^2)} C_{ij} \tag{5.16}$$

It should be noted that the term "buckling load" used here refers to the lowest classical critical load which means there is no allowance for imperfection sensitivity.

It is worth mentioning that the displacements, accelerations and non-dimensionalised stresses derived in chapter 3 remain unchanged for varying values of R, h, ρ, and E as long as the ratio $B = \rho h R/E$ is constant. However, when pre-loading is included, the density and modulus of elasticity affects the stiffness term k_{33} in eqn (5.11). So the resulting natural frequencies depend on the values of ρ, and E rather than just their

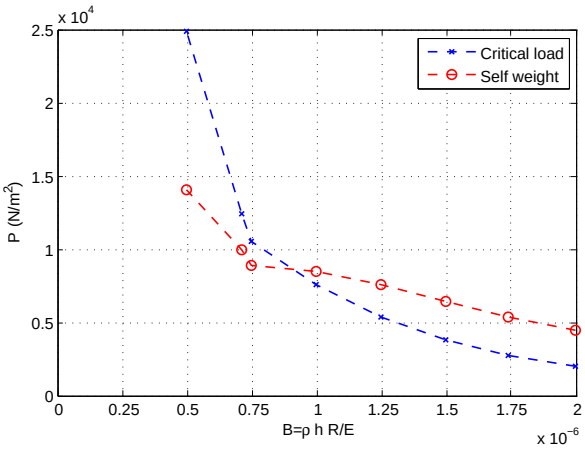

(a) $L_y/L_x = 0.5$

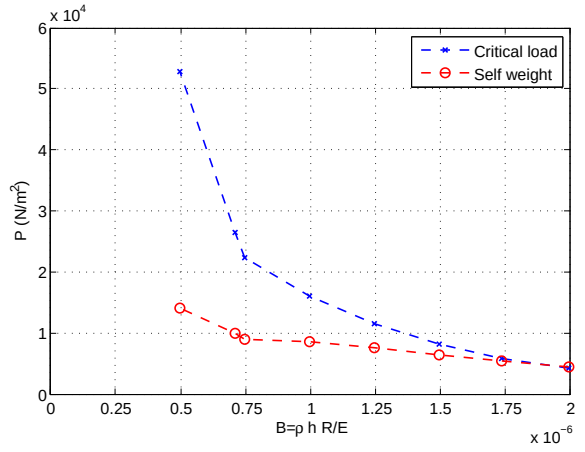

(b) $L_y/L_x = 1$

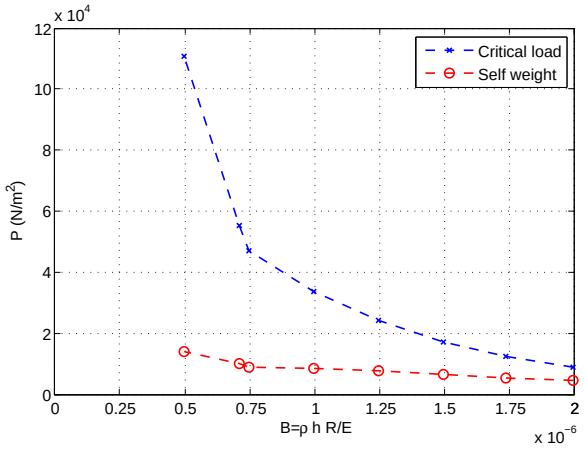

(c) $L_y/L_x = 2$

Figure 5.3: Critical load and self-weight verses the non dimensional parameter $B = \rho h R/E\ s^2$, for shells having $\Phi = \pi/3$, $R = 104.8\ m$, $h = R/500$ and various L_y/L_x

ratio. This means the results would no longer remain unchanged for a constant ratio of $B = \rho hR/E$ but having different values of R, h, ρ, and E. However in order to be consistent and for the comparison of the results with those in chapter 3, the values of R, h, ρ, and E are considered to be the same as those in chapter 3.

Fig 5.3 summarises the buckling loads and the self-weight for the cases of the shells considered in chapter 3. This provides the first step in identifying instability of the roof under its self-weight. The variation of geometry is considered in the ratio of $\frac{L_y}{L_x}$ while the variations of material density and modulus of elasticity are contained within parameter B ($\equiv \rho hR/E$). For each ratio of $\frac{L_y}{L_x}$, the variation of parameter B depends on the values of R, h, ρ and E, for which in this study $R = 104.8\ m$, and $h = R/500$ are considered constant for all cases, while the value of ρ and E are changed from the case of $B = 0.5 \times 10^{-6}\ s^2$ with $E = 30 \times 10^{10}\ N/m^2$ and $\rho = 6840kg/m^2$ to a concrete shell of $B = 2 \times 10^{-6}\ s^2$ with $E = 24 \times 10^9\ N/m^2$ and $\rho = 2184kg/m^2$. The cases in between represent non-specific materials, for which their ratios of density to modulus of elasticity satisfy the required value of parameter B. With the assumptions of a fixed radius and thickness, an increase in B implies the decrease in modulus of elasticity is greater than the decrease in density. Also, an increase in the L_y/L_x ratio in Fig 5.3 implies a decrease in L_x.

Fig 5.3 shows for some cases, the self-weight is greater than the buckling load; so the structure does not resist its own weight without buckling. This situation occurs for example when $L_y/L_x = 1$, with $B > 1.75 \times 10^{-6}\ s^2$ in Fig 5.3(b) or $L_y/L_x = 0.5$, with $B > 0.75 \times 10^{-6}\ s^2$ in Fig 5.3(a). This means the results in chapter 3 and 4 are of no practical interest for these cases. However, the presented displacement and stresses results are valid for other ratios of $\frac{L_y}{L_x}$, and B as the buckling load is higher than the self-weight.

The comparison between self-weight and critical buckling load is then repeated for concrete shells with constant ratios of $\frac{L_y}{L_x}$, $\frac{R}{h}$, and various radius of curvature. These examples help to better understand the effect of radius, and ratios of $\frac{L_y}{L_x}$ for a shell with constant material property.

As can be seen from Fig 5.4 a shell with constant opening angle would achieve higher

buckling loads and remain stable for higher values of radius for larger ratios of $\frac{L_y}{L_x}$. It is shown that self-weight remains less than buckling load for radius less than $R = 180\ m$ for $\frac{L_y}{L_x}$=2, $R = 90\ m$ for $\frac{L_y}{L_x}$=1, and finally $R = 45\ m$ for $\frac{L_y}{L_x} = 0.5$.

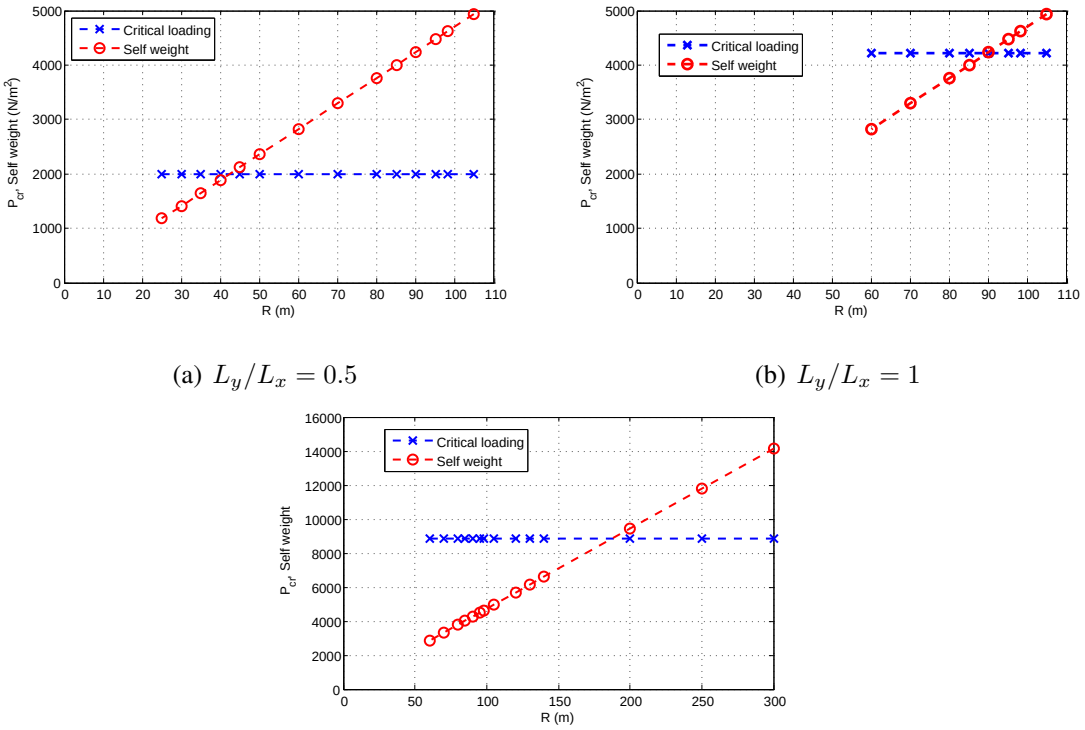

(a) $L_y/L_x = 0.5$

(b) $L_y/L_x = 1$

(c) $L_y/L_x = 2$

Figure 5.4: Critical load for a concrete shell having $R/h = 500$, $E = 2.4 \times 10^{10}\ N/m^2$, $\rho = 2184\ kg/m^3$ compared with self-weight for concrete shells having varying radius of curvature

As it can be seen from eqns (5.9)-(5.12) the inclusion of self-weight would change the frequency extraction equation and consequently will change the resulting natural frequencies of the shell. It is expected that including self-weight in calculating the natural frequencies would influence the displacement, acceleration and stress responses. However, the rates of change would be greatly influenced by the relationships between the displacement and acceleration spectra of the earthquake and the natural frequencies of the shell. As it can be seen from Fig 5.3 the difference between the self-weight and buckling load is dependent upon the ratios of B. It is expected that as the buckling load becomes closer to the self weight, the responses to earthquake would be affected more significantly.

In order to examine the significance of self-weight in the frequency responses, the next section derives the changes of the frequencies for the case where self-weight is included in the eigenvalue problem and compares these with those where it is neglected. Shells are selected for which the self-weight is less than the critical loading.

5.3 Effect of self weight on natural frequencies

According to eqn (5.15) there is a nonlinear relationship between pre-loading and resulting frequency. As the pre-loading increases, the resulting frequency decreases. However, the rate of decrease is different in various modes as C_{ij} has different values for different modes. Also it is expected that the ratio of pre-loading to the buckling load would influence the results; this too differs for different modes. To examine the changes in natural frequencies due to including self-weight a number of examples of shells with different ratios of self-weight to buckling load are chosen in Fig 5.3.

The frequencies are first derived for a shell having $L_y/L_x = 2,\ B = 0.5 \times 10^{-6}\ s^2$ (Fig5.3(c)). This shell has the highest difference between buckling load and self-weight ($\approx \frac{P_{s1}}{P_{cr}} = \frac{1.404}{11.09} = 12\%$) among other shells in Fig 5.3. Table 5.1 summarises selected frequencies for the case of neglecting the self-weight and those for which self-weight is included, along with the errors in neglecting self-weight compared with those taking self-weight into account. The insignificant errors with a maximum of 7.02% corresponding to mode $(i, j) = (6, 1)$ shows that when the level of buckling load is much higher than the self-weight the difference between the governing frequencies are not noticeable.

It is also noticed that the maximum error does not correspond to the minimum frequency for the case of this shell. Neglecting self-weight in mode $(i, j) = (5, 1)$ having the natural frequency of $f = 2.19\ Hz$ produces slightly less error (6.04%) in comparison with 7.02% error in mode $(i, j) = (6, 1)$ having natural frequency equal to $2.45\ Hz$. However, it will be shown in section 5.4 that mode $(i, j) = (6, 1)$ is associated with the lowest critical load. This shows that although there is normally a relationship between the modes of lowest critical load and lowest frequencies, sometimes they do differ slightly, as for the case of the shell in this example.

	Shell								
	Including self-weight			Neglecting self-weight			error %		
i	$j=1$	$j=2$	$j=3$	$j=1$	$j=2$	$j=3$	$j=1$	$j=2$	$j=3$
1	8.1254	9.5574	10.051	8.1241	9.5563	10.05	0.02	0.01	0.01
2	5.2299	8.2553	9.429	5.2219	8.2501	9.4245	0.15	0.06	0.05
3	3.3533	6.785	8.5989	3.3249	6.7709	8.5878	0.85	0.21	0.13
4	2.4222	5.5557	7.7631	2.3512	5.525	7.7411	3.019	0.56	0.28
5	2.1903	4.7439	7.0864	2.0656	4.6875	7.0488	6.04	1.20	0.53
6	2.4567	4.3994	6.6783	2.2956	4.3115	6.6207	**7.02**	2.04	0.87
7	3.0284	4.4957	6.5926	2.851	4.3782	6.513	6.22	2.68	1.22
8	3.7907	4.9516	6.8322	3.6064	4.812	6.7317	5.11	2.90	1.49
9	4.6952	5.6755	7.3639	4.5077	5.5214	7.2458	4.15	2.79	1.63
10	5.7231	6.5998	8.1406	5.5338	6.4363	8.0086	3.42	2.54	1.65

Table 5.1: Natural frequencies, $f(Hz)$, for a shell with $R = 104.8m$, $L_y/L_x = 2$, $\Phi = \pi/3$, $h = R/500$, $B = \rho hR/E = 0.5\times10^{-6}\ s^2$, $\rho = 6840kg/m^3$, $E = 30\times10^{10}N/m^2$

In another attempt to better understand the effect of self-weight on natural frequency, another shell having $B = 1.25 \times 10^{-6}\ s^2$, $L_y/L_x = 1$ (5.3(b)) is chosen. The proportion of the self-weight to the buckling load is equal to $\frac{P_{s1}}{P_{cr}} = \frac{7593}{11440} = 66.3\%$, which is much higher than the previous example. The resulting natural frequencies in Table 5.2 shows a high percentage of error with a maximum of 72.5% associated with mode $(i, j) = (4, 1)$ having the lowest frequency.

In a final example the natural frequencies are derived for a shell having $L_y/L_x = 1$, $B = 1.5 \times 10^{-6}\ s^2$ (Fig 5.3(b)). In this example self-weight is close to the buckling load with a ratio of 80% ($\frac{P_{s1}}{P_{cr}} = \frac{6452}{8093} = 80\%$).

As it can be seen in Table 5.3 ignoring self-weight in the calculation of natural frequencies results in very high errors in the governing natural frequencies up to 122.1% for $(i, j) = (4, 1)$ which has the minimun frequency and minimum classical critical load.

Between the three cases of shells discussed in this section, the one having the lowest difference between the values of self-weight and critical classical buckling load

	Shell								
	Including self-weight			Neglecting self-weight			error %		
i	$j=1$	$j=2$	$j=3$	$j=1$	$j=2$	$j=3$	$j=1$	$j=2$	$j=3$
1	3.210	5.150	5.780	3.210	5.150	5.780	0.1	0	0
2	1.360	3.310	4.540	1.330	3.300	4.530	2.3	0.4	0.2
3	0.770	2.120	3.380	0.630	2.080	3.350	21.3	2.2	0.8
4	0.710	1.530	2.580	0.410	1.420	2.510	**72.5**	8.1	2.6
5	0.940	1.390	2.160	0.590	1.180	2.040	58.7	17.5	6.2
6	1.290	1.560	2.090	0.950	1.290	1.900	35.6	20.9	10.1
7	1.740	1.920	2.300	1.410	1.620	2.060	23.6	18.1	11.6
8	2.260	2.400	2.690	1.930	2.100	2.430	16.9	14.4	11
9	2.840	2.970	3.220	2.520	2.670	2.940	12.7	11.5	9.5
10	3.500	3.630	3.850	3.180	3.320	3.560	10	9.2	8.1

Table 5.2: Natural frequencies, $f(Hz)$, for a shell with $R = 104.8\ m$, $L_y/L_x = 1$, $\Phi = \pi/3$, $h = R/500$, $B = \rho hR/E = 1.25 \times 10^{-6}$, $\rho = 3692\ kg/m^3$, $E = 65 \times 10^9\ N/m^2$

($L_y/L_x = 1$, $B = 1.5 \times 10^{-6}\ s^2$, Fig 5.3(b)) introduces the highest error in frequency by neglecting self-weight. It is again noticed that the highest error does not necessarily correspond to the mode with lowest frequency.

Although the highest errors in Tables 5.2 and 5.3, correspond to the mode having the lowest frequency, the highest error does not correspond to the lowest frequency for the shell in Table 5.1. Furthermore, the results in Tables 5.1 to 5.3 show that some modes are more affected by the inclusion of the self-weight in the frequency extraction equation than the others.

So further investigation is needed to answer questions such as:

- In which modes do the lowest buckling loads occur and especially the lowest (classical) critical load?

- Is the mode having the lowest frequency, the same as that corresponding to the critical classical buckling load?

	Shell								
	Including self-weight			Neglecting self-weight			error %		
i	$j=1$	$j=2$	$j=3$	$j=1$	$j=2$	$j=3$	$j=1$	$j=2$	$j=3$
1	2.932	4.698	5.277	2.928	4.696	5.275	0.1	0.0	0.0
2	1.242	3.024	4.142	1.208	3.010	4.132	2.8	0.5	0.2
3	0.701	1.939	3.086	0.550	1.889	3.055	27.5	2.6	1.0
4	0.652	1.401	2.356	0.294	1.274	2.282	**122.1**	9.9	3.2
5	0.856	1.266	1.975	0.450	1.036	1.836	90.4	22.3	7.6
6	1.182	1.420	1.911	0.794	1.119	1.699	48.8	26.9	12.5
7	1.586	1.751	2.098	1.214	1.422	1.832	30.7	23.1	14.5
8	2.058	2.192	2.459	1.695	1.855	2.164	21.4	18.2	13.6
9	2.596	2.715	2.940	2.239	2.376	2.630	15.9	14.3	11.8
10	3.197	3.309	3.512	2.844	2.970	3.195	12.4	11.4	9.9

Table 5.3: Natural frequencies, $f(Hz)$, for a shell with $R = 104.8\ m$, $L_y/L_x = 1$, $\Phi = \pi/3$, $h = R/500$, $B = \rho hR/E = 1.5 \times 10^{-6}\ s^2$, $\rho = 3137.2\ kg/m^3$, $E = 46 \times 10^9\ N/m^2$

- Does the mode having the lowest classical critical load show the greatest variation in frequency?

- How are the modes other than the ones corresponding to the minimum frequency or the classical buckling load affected by the inclusion of self-weight?

These questions will be addressed in section 5.4. Finally Fig 5.5 summarises the changes in minimum frequency through the addition of self-weight in the analysis for all cases of the shells in Fig 5.3. As discussed earlier it might be noted that modes having the minimum frequency are not necessarily the modes exhibiting the maximum variation when the effects of self-weight are included in the governing equation for frequency.

As it can be seen in Fig 5.5 for the cases where the critical buckling loads are much higher than the shell self-weight, the inclusion of self-weight in the analysis does

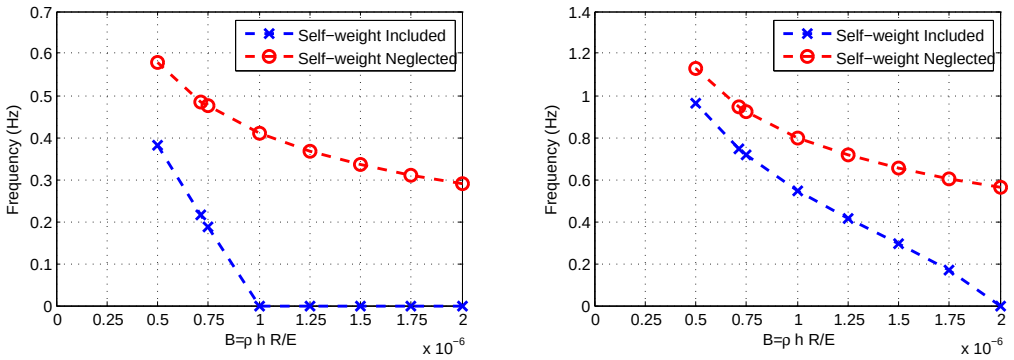

(a) $L_y/L_x = 0.5$ (b) $L_y/L_x = 1$

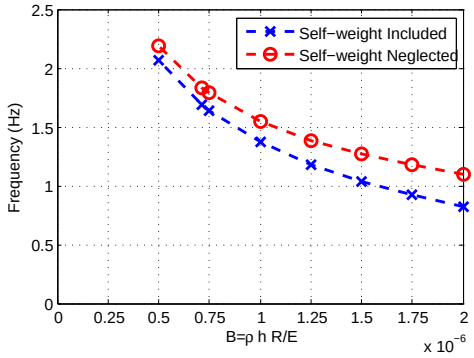

(c) $L_y/L_x = 2$

Figure 5.5: Comparisons between the minimum natural frequency with and without self-weight, for $R/h = 500$

not greatly changes the resulting frequencies such as the shell with $L_y/L_x = 2$, $B = 0.5 \times 10^{-6}\ s^2$. However, for the cases where the critical loads are close to the self-weight, the changes in frequency are high. For shells where the natural frequencies do not change significantly, it is then safe to find the dynamic responses without including the self-weight in the determination of the natural frequencies.

The comparison of the frequency results between FE method in chapter 4 and analytical method in chapter 3, in situations where the effects of self-weight are ignored in calculation of the natural frequencies, showed the results were effectively identical. This implies that the linear modal analysis option in FE programmes has been formulated on the basis of ignoring the self-weight in calculating the natural frequencies of the shell unless the operator choose to include the pre-loading in calculation. Although it would not appear to be normal practice [7] it will be explained in section 7 how the effects of pre-stressed loading might be incorporated in FE modelling.

While the inclusion of self-weight in the analysis might have little effect on the resulting natural frequency, displacements, and stresses in ordinary buildings or shells with small or medium length and radius, it could change the results substantially in large, slender, roof shells. However, a detailed geometric study for shells with constant material properties should usefully be performed to define the range of radius, length, and opening angle for which it is necessary to include self-weight in the analysis. It will be demonstrated in section 5.5, how inclusion of self-weight could have a significant influence on the predicted responses of the three cases of shells under investigation in Tables 5.1 to 5.3.

5.4 Relationship between different levels of pre-loading and natural frequencies

In section 5.1 the eigenvalue problem is derived for a shell having the effects of pre-loading included. Unlike chapter 3, the effects of second order strains were also taken into account in the derivation of equilibrium equations. As it is shown in section 5.1 the eigenvalue equations were changed due to the addition of the term $-\frac{PR(1-\nu^2)}{Eh}(\frac{i\pi}{\phi})^2$ to the stiffness coefficient k_{33}, which includes the weight of the structure and imposed load such as snow load. The eigenvalue equations were also changed by the inclusion of the additional added mass in Δ due to the imposed load P_{s2}. Using eqns (5.14), (5.15) showed a linear relationship between Δ and pre-loading and a nonlinear relationship between frequency and pre-loading, respectively (Figs 5.1 and 5.2).

In this study the changes in the frequencies due to pre-loading are investigated for a total of 10 circumferential half waves, i, and $j = 1$, for the cases of shells discussed in Tables 5.1 to 5.3. The relationships between the non-dimensionalised frequencies, Δ, and the frequency squared, f^2, against pre-loading P, which includes both the self-weight of the structure and additional loading are plotted in Figs 5.6 to 5.9. However, in this study the wind loading is neglected so $P = P_s$, which is the sum of self-weight and additional imposed load.

In order to plot the figures, the analysis is first performed for a shell neglecting the

effect of pre-loading. In this step only the mass of the structure is included in Δ and k_{33} is identical to that given in eqn (3.5). The governing frequencies for this step would be the same as those derived in chapter 3, where the effects of pre-loading were neglected. The resulting non-dimensionalised frequencies and frequencies squared, which corresponds to the pre-loading of $P = 0$, are shown as points depicted as (a) in Figs 5.6 to 5.11 for mode $(9, 1)$. The region between (a) and (b) does not have any physical meaning and is just connecting point (a) and (b).

The next point on the graph, depicted as (b), was derived by including only the weight of the structure, $P_{s1} = \rho g h$, but also including the prestress N_θ^F in eqn (5.7) and consequently in the stiffness term k_{33} in eqn (5.11). The resulting non-dimensionalised frequencies and frequencies squared are tagged as points (b) for mode $(i, j) = (9, 1)$ in Figs 5.6 to 5.11.

The points after point (b) are derived for a constant value of $P_{s1} = \rho g h$ and increasing value of P_{s2}. The mass considered in Δ also includes the mass of the structure, which is constant plus the varying additional mass due to the varying imposed load P_{s2}.

Finally, a linear buckling analysis is performed to find the third point for each mode, which represents the classical buckling load. The buckling load would be derived for each mode of (i, j) by setting the frequency of that mode equal to zero in eqn (3.4). This point is tagged as (c) for mode $(i, j) = (9, 1)$ in Figs 5.6 to 5.11.

As explained earlier and can be seen from Figs 5.6, 5.8, and 5.10, the non-dimensionalised frequency, Δ, is linearly dependent upon the pre-loading, P. However, as discussed earlier there is a nonlinear relationship between f, and pre-loading, P, in Figs 5.7, 5.9, and 5.11. The region between (b), (c) follow eqn (5.15), while point (a) is derived based on eigenvalue problem of eqn (3.4) and eqn (3.5).

As mentioned in section 5.3 the highest percentage of error as a result of the inclusion of self-weight for the shell in Table 5.1 occurs at mode $(i, j) = (6, 1)$. It was noticed that mode $(i, j) = (6, 1)$ does not correspond to the mode having the minimum frequency. However Fig 5.6 shows that this mode corresponds to the mode corresponding to the classical buckling load. Although mode $(5, 1)$ has the minimum frequency when the self-weight is ignored (point (a)) and even remains minimum when the self-weight

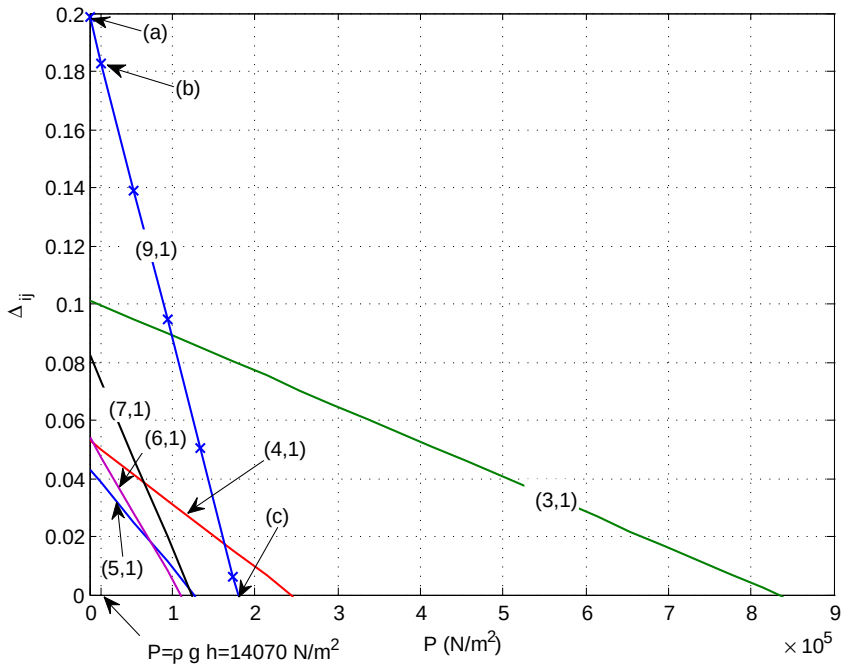

Figure 5.6: Relation between non-dimensionalised frequency and loading for $L_y/L_x = 2$, $B = 0.5 \times 10^{-6}\ s^2$

is taken into account (point (b)), the frequency of mode $(6,1)$ decreases at a greater rate with load and after a certain level of pre-loading the frequency of mode $(6,1)$ becomes less than frequency of mode $(5,1)$. It was also noted in relation to Table 5.1, that different modes had different levels of error arising from taking into account the effect of self-weight, which is because of different energy content of each mode.

As expected, Fig 5.7(a) shows that the frequency squared decreases nonlinearly for the level of loading higher than self-weight. The region of pre-loading between $0.6 \times 10^5\ N/m^2$ and $1.3 \times 10^5\ N/m^2$, zoomed in Fig 5.7(b), shows that the buckling load corresponds to mode $(6,1)$. Fig 5.7(b) also shows the intersection of some modes at different levels of pre-loading, such as modes $(3,1)$ and $(9,1)$ intersecting at $P = 10^5\ N/m^2$, and modes $(4,1)$ and $(7,1)$ at $P = 7 \times 10^4\ N/m^2$. Fig 5.8 and 5.10 show that the minimum non-dimensionalised frequency corresponds to mode $(i,j) = (4,1)$ at zero external loading and remain minimum as the pre-loading is increased up to the buckling load. As for Fig 5.7, the changes in frequency squared in Fig 5.11 and 5.9 become nonlinear for pre-loading higher than self-weight. However, no intersection of modes are noticed for the pre-loading between self-weight and critical

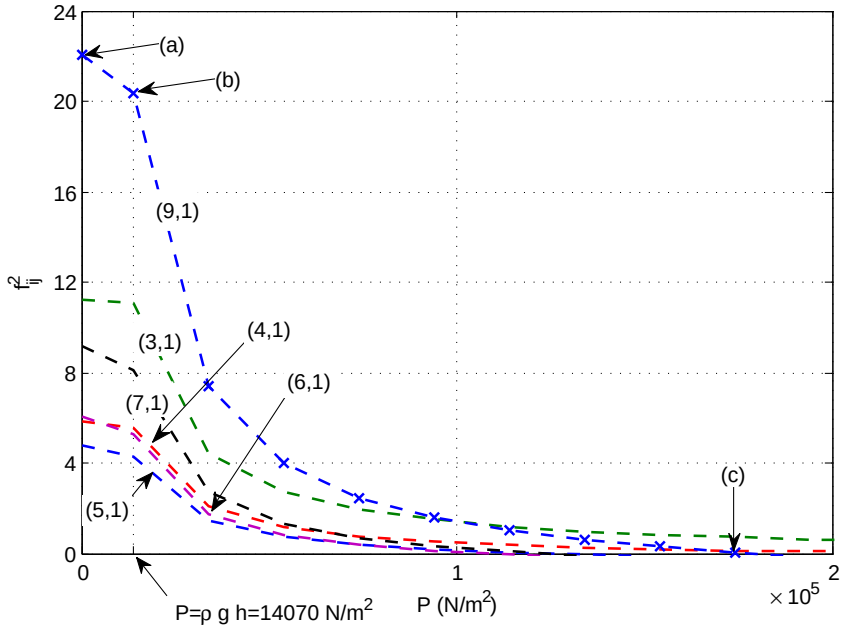

(a)

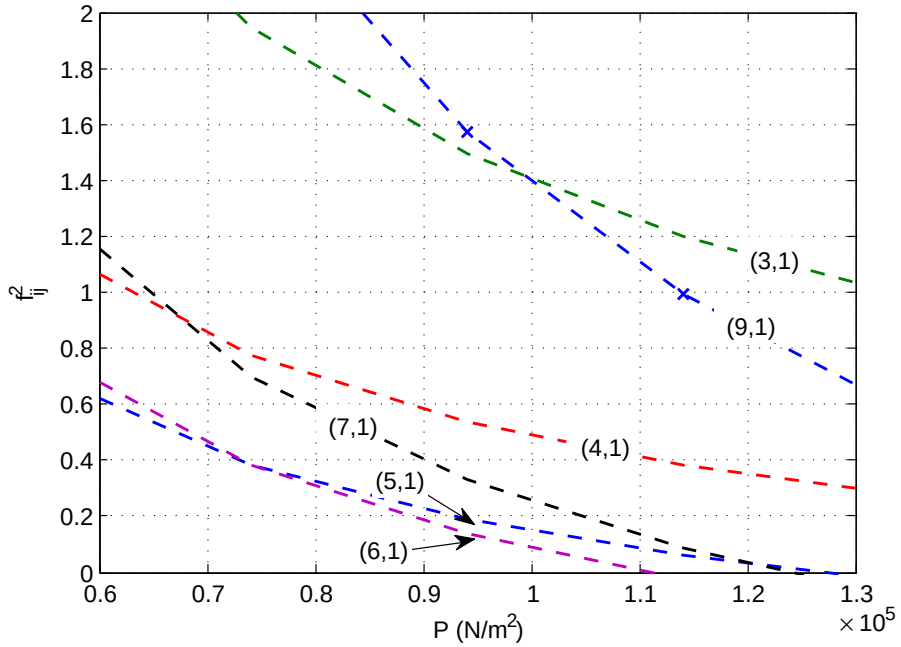

(b) Section between $0.6 \times 10^5 < P < 1.3 \times 10^5$

Figure 5.7: Relation between frequency squared and loading for $L_y/L_x = 2$, $B = 0.5 \times 10^{-6}\ s^2$

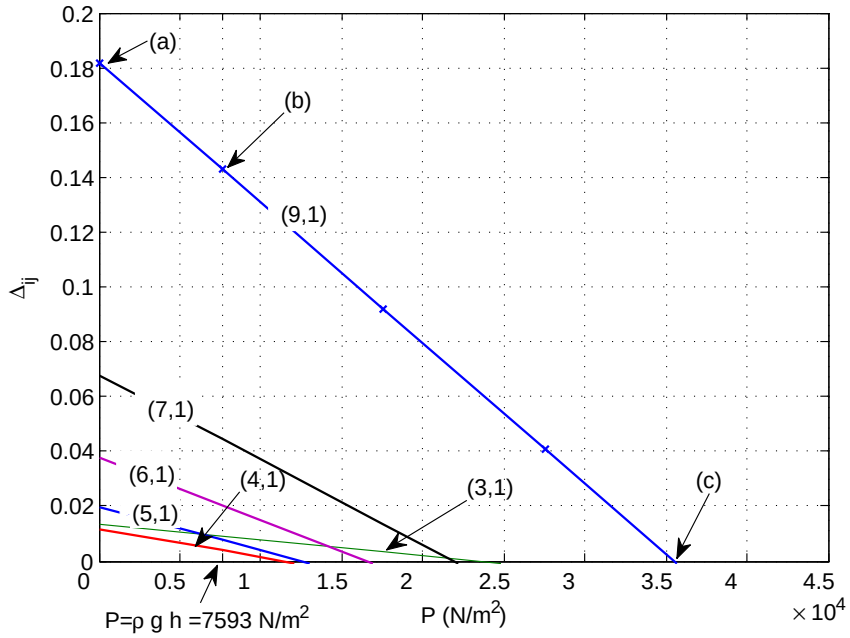

Figure 5.8: Relation between non-dimensionalised frequency and loading for $L_y/L_x = 1$, $B = 1.25 \times 10^{-6}\ s^2$

buckling load. These three examples show the significant reduction of frequency due to consideration of self-weight and additional imposed loading with different rates of reduction exhibited for each mode. The changes in frequency would consequently change the displacement, acceleration and stress responses of the shell subjected to earthquake loading. The reduction of frequencies also caused some modes to have the same frequency at some levels of loading. The intersecting modes and associating frequency could become very important for the earthquakes with high displacement spectra at this frequency as it will simultaneously accentuate two modes. This will be discussed in section 5.5. In order to better understand the nature of the response when the pre-loading is considered in the analysis, a detailed study of the contribution of each mode to the response is performed in the next section.

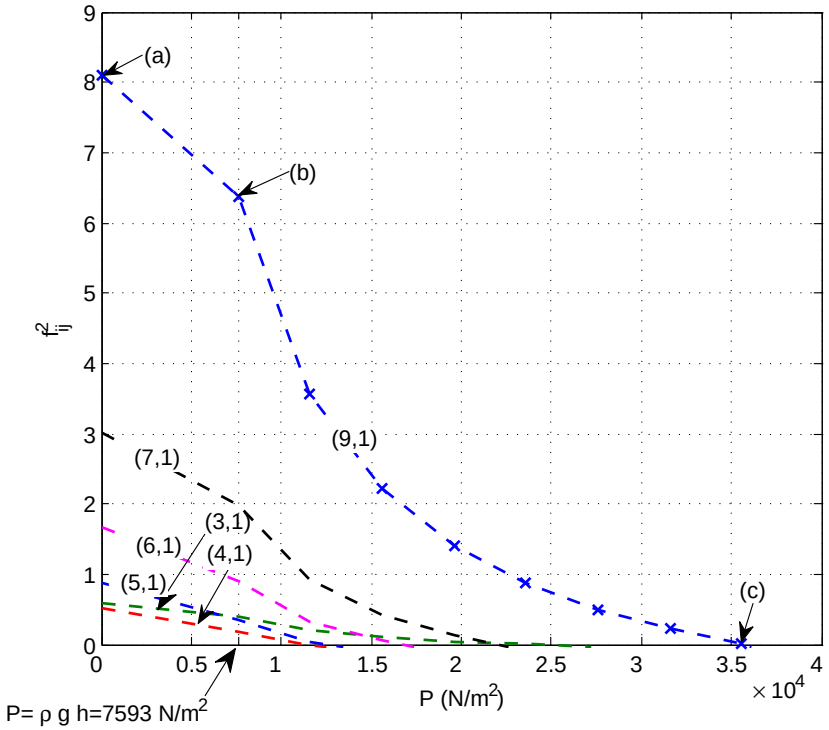

Figure 5.9: Relation between frequency squared and loading for $L_y/L_x = 1$, $B = 1.25 \times 10^{-6}\ s^2$

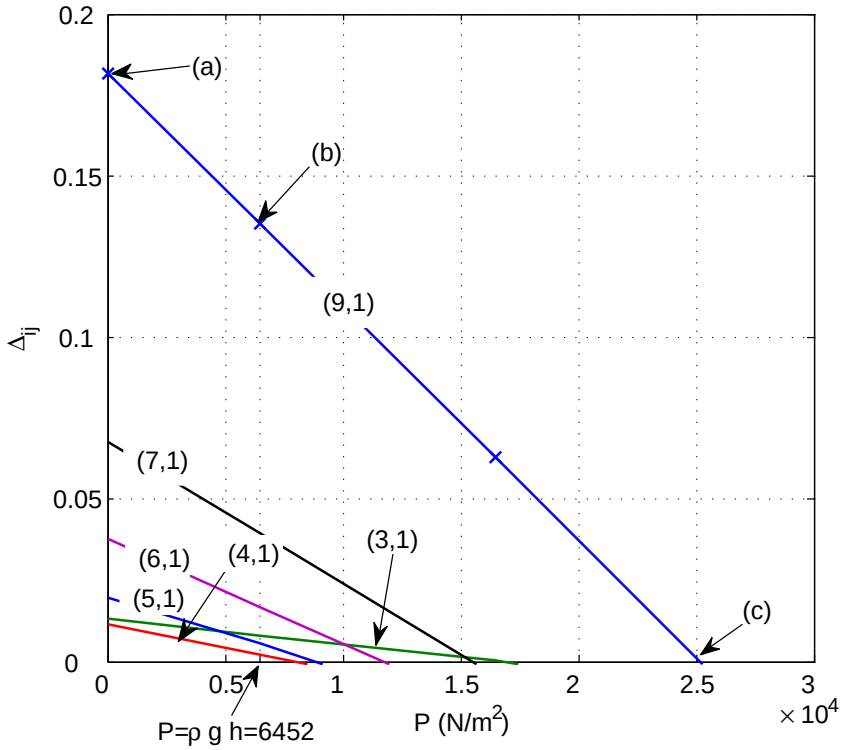

Figure 5.10: Relation between non-dimensionalised frequency and loading for $L_y/L_x = 1$, $B = 1.5 \times 10^{-6}\ s^2$

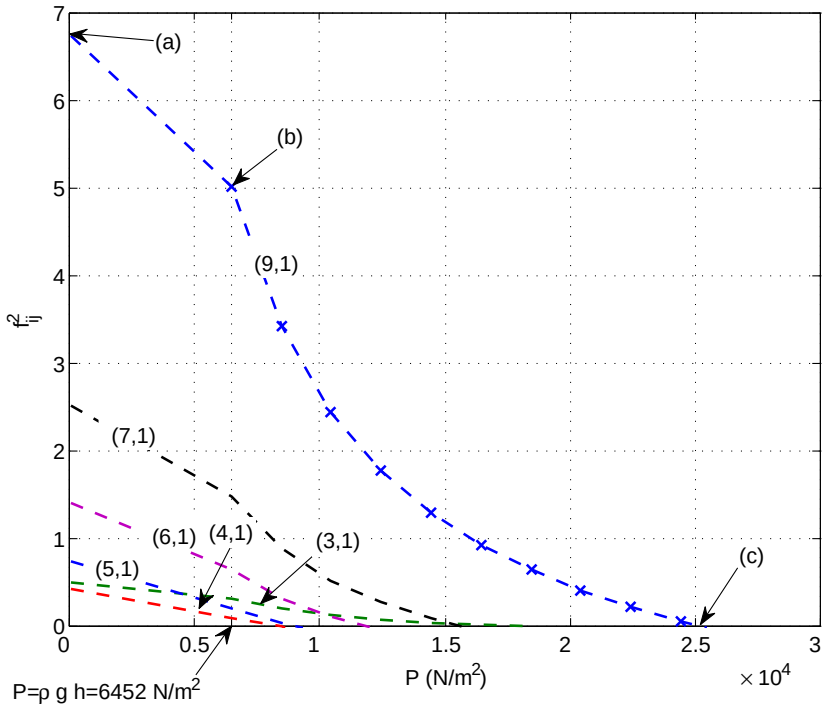

Figure 5.11: Relation between frequency squared and loading for $L_y/L_x = 1$, $B = 1.5 \times 10^{-6}\ s^2$

5.5 Contribution of different modes to earthquake response

As discussed in the previous section the natural frequencies of shells reduce when the effects of pre-loading are taken into account in the frequency extraction equations. Of considerable importance is to understand how these reduced frequencies would affect the displacement and stress responses of the shell subjected to earthquake loading. However, it should be noted that the changes in response due to the effects of pre-loading would be highly dependent on the relationships between the natural frequencies of the shell and response spectrum of the earthquake.

The goal of this section is to better understand the effects of pre-loading on the modal contributions to the total earthquake response of a shell. Using the results of this section then makes it possible to find a relationship between the maximum response of a shell in the form of modal participation factors (MPF), correlated with the frequency content of earthquake and the natural frequencies of the shell which will be discussed in section 6.2.

Finding the relationship between the above mentioned parameters could help the designer to perform an accurate and fast design using a single degree of freedom system by identifying the most important modes affecting the results, without the need to go through a full modal time history analysis. It could also be helpful in the optimization of shells by changing the geometry of the shell so that the natural frequencies corresponding to modes with high modal participation factors fall into the frequency range of earthquake with lower response spectra.

There is therefore a need for more detailed analyses of the changes in the response of each mode due to the pre-loading, which has not been tackled by previous researchers in the field of responses of roof shells to earthquakes. The participation of different modes in the displacement response and their relationships with the modal participation factor and frequency content of a typical earthquake is investigated for one of the three cases of shells presented in section 5.4 having $R = 104.8\ m,\ L_x = 104.8\ m,\ \phi = \pi/3,\ R/h = 500,\ \nu = 0.3,\ E = 46 \times 10^9 N/m^2,\ \rho = 3137.2\, kg/m^3$ with $L_y/L_x = 1$,

and $B = 1.5 \times 10^{-6}\ s^2$. This shell had the highest changes in natural frequencies due to the inclusion of self-weight (Table 5.3, Fig 5.10, 5.11).

For convenience, the modal damping ratio, ζ_{ij}, is again considered to be 0.05 for each mode. The time history modal analysis is carried out for the vertical component of the Landers earthquake with the displacement response spectra as summarised in Fig 6.1. The maximum response of the shell over the time history response, for a total number of 19 half-waves in each of the axial and circumferential directions, is derived and plotted across the center-line bb in Fig 5.12; the response is symmetric about the center line aa (Fig 3.1). The shell is divided into 51×51 divisions for which the maximum absolute displacement is derived for three different conditions: neglecting self-weight; including self-weight; and different levels of additional loading, involving proportionate added mass, over the surface of the shell.

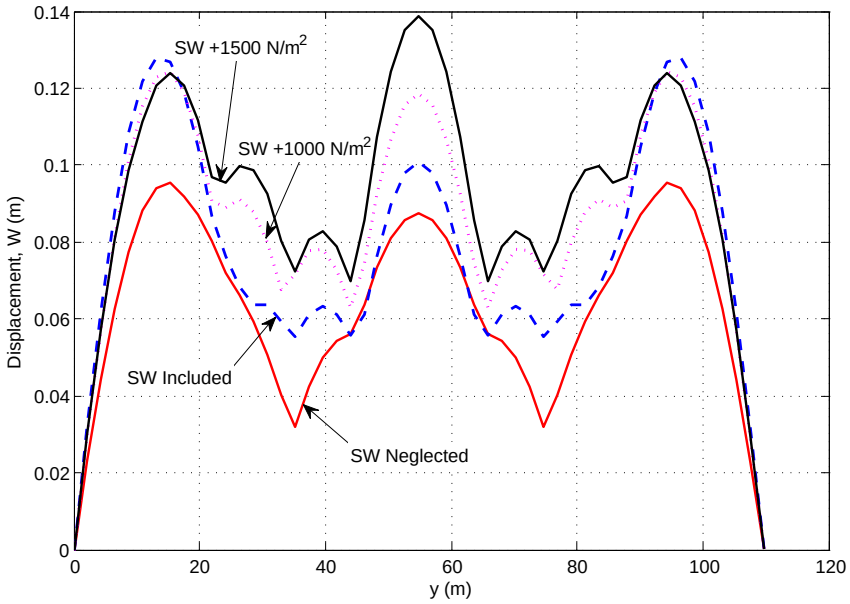

Figure 5.12: Total maximum absolute displacement response across center-line bb, $R = 104.8\ m$, $L_y/L_x = 1$, $\Phi = \pi/3$, $h = R/500m$, $\rho hR/E = 1.5 \times 10^{-6}\ s^2$, $\rho = 3137.2\ kg/m^3$, $P_c = 8093\ N/m^2$, $E = 46 \times 10^9\ N/m^2$, self-weight$= 6452\ N/m^2$ and total number of 19 axial and circumferential half wave

Fig 5.12 shows the maximum response is considerably increased when the self-weight, equal to $6452\ N/m^2$, is included in the analysis compared with when it is neglected. However, the increase in the pre-loading additional to self-weight does not always

cause an increase in the total response. For example, when the pre-loading is equal to self-weight plus an additional $1000\ N/m^2$ the maximum displacement is marginally less than with just the self-weight; this can be seen in the area near the longitudinal boundaries at both ends of center-line bb in Fig 5.12. Comparing the two cases of neglecting the self-weight and including self-weight plus an additional $1500\ N/m^2$ in Fig 5.12 shows that in addition to an increase in the responses the location of the maximum response is also shifted from near the longitudinal boundaries to the middle of center-line bb.

To investigate the changes in maximum response due to the different pre-loading it is necessary to find the contributions of each individual mode to the maximum total response. In order to do so, a Matlab program was written to find and plot the response of each mode along the circumferential width of the shell. As mentioned earlier Fig 5.12 represents the maximum responses at a particular location, so that different parts of the curves occur at different times. But in order to find the participation of each mode to the maximum total response, the response of each mode is derived at the time when the maximum total response occurs during the response time history.

The programme first finds the value, time, and location over the surface of the shell

$Pre-loading$	$Max-Disp$	$Time(s)$	(x,y)
None	0.0953	11.605	(52.414,16.127)
$Self-Weight(SW)$	0.128	12.045	(52.414,16.127)
$SW+1000N/m^2$	0.1244	11.215	(52.414,16.127)
$SW+1500N/m^2$	0.1387	12.22	(52.414,52.414)

Table 5.4: Times and locations of the maximum displacement for a shell with $R = 104.8\ m$, $L_y/L_x = 1$, $\Phi = \pi/3$, $h = R/500$, $\rho hR/E = 1.5 \times 10^{-6}\ s^2$, $\rho = 3137.2\ kg/m^3$, $P_c = 8093\ N/m^2$, $E = 46 \times 10^9\ N/m^2$ and total number of 19 axial and circumferential half waves

associated with the maximum total displacement response as summarised in Table 5.4. The analysis is performed for a total of 19 axial and circumferential half-waves. It is

repeated for different values of pre-loading. The summarised results in Table 5.4 show that for all levels of pre-loadings the maximum total displacement response occurs at mid-length of the shell (center-line bb), yet at different times.

For each condition stated in Table 5.4, the actual response of the shell is then plotted along center line bb at the time when the maximum displacement occurs (Table 5.4). Only the modes with significant contribution to the total response are plotted in Fig 5.13.

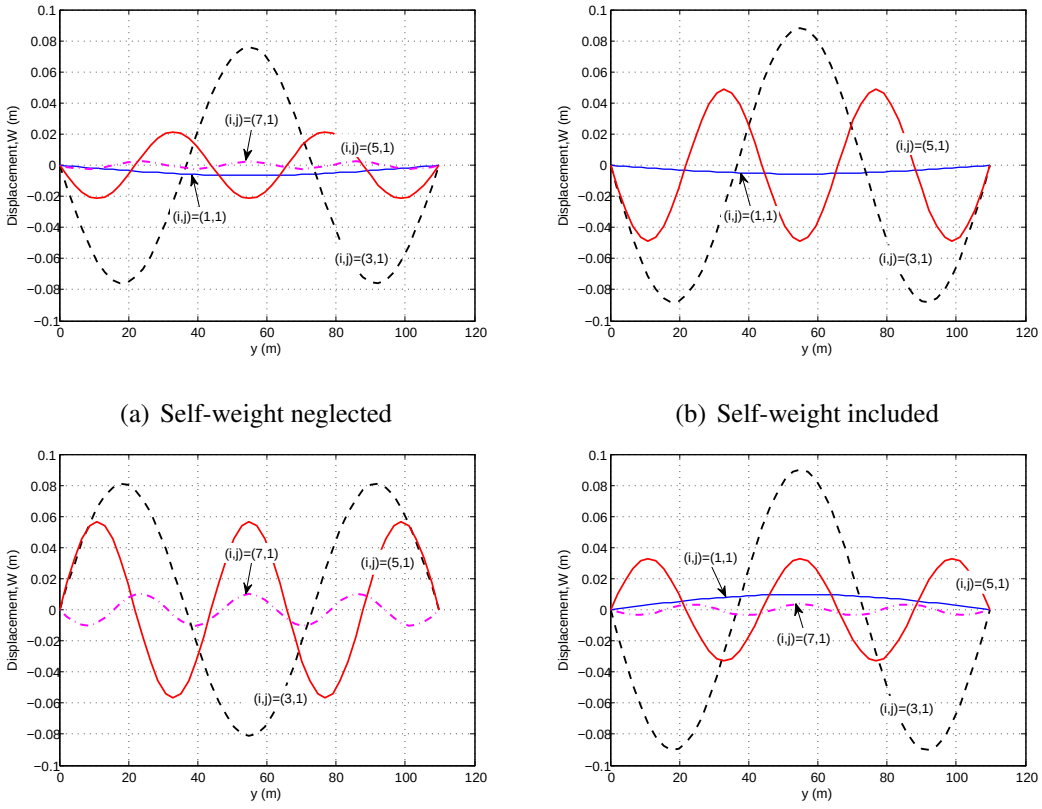

(a) Self-weight neglected

(b) Self-weight included

(c) Self-weight+$1000 N/m^2$

(d) Self-weight+$1500 N/m^2$

Figure 5.13: Modal contribution to the displacement response on section bb, for $L_y/L_x = 1$, $B = 1.5 \times 10^{-6}\ s^2$

Fig 5.13 shows that mode $(i, j) = (3, 1)$ has the highest contribution to the maximum total response at the time when it occurs. This contribution is slightly increased in Fig 5.13(b) when the self-weight is included in the analysis, and then is marginally decreased by adding $1000\ N/m^2$ pre-loading, and finally increased back to the same level as in Fig 5.13(b) for the pre-loading equal to $1500\ N/m^2$ in Fig 5.13(d). It is worth noting that in Fig 5.10 there is very little changes in frequency of mode $(3, 1)$ over

the load range for Fig 5.12 and Table 5.4. The little variation of the natural frequency of mode $(3,1)$ explains the reason for the insignificant variation in the displacement responses of this mode over the load range in Fig 5.12. It is because there is a relationship between the natural frequencies of the shell and response spectra of earthquake.

Unlike mode $(3,1)$, mode $(5,1)$ exhibits substantial changes in frequencies over this same range of pre-loading (Fig 5.10). The contribution of mode $(i,j)=(5,1)$ is seen to increase from Fig 5.13(a) to (c), by increasing the pre-loading, but eventually as shown in Fig 5.13(d) starts to decrease. As will be shown in Fig 5.14 the displacement response spectrum for the frequency of this mode increases by increasing the load over the range of loading in Fig 5.12, so the reason for mode $(5,1)$ hitting its peak displacement response at the frequency corresponding with self-weight$+1000\ N/m^2$ is not because of a sudden reduction in displacement response spectrum at the frequency corresponding with self-weight$+1000\ N/m^2$. It is because Fig 5.13 only presents the participation of each mode at the time of the maximum total response, however the maximum of each mode can occur at different times. In Fig 5.14, which will be discussed later in this section, it will be shown that for the maximum modal responses over the time history of earthquake the contribution of mode $(5,1)$ would increase constantly over the range of loading in Fig 5.13 and unlike Fig 5.13 hit the maximum at the frequency corresponding to self-weight$+1500\ N/m^2$.

According to Fig 5.13 mode $(i,j)=(1,1)$ does not contribute significantly to the response. However, as will be found in the later discussion of Fig 6.2(b), mode $(i,j)=(1,1)$ has the highest modal participation factor (MPF), from which it might be expected that this mode would have a significant participation in the total response. MPF is a measure of the importance of each mode to the level of loading, which will be introduced later in section 6.1. One reason for the apparently low participation of mode $(1,1)$ in the total response is because Fig 5.13 is just presenting the response of different modes along center-line bb at the time when the maximum displacement happens. However, it does not necessarily represent the maximum contribution of each mode to the response over the total duration of earthquake and over the entire surface of the shell.

This leads to the study of the maximum displacement response of the shell over the entire time history of earthquake. The maximum response of each mode is then related to the maximum total response using modal combination methods as will be explained in section 6.2. The analysis is performed to find the maximum response of each mode over the duration of earthquake. The maximum absolute displacement response for each separate mode of the shell is derived over the duration of earthquake and plotted along center line bb, as shown in Fig 5.14. The maximum response of each mode is plotted along center line bb because the maximum total response occurs along this line as shown in Table 5.4. Fig 5.14 (a),(b) show the maximum modal response of the shell when the effects of pre-loading are neglected. For clarity purpose the responses are presented in two parts: Fig 5.14(a) presents the modes with maximum responses of more than $0.003\ m$; Fig 5.14(b) shows the modes with maximum responses between $0.001\ m$ and $0.003\ m$; while modes with responses less than $0.001\ m$ are not shown. Fig 5.14(c)-(e) present the response for each of the cases of: self-weight (SW), self-weight plus the additional $1000\ N/m^2$ (SW+$1000\ \ N/m^2$), and self-weight plus the additional $1500\ N/m^2$ (SW+$1500\ N/m^2$).

The contributions of modes in Fig 5.14(c)-(d) exhibit quite different patterns from those in Fig 5.13(a). Although the most significantly contributing modes are still $(i,j) = (3,1),(5,1),(1,1),(7,1)$, their relative contributions are different. For example, the contribution of mode $(i,j) = (5,1)$ are significantly higher in Fig 5.14(e) than in Fig 5.13(d). It is also appears that more modes are contributing to the response in Fig 5.14(c),(e) in comparison to Fig 5.13(b)-(d). This can be seen in modes $(9,1)$, $(7,1)$ in Fig 5.14(c); modes $(1,1)$, $(9,1)$ in Fig 5.14(d) and $(1,3)$, $(9,1)$, $(5,3)$ in Fig 5.14(e).

In Fig 5.14 it is also noticed that modes $(1,1)$ and (3,1) are very little changed from Fig 5.14(c) to (e), while modes $(5,1)$ and $(7,1)$ show monotonic increases as self-weight and imposed load are added.

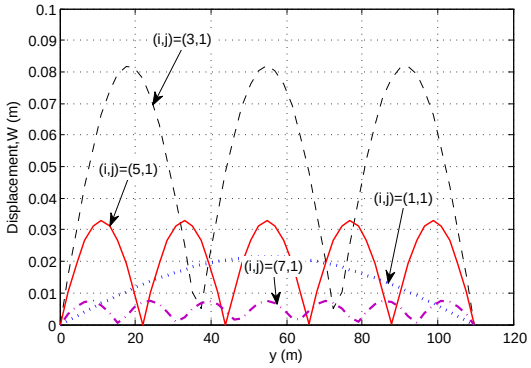

(a) Self-weight neglected, (max response more than $0.003\ m$)

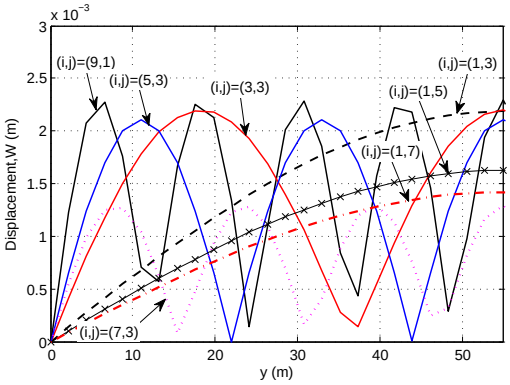

(b) Self-weight neglected, max response between $0.001\ m$ and $0.003\ m$)

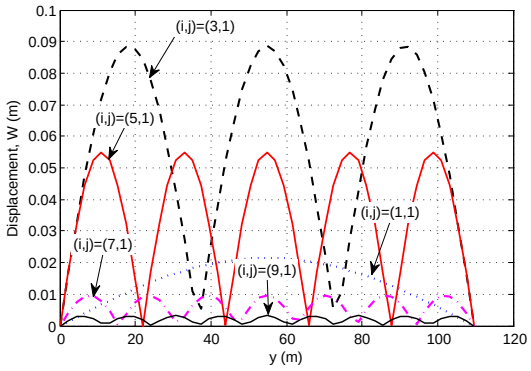

(c) SW

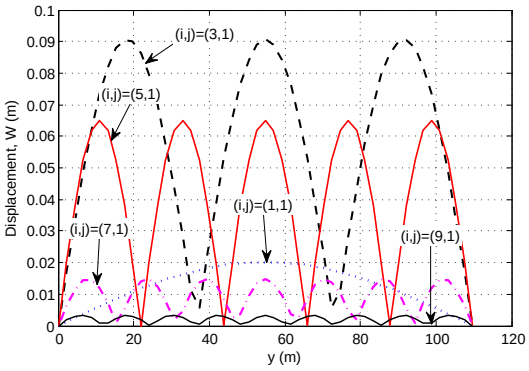

(d) SW+$1000N/m^2$

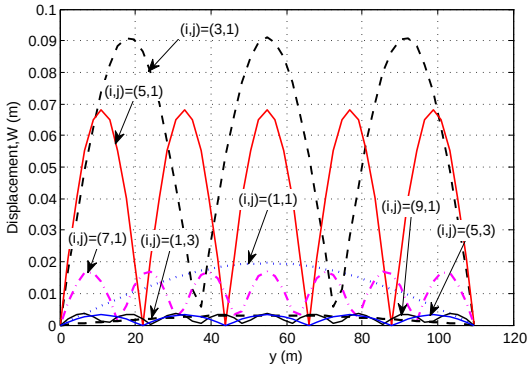

(e) SW+$1500N/m^2$

Figure 5.14: Maximum absolute modal displacement responses for a shell having $L_y/L_x = 1$, $B = 1.5 \times 10^{-6}\ s^2$ and for different pre-loadings

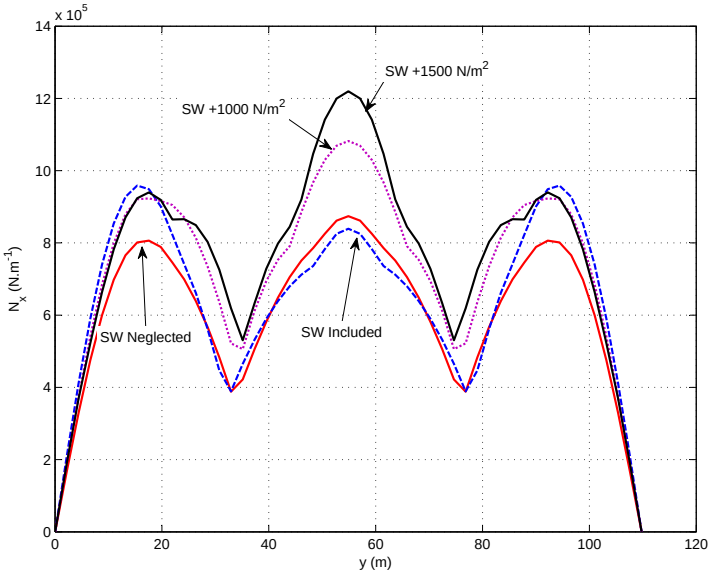

Figure 5.15: Total maximum absolute membrane stress response across center-line bb, $R = 104.8\ m$, $L_y/L_x = 1$, $\Phi = \pi/3$, $h = R/500m$, $\rho hR/E = 1.5 \times 10^{-6}\ s^2$, $\rho = 3137.2\ kg/m^3$, $P_c = 8093\ N/m^2$, $E = 46 \times 10^9\ N/m^2$, self-weight$= 6452\ N/m^2$ and total number of 19 axial and circumferential half waves

A similar analysis to displacement response is performed for stress resultant. The maximum absolute axial membrane stress is derived for different pre-stress loading and plotted along center-line bb in Fig 5.15. As for the displacement responses the analysis is performed for a total of 19 half-waves in the circumferential and axial directions, and for different pre-loadings.

Fig 5.15 shows that the maximum stress increases when the self-weight is included compare with when it is neglected and continues increasing with the increase in the pre-loading. The location of the maximum stress is shifted from being in the center for the cases when self-weight is neglected, $SW + 1000\ N/m^2$, and $SW + 1500\ N/m^2$ to the longitudinal boundaries at both ends of center-line bb for the condition when SW is included. However, as the design significance of maximum tension could be very different to maximum compression, Table 5.5 reports whether the maximum absolute stresses are tension or compression stresses.

A similar analysis to displacement response is performed for stress resultant, for which

a programme was written to find the maximum absolute stress together with the time and location corresponding to the maximum stresses, as summarised in Table 5.5. Most

Pre-loading	Response	Max stress ($\times 10^5$)	Time (s)	Location of max stress (x, y)
None	$N_x\ (N.m^{-1})$	-8.7406	12.370	$(52.414, 54.888)$
	$N_y\ (N.m^{-1})$	5.737	10.385	$(52.414, 54.888)$
	$N_{xy}\ (N.m^{-1})$	± 6.1756	10.675	$(0, 0)$
	$M_x\ (N.m)$	0.17751	10.96	$(52.414, 94.4075)$
	$M_y\ (N.m)$	0.44826	11.4950	$(56.4142, 10.9776)$
	$M_{xy}\ (N.m)$	± 0.1177	11.535	$(0, 0)$
SW	$N_x\ (N.m^{-1})$	-9.5884	12.025	$(52.4142, 15.3687)$
	$N_y\ (N.m^{-1})$	11.243	10.135	$(8.3863, 54.8881)$
	$N_{xy}\ (N.m^{-1})$	± 5.7066	11.055	$(0, 0)$
	$M_x\ (N.m)$	-0.25235	12.13	$(52.4142, 96.6030)$
	$M_y\ (N.m)$	-0.64955	12.12	$(52.4142, 96.6030)$
	$M_{xy}\ (N.m)$	± 0.13644	12.03	$(0, 0)$
$SW + 1000$	$N_x\ (N.m^{-1})$	10.821	12.215	$(52.4142, 54.888)$
	$N_y\ (N.m^{-1})$	12.395	11.33	$(44.028, 54.888)$
	$N_{xy}\ (N.m^{-1})$	± 6.663	11.125	$(0, 0)$
	$M_x\ (N.m)$	0.26539	11.35	$(52.4142, 96.6030)$
	$M_y\ (N.m)$	0.6845	11.35	$(52.4142, 13.1731)$
	$M_{xy}\ (N.m)$	0.12835	11.12	$(0, 0)$
$SW + 1500$	$N_x\ (N.m^{-1})$	12.196	12.25	$(52.4142, 54.888)$
	$N_y\ (N.m^{-1})$	13.334	11.35	$(44.028, 54.888)$
	$N_{xy}\ (N.m^{-1})$	± 6.4682	11.13	$(0, 0)$
	$M_x\ (N.m)$	0.26089	11.36	$(52.4142, 15.3687)$
	$M_y\ (N.m)$	0.68330	11.545	$(52.4142, 98.7985)$
	$M_{xy}\ (N.m)$	± 0.12288	10.12	$(0, 0)$

Table 5.5: Times and locations of the maximum absolute stress resultants for a shell with $R = 104.8\ m$, $L_y/L_x = 1$, $\Phi = \pi/3$, $h = R/500$, $\rho hR/E = 1.5 \times 10^{-6}\ s^2$, $\rho = 3137.2\ kg/m^3$, $P_c = 8093\ N/m^2$, $E = 46 \times 10^9\ N/m^2$ and total number of 19 axial and circumferential half waves

of the maximum stress responses occurred along center-line bb, but at different times.

Fig 5.16 shows the actual membrane stress along center-line bb at the time when the maximum membrane stress occurred (Table 5.5). It should be noted that only the significant modes are plotted in Fig 5.16. Like the displacement responses, the modal contributions change by including self-weight and additional loading; such as response of mode $(3, 1)$ which increases when the self-weight is included in the analysis (5.16(b)) in comparison with the case when it is ignored (5.16(a)), it then slightly decreases in Fig 5.16(c) and finally increase back again in Fig 5.16(d).

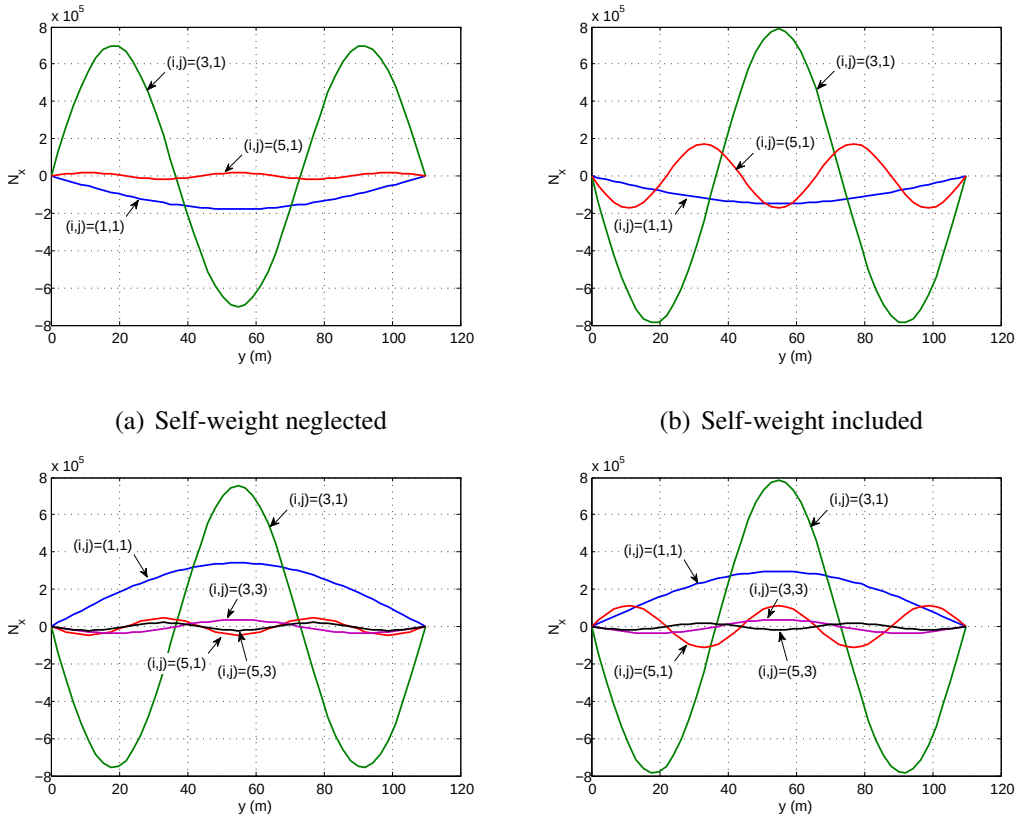

(a) Self-weight neglected

(b) Self-weight included

(c) SW+1000N/m^2

(d) SW+1500N/m^2

Figure 5.16: Axial membrane stress modal contributions for a shell having $L_y/L_x = 1$, $B = 1.5 \times 10^{-6}\ s^2$ and for different pre-loadings

However, as for the displacements (Fig 5.13), Fig 5.16 again does not present the maximum modal responses over the time history of earthquake. So in order to find the maximum modal response related to membrane stress another study is performed, with the result shown in Fig 5.17 for the two cases of neglecting self-weight and including

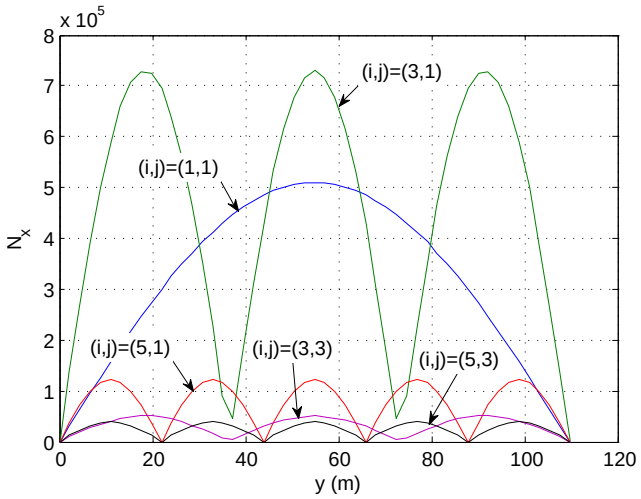

(a) Self-weight neglected

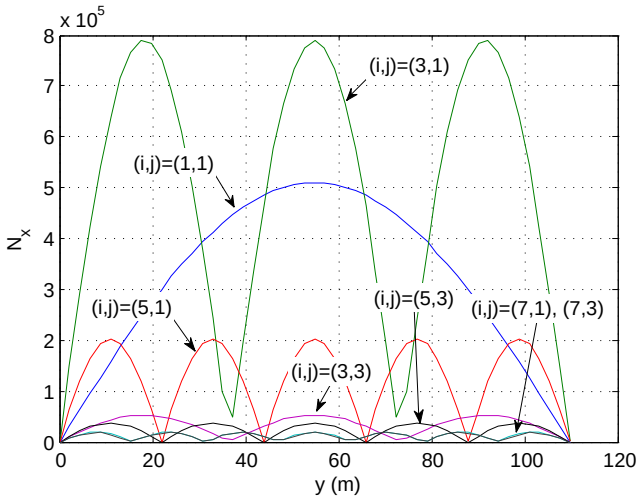

(b) Self-weight included

Figure 5.17: Maximum axial membrane stress modal contribution for a shell having $L_y/L_x = 1$, $B = 1.5 \times 10^{-6}\ s^2$ and for different pre-loadings

self-weight in the analysis. As it can be seen in Fig 5.17 the modal participation is quite different from that shown in Fig 5.16 and furthermore a greater number of modes are contributing to the response.

Of great importance in the earthquake analysis of shells, as indeed any structure, is to find a relationship between the maximum responses of the structure and response spectrum of earthquake. It would be beneficial if the behaviour discussed above could be anticipated by looking only at the displacement response spectrum of the earthquake and natural frequencies spectrum of the shell. If a relationship can be established,

which allows the maximum response of the shell to be found, by means of just the natural frequencies of the shell and response spectrum of the earthquake, this would significantly decrease the calculation time and help designers to develop a clear vision of the most significant modes affecting the response. This will be discussed in chapter 6.

5.6 Effect of self-weight in maximum response

As shown in section 5.3 and 5.4 the inclusion of pre-loading in the analysis changes the natural frequencies of the shell. It is also shown in section 5.5 that the contribution of each mode to the total response changes by the inclusion of pre-loading in the analysis. However, it is worthy to mention that the changes in the response of different modes depend significantly on the relationships between the frequency content of earthquake and the changes in the natural frequencies of the shell caused by the imposed load.

This section presents the changes in maximum displacement and stress responses based on the two assumptions of including and neglecting self-weight in the analysis. The results are only presented for those cases of shell considered in Fig 5.3, where their self-weight is less than the critical buckling load. For these cases of shells the maximum responses are plotted in Figs 5.18 to 5.20.

The displacement and stress responses in Figs 5.18-5.20 are the maximum absolute dynamic responses over the entire duration of earthquake and over the shell surface that are found using the modal time history analysis.

Fig 5.18 shows the maximum absolute radial displacement response. For all cases, the inclusion of self-weight in the analysis increases the response except for the two cases of $L_y/L_y = 2$, $B = 1 \times 10^{-6}\ s^2$ and $B = 0.5 \times 10^{-6}\ s^2$ that remain constant. However, the percentage of the increase differs for each geometry and material property of shell. Including the self-weight also increases the in-plane displacements for all cases of shell, except for the shell having $L_y/L_x = 2$, and $B = 0.5 \times 10^{-6}\ s^2$ to $B = 1 \times 10^{-6}\ s^2$ as shown in Fig 5.19. Bending stresses in Figs 5.20(a)-(c) show similar trends. The responses are increased by the inclusion of self-weight in the analysis, except for shells having $L_y/L_x = 2$, and $B = 0.75 \times 10^{-6}\ s^2$ to $B = 1 \times 10^{-6}\ s^2$

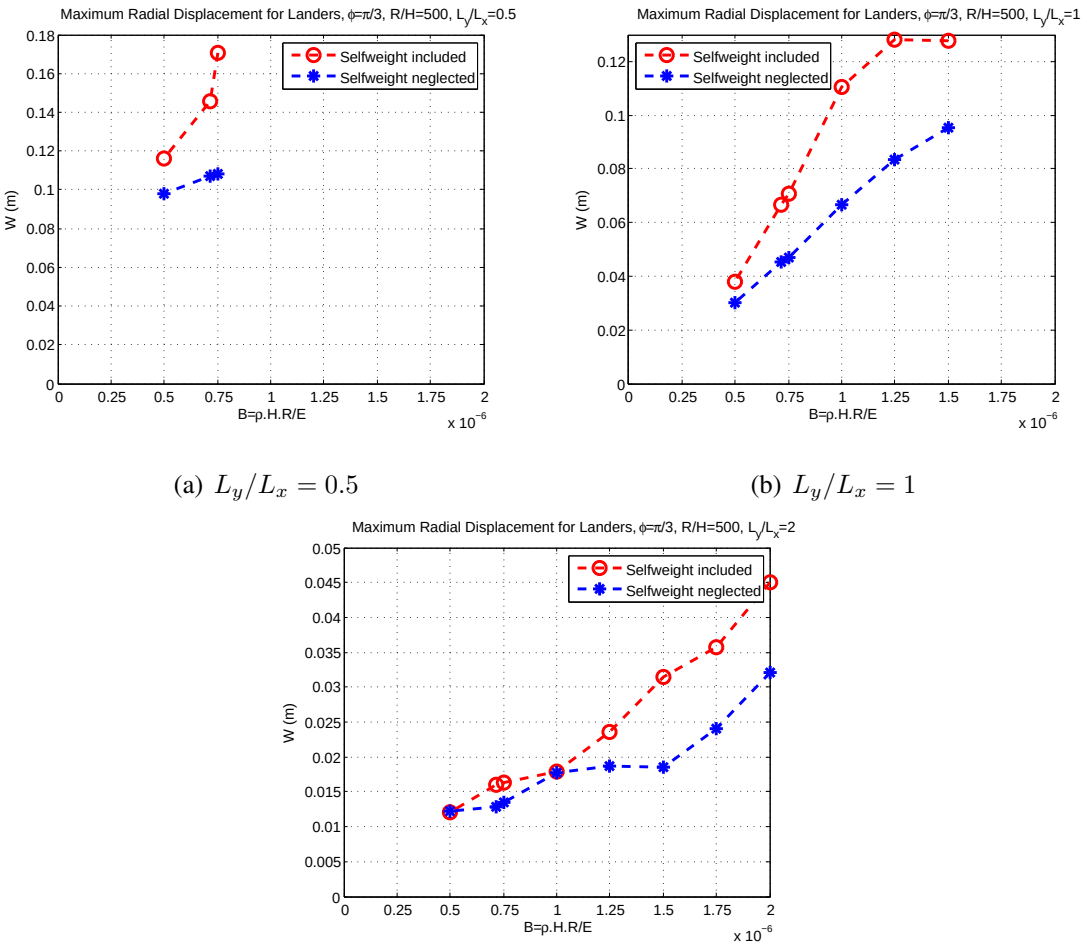

(a) $L_y/L_x = 0.5$ (b) $L_y/L_x = 1$

(c) $L_y/L_x = 2$

Figure 5.18: Maximum radial displacement response

which remain essentially constant. For these cases, although the natural frequencies of shell is changed, the total responses remained constant.

The membrane stresses are also increased by the inclusion of self-weight in the analysis, with N_{xy} showing the minimum changes and membrane hoop stress and N_y the maximum changes. It should be noted that $N_y^F = PR$ is added to the dynamic membrane hoop stress response. Membrane stresses have different behaviour than the bending stresses. The membrane axial and hoop stresses are increased by including the self-weight in the analysis (Fig 5.20(d),(e)). However shear membrane stress has not been increased significantly and even decreases for some cases of shells as in Fig 5.20(f).

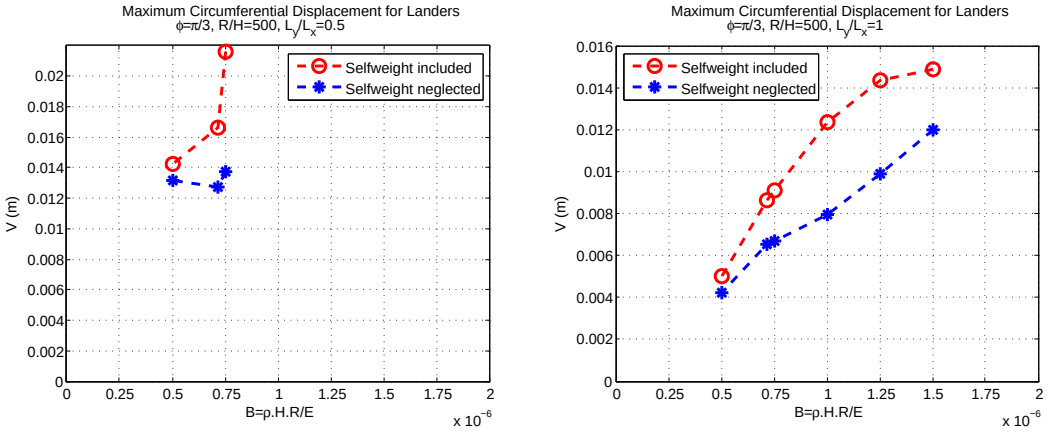

(a) $L_y/L_x = 0.5$ (b) $L_y/L_x = 1$

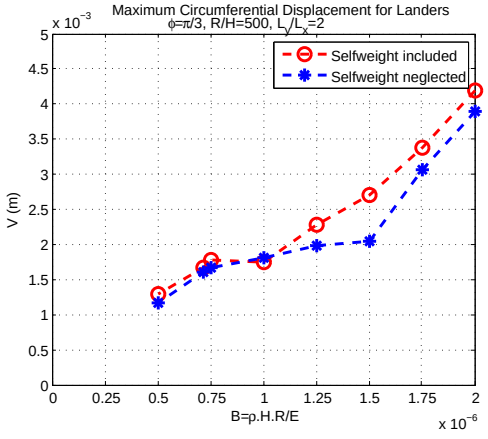

(c) $L_y/L_x = 2$

Figure 5.19: Maximum circumferential displacement response

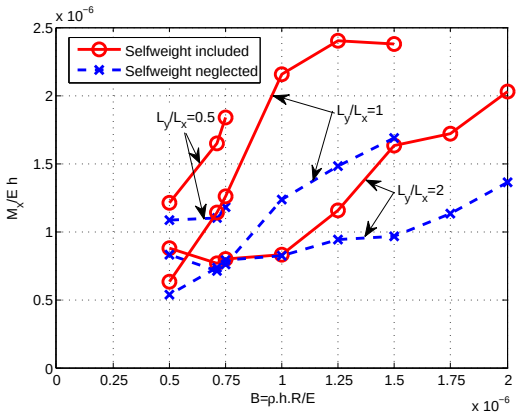

(a) M_x

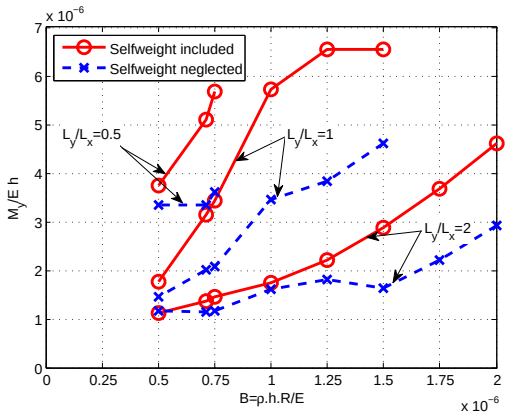

(b) M_y

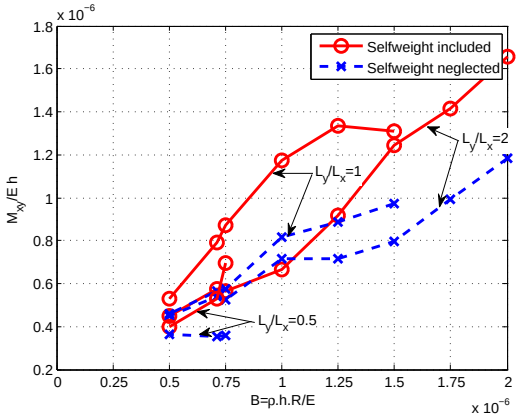

(c) M_{xy}

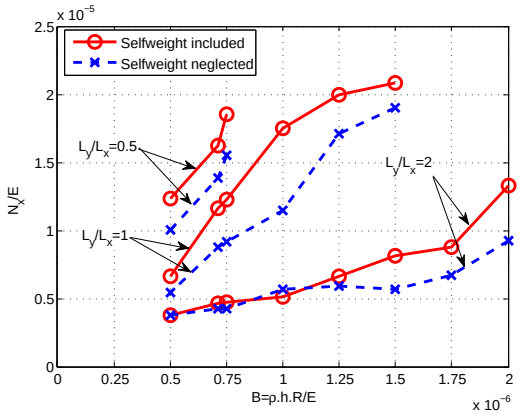

(d) N_x

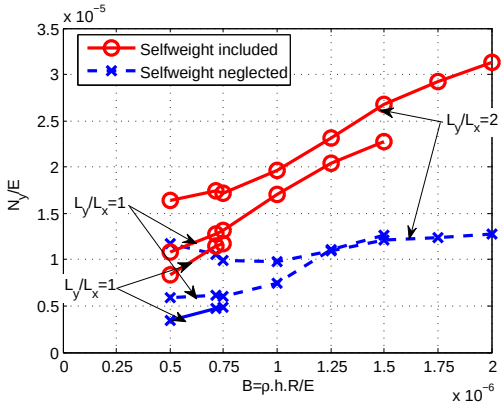

(e) N_y

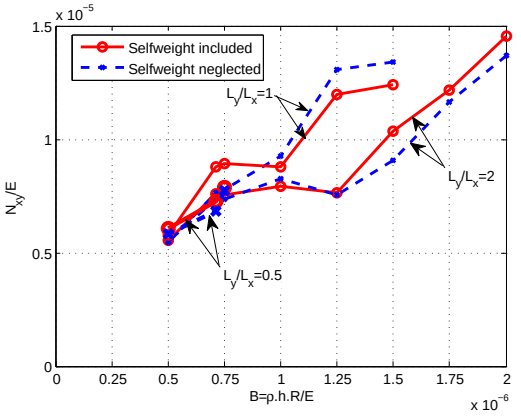

(f) N_{xy}

Figure 5.20: Maximum absolute stress response

Chapter 6

Interpretation of Effect of Pre-loading on the Dynamic Response Using the Response Spectrum

6.1 Relationship between MPF, earthquake response spectrum and maximum response

As shown in the previous chapter, the natural frequencies and responses of a shell changed due to inclusion of typical levels of pre-loading. It would be helpful to find simple relationships between the response spectrum of the earthquake and the observed changes in the maximum response of shell due to inclusion of pre-loading. These relationships would help designers to find the maximum responses without the need to go through extensive time history analysis.

To address this need another study is performed, which attempts to relate the displacement response spectrum of the Landers earthquake (Fig 6.1) to the changes in frequency due to taking into account self-weight and increasing pre-loading (Fig 6.2(a)), making use of the MPF of each mode (Fig 6.2(b)). MPF has been derived in chapter 3, and is obtained by dividing the modal force, P_{ij} (see eqn (3.58)) by the modal mass M_{ij} and was given (see eqn (3.40)) as

$$MPF = \frac{P_{ij}(t)}{M_{ij}} = \frac{4(-1+\cos i\pi)(-1+\cos j\pi)(\overline{w}i\pi - \overline{v}\phi)}{j\pi(i\pi-\phi)(i\pi+\phi)}\cos\frac{\phi}{2} \qquad (6.1)$$

This effectively shows the inertial participation of each mode.

Using MPF, the modes with higher contributions to the response would be identified. The maximum response of each mode can then be found by multiplying the values of the MPF of each selected mode by the response spectrum of the earthquake (Fig 6.1) at the corresponding natural frequencies of the shell in that mode (Fig 6.2(a)).

For example, the frequency of mode $(1,1)$ when the effect of pre-loading is neglected has the highest MPF equal to 1.4 (Fig 6.2(b)). The natural frequency of this mode is equal to $2.928\ Hz$ (Fig 6.2(a)), for which the corresponding displacement response spectrum of earthquake S_d is equal to $0.01618\ m$ (Fig 6.1). Looking at Fig 5.14, which represent the maximum displacement of the shell along center line bb, it is noticed that the maximum response of mode $(1,1)$ is equal to $0.02262\ m$ (5.14(a)). This value is exactly equal to the result of multiplying the value of $MPF = 1.4$ by the value of $S_d = 0.01618$ at mode $(i,j) = (1,1)$.

Despite the increase in the levels of pre-loading through Fig 5.14(a) to 5.14(e) and the consequent 11% decrease in natural frequency as a result of including self-weight and the addition of self-weight plus $1500\ N/m^2$, which reduces the natural frequency in mode $(1,1)$ from $f = 2.928\ Hz$ to $f = 2.637\ Hz$ (Fig 6.2), it is noticed that displacement response of mode $(i,j) = (1,1)$ remains effectively constant. Using Fig 6.1 shows that the displacement response spectrum for this earthquake in the range of frequency between $f = 2.928\ Hz$ and $f = 2.637\ Hz$ remains constant. This explains the insignificant changes in displacement response of this mode in Fig 5.14(a) to 5.14(e).

It should be noted that MPF of eqn (6.1) should change for different levels of pre-loadings due to the changes in $\bar{w}$ and $\bar{v}$. But as the changes in $\bar{w}$ and $\bar{v}$ are insignificant, the MPF in Fig 6.2(b) remains constant for all levels of pre-loading.

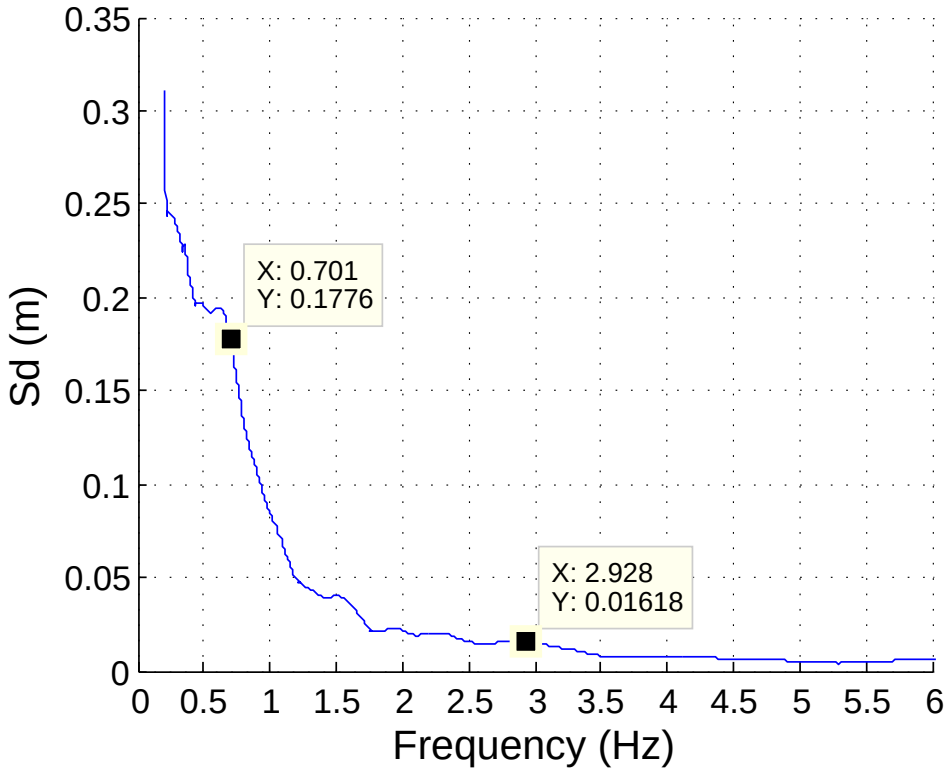

Figure 6.1: Landers earthquake displacement response spectrum

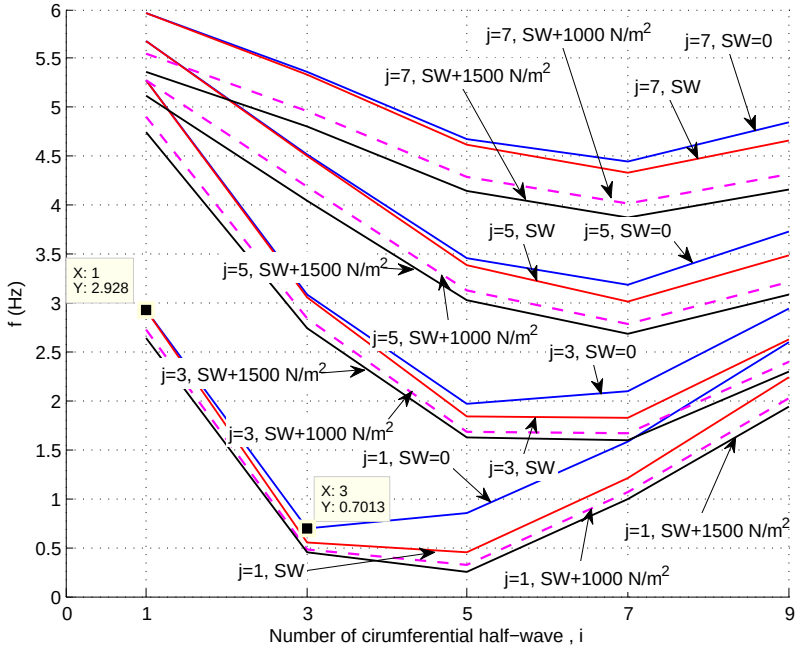

(a) Changes in natural frequency

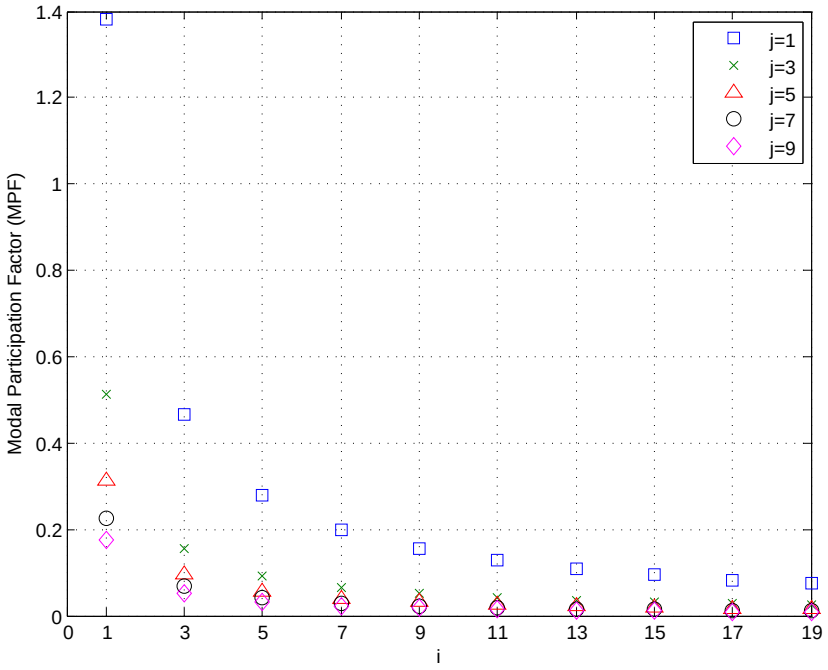

(b) Modal Participation Factor (MPF)

Figure 6.2: Active modes in response and modal participation factor for a shell with $L_y/L_x = 1$, $B = 1.5 \times 10^{-6}\ s^2$

Repeating the same procedure for mode $(i, j) = (3, 1)$ for the case when the pre-loading is neglected, the maximum response of $0.08253\ m$ would be derived by multiplying $S_d = 0.1776\ m$ (Fig 6.1) corresponding to the natural frequency of mode $(3, 1)$ which is equal to $0.7013\ Hz$ (Fig 6.2(a)), by $MPF = 0.4647$ (Fig 6.2(b)). This value is very close to the maximum displacement of $0.08192\ m$ experienced by this mode as shown in Fig 5.14(a). The reason for this small difference is that S_d in Fig 6.1 is found for increments of 0.001 in frequency. However, the natural frequency of the shell in mode $(i, j) = (3, 1)$ is equal to 0.7013 which is slightly higher than the frequency of $0.701\ Hz$ on the displacement response spectrum (Fig 6.1). It can be seen from Fig 6.1 that S_d would be slightly higher than $0.1776\ m$ for the frequency of $0.7013\ Hz$, which would consequently explain the difference between the two governing maximum displacements.

Unlike modes $(1, 1)$ and $(3, 1)$, Fig 5.14 shows that modes $(5, 1)$ and $(7, 1)$ display quite considerable variations as the pre-loading increases. Fig 5.14(a) shows maximum displacement of modes $(5, 1)$ equal to $0.032\ m$ when the pre-loading is neglected. It increases to $0.055\ m$ when including self-weight in Fig 5.14(c), then increases to $0.065\ m$ in Fig 5.14(d) corresponding to self-weight plus $1000\ N/m^2$ additional loading, and finally reaches to $0.069\ m$ in Fig 5.14(e) for self-weight plus $1500\ N/m^2$ additional loading. The corresponding frequencies for these four cases of loading in Fig 5.14(a),(c),(d),(e) are equal to $0.8562\ Hz$, $0.4498\ Hz$, $0.3224\ Hz$, and $0.253\ Hz$, respectively as shown in Fig 6.2(a).

Unlike mode $(1, 1)$, the earthquake displacement response spectra corresponding to these frequency show significant variation in Fig 6.1. It changes from $0.1176\ m$, to $0.1967\ m$, then, $0.2326\ m$, and finally $0.2443\ m$ corresponding to the aforementioned changes in frequency, respectively. This corresponds to 107% increase in response of mode $(5, 1)$ due to inclusion of self-weight and $1500N/m^2$ additional loading.

The maximum displacement spectrum for mode $(5, 1)$ is then derived by multiplying $MPF = 0.28$ by S_d, which is equal to $0.0329\ m$, $0.0551\ m$, $0.0651\ m$, and $0.0684\ m$, respectively. Comparing these results of $0.0329\ m$, 0.0551, $0.0651\ m$, $0.0684\ m$ with

the maximum displacements of $0.032\ m$, $0.055\ m$, $0.065\ m$, $0.069\ m$ corresponding with mode $(5,1)$ in Fig 5.14 (a),(c),(d),(e), which are derived based on complete time history analysis shows that they are effectively identical for practical purposes.

It is concluded that the reason for the considerable variation of displacement of mode $(5,1)$ is because the resulting frequencies fall into a part of the earthquake displacement response spectrum, for which there is a significant variation in S_d. It should be noted that the significant decrease in frequencies are the result of the pre-loads representing a significant proportion of the critical buckling loads in this mode. These frequency changes become significantly effective as a result of the frequencies being at the sensitive area of the response spectrum.

A similar condition occurs for mode $(7,1)$. The significant variations of displacements of mode $(7,1)$ in Fig 5.14 are because of the considerable variation in S_d in Fig 6.1, which are the result of the variations of frequency of this mode in Fig 6.2(a) caused by the increase in pre-loading.

Stresses can also be derived in a similar way to displacements. After finding the modal displacement, stresses would be derived by replacing them into eqn (3.46). Maximum stresses are governed by multiplying the values of MPF of the selected modes by displacement response spectrum of the earthquake at the corresponding natural frequencies of the shell in that mode, and finally multiplying by stress factor given by the equation of stresses (eqn (3.46)).

As the distributions of responses are not the concern of this present study the double trigonometric series in eqn (3.46) is not taken into account. In order to verify this method for stress, using eqn (3.46) the values of $N_x = \frac{Eh}{1-\nu^2}(-\bar{u}_{ij}\frac{j\pi}{l} - \nu\frac{i\pi}{R\phi}\bar{v}_{ij} + \frac{\nu}{R}\bar{w}_{ij})$ in eqn (3.46) are plotted in Fig 6.3 for each of the modes $i = 1,3,\ldots,19$, and $j = 1,3,5$. For each value of i and j this factor is then multiplied by the MPF in Fig 6.2(b) and the displacement response spectrum corresponding to each frequency in Fig 6.1. The results of this multiplication are shown in Fig 6.4. Comparing the maximum N_x derived using this simplified method in Fig 6.4 and the maximum modal stress in Fig 5.17(a) shows that they are again basically the same. For example, the maximum

value of stress resultant, N_x, at mode $(1,1)$ in Fig 5.17 is equal to $5.096 \times 10^5\ N/m$. Within current accuracy this is the same as in Fig 6.4, which arises from the multiplication of the $MPF = 1.4$ by the value of $S_d = 0.01616\ m$ for mode $(1,1)$ by the value of $N_x = 2.282 \times 10^7\ N/m^2$ in Fig 6.3; the result would be equal to $1.4 \times 0.01616 \times 2.282 \times 10^7 = 5.096 \times 10^6\ N/m$. Comparing the maximum values of the rest of the modes in Fig 5.17(a) with the results in Fig 6.4 confirms that they too are effectively the same.

Using this method, a graph similar to the displacement response spectrum of earthquake (Fig 6.1) can be plotted for different stress resultant. However, it should be noted that unlike the displacement response spectrum (Fig 6.1), which is entirely dependent upon the earthquake, the stress response spectrum is also dependent on the formulation of stress itself, which in turn is dependent to the geometry of shell. The stress response can then be derived by multiplication of the stress response spectrum by MPF. However, when stress responses are plotted in terms of frequencies as in Figs 6.5-6.7 it aids visualization of what range of frequencies are more important in the various membrane and bending stress resultants. It is also useful to find the maximum total stress resultant response using these maximum responses, which will be discussed in section 6.2.

As the maximum total responses are important in design, the only aspect needed to complete the discussion is to relate the maximum modal responses to the maximum total response of shell. For ordinary frame buildings this can normally be achieved using the modal combination rule. Section 6.2 deals with the modal combination rules, and focuses on two methods for investigating whether these methods give accurate approximation of the maximum responses for shells.

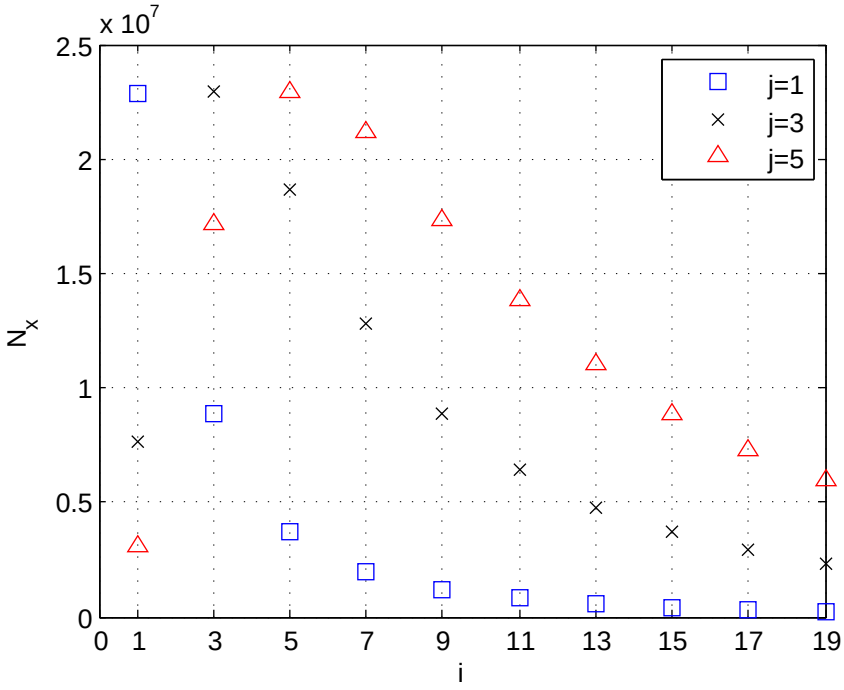

Figure 6.3: $N_x = \frac{Eh}{1-\nu^2}(-\bar{u}_{ij}\frac{j\pi}{l} - \nu\frac{i\pi}{R\phi}\bar{v}_{ij} + \frac{\nu}{R}\bar{w}_{ij})$ based on eqn (3.46)

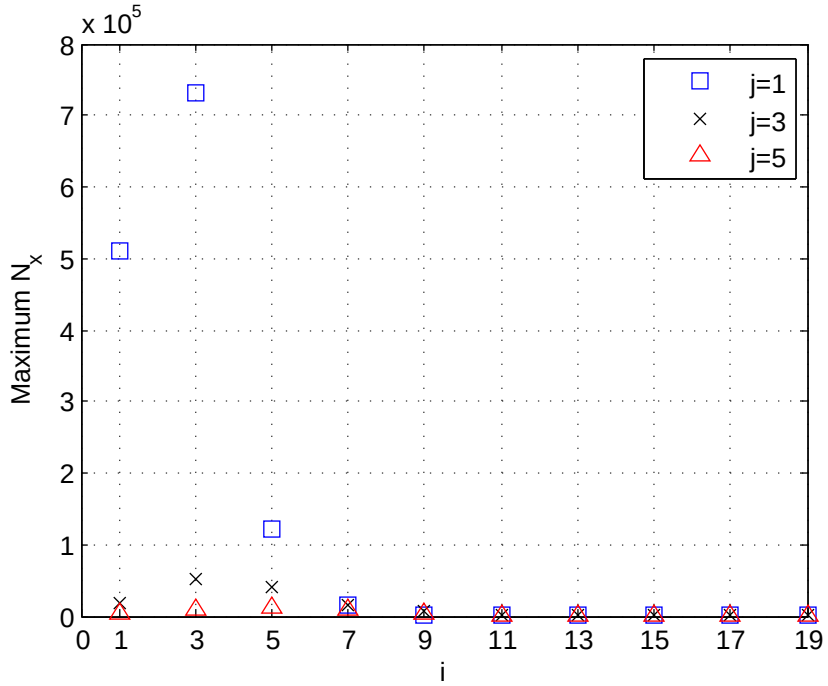

Figure 6.4: Maximum modal N_x found by multipying $N_x = \frac{Eh}{1-\nu^2}(-\bar{u}_{ij}\frac{j\pi}{l} - \nu\frac{i\pi}{R\phi}\bar{v}_{ij} + \frac{\nu}{R}\bar{w}_{ij})$ by the MPF in Fig 6.2(b) and the Landers earthquake displacement response spectrum in Fig 6.1 for a shell having $L_y/L_x = 1$, and $B = 1.5 \times 10^{-6}\ s^2$

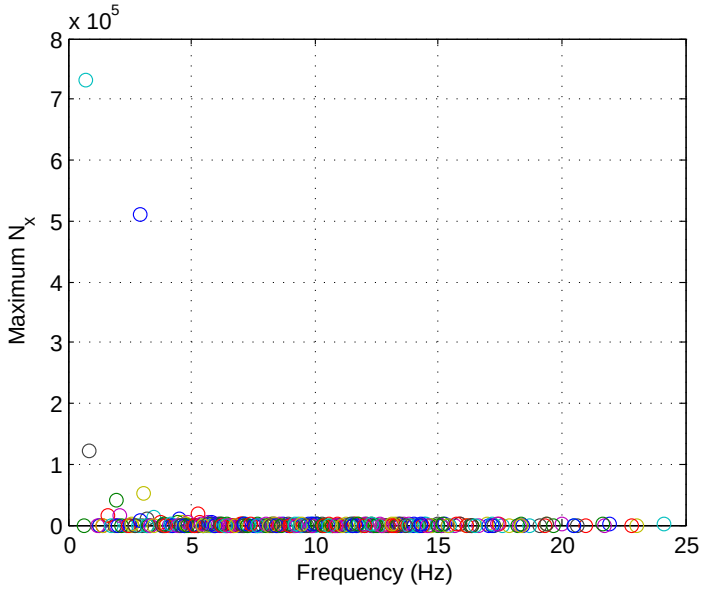

(a) N_x

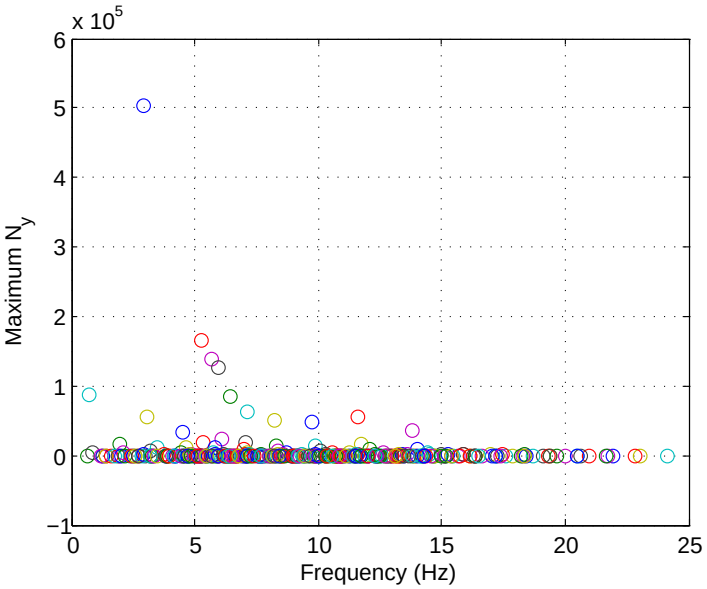

(b) N_y

Figure 6.5: Membrane stress modal contribution for a shell having $L_y/L_x = 1$, $B = 1.5 \times 10^{-6}\ s^2$ (ignoring self-weight)

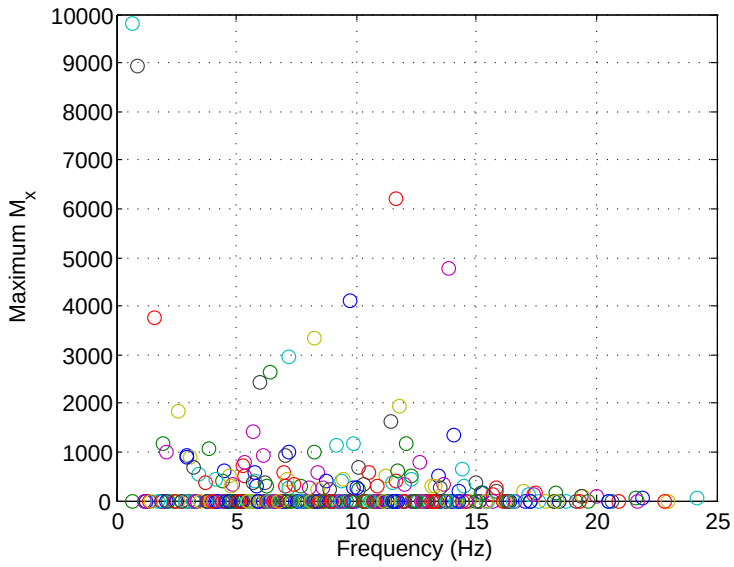

(a) M_x

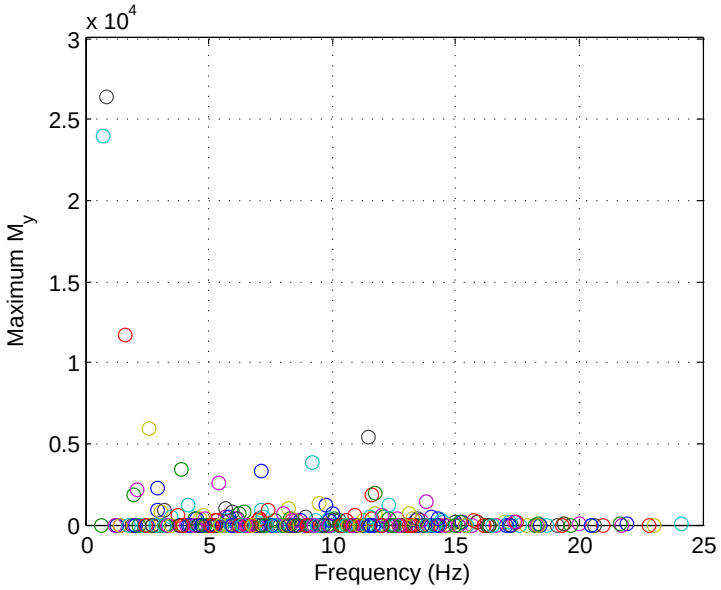

(b) M_y

Figure 6.6: Stress modal contribution for a shell having $L_y/L_x = 1$, $B = 1.5 \times 10^{-6}\ s^2$ (ignoring self-weight)

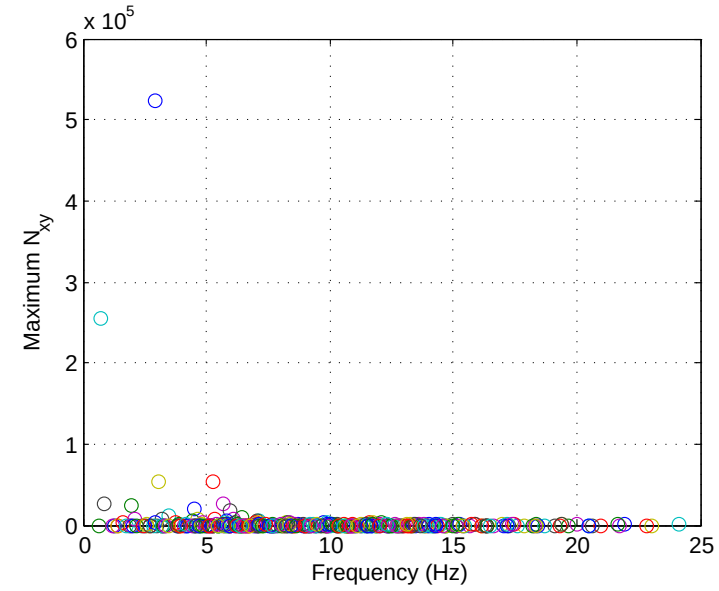

(a) N_{xy}

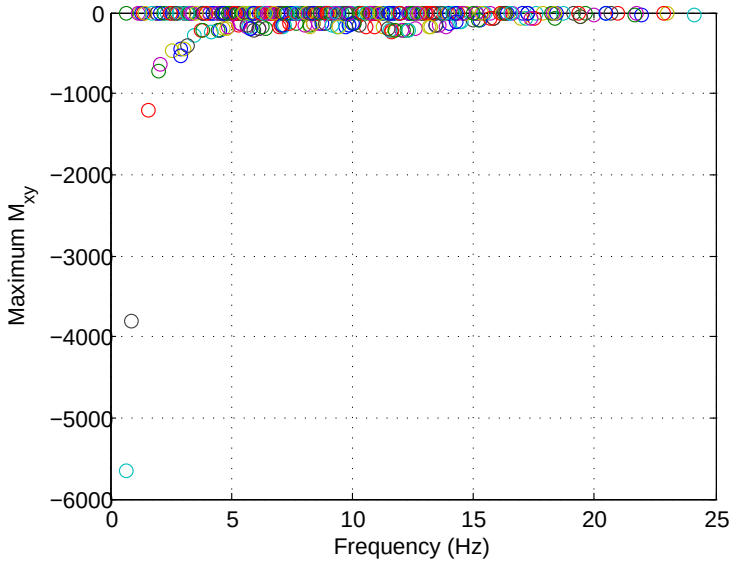

(b) M_{xy}

Figure 6.7: Bending and membrane stress modal contribution for a shell having $L_y/L_x = 1$, $B = 1.5 \times 10^{-6}\ s^2$ (ignoring self-weight)

6.2 Modal combination methods

In the previous section the relationships between the modal maximum response, natural frequencies of shell, and displacement and stress response spectrum of an earthquake were developed. Using these relationships makes it easy to find the maximum responses such as displacements and stress resultants in each mode without the need to go through the complete time history modal analysis.

As structural design is usually based on the peak total response values, the discussion would not be complete until the maximum modal responses could be related to the maximum total responses of the shell. This can be achieved using the modal combination methods.

Chopra [97] has outlined several methods for combining modes, while mentioning that none of these methods give exact results as the governing results are not identical to the total response using the complete time history analysis. The reason that the responses using one or other modal combination methods are not exact, is because the modal responses reach their peak values at a different instant in time and the total maximum responses attains its peak at yet another instant in time (Table 5.4). However, it is indicated that the predicted approximate responses would be accurate enough for practical structural design analysis.

In this section, two methods of modal combination will be discussed with their predictions compared with the known maximum total responses. The response of the shell in Fig 5.14 (a), (b), where the effects of pre-loading are not taken into account, will be examined for each of these methods. The reason for choosing this shell is that the contributions of modes having lower responses are also plotted as in Fig 5.14 (b), and consequently would give more convergent results. However, the rest of the cases in Figs 5.14 (c)-(e) have ignored the contributions of modes having a maximum displacement contribution less than $0.002\ m$, so they consequently cannot provide converged results as well. Use of these cases would have errors consisting of both those arising from the modal combination method and those from the non-converged results. The

results would not be then suitable for comparing with the total maximum response of Fig 5.12 using an accurate time history analysis with inclusion of a total of 19 by 19 half-waves in both circumferential and axial directions. The reason for not showing all contributing modes in the previous section was that the convergence of the results for total response was not the primary concern. For the sake of clarity of the plots, the contributions of modes with low responses were consequently neglected.

Multiplication of S_d by eqn (3.2) is one of the methods to find the maximum response of each mode over the time history of the earthquake. The maximum modal response can then be used for estimating the maximum total response using one of the modes combining method.

The maximum response of each mode can also be derived by multiplying MPF by S_d. As explained in section 5.5 these two methods give similar results. It is worthy to mention that this form of superposition is meant to take account of the fact that the maximum response in each mode occur at different instants of time, but at specific spatial locations on the shell surface. However another study is performed and will be presented later in this section, which examines the validity of modal combination methods when they are found regardless of the time of occurrence and its location over the surface of the shell.

The first method that will be presented here is the Square Root of the Sum of Squares (SRSS), first suggested by E. Rosenblueth as part of his PhD thesis [103], so that

$$r \approx (\sum_{n=1}^{N} r_n^2)^{0.5} \tag{6.2}$$

where r_{no} is the peak response in each mode n, and r_o is the maximum value of the estimated total response ($r_o = max\,|r(t)|$). In order to check the validity of this method for shells, the maximum response of each mode regardless of time are presented in Table 6.1 for the shell in Fig 5.14(a),(b).

Using the SRSS method, the maximum total displacement would be $0.0914\ m$. By comparing the governing maximum response using the SRSS method against the total maximum response found from the time history analysis (THA) of $0.0953\ m$ shown in

(i, j)	$Max - Disp$
$(3, 1)$	0.08192
$(5, 1)$	0.03286
$(1, 1)$	0.0215
$(7, 1)$	0.007467
$(9, 1)$	0.002273
$(5, 3)$	0.002103
$(3, 3)$	0.002193
$(1, 3)$	0.002187
$(1, 5)$	0.001626
$(1, 7)$	0.001416
$(7, 3)$	0.001288

Table 6.1: Maximum modal displacement for a shell having $L_y/L_x = 1$, $B = 1.5 \times 10^{-6}\ s^2$ as discussed in Fig 5.14(a),(b)

Fig 5.12, it will be noticed that there is a 4.2% error as can be seen in Table 6.2 for a shell with $L_y/L_x = 1$, $B = 1.5 \times 10^{-6}\ s^2$.

As Chopra explained [97] the SRSS method gives practically accurate estimates of the responses in structures with well-separated frequencies such as frames. However, for systems with closely spaced natural frequencies such as pipings and multi-storey buildings with unsymmetrical plan it will not provides accurate responses. As the shell is a system with closely spaced natural frequencies, this method may not always be used reliably.

The next method for modal combination is the Complete Quadratic Combination (CQC), which is applicable to a wider range of structures and is suggested to provide accurate results for structures with closely-spaced frequencies [97]. The maximum total response using CQC method is derived using

$$r_o \approx (\sum_{i=1}^{N} \sum_{n=1}^{N} \rho_{in} r_{io} r_{no})^{0.5} \tag{6.3}$$

where r_{io}, and r_{no} are the peak responses in the i^{th} and n^{th} modes and ρ_{in} is the correlation coefficient for these two modes. ρ_{in} varies between 0 and 1 and it is equal to 1 when $i = n$. Eqn (6.3) can be rewritten as the sum of the SRSS plus the additional term as

$$r_o \approx (\sum_{n=1}^{N} r_{no}^2 + \underbrace{\sum_{i=1}^{N}\sum_{n=1}^{N}}_{i\neq n} \rho_{in} r_{io} r_{no})^{0.5} \tag{6.4}$$

The first term in eqn (6.4) is identical to SRSS and is positive, however the second term may be positive or negative. Thus the result using CQC method could be either less or more than the governing results using SRSS method. There are several definition for the correlation coefficient proposed by researchers. However, in this section the Rosenblueth-Elorduy definition which is given by Newmark and Rosenblueth in the textbook Fundamentals of Earthquake Engineering [104] is used for a constant value of damping ratio, ζ, in all modes as

$$\rho_{in} = \frac{\zeta^2(1+\beta_{in})^2}{(1-\beta_{in})^2 + 4\zeta^2\beta_{in}} \tag{6.5}$$

where $\beta_{in} = \frac{\omega_i}{\omega_n}$ is the ratio of frequencies in modes i and n.

The maximum displacement prediction using the CQC method for the shell in Fig 5.14(a),(b) is equal to $0.0974\ m$, which as can be seen in Table 6.2 for the shell with $L_y/L_x = 1$, $B = 1.5 \times 10^{-6}\ s^2$, has just a 2.2% error as compared with the maximum displacement of $0.0953\ m$ using the time history analysis. This is lower than the 4.09% error using the SRSS method as shown in Table 6.2.

As mentioned earlier two methods are chosen in this study to find the maximum responses of the shell. First method finds the maximum responses of the shell for every points over the surface of the shell but only regardless of the time. The second method finds the maximum responses of the shell regardless of where and when they occur.

Table 6.2 provides the summary of the maximum displacement and stress responses for three cases of shell using the complete modal time history analysis (THA) method and compares with the responses using the SRSS, CQC at the same location where the maximum response using the time history analysis occurs. However, this analysis is performed for all 24 cases of shells used in this research, and is reported in Appendix

A. As mentioned, the peak responses using either SRSS or CQC method are governed by finding the maximum modal response regardless of the time of occurrence but taking into account their location over the surface of the shell. In other words it finds the maximum modal response at each point over the surface of the shell and combines them accordance with one of the combination methods (SRSS and CQC). In this way a maximum response would be attained for every point over the surface of the shell.

The modal combination methods are also used to find the maximum stress resultants. The maximum modal stress resultants shown in Table 6.2 for three cases of shells, are derived using the maximum modal stresses governed by the method described in section 6.1. However, again the responses for all 24 cases of shells are reported in Appendix A. The maximum stress responses are derived over the time history of earthquake and at each point over the surface of the shell. Same as displacements, the maximum stresses and their location are found using the THA method. The maximum stresses are then compared with the maximum stresses using the SRSS and CQC method at the location where the maximum stress resultants are found using THA method; these are reported in Table 6.2.

In Table 6.2 the error in SRSS and CQC method are expressed as a percentage of the maximum result derived using the time history modal analysis. It is noticed that the peak response using approximate methods can be either lower or higher than the THA value. The error is different for each of the membrane and bending stress resultants; for example for the case of shell with $L_y/L_x = 1$ and $B = 1 \times 10^{-6}\ s^2$, the error in N_x is less than the error in N_y, M_y, and M_x (Table 6.2). The reason that the error is smallest in N_x is that the modes with higher frequencies do not contribute to the total response as can be seen from Fig 3.16. However, modes with higher frequencies contribute to the total response more significantly in N_y, M_y, and M_x (Fig 3.16, Table 3.5); so the error of using the combination methods are higher in these responses. The error in displacement for this case of shell ($L_y/L_x = 1$ and $B = 1 \times 10^{-6}\ s^2$) is also small; again because the modes participating in the total responses have low frequencies as can be seen in Fig 3.16(a). The SRSS and CQC methods do not give the same estimates of peak stress responses. Analysis on three cases of shells in Table 6.2 shows that the

	L_y/L_x	B	THA	SRSS	CQC	% error SRSS	% error CQC
W (m)	1	1	0.0663	0.0593	0.0585	10.56	11.76
	1	1.5	0.0953	0.0914	0.0974	4.02	2.2
	2	1.5	0.0183	0.0161	0.015	12.02	18.03
N_x $(N.m^{-1})$	1	1	1.0494	0.9820	0.9935	6.43	5.33
$\times 10^6$	1	1.5	0.8741	0.9016	0.9419	3.16	7.77
	2	1.5	0.2607	0.2943	0.2936	12.91	12.63
N_y $(N.m^{-1})$	1	1	0.7897	0.4707	0.6623	40.39	16.14
$\times 10^6$	1	1.5	0.5737	0.5918	0.5825	3.15	1.54
	2	1.5	0.5835	0.4294	0.4170	26.41	28.54
N_{xy} $(N.m^{-1})$	1	1	0.9348	0.6042	0.6745	35.36	27.85
$\times 10^6$	1	1.5	0.6176	0.5902	0.6374	4.43	3.21
	2	1.5	0.4131	0.3253	0.3482	21.25	15.71
M_x $(N.m)$	1	1	2.5194	1.6260	1.9647	35.46	22.02
$\times 10^4$	1	1.5	1.7751	1.3679	1.3648	22.94	23.12
	2	1.5	1.5797	1.7111	1.4289	8.32	9.55
M_y $(N.m)$	1	1	0.6663	0.4302	0.4619	35.43	30.67
$\times 10^5$	1	1.5	0.4483	0.3444	0.3163	23.16	29.44
	2	1.5	0.1698	0.1560	0.1575	8.18	7.26
M_{xy} $(N.m)$	1	1	1.8188	0.9580	1.2093	47.33	33.51
$\times 10^4$	1	1.5	1.1770	0.7249	0.8038	38.42	31.71
	2	1.5	0.8243	0.4833	0.6165	41.36	25.20

Table 6.2: Comparison of the results between modal time history analysis, CQC, and SRSS for a total number of 19 axial and circumferential half waves including effect of location

CQC method does not always produce lower percentage errors than the SRSS method as is often accepted by many researchers [97].

However, another method is proposed in this research, which can be named as second approach for finding the maximum response. This method also uses the method of section 6.1 in finding the maximum responses not only over the duration of earthquake, but also over the surface of the shell. The displacement and the stress resultants using this method are shown in Table 6.3. As can be seen, the percentage of error for CQC and SRSS method for shells using this second method can be either higher or lower than the first method. However, the maximum displacement (W), N_{xy} and M_{xy} response in Table 6.2 seems to be the same as in Table 6.3.

As can be seen by comparing Tables 6.2 and 6.3 some stress resultants have changed significantly as a result of taking into account the location over the surface of the shell in finding the modal peak responses; such as the error corresponding to CQC method in M_x for a shell with $L_y/L_x = 2$, $B = 1.5 \times 10^{-6}\ s^2$, that has reduced from 103.87% in Table 6.3 to 9.55% in Table 6.2. It is noted that using these two methods does not change the governing peak displacement response using SRSS method. The significant change in the result using CQC method based on the two aforementioned methods is a result of the cross-correlation coefficient being significant when the peak modal displacement responses are chosen, regardless of its location over the surface of the shell. This shows that CQC method is sensitive to the location of the peak modal responses over the surface of the shell and peak responses happening at different locations of the shell can not simply be combined using the CQC method. In other words in CQC method, the maximum modal displacement responses that are derived regardless of the time of occurrence over the time history of earthquake but taking into account the location are more reliable. The maximum responses over the surface of the shell can then be found from the peak nodal responses. However, finding the peak responses regardless of time and location has the advantage of reducing the calculation time significantly. As both methods give the same displacement response as of SRSS method, the latter method can be accurately used for SRSS method.

For the three cases of shells in Table 6.2 the maximum error using SRSS remain less than 12.02% and for CQC less than 18.03% for displacement. However, for stress re-

	L_y/L_x	B	THA	SRSS	CQC	% error SRSS	% error CQC
W (m)	1	1	0.0663	0.0593	0.0638	10.56	3.77
	1	1.5	0.0953	0.0914	0.864	4.09	9.34
	2	1.5	0.0183	0.0201	0.02	9.84	9.29
N_x $(N.m^{-1})$	1	1	1.0494	1.074	1.135	2.34	8.16
$\times 10^6$	1	1.5	0.8741	0.9016	0.9121	3.15	4.35
	2	1.5	0.2607	0.2943	0.2813	12.89	7.90
N_y $(N.m^{-1})$	1	1	0.7897	0.7552	1.0775	4.37	36.44
$\times 10^6$	1	1.5	0.5737	0.5918	0.7737	3.15	34.86
	2	1.5	0.5835	0.6646	0.8167	13.90	39.97
N_{xy} $(N.m^{-1})$	1	1	0.9348	0.6042	0.6745	35.37	27.85
$\times 10^6$	1	1.5	0.6176	0.5902	0.6374	4.44	3.21
	2	1.5	0.4131	0.3253	0.3482	21.25	15.71
M_x $(N.m)$	1	1	2.5194	2.6736	3.9476	6.12	56.69
$\times 10^4$	1	1.5	1.7751	1.8441	2.9145	3.89	64.19
	2	1.5	1.5797	1.9659	3.2205	24.74	103.87
M_y $(N.m)$	1	1	0.6663	0.5267	0.6015	20.95	9.73
$\times 10^5$	1	1.5	0.4483	0.3951	0.412	11.87	8.10
	2	1.5	0.1698	0.1837	0.2509	8.19	47.76
M_{xy} $(N.m)$	1	1	1.8188	0.958	1.2093	47.33	33.51
$\times 10^4$	1	1.5	1.177	0.7249	0.8038	38.41	31.71
	2	1.5	0.8906	0.4386	0.6233	50.75	30.01

Table 6.3: Comparison of the results between modal time history analysis, CQC, and SRSS for a total number of 19 axial and circumferential half waves neglecting effect of location

sultants such as N_y the errors are respectively less than 40.39% and 28.54%. The error for axial stress, N_x, which has only the contribution from modes with low frequencies also remain less than 12.91% and 12.63% respectively using SRSS and CQC method.

It can be concluded that the modal combination method can only give practially acceptable errors for displacement and axial membrane stress resultant. However, the stress resultants other than N_x can not be estimated accurately using the modal combination methods.

The results of this section show that the percentage of error is different for each of the membrane, bending stress resultant, and displacement responses. The results are also dependent on the material properties and geometry of the shell, which determine the natural frequencies of the shell. Using the combination methods for finding the displacements are more reliable than for stresses; this can be seen in Table 6.2.

Chapter 7

Effects of Pre-loading on the Dynamic Response of Cylindrical Shell Roof-FE

ABAQUS does not automatically consider the effects of self-weight in the extraction of natural frequencies. Most research reports also appear to neglect the effects of pre-loading in the analysis of roof shell using the FE method based on a geometrically linear analysis [59], [7], [105]. As shown in section 5.3 and 5.4 performing a geometrically linear modal analysis could lead to a great underestimation of responses for large roof shells. This section shows why the FE programme should be instructed to account for geometric nonlinearities.

7.1 Linear eigenvalue buckling analysis

The first form of numerical analysis for the present research is the classical buckling load. This analysis is performed to allow comparison with the analytical method described in section 5.1 based on idealized membrane theory; it also enables upper estimates to be found for collapse load. Generally, eigenvalue buckling analysis is used to estimate the critical buckling load of stiff structures, which prior to any buckling carry their design loads by axial or membrane compressive action and suddenly bend under critical loading. As the response of the stiff structures involves very little deformation prior to buckling, the linear eigenvalue buckling analysis ignores any elastic deformations and the elements are assumed to remain in their undeformed original

state. Moreover, for structures which are not stiff, such as shell structures, and might have a nonlinear response before collapse, this eigenvalue buckling analysis can assist in the prediction of collapse mode shapes. However. in this case it can not predict the collapse load correctly.

In an eigenvalue buckling analysis the critical loads are derived when the stiffness matrix in eqn (7.1) becomes singular

$$K^{NM}\phi_i^M = 0 \tag{7.1}$$

Same as eqn (4.1), K^{NM} is the tangent stiffness matrix. In ABAQUS K^{NM} is defined as $K_0^{NM} + \lambda_i K_\Delta^{NM}$, in which K_0^{NM} is the stiffness matrix of the base state; it includes the effect of pre-loading (P^N) should any exist, K_Δ^{NM} is the sum of the differential initial stress and load stiffness matrix due to the incremental loading pattern, Q^N, λ_i are the eigenvalues; υ_i^M are the critical modes shapes; M and N are degrees of freedom of the whole model, and i defines a ranking of the critical loads. If pre-loading (P^N) is included in the analysis the critical loads are then given as $P^N + \lambda_i Q^N$. Otherwise they are given by $\lambda_i Q^N$. Usually the smallest λ and its associated critical mode shapes (ϕ_i^M) are of interest.

Same as the procedure for finding the natural modes in section 4.3, in ABAQUS the critical mode shapes are normalized vectors so that the maximum displacement component has a magnitude of 1.0. Therefore, they do not represent the actual magnitude of the deformation at critical load. However, these critical mode shapes are useful in predicting the possible buckling failure mode of the structure.

ABAQUS allows the critical loads and the associated mode shapes to be derived using the *BUCKLE command. There are two iteration methods built in ABAQUS for the extraction of critical loads; the ”Lanczos” method and ”Subspace” method. In this study the ”Subspace” method is chosen, for which it is possible to specify the desired number of eigenvalues or the maximum eigenvalue of interest. ABAQUS will extract eigenvalues until either the requested number of modes has been extracted or the last eigenvalue extracted exceeds the level of the maximum eigenvalue of interest.

During an eigenvalue buckling prediction step, ABAQUS first performs a static perturbation analysis to create the incremental stresses, $\Delta\sigma$, due to loading vector Q^N. In this static perturbation analysis, the tangent stiffness K_0^{NM} is used and the stiffness matrix K_Δ^{NM}, corresponding to the incremental stress and loading vector is formed.

In order to compare the numerical solution with the analytical solution developed in section 5.1, the lowest 10 critical loads are derived and presented in Tables 7.1 to 7.3 for the same three cases of shells as in section 5.3. As explained in section 5.1, in the analytical solution, the self-weight and additional imposed load are approximated to be in the radial direction, since the shells are considered to be shallow shell. The buckling load in FE is also derived in the radial direction to be comparable with the analytical solutions. However, to check the accuracy of the approximation another analysis is performed later in this section, which compares the buckling loads derived based on the load being applied in radial and vertical directions.

$Analytical(i,j)$	ABAQUS Mesh 60×60	ABAQUS Mesh 120×120	error (%)
$8093.2788(4,1)$	$7985(3.9,1)$	7984.7	1.34
$8911.2217(5,1)$	$9126(4.8,1)$	9125.7	2.41
$11770.8207(6,1)$	$12302(5.5,1)$	12300	4.50
$15563.8459(7,1)$	$13472(4.6,1)$	13471	13.4
$16751.9128(3,1)$	$15104(6,2)$	15101	9.86
$17008.6539(6,2)$	$15693(5,2)$	15690	7.75
$18971.0297(7,2)$	$17546(7,2)$	17542	7.51
$19498.5117(5,2)$	$17785(6.5,1)$	17781	8.81
$20057.5858(8,1)$	19611	19605	2.25
$22743.8916(8,2)$	$19624(5.8,2.8)$	19617	13.74

Table 7.1: Lowest 10 critical loads for a shell with $R = 104.8\ m$, $L_y/L_x = 1$, $\Phi = \pi/3$, $h = R/500$, $B = \rho hR/E = 1.5 \times 10^{-6}\ s^2$, $\rho = 3137.2\ kg/m^3$, $E = 46 \times 10^9\ N/m^2$ (Case 3), having the natural frequencies as in Table 5.3

Table 7.1 presents the comparison between the lowest 10 critical loads using analytical and FE methods for a shell having $R = 104.8\ m$, $L_y/L_x = 1$, $\Phi = \pi/3$, $h = R/500m$, $B = \rho hR/E = 1.5 \times 10^{-6}\ s^2$, $\rho = 3137.2\ kg/m^3$, $E = 46 \times 10^9\ N/m^2$; this is the same shell having frequencies as in Table 5.3. Comparing two different mesh sizes shows that the results are adequately converged using a 60×60 mesh. Unlike the analytical model, the mode shapes in Fig 7.1 and 7.2 are not pure sinusoidal waves. Finding the equivalent (i, j) is possible by looking at the wavelengths associated with the most dominant part of the modal deformation. For example the i value corresponding to 8^{th} mode is approximately 6.5. This is found by dividing the total length of the section, $w = 104.8\ m$, by the half-wave length between points of contraflexures associated with the dominant part of this mode shape, $l = 16\ m$. The corresponding mode shapes in Fig 7.1 shows that in the FE analysis some modes such as mode 4 (Fig 7.1(d)) has contributions from different modes. The difference between the resulting critical load using the analytical and FE methods is because of the analytical results are based on an idealized membrane state; but in FE there would be some deformations as a result of boundary conditions. Fig 7.2 shows the normalized displacements along center-line bb for some selected modes. These mode shapes such as 3^{rd}, 4^{th}, 8^{th}, and 10^{th} modes clearly involve coupling between the equivalent analytical modes. For example in Fig 7.2(c), 8^{th} mode has appeared to be created from coupling of modes $(7, 1)$ and $(3, 1)$.

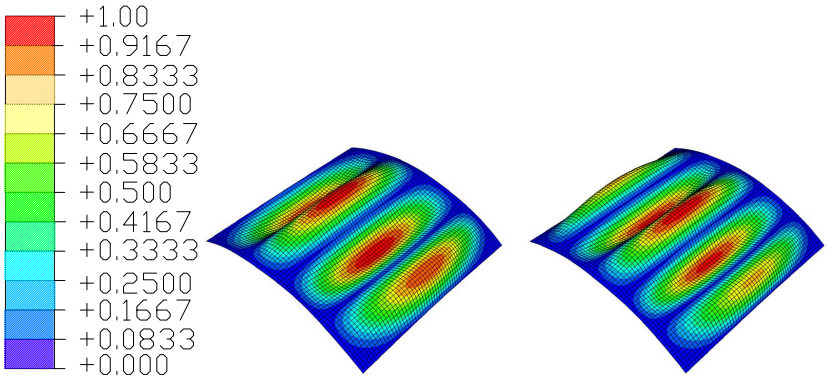

(a) Displacement magnitude (b) $P_c = 7985\ (N/m^2)$ (c) $P_c = 9126\ (N/m^2)$

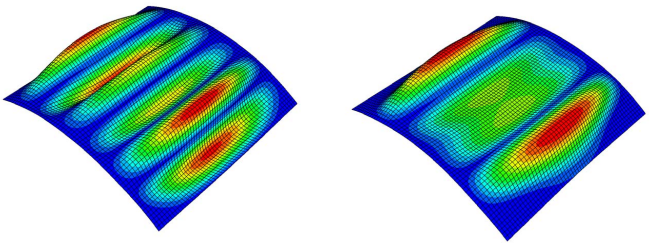

(d) $P_c = 12302\ (N/m^2)$ (e) $P_c = 13472\ (N/m^2)$

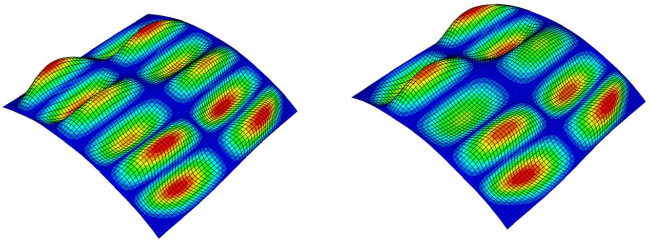

(f) $P_c = 15104\ (N/m^2)$ (g) $P_c = 15693\ (N/m^2)$

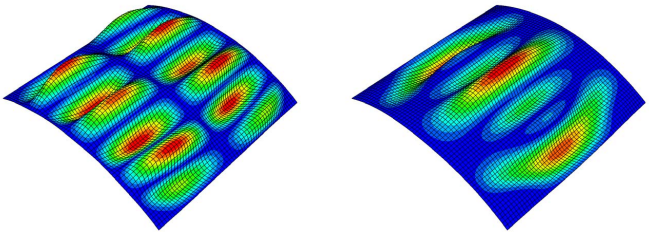

(h) $P_c = 17546\ (N/m^2)$ (i) $P_c = 17785\ (N/m^2)$

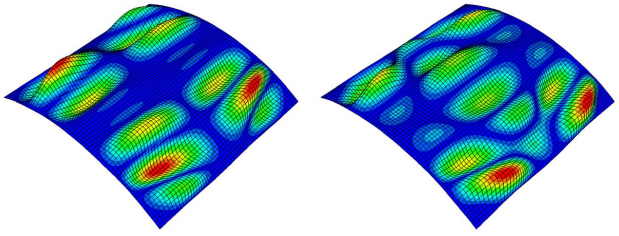

(j) $P_c = 19611\ (N/m^2)$ (k) $P_c = 19624\ (N/m^2)$

Figure 7.1: Lowest 10 critical modes for case 3

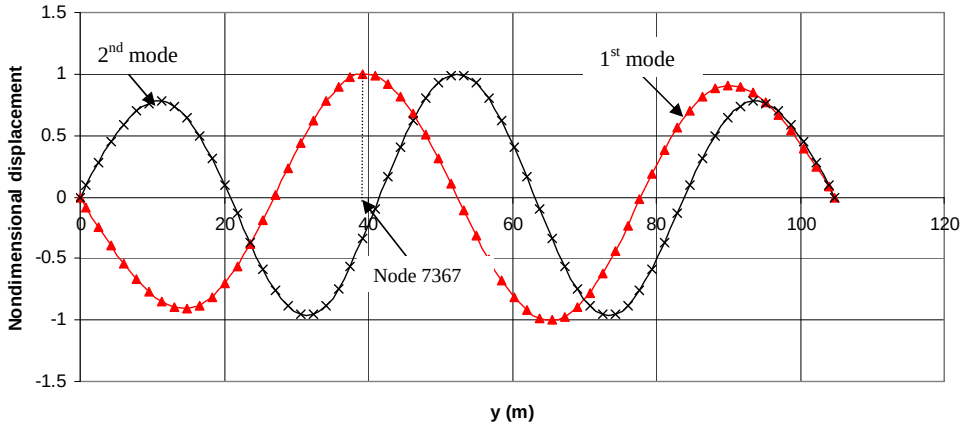

(a) 1^{st} critical load $= 7985\ (N/m^2)$, 2^{nd} critical load $= 9126\ (N/m^2)$

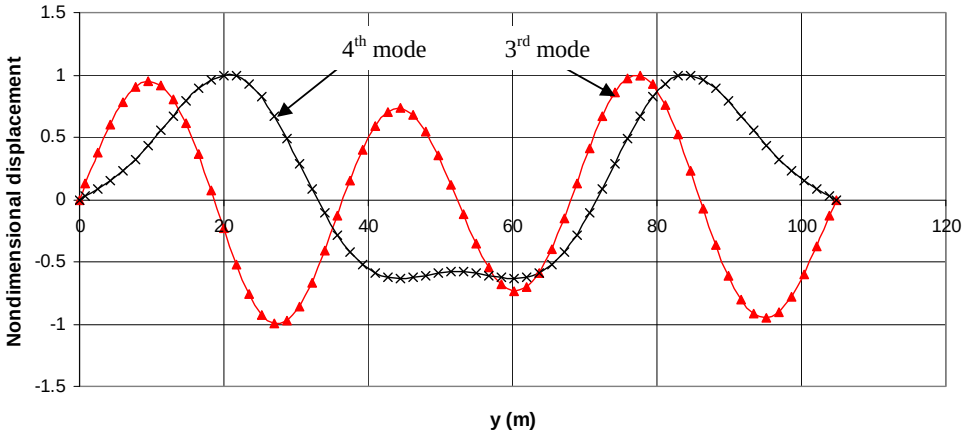

(b) 3^{rd} critical load $= 12302\ (N/m^2)$, 4^{th} critical load $= 13472\ (N/m^2)$

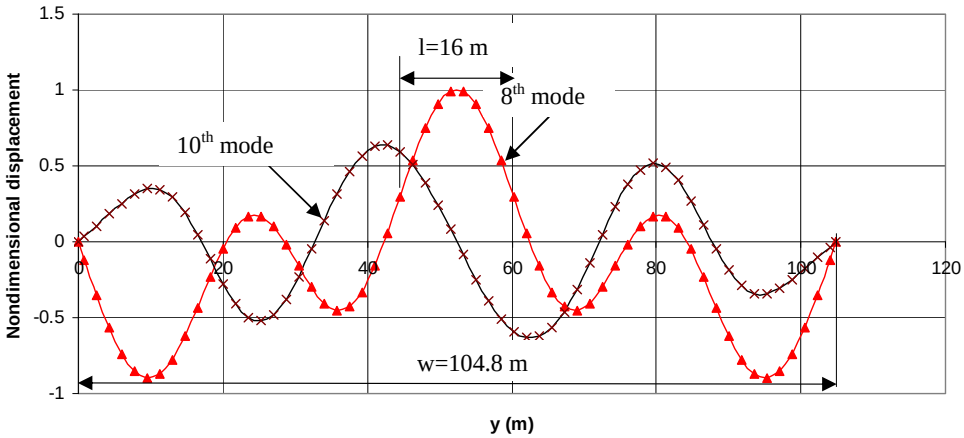

(c) 8^{th} critical load $= 17785\ (N/m^2)$, 10^{th} critical load $= 19624\ (N/m^2)$

Figure 7.2: Normalised FE model displacement profiles along center-line bb at critical modes for shell with $R = 104.8\ m$, $L_y/L_x = 1$, $\Phi = \pi/3$, $h = R/500m$, $B = \rho hR/E = 1.5 \times 10^{-6}\ s^2$, $\rho = 3137.2\ kg/m^3$, $E = 46 \times 10^9\ N/m^2$

$Analytical(i,j)$	ABAQUS Mesh 60×60	error (%)
$11436.15(4,1)$	$11284(3.96,1)$	1.33
$12591.94(5,1)$	$12894(4.8,1)$	2.40
$16632.68(6,1)$	$17383(5.5,1)$	4.51
$21992.39(7,1)$	$19037(4.6,1)$	13.44
$23671.18(3,1)$	$21343(6,2)$	9.84
$24033.97(6,2)$	$22175(5,2)$	7.73
$26806.89(7,2)$	$24794(7,2)$	7.51
$27552.24(5,2)$	$25130(6.5,1)$	8.79
$28342.24(8,1)$	27711	2.23
$32138.11(8,2)$	$27729(5.8,2.8)$	13.7

Table 7.2: Lowest 10 critical loads for a shell with $R = 104.8\ m$, $L_y/L_x = 1$, $\Phi = \pi/3$, $h = R/500m$, $B = \rho hR/E = 1.25 \times 10^{-6}\ s^2$, $\rho = 3692\ kg/m^3$, $E = 65 \times 10^9\ N/m^2$ (Case 2), having the natural frequencies as in Table 5.2

Table 7.2 also compares the critical loads for a shell with $R = 104.8\ m$, $L_y/L_x = 1$, $\Phi = \pi/3$, $h = R/500m$, $B = \rho hR/E = 1.25 \times 10^{-6}\ s^2$, $\rho = 3692\ kg/m^3$, $E = 65 \times 10^9\ N/m^2$ having the natural frequencies as presented in Fig 5.9. The mode shapes of the analytical solution are shown in parenthesis and are based on a pure membrane state. The lowest critical eigenvalue of $11284\ N/m2$ obtained from ABAQUS was found to be very close to that obtained from the analytical approach, $11436\ N/m^2$. Fig 7.3 shows the mode shapes corresponding to the lowest 10 critical loads from the FE analysis. Also, Fig 7.2 shows the radial displacement profile of some selected modes along center line bb. It can be seen that none of the mode shapes are a pure sinusoidal wave as in the analytical solutions. In addition different modes can be seen to contribute to a given mode shape as in for example the displacement profiles of the critical modes in Fig 7.2. The mode coupling could be due to the effect of boundary conditions which introduce nonlinearities to the system.

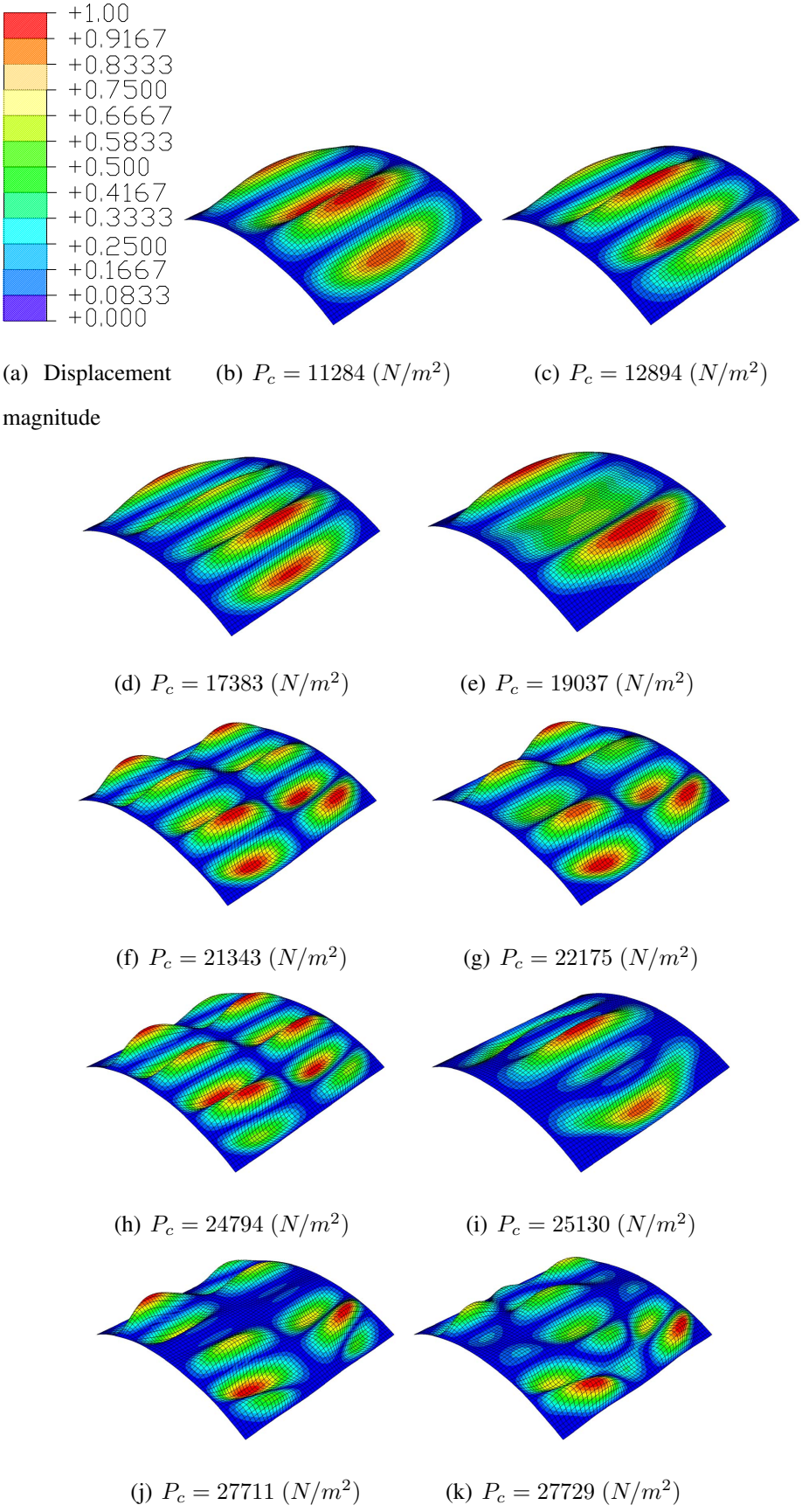

(a) Displacement magnitude (b) $P_c = 11284\ (N/m^2)$ (c) $P_c = 12894\ (N/m^2)$

(d) $P_c = 17383\ (N/m^2)$ (e) $P_c = 19037\ (N/m^2)$

(f) $P_c = 21343\ (N/m^2)$ (g) $P_c = 22175\ (N/m^2)$

(h) $P_c = 24794\ (N/m^2)$ (i) $P_c = 25130\ (N/m^2)$

(j) $P_c = 27711\ (N/m^2)$ (k) $P_c = 27729\ (N/m^2)$

Figure 7.3: Lowest 10 critical modes for case 2

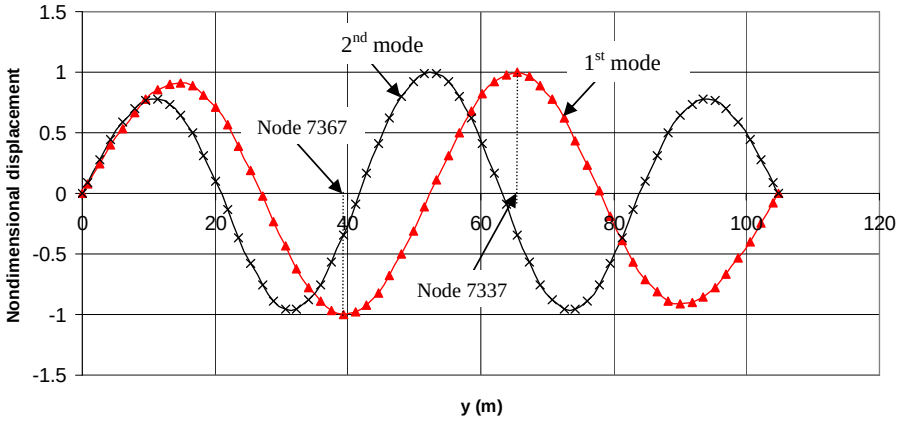

(a) 1^{st} critical load $= 11284\ (N/m^2)$, 2^{nd} critical load $= 12894\ (N/m^2)$

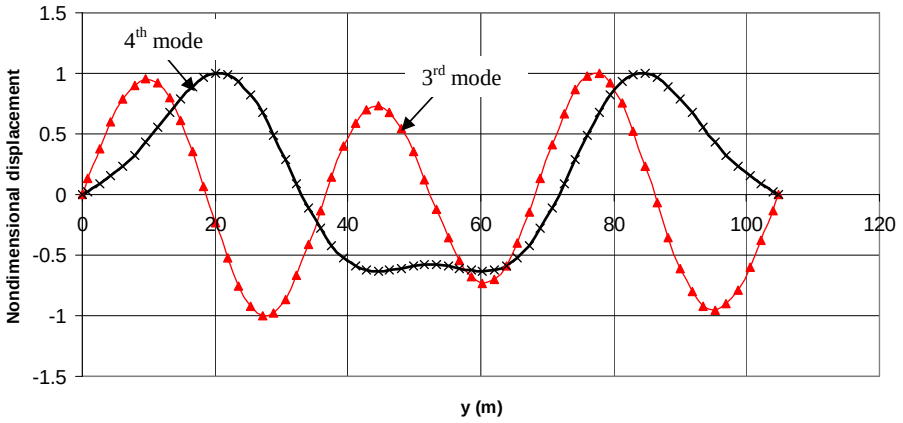

(b) 3^{rd} critical load $= 17383\ (N/m^2)$, 4^{th} critical load $= 19037\ (N/m^2)$

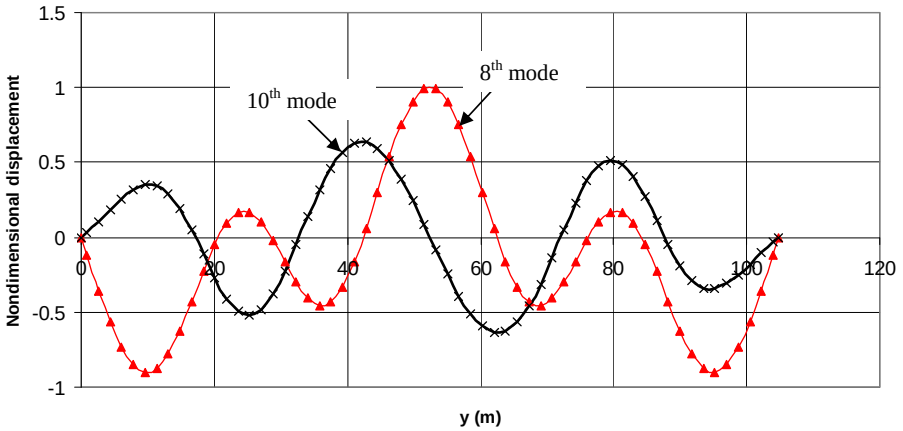

(c) 8^{th} critical load $= 25130\ (N/m^2)$, 10^{th} critical load $= 27729\ (N/m^2)$

Figure 7.4: Normalised displacement profiles along center-line bb at critical modes for shell with $R = 104.8\ m$, $L_y/L_x = 1$, $\Phi = \pi/3$, $h = R/500m$, $B = \rho hR/E = 1.25 \times 10^{-6}$, $\rho = 3692\ kg/m^3$, $E = 65 \times 10^9\ N/m^2$

$Analytical(i,j)$	ABAQUS Mesh 60×60	error (%)
$110926(6,1)$	$110896(5.6,1)$	0.03
$123724(7,1)$	$120765(5.1,1)$	2.39
$127164(5,1)$	$126714(6.1,1)$	0.35
$148329.7(8,1)$	$149277(7.4,1)$	0.64
$179729(9,1)$	$188862(8.6,1)$	5.08
$216236(10,1)$	$205000(7.5,1)$	5.19
$243637.8(4,1)$	224224	7.97
$253099.8(8,2)$	226934	10.34
$257211.9(11,1)$	243690	5.26
$262633.5(9,2)$	244252	7.00

Table 7.3: Lowest 10 critical load for a shell with $R = 104.8\ m$, $L_y/L_x = 2$, $\Phi = \pi/3$, $h = R/500m$, $B = \rho hR/E = 0.5 \times 10^{-6}\ s^2$, $\rho = 6840\ kg/m^3$, $E = 30 \times 10^{10}\ N/m^2$ (Case 1)

A third example shows the critical loads for a shell with $R = 104.8\ m$, $L_y/L_x = 2$, $\Phi = \pi/3$, $h = R/500m$, $B = \rho hR/E = 0.5 \times 10^{-6}\ s^2$, $\rho = 6840\ kg/m^3$, $E = 30 \times 10^{10}\ N/m^2$. The analytical natural frequencies of this shell were previously shown in Fig 5.11. The associated critical modes are summarized in Fig 7.5. The lowest critical load derived by ABAQUS is identical with the analytical one. However, the mode shapes are not identical to those found using analytical method. Fig 7.6 summarizes the radial displacement profile along center-line bb for some selected modes. It is noticed that unlike the mode shapes in the analytical solutions, none of the mode shapes in FE corresponds to a perfect sinusoidal waves. However, as explained earlier the equivalent (i,j) in FE is derived by measuring the ratio of the length to the wavelength between two contraflexure point associated with the most dominant part of the modal deformation. For example in mode 5 the equivalent circumferential half-waves is $i = 8.6$; this is found by dividing the total length, $w = 104.8\ m$, by the half-wave length between the two points of contraflexure, $l = 12\ m$. Using the same method $i = 7.5$ for the 6^{th} mode; it is found by dividing $w = 104.8\ m$ by $l = 14\ m$ as shown

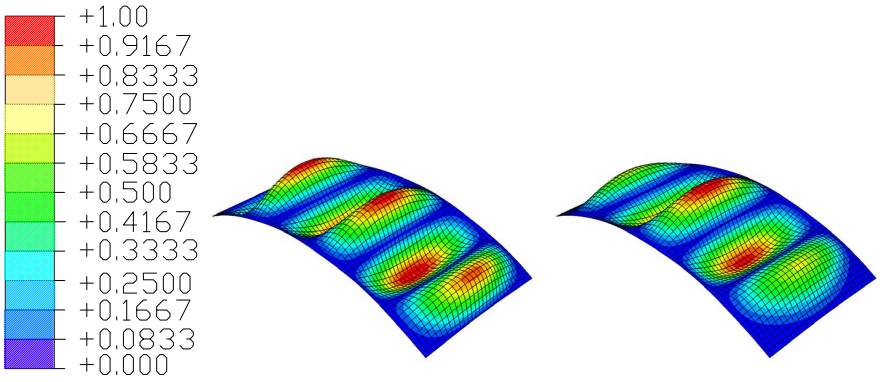

(a) Displacement magnitude (b) $P_c = 110896\ (N/m^2)$ (c) $P_c = 120765\ (N/m^2)$

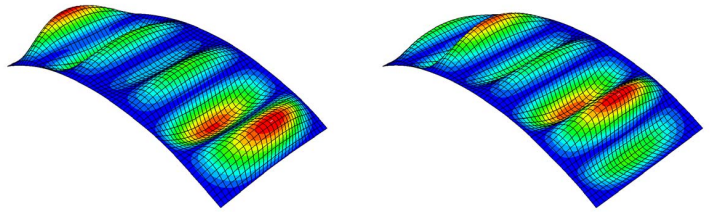

(d) $P_c = 126714\ (N/m^2)$ (e) $P_c = 149277\ (N/m^2)$

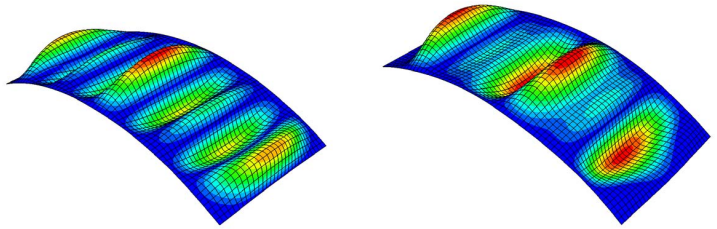

(f) $P_c = 188862\ (N/m^2)$ (g) $P_c = 205000\ (N/m^2)$

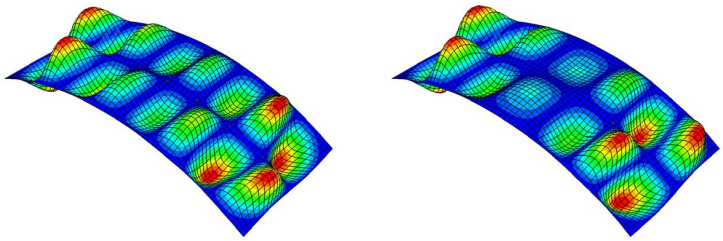

(h) $P_c = 224224\ (N/m^2)$ (i) $P_c = 226934\ (N/m^2)$

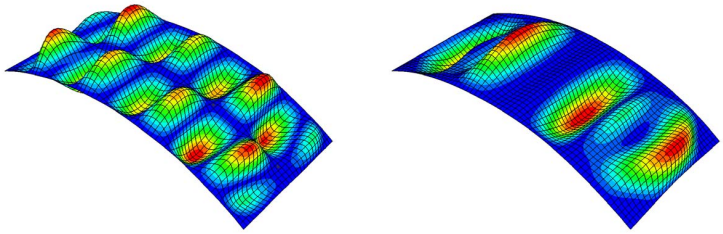

(j) $P_c = 243690\ (N/m^2)$ (k) $P_c = 244252\ (N/m^2)$

Figure 7.5: Lowest 10 critical modes for case 1

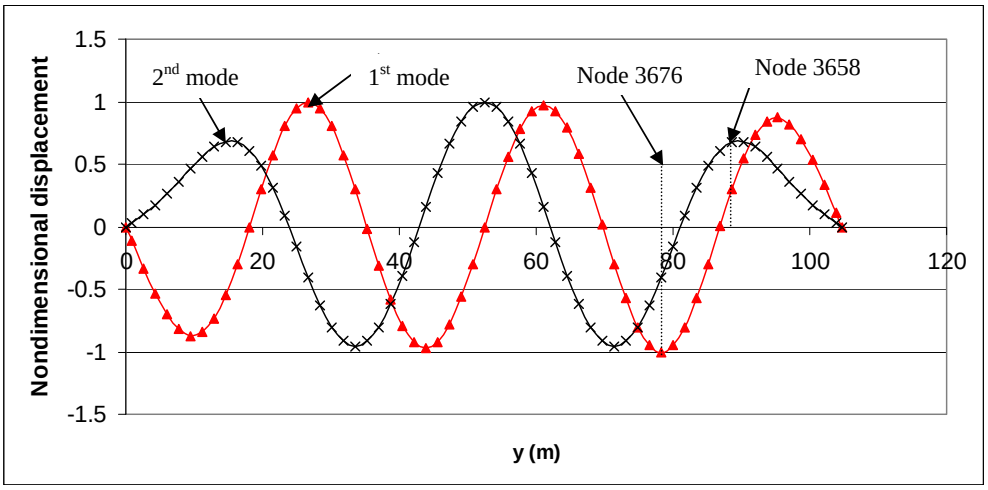

(a) First and second modes

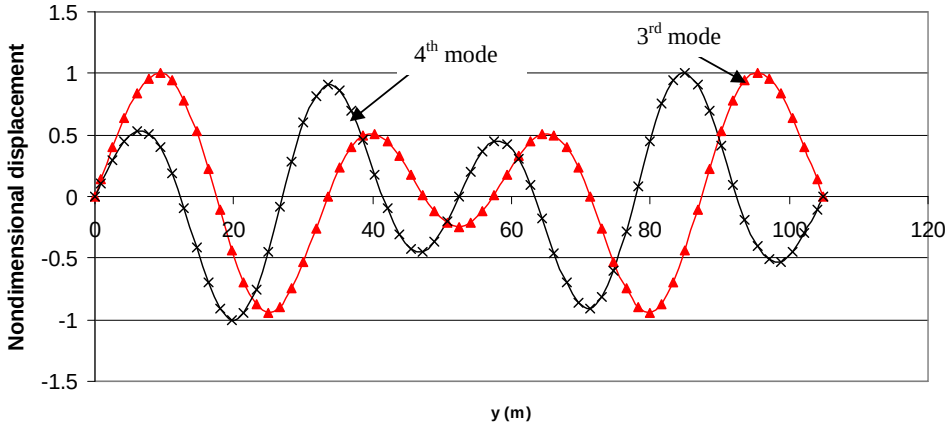

(b) Third and fourth modes

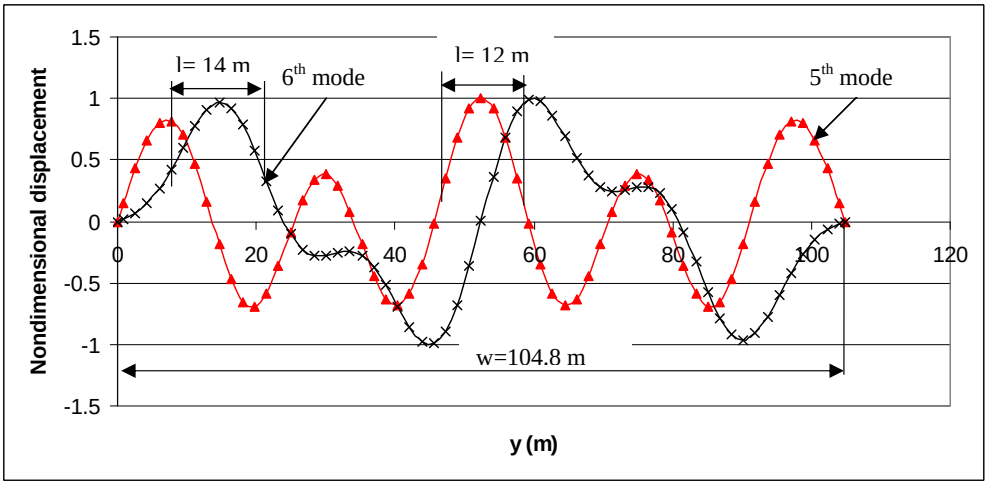

(c) Fifth and sixth modes

Figure 7.6: Nondimensional radial displacement along center-line bb for the lowest 6 critical modes for shell with $R = 104.8\ m$, $L_y/L_x = 2$, $\Phi = \pi/3$, $h = R/500m$, $B = \rho hR/E = 0.5 \times 10^{-6}$, $\rho = 6840\ kg/m^3$, $E = 30 \times 10^{10}\ N/m^2$

in Fig 7.6(c).

Tables 7.1 to 7.3 show that FE analysis generally produces lower critical loads in comparison with the analytical results based on idealized membrane state. It is because although FE analysis is a linear analysis it finds the critical loads on the basis of bending and membrane fundamental state. The effect of realistic boundary conditions performs as a source of imperfection. This causes modal interaction in modes such as Fig 7.1 to 7.6.

7.2 Approximation of vertical load with the load in radial direction

In section 5.1, the self-weight and additional imposed load is approximated to be in the radial direction. Yamada [8] has also reported the frequencies for a cylindrical shell based on the same simplification. For shallow shells the curvilinear coordinate is often approximated by the global coordinate. So for shallow shells it should be legitimate to accurately approximate vertical loads with the loads with the same magnitude but in radial direction. However, to check the level of approximation for the shells in this research the critical loads are found for the two cases of loads in the radial and vertical directions. The 10 lowest critical loads, summarized in Table 7.4, show that the load in vertical direction can be accurately approximated by loads in radial direction.

It is noticed that the critical loads for vertical loads are slightly higher than the counterparts for radial loading. The reason is presumably that it is the radial component of the vertical loads that are predicting the destabilization.

7.3 Nonlinear analysis

In the previous section the geometric nonlinearities were not considered in the derivation of critical load. The critical loads were derived on the basis of neglecting the effect of geometry change in establishing equilibrium for the initial state. However, the boundary conditions introduced imperfection in the analysis, which resulted in critical load being different with those found using the analytical method based on idealized

Vertical load (N/m^2)	Radial load (N/m^2)	error (%)
8220.7	7985	2.9
9375.0	9126	2.7
12730.	12302	3.4
14000	13472	3.8
15543	15104	2.8
16187	15693	3.1
17916	17546	2.1
18203	17785	2.3
20090	19611	2.4
20124	19624	2.5

Table 7.4: Comparison between the lowest 10 critical loads in vertical and radial directions

membrane state.

For stiff structures, the simple linear eigenvalue analysis is sufficient for design evaluation, for which the behaviour of the structure is linear before reaching its classical critical load. But if the structure is not stiff and has nonlinear deformation before buckling, the linear eigenvalue analysis is not able to estimate the tangent stiffness, $K_0^{NM} + \lambda_i K_\Delta^{NM}$ precisely. So for cases when significant geometry change is involved in the initial state, there is a possibility of unstable post buckling response and a geometrically nonlinear load-displacement analysis should be performed to determine the collapse loads. This is especially true for imperfection-sensitive structures such as shells. The nonlinear path analysis is known as "Riks" analysis in ABAQUS. This analysis can be done using *STATIC, RIKS command.

The load magnitude is treated as an additional unknown in the "Riks", for which the loads and displacements are solved simultaneously. ABAQUS uses the arc length

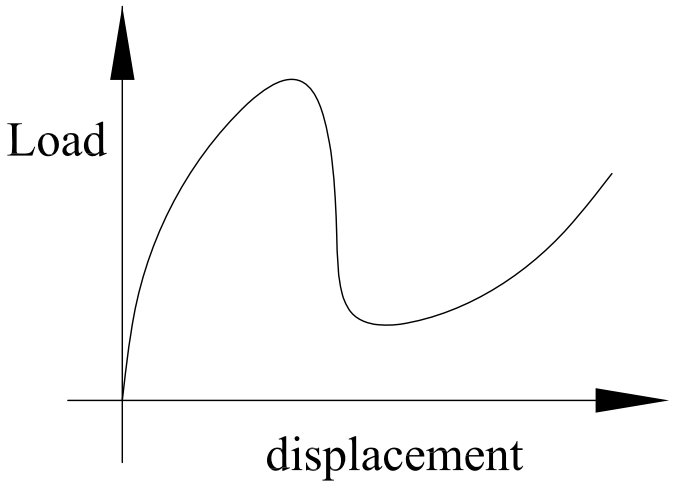

Figure 7.7: Unstable static response

l, along the equilibrium path in the load-displacement space as the progress parameter. The solution is regarded to have only a single equilibrium path in a space of nodal displacements and rotation and the loading parameter. This approach finds the solution regardless of whether the response is stable or unstable as it can be seen in Fig 7.7.

The nonlinear equilibrium equations are solved using Newton's method. The solution is usually obtained as a series of increments, with iterations to obtain equilibrium within each increment. Newton's method has a finite radius of convergence so the increment should be kept small to ensure correct modelling of the response path and ensure that the increment is not outside the radius of convergence. Moreover, if the increments are too large, more iterations will be required.

Only a 1% extrapolation of the strain increment is used by the Riks method. The initial load proportionality factor, $\Delta\lambda_{in}$, is computed as

$$\Delta\lambda_{in} = \frac{\Delta l_{in}}{l_{period}} \tag{7.2}$$

in which Δl_{in} is the initial increment in arc length along the static equilibrium path; this is a user defined parameter and l_{period} is a user defined total arc length scale factor. The value of $\Delta\lambda_{in}$ is used during the first iteration of a Riks step. For the rest of the iterations and increments the value of λ is computed automatically, and there is no control over the load magnitude. However, the minimum and maximum arc length increments,

Δl_{min} and Δl_{max}, can be used to control the automatic incrementation.

The snap buckling analysis is carried out for the three cases of shell treated in section 7.1 that have different levels of ratios of classical critical load to self-weight. The first case represents a shell with $B = 1.5 \times 10^{-6}\ s^2$, $L_y/L_x = 1$ for which, a nonlinear load-displacement analysis is carried out.

The linear eigenvalue analysis in section 7.1 produced the classical critical load, $P_c = 7985\ N/m^2$ (see Table 7.1) with the location of the maximum displacement occurring at node 7367 having the coordinate of $(x, \theta) = (52.414, 21.2^\circ)$ as shown in Fig 7.2(a). Having the location of maximum displacement within the lowest critical mode allows the nonlinear load-displacement path of the shell to be represented at this node as shown in Fig 7.8. In this Fig the applied load, P, is normalized with respect to P_c, and the displacement is normalized with respect to the shell thickness.

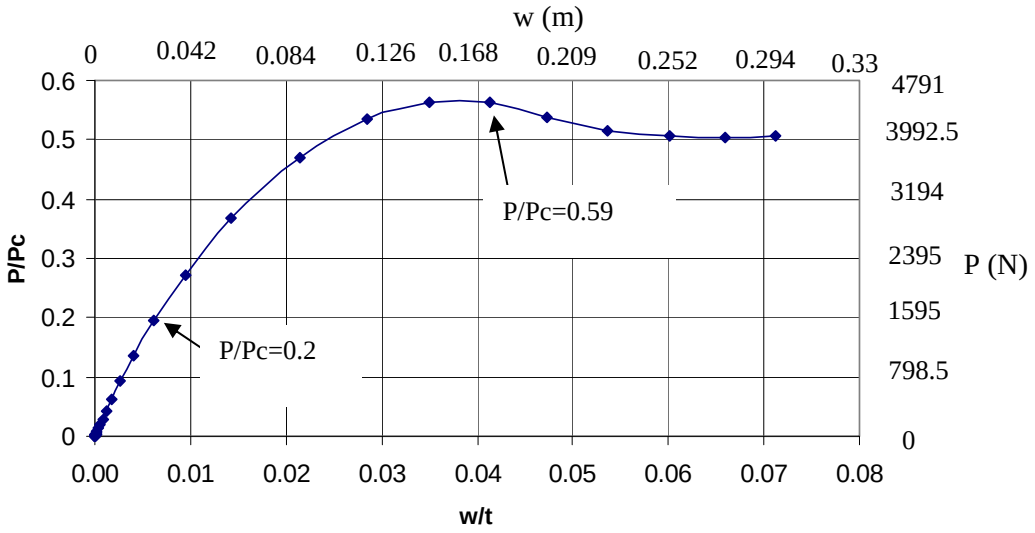

Figure 7.8: Nonlinear load-displacement path at node 7367 for a shell having $R = 104.8\ m$, $L_y/L_x = 1$, $\Phi = \pi/3$, $h = R/500m$, $B = \rho hR/E = 1.5 \times 10^{-6}\ s^2$, $\rho = 3137.2\ kg/m^3$, $E = 46 \times 10^9\ N/m^2$ with critical loads as Table 7.1

It is noticed that the load-displacement path is basically linear between the origin and load level of $P/P_c = 0.2$. After this load level, the load displacement becomes increasingly non-linear and eventually a snap buckling occurs at $P/P_c = 0.59$. The system

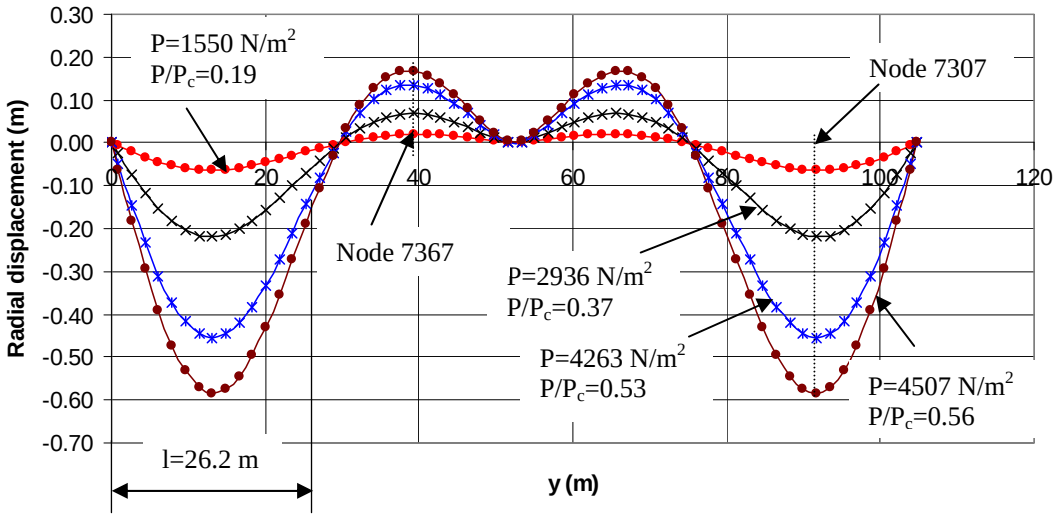

Figure 7.9: Nonlinear load-displacement path along center-line bb for a shell having $R = 104.8\ m$, $L_y/L_x = 1$, $\Phi = \pi/3$, $h = R/500m$, $B = \rho hR/E = 1.5 \times 10^{-6}\ s^2$, $\rho = 3137.2\ kg/m^3$, $E = 46 \times 10^9\ N/m^2$ with critical loads as Table 7.1

is then predicted to unload while the magnitude of the displacement still continues to increase. However, it should be noted that as the displacements becomes too large then most of the steps after reaching to nonlinear buckling load ($P/P_c = 0.59$), are of no interest in the current study. Fig 7.8 shows the nonlinear buckling load is a lot smaller than the classical critical load of $7985\ N/m^2$ in Table 7.1. Fig 7.9 shows the radial displacements along center-line bb. It shows that unlike Fig 7.2(a) indicating that the maximum displacement would occur at node 7367 associated with the lowest critical load, for the nonlinear analysis the maximum displacement shifts and occurs at node 7307 for increasing levels of loading. Fig 7.9 shows that for the load level equal to snap loading the maximum radial displacement occurs at node 7307.

The critical load analysis of Table 7.1 includes modes having even values of i; this means they are asymmetric about the shell center. However, even modes do not seem to participate in the nonlinear analysis as in Fig 7.9; as the modes are symmetric about the shell center. So it seems that the snap load should be compared to the bifurcation in the lowest symmetric mode; this means it should be compared to mode $(5, 1)$ for which $P_c = 9126\ N/m^2$ rather than $P_c = 7985\ N/m^2$. However, in Fig 7.8 and 7.9 the lowest critical load $P_c = 7985\ N/m^2$ is used. It is because at the location of the maximum

displacement, the length between the two point of contraflexure is closer to the length of half-wave corresponding to mode $(4, 1)$ rather than $(5, 1)$. So in this case (Fig 7.9) a localisation has occurred in the shell, a process that sometimes happens for shells. It is because of the initial imperfection due to the boundary constrains producing bending and probably a localised component of the mode associated with the lowest critical load that has its maximum amplitude near the boundary causes the localisation. By increasing the load it is most rapidly growing in a local form of the lowest critical mode. As in Fig 7.9 the ratio of the total length, $104.8\ m$, to the half-wave length of the localised mode, $l = 26.2\ m$, is equal to 4; this is equal to wave-length number corresponding to the lowest critical mode in Table 7.1 ($i = 4$). This means a localised form of the lowest critical mode is developed in Fig 7.9.

The nonlinear analysis is also performed for the shell having the critical loads presented in Table 7.2. Fig 7.10 shows the nonlinear load-displacement path for this shell at node 7367 (Fig 7.10), where the maximum displacement occurred at the classical critical load as shown in Fig 7.4. The collapse load occurs at $P/P_c = 0.568$. A detailed graph of displacement along center-line bb for different levels of loading shows that the maximum displacement occurs at node 7397 (Fig 7.11). Despite the fact that the deformation in Fig 7.11 is symmetric and it seems that the asymmetric modes such as mode $(4, 1)$ are not involved in the response, the snap buckling is compared with the lowest critical $P_c = 11284\ N/m^2$ corresponding to mode $(4, 1)$. As explained earlier it is because buckling half wave-length is nearer to $i = 4$ than $i = 5$; this is found by dividing the total length to the buckling half-wavelength, $104.8/25.7 = 4.08$ (Fig 7.11). This means it is a localisation of lowest critical mode.

Fig 7.12 also presents the nonlinear load-displacement path for the shell in Table 7.3 at node 3676, associated with the maximum displacement at the lowest critical load in Fig 7.6(a). It is noticed that the snap load is 53% of the classical critical load, where the lowest critical load equals to $P_c = 110896\ N/m^2$ is chosen as critical load. The displacement along center line bb for different levels of loading also indicates that the maximum displacement occurs at node 3754 rather than node 3676 of Fig (7.6(a)).

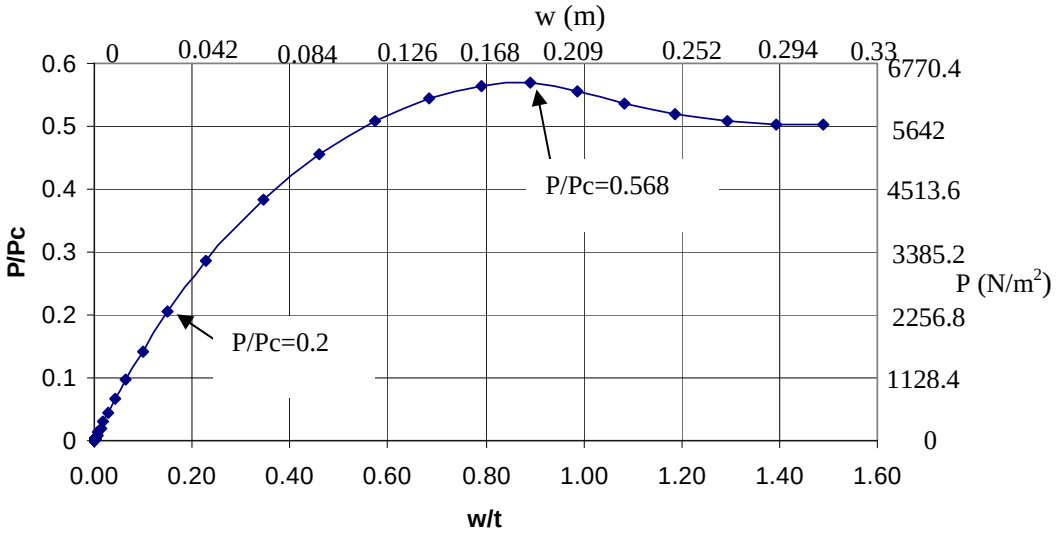

Figure 7.10: Nonlinear load-displacement path at node 7367 for a shell having $R = 104.8\ m$, $L_y/L_x = 1$, $\Phi = \pi/3$, $h = R/500m$, $B = \rho hR/E = 1.25 \times 10^{-6}\ s^2$, $\rho = 3692\ kg/m^3$, $E = 65 \times 10^9\ N/m^2$ with critical loads as Table 7.2

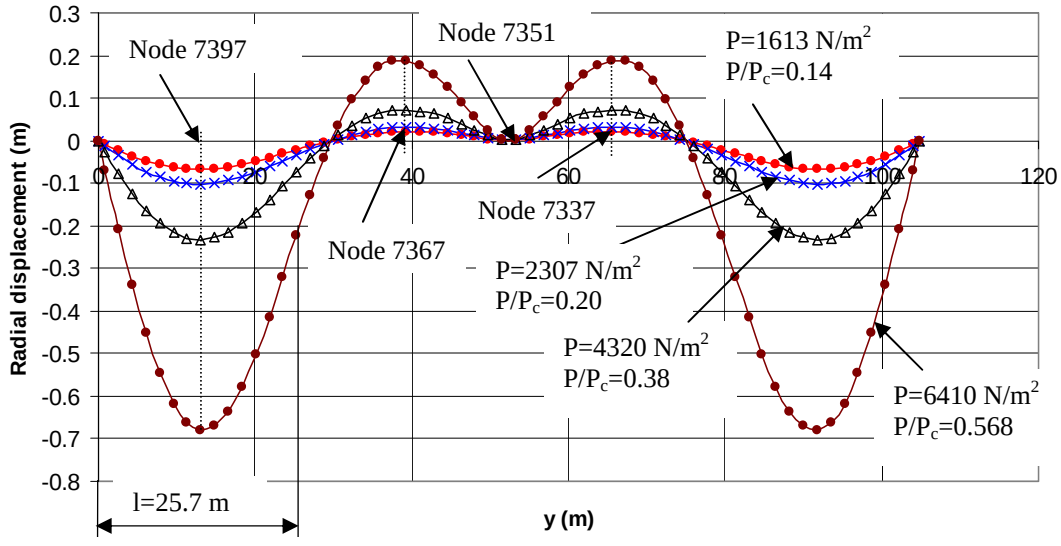

Figure 7.11: Nonlinear load-displacement path along center-line bb for a shell having $R = 104.8\ m$, $L_y/L_x = 1$, $\Phi = \pi/3$, $h = R/500m$, $B = \rho hR/E = 1.25 \times 10^{-6}\ s^2$, $\rho = 3692\ kg/m^3$, $E = 65 \times 10^9\ N/m^2$ with critical loads as Table 7.2

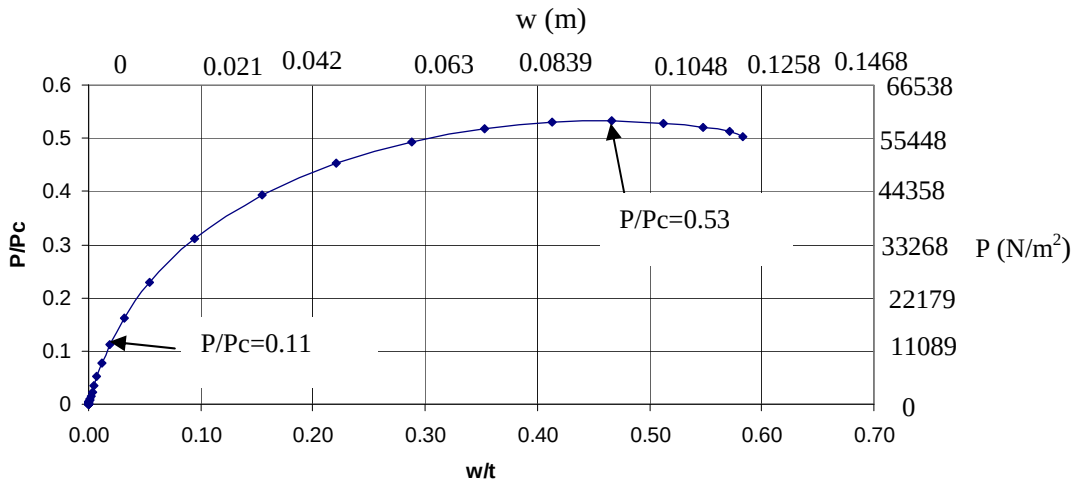

Figure 7.12: Nonlinear load-displacement path at node 3676 for a shell having $R = 104.8\ m$, $L_y/L_x = 2$, $\Phi = \pi/3$, $h = R/500m$, $B = \rho hR/E = 0.5 \times 10^{-6}\ s^2$, $\rho = 6840\ kg/m^3$, $E = 30 \times 10^{10}\ N/m^2$ with critical loads as Table 7.3

As explained earlier the boundary constrains probably has a localised component of the mode associated with the lowest critical load that has its maximum amplitude near the boundary. This localised component most rapidly growing local form of the lowest critical mode. As Fig 7.13 shows dividing the total length, $104.8\ m$, by the length between the two points of contraflexure, $17.47\ m$, result in $i = 6$. This means the localised mode is nearer to $i = 6$, the lowest critical load in Table 7.3. So the deformation response is trying to develop the wavelength of the lowest critical mode. However, it can not fit it into the shell width, hence amplitude of the response near the center-line (between $20\ m$ to $80\ m$) is dampened. But as can be seen in Fig 7.13 as localised form of the lowest critical mode will develop at the location of the local maximum amplitude.

This section showed that the snap buckling found on the basis on bending fundamental nonlinear state is much less than classical buckling loads in section 7.1, which are found based on idealized membrane linear state. It is therefore expected that the resulting frequencies based on the nonlinear load-displacement path would be different from those found on the basis of a bending and membrane state in section 5.4. It is important to find the difference between the resulting frequencies based on these two assumptions.

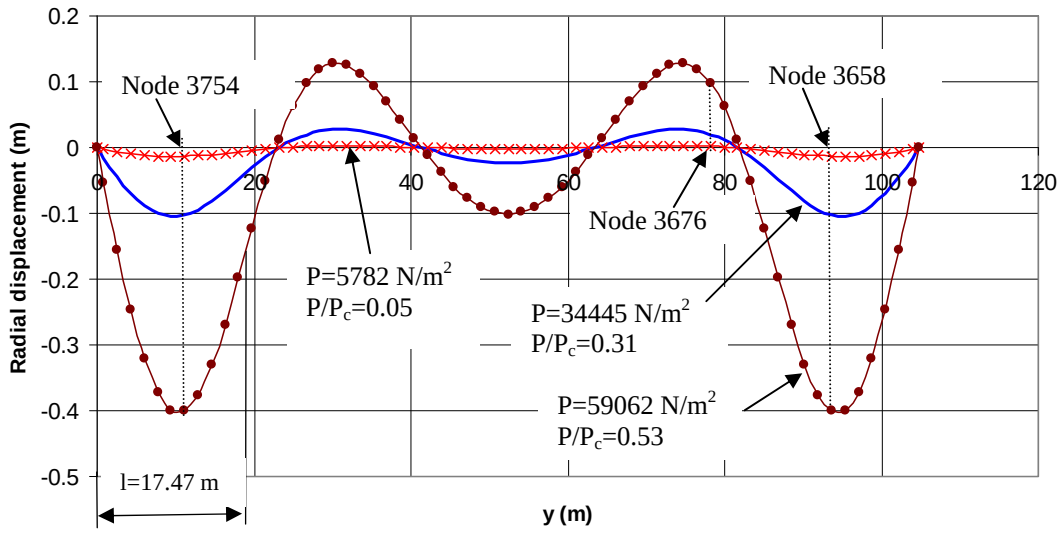

Figure 7.13: Nonlinear load-displacement path along center-line bb for a shell having $R = 104.8\ m$, $L_y/L_x = 2$, $\Phi = \pi/3$, $h = R/500m$, $B = \rho hR/E = 0.5 \times 10^{-6}\ s^2$, $\rho = 6840\ kg/m^3$, $E = 30 \times 10^{10}\ N/m^2$ with critical loads as Table 7.3

7.4 Natural frequencies on the basis of linear and nonlinear fundamental state

In section 5.4 the natural frequencies of three cases of shell are derived for different levels of pre-loading based on the idealized membrane assumption. However, as shown in Fig 7.8 to 7.13 the nonlinear snap buckling is a lot smaller than the classical critical load as presented in Tables 7.1 to 7.3. It would consequently be of interest to check how the natural frequencies based on the nonlinear bending theory would differ from the ones obtained using the idealized model. In case of large discrepancies, the displacement and stress responses could be strongly affected and consequently would exert important influences on the shell design. It is expected that the lowest frequency would reach zero at the level of snap buckling load which is less than the classical critical load.

In order to investigate the effect of the nonlinear response on natural frequencies, the three cases of shell as in section 7.1 are chosen. However, two of these cases are not suitable for this comparison study as their snap buckling load is less than the self-weight of the shell. First one, the shell in Table 7.1, has a classical critical load equal to $7985\ N/m^2$ and a snap buckling equal to $P = 0.59\ P_c = 4711\ N/m^2$ (Fig 7.8), which

is less than the self-weight of the shell ($\rho gh = 3137.2 \times 9.81 \times 0.20965 = 6452\ N/m^2$). Second one is the shell having the critical loads as in Table 7.2; this shell has a classical critical load equal to $11284\ N/m^2$ (Table 7.2) and a snap buckling equal to $P = 0.568\ P_c = 6409\ N/m^2$ (Fig 7.10), which is again less than the self-weight of the shell ($\rho gh = 3692 \times 9.81 \times 0.20965 = 7593\ N/m^2$). So the third shell having the critical loads as Table 7.3 is used for the comparison study. This shell has a classical critical load equal to $110896\ N/m^2$ (Table 7.3) and a snap buckling equal to $P = 0.53\ P_c = 58775\ N/m^2$ (Fig 7.12), which is higher than the self-weight of the shell ($\rho gh = 6840 \times 9.81 \times 0.20965 = 14068\ N/m^2$)

In this study the minimum natural frequencies are derived based on two methods; idealized method (as explained in section 5.1) and full nonlinear bending theory for different levels of pre-loading using ABAQUS.

ABAQUS takes into account geometric nonlinearities using NLGEOM command. In order to find the frequencies in ABAQUS first a nonlinear analysis is performed using NLGEOM command to find the deformed shapes. Then a linear eigenvalue analysis is performed about the deformed shape to find the natural frequencies.

Fig 7.14 shows the comparison of the governing frequencies based on these two methods for the shell with the nonlinear behaviour as in Fig 7.12.

The comparison shows that both methods give very close frequencies for the zero and different levels of pre-loading up to snap buckling load. In ABAQUS the shell becomes unstable and the minimum frequency reaches to zero very unexpectedly at the level of snap buckling. But the governing frequency using the analytical model, based on the idealized method, continues to decrease smoothly until it reaches to zero at classical critical load equal to $110896\ N/m^2$ (Table 7.3). However, as shown for critical loads the mode shapes using these two methods are not the same. This is because the boundary conditions introduce nonlinearities into the system. So it is expected that the distribution of the shell responses over the surface of the shell would be different using these two methods. Moreover, for the cases of shells, where the snap buckling is much less than the lowest critical load, a linear modal analysis might not be valid, especially when the pre-loadings are close to nonlinear snap buckling load.

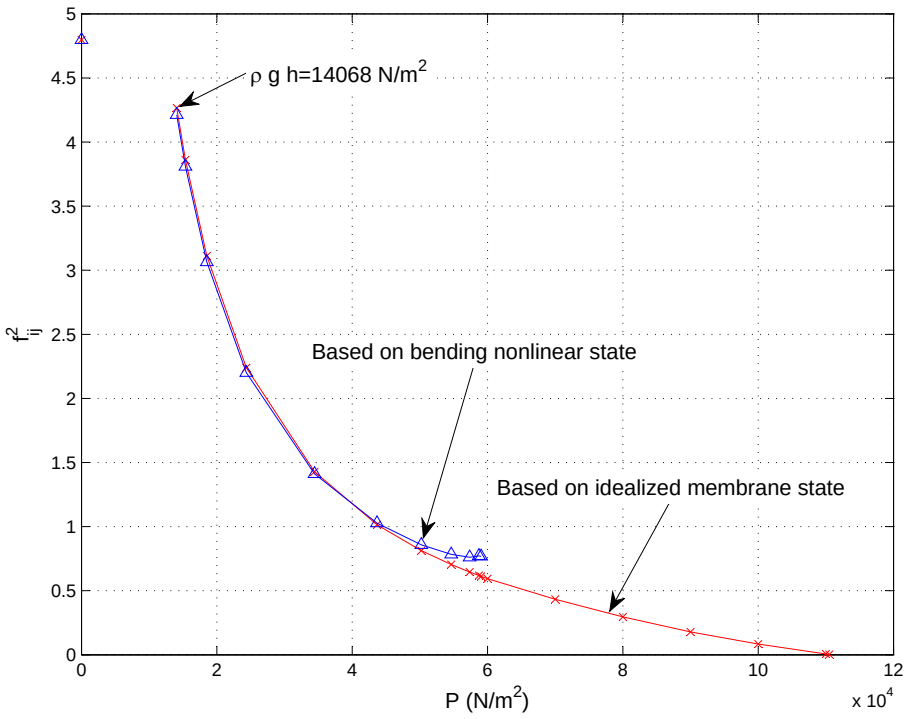

Figure 7.14: Comparison between frequencies based on idealized method and nonlinear bending method for the shell having critical loads as Table 7.3

Chapter 8

Modelling of Doubly Curved Shells

8.1 Basic assumptions

In this chapter the investigation on single curvature shells are extended to doubly curved shells by adding a curvature in another direction. The same assumptions as for the cylindrical shell are considered for the doubly curved shell. The thin shell theory for which the thickness is small in comparison to other dimensions of the shell is considered in this study. Stress-strain relationships are derived based on Love's first approximation as explained in 2.1. In addition to the Love-Kirchhoff assumptions, the material is considered elastic, homogeneous and isotropic.

The aim of this chapter is to investigate how adding a curvature can affect the natural frequencies of the shell and consequently affect the responses of the shell to the earthquake loading. The study is limited to the linear analysis of a doubly curved shell with simply supports with the effect of pre-loading neglected.

8.2 Shallow shells

A shell is regarded as shallow shell when the maximum rise is small compared with the span, and may be regarded as a slightly curved plate. Leissa considers a shell as a shallow shell when its smallest radius is large compared to its greatest span [1] without suggesting a radius to span ratio. Valsov classified a shell covering a rectangular plan as being a shallow shell when its ratio of the rise to smallest side of the rectangle plane is less than $1/5$. Most researchers have considered this ratio as criteria for adoption of

shallow shell theory.

For a shallow shell the difference between the actual arc lengths and their projections is negligible. However, in this study the actual length measured over the surface is considered, but in the dynamic analysis of the shell against earthquake, the vertical component of earthquake is approximated by considering it as acting normal to the surface using the assumptions of shallow shell.

8.3 Geometry of doubly curved shell

A circular doubly curved shell is considered in this study. The main focus of this chapter is to compare the frequency, displacements, and stresses results with the responses of cylindrical shell presented in chapter 3 and 4.

Circular doubly curved shells can be created by cutting a dome by vertical planes, or by translation of a generator curve along another curve. However, the shells used in this study are surfaces of translation and are generated by translation of a generator curve consisting of a circular curve having radius of R_x and angle of ϕ_x along another circular curve having radius of R_y and angle of ϕ_y (Fig 8.1). The total rise of the circular doubly curved shell would be

$$R_x(1-\cos\frac{\phi_x}{2})+R_y(1-\cos\frac{\phi_y}{2}) \tag{8.1}$$

8.4 Compatibility

In order to ensure that every part of the structure, no matter what the strain, remains in contact with the adjacent parts after the deformation, the compatibility of the strains should be satisfied. Strains are considers in terms of displacements, where the displacements along the curvilinear coordinate system in the x, y, and z directions are taken as u, v, and w.

8.5 Strains

Strain-displacement relationships are derived in the same way as for cylindrical shells. The total strains across a section consist of the strains due to membrane and bending

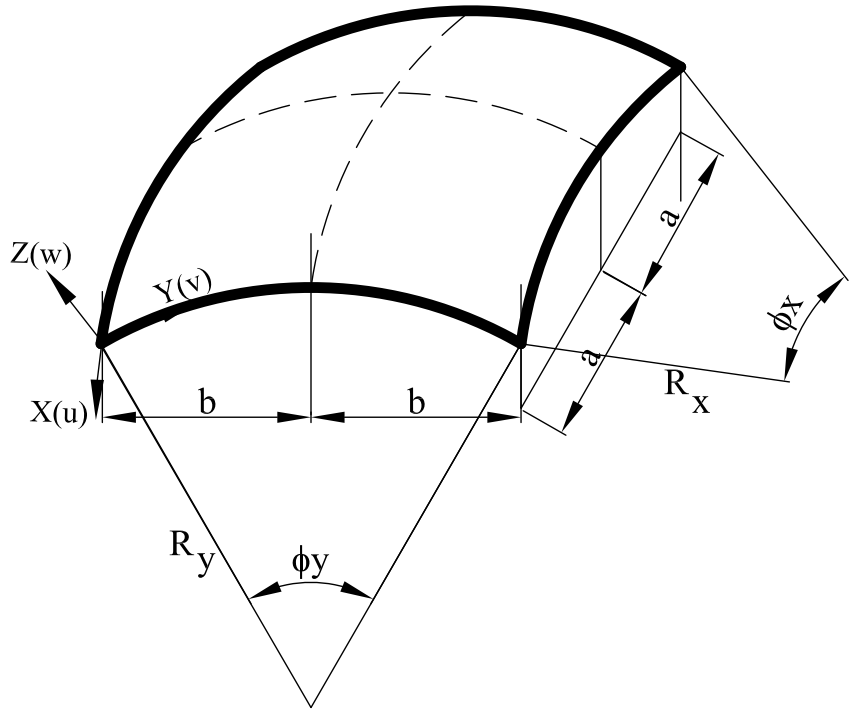

Figure 8.1: Circular doubly curved shell

actions. At a distance z from the middle surface the strains presented as in eqn (2.10), with the difference that the curvature will be introduced in both directions. The membrane and bending strains of the middle-surface also remains as eqn (2.11) except for ϵ'_x, χ_x, and χ_{xy} that are changed to eqn 8.2 due to introducing curvature in x direction

$$\begin{aligned} \epsilon'_x &= \frac{\partial u}{\partial x} + \frac{w}{R_x} \\ \chi_x &= -\frac{\partial^2 w}{\partial x^2} + \frac{1}{R_x}\frac{\partial u}{\partial x} \\ \chi_{xy} &= -\frac{\partial^2 w}{\partial x^2 \partial y^2} + \frac{1}{R_y}\frac{\partial v}{\partial x} + \frac{1}{R_x}\frac{\partial u}{\partial y} \end{aligned} \tag{8.2}$$

Using the Hooke's Law, the stresses can be written as in eqn (2.12), with the membrane and bending stress resultants derived using eqn (2.13).

8.6 Energy formulation

The equations of motion are derived based on Euler-Lagrangian equations. As explained in chapters 2 and 3, the Lagrangian is $L = U - T$ where U is the potential energy and T is the kinetic energy. The potential energy is derived by multiplying the

stresses by the relevant strains and integrating them over the surface, and again the total potential energy may usefully be divided into the membrane and bending energy components. In order to investigate the contribution of different energy components in different modes, the energy is then presented as its separate components. It should be noted that the pre-loading is not considered in this chapter so the contribution from the external load potential is neglected in the strain energy. The separate contribution to the membrane energy can be written as

$$\begin{aligned} U_m^x &= \frac{1}{2}\int_0^{R\phi_x}\int_0^{R\phi_y} N_x\epsilon_x' \, dx \, dy \\ U_m^y &= \frac{1}{2}\int_0^{R\phi_x}\int_0^{R\phi_y} N_y\epsilon_y' \, dx \, dy \\ U_m^{xy} &= \frac{1}{2}\int_0^{R\phi_x}\int_0^{R\phi_y} N_{xy}\epsilon_x' \, dx \, dy \end{aligned} \tag{8.3}$$

Similarly, the contributions to the bending energy can be written as

$$\begin{aligned} U_b^x &= \frac{1}{2}\int_0^{R\phi_x}\int_0^{R\phi_y} M_x\chi_x \, dx \, dy \\ U_b^y &= \frac{1}{2}\int_0^{R\phi_x}\int_0^{R\phi_y} M_y\chi_y \, dx \, dy \\ U_b^{xy} &= \frac{1}{2}\int_0^{R\phi_x}\int_0^{R\phi_y} M_y\chi_{xy} \, dx \, dy \end{aligned} \tag{8.4}$$

By representing the stress resultants and strains in terms of the displacements, the membrane and bending strain energy components can be written as

$$
\begin{aligned}
U_m^x &= \frac{K}{2}\int_0^{R\phi_x}\int_0^{R\phi_y}[(\frac{\partial u}{\partial x})^2+(\frac{w}{R_x})^2-2(\frac{\partial u}{\partial x})(\frac{w}{R_x})+\nu(\frac{\partial v}{\partial y})(\frac{\partial u}{\partial x})- \\
&\quad \nu(\frac{w}{R_x})(\frac{\partial v}{\partial y})+\nu\frac{w^2}{R_xR_y}-\nu(\frac{w}{R_y})(\frac{\partial u}{\partial x})]dx\,dy \\
U_m^y &= \frac{K}{2}\int_0^{R\phi_x}\int_0^{R\phi_y}[(\frac{\partial v}{\partial y})^2+(\frac{w}{R_y})^2-2\frac{\partial v}{\partial y}\frac{w}{R_y}+ \\
&\quad \nu\frac{\partial u}{\partial x}\frac{\partial v}{\partial y}-\nu\frac{w}{R_y}\frac{\partial u}{\partial x}-\nu\frac{w}{R_x}\frac{\partial v}{\partial y}+\nu\frac{w^2}{R_xR_y}]dx\,dy \\
U_m^{xy} &= \frac{K}{2}\frac{1-\nu}{2}\int_0^{R\phi_x}\int_0^{R\phi_y}[(\frac{\partial u}{\partial y})^2+(\frac{\partial v}{\partial x})+2\frac{\partial u}{\partial y}\frac{\partial v}{\partial x}]dx\,dy \\
U_b^x &= \frac{D}{2}\int_0^{R\phi_x}\int_0^{R\phi_y}[(\frac{\partial^2 w}{\partial x^2})^2+\frac{1}{R_x^2}(\frac{\partial u}{\partial x})^2+\frac{2}{R_x}\frac{\partial^2 w}{\partial x^2}\frac{\partial u}{\partial x}+\nu\frac{\partial^2 w}{\partial x^2}\frac{\partial^2 w}{\partial y^2}+ \\
&\quad \frac{\nu}{R_y}\frac{\partial^2 w}{\partial x^2}\frac{\partial v}{\partial y}+\frac{\nu}{R_x}\frac{\partial u}{\partial x}\frac{\partial^2 w}{\partial y^2}+\frac{\nu}{R_xR_y}\frac{\partial u}{\partial x}\frac{\partial v}{\partial y}]dx\,dy \\
U_b^y &= \frac{D}{2}\int_0^{R\phi_x}\int_0^{R\phi_y}[(\frac{\partial^2 w}{\partial y^2})^2+\frac{1}{R_y^2}(\frac{\partial v}{\partial y})^2+\frac{2}{R_y}\frac{\partial^2 w}{\partial y^2}\frac{\partial v}{\partial y}+\nu\frac{\partial^2 w}{\partial x^2}\frac{\partial^2 w}{\partial y^2}+ \\
&\quad \frac{\nu}{R_y}\frac{\partial^2 w}{\partial x^2}\frac{\partial v}{\partial y}+\frac{\nu}{R_x}\frac{\partial u}{\partial x}\frac{\partial^2 w}{\partial y^2}+\frac{\nu}{R_xR_y}\frac{\partial u}{\partial x}\frac{\partial v}{\partial y}]dx\,dy \\
U_b^{xy} &= D(1-\nu)\int_0^{R\phi_x}\int_0^{R\phi_y}[(\frac{\partial^2 w}{\partial x\partial y})^2+\frac{1}{R_y^2}(\frac{\partial v}{\partial x})^2+\frac{1}{R_x^2}(\frac{\partial u}{\partial y})^2+ \\
&\quad \frac{2}{R_y}(\frac{\partial^2 w}{\partial x\partial y})(\frac{\partial v}{\partial x})+\frac{2}{R_x}\frac{\partial^2 w}{\partial x\partial y}\frac{\partial u}{\partial y}]dx\,dy
\end{aligned}
\tag{8.5}
$$

with the total strain energy expressed as

$$U = U_m^x + U_m^y + U_m^{xy} + U_b^x + U_b^y + U_b^{xy} \tag{8.6}$$

The kinetic energy is also the same as in eqn (2.27).

8.7 Equation of motion

The equations of motion are derived using the Euler-Lagrangian equations. Making use of the eqns (8.6) and (8.5) and employing the strain-displacement relations (2.11) and (8.2), the Euler-Lagrange equations (2.21) will be simplified to the differential equation of motions of eqn (2.28). $Sx(u,v,w)$, $Sy(u,v,w)$, and $Sz(u,v,w)$ in eqn (2.28) are

static equation of equilibrium for doubly curved shell in the form of

$$\begin{aligned}
S_x =& - K[\frac{\partial^2 u}{\partial x^2} + \frac{1-\nu}{2}\frac{\partial^2 u}{\partial y^2} + \frac{1+\nu}{2}\frac{\partial^2 v}{\partial x \partial y} + (\frac{1}{R_x} + \frac{\nu}{R_y})\frac{\partial w}{\partial x}] - \\
& D[-\frac{1}{R_x}\frac{\partial^3 w}{\partial x^3} + \frac{1}{R_x^2}\frac{\partial^2 u}{\partial x^2} + \frac{2(1-\nu)}{R_x^2}\frac{\partial^2 u}{\partial y^2} - \frac{2-\nu}{R_x}\frac{\partial^3 w}{\partial x \partial y^2} + \frac{2-\nu}{R_x R_y}\frac{\partial^2 v}{\partial x \partial y}] \\
S_y =& - K[\frac{\partial^2 v}{\partial y^2} + \frac{1-\nu}{2}\frac{\partial^2 v}{\partial x^2} + \frac{1+\nu}{2}\frac{\partial^2 u}{\partial x \partial y} + (\frac{\nu}{R_x} + \frac{1}{R_y})\frac{\partial w}{\partial y}] - \\
& D[-\frac{1}{R_y}\frac{\partial^3 w}{\partial y^3} + \frac{1}{R_y^2}\frac{\partial^2 v}{\partial y^2} + \frac{2(1-\nu)}{R_y^2}\frac{\partial^2 v}{\partial x^2} - \frac{2-\nu}{R_y}\frac{\partial^3 w}{\partial x^2 \partial y} + \frac{2-\nu}{R_x R_y}\frac{\partial^2 u}{\partial x \partial y}] \qquad (8.7) \\
S_z =& K[(\frac{1}{R_x} + \frac{\nu}{R_y})\frac{\partial u}{\partial x} + (\frac{\nu}{R_x} + \frac{1}{R_y})\frac{\partial v}{\partial y} + (\frac{1}{R_x^2} + \frac{2\nu}{R_x R_y} + \frac{1}{R_y^2})w] + \\
& D[\frac{\partial^4 w}{\partial x^4} + \frac{\partial^4 w}{\partial y^4} + 2\frac{\partial^4 w}{\partial x^2 \partial y^2} - \frac{1}{R_y}\frac{\partial^3 v}{\partial y^3} - \frac{2-\nu}{R_y}\frac{\partial^3 v}{\partial x^2 \partial y} - \frac{1}{R_x}\frac{\partial^3 u}{\partial x^3} - \frac{2-\nu}{R_x}\frac{\partial^3 u}{\partial x \partial y^2}]
\end{aligned}$$

It should be noted that the resulting equation of motion are based on neglecting the effect of pre-loading.

The boundary conditions are assumed to be simply supports along the four edges

$$\begin{aligned}
v = w = 0,\ \frac{\partial u}{\partial x} = \frac{\partial^2 w}{\partial x^2} = 0 \quad at\ x = 0,\ R_x\ \phi_x \\
u = w = 0,\ \frac{\partial v}{\partial y} = \frac{\partial^2 w}{\partial y^2} = 0 \quad at\ y = 0,\ R_y\ \phi_y
\end{aligned} \qquad (8.8)$$

It is now possible to find the exact solutions for differential equations of eqn (2.28) in the form of double trigonometric series as in eqn (3.1) in which

$$\begin{aligned}
u_{ij}(x,y) &= \overline{u}_{ij} cos\frac{j\pi x}{2a} sin\frac{i\pi y}{2b} \\
v_{ij}(x,y) &= \overline{v}_{ij} sin\frac{j\pi x}{2a} cos\frac{i\pi y}{2b} \\
w_{ij}(x,y) &= \overline{w}_{ij} sin\frac{j\pi x}{2a} sin\frac{i\pi y}{2b}
\end{aligned} \qquad (8.9)$$

where $2a$, and $2b$ are the arc lengths in x, and y direction respectively and i and j represent the number of half waves in the y and x directions. As explained in section 3.2.1, the generalized time response, used for solving the eigenvalue problem, is taken as $q_{ij}(t) = sin(\omega_{ij} t + \theta_{ij})$. This equation is on the basis of the assumption that free-vibration motion is harmonic.

By substituting the displacements into eqns (2.28) and (8.7), equilibrium equations can be represented in terms of the incremental displacement, and presented as an eigenvalue

problem, in which the eigenvalues are associated with the natural frequencies, ω_{ij}, and the eigenmodes with amplitude $\overline{u}_{ij}$, $\overline{v}_{ij}$, $\overline{w}_{ij}$.

$$\begin{bmatrix} k_{11} & k_{12} & k_{13} \\ k_{21} & k_{22} & k_{23} \\ k_{31} & k_{32} & k_{33} \end{bmatrix} \cdot \begin{Bmatrix} \bar{u}_{ij} \\ \bar{v}_{ij} \\ \bar{w}_{ij} \end{Bmatrix} = \begin{Bmatrix} 0 \\ 0 \\ 0 \end{Bmatrix} \tag{8.10}$$

The coefficient of the matrix are as follows

$$\begin{aligned}
k_{11} &= \frac{(1-\nu)i^2\pi^2}{8b^2} + \frac{1}{4}\frac{j^2\pi^2}{a^2} - \frac{h^2}{12}(-\frac{(1-\nu)i^2\pi^2}{2b^2R_x^2} - \frac{j^2\pi^2}{4R_x^2a^2}) - \Delta_{ij} \\
k_{12} &= \frac{(1+\nu)ij\pi^2}{8ab} - \frac{h^2}{12}(\frac{(2-\nu)ij\pi^2}{4R_xR_yab}) \\
k_{13} &= -\frac{1}{2}(\frac{1}{R_x} + \frac{\nu}{R_y})\frac{j\pi}{a} - \frac{h^2}{12}\left[\frac{1}{8}\left(\frac{\nu}{R_x} + \frac{2-2\nu}{R_x}\right)\frac{i^2j\pi^3}{ab^2} + \frac{1}{8}\frac{j^3\pi^3}{R_xa^3}\right] \\
k_{21} &= k_{12} \\
k_{22} &= \frac{(1-\nu)j^2\pi^2}{8a^2} + \frac{i^2\pi^2}{4b^2} + \frac{h^2}{12}\left(\frac{(1-\nu)j^2\pi^2}{2R_y^2a^2} + \frac{i^2\pi^2}{4R_y^2b^2}\right) - \Delta_{ij} \\
k_{23} &= -\frac{1}{2}\left(\frac{\nu}{R_x} + \frac{1}{R_y}\right)\frac{i\pi}{b} - \frac{h^2}{12}\left[-\frac{1}{8}\left(\frac{\nu-2}{R_y}\right)\frac{ij^2\pi^2}{a^2b} + \frac{1}{8}\frac{i^3\pi^3}{R_yb^3}\right] \\
k_{31} &= k_{13} \\
k_{32} &= k_{23} \\
k_{33} &= \frac{1}{R_x^2} + \frac{2\nu}{R_xR_y} + \frac{1}{R_y^2} + \frac{h^2}{12}\frac{\pi^4}{16}\left(\frac{j^2}{a^2} + \frac{i^2}{b^2}\right)^2 - \Delta_{ij}
\end{aligned} \tag{8.11}$$

where

$$\Delta_{ij} = \frac{\rho\omega_{ij}^2(1-\nu^2)}{E} \tag{8.12}$$

8.8 Frequency verification

The analytically derived frequencies have been verified with the results reported by Liew and Lim [106] for a free-supported edge doubly-curved shell and with the FE solution derived by Olson and Lindbuerg in a separate study [45] and reported by Liew and Lim [106]. Both Liew and Lim, and Olson and Lindbuerg verified the frequency parameter with the closed-form solution, obtained from the shell theory [107]. The term freely-supported edge referred in their research means that just the in-plane deflection tangential to the edge and the transverse deformation are constrained; this conforms

with the present simply supported boundary conditions of eqn (8.8). The comparisons are done for a doubly-curved circular shell ($\frac{R_y}{R_x} = 1$), having a square planform ($\frac{a}{b} = 1$) with poisson's ratio $\nu = 0.3$, and $\frac{R_y h}{(2a)^2} = 0.005$. To satisfy the ratio of $\frac{R_y h}{(2a)^2} = 0.005$ a shell having $R_x = 141.42\ m$, $R_y = 141.42\ m$, $h = \frac{R_y}{100}$,$\rho = 2400\ kg/m^3$, $E = 24 \times 10^9 N/m^2$, $a = 100\ m$, $b = 100\ m$ is chosen. The rise of this shell according to eqn (8.1) is equal to $82.82\ m$, which make $rise/span = 0.41$. Although Liew and Lim [106] and Olson and Lindbuerg [45] categorised this shell as being a shallow shell, it is not considered as being a shallow shell because the rise to span ratio is higher than $1/5$ as defined by Valsov.

A closed form analytical solution for this case may be obtained from the shell theory [107], and is given as

$$\omega_{ij}^2 = \frac{E}{\rho R^2}[1 + \pi^4(\frac{Rh}{(2a)^2})^2 \frac{(i^2 + j^2)^2}{12(1 - \nu^2)}] \tag{8.13}$$

The analytical solution is derived by neglecting the in-plane inertia in the eigenvalue problem. The eigen-frequencies in this section is derived based on neglecting the in-plane inertia (by neglect of Δ_{ij} in k_{22} and k_{33} in eqn (8.11)). This is only for the purpose of the comparison of eigen-frequencies with the available literatures [106] [45] [107], which are all based on neglecting the in-plane inertia. However, in the next section the effects of in-plane modes in the resulting out-of-plane frequencies will be investigated. It should also be noted that the changes in curvatures are simplified by the above mentioned researchers [106], [45], and [107] since they neglected the terms $\frac{1}{R_x}\frac{\partial u}{\partial x}$ in χ_x, $\frac{1}{R_y}\frac{\partial v}{\partial y}$ in χ_y, and $\frac{1}{R_y}\frac{\partial v}{\partial x} + \frac{1}{R_x}\frac{\partial u}{\partial y}$ in χ_{xy}. Therefore, it is expected that the results of the present study would differ a little from the results of [106], [45], and [107]. Symmetry requires that $\omega_{ij} = \omega_{ji}$, so only one of them is presented in Table 8.1.

Table 8.1 indicates that the frequency parameters found in the present research based on the neglect of the in-plane inertia in the equations of motion are in good agreement with those reported in [106] [45] and [107]. It also shows the result from FE methods has the largest differences with the closed-form solution. Also, the present results are always lower than the frequency parameters derived using closed form equations. This

(i,j)	closed form eqn (8.13)	FE [106] [45]	Liew and Lim [106]	Present (in-plane inertia neglected)
(1,1)	1.00089	1.00092	1.00089	1.00061
(1,2)	1.00558	1.00572	1.00558	1.00488
(2,2)	1.01427	1.01501	1.01427	1.01303
(1,3)	1.02230	1.02297	1.02230	1.02100
(2,3)	1.03769	1.04013	1.03769	1.03573
(1,4)	1.06445	1.06679	1.064457	1.06231
(3,3)	1.07225	1.07888	1.07225	1.06943
(2,4)	1.08920	1.09344	1.08920	1.08635
(3,4)	1.13938	1.15289	1.13938	1.13552
(1,5)	1.15075	1.15846	1.15075	1.14756
(2,5)	1.18755	1.20166	1.18755	1.18359
(4,4)	1.22836	1.25510	1.22836	1.22331
(3,5)	1.27580	1.28079	1.25780	1.25274
(1,6)	1.30530	1.31391	1.30530	1.30080
(2,6)	1.35681	1.38715	1.35681	1.35154
(4,5)	1.37487	1.42418	1.37488	1.36848
(3,6)	1.45159	1.51743	1.45159	1.44514
(1,7)	1.55752	1.58882	1.55752	1.55149
(5,5)	1.55752	1.58810	1.55781	1.54961
(4,6)	1.60301	1.66077	1.60325	1.595098
(2,7)	1.62642	1.69589	1.62643	1.61960
(3,7)	1.75019	1.83781	1.75059	1.74214
(5,6)	1.82980	1.96834	1.83076	1.82023
(1,8)	1.94220	2.03518	1.94222	1.93441
(4,7)	1.94220	2.14684	1.94330	1.93259

Table 8.1: Comparison of frequency parameter $\lambda = \rho R^2 \omega_{ij}^2 / E$ of the present results (with no in-plane inertia) and past research on a simply supported doubly curved shell with $\nu = 0.3$, $a/b = 1$, $R_y/R_x = 1.0$, $Rh/a^2 = 0.005$

additional flexibility might be the consequence of neglecting the terms in χ_x, χ_y, and χ_{xy} as discussed earlier.

8.9 Effect of In-plane modes in the out-of-plane modes

In the previous section the frequency parameters are derived based on ignoring the in-plane inertia in the eigenvalue analysis for the purpose of comparison with the results from available research. Ignoring the in-plane inertia in the eigenvalue analysis can help reducing the calculation time. However, it is necessary to ensure that in doing so there is not a reduction in the accuracy of the results in doubly curved shells. In order to check the accuracy of the results, another study is performed for a shell having the same geometry and material property as in previous section. The analysis is performed for the two cases of including and neglecting the in-plane inertia in the frequency extraction procedure. The results for both assumptions are summarized in Table 8.2 with the corresponding percentages of error.

As seen from Table 8.2, neglect of the in-plane inertia can produce a result 18.57% higher than when in-plane inertia is included. This means that the actual frequency of the shell in mode, $(i, j) = (1, 1)$ is less than the frequency when the in-plane inertia is neglected. The errors are highest for modes with the longest wavelengths, and especially for $(i, j) = (1, 1)$. As the longer wavelength modes usually have a considerable contribution to the displacement and stresses responses of shells subject to earthquakes, the in-plane inertia should be included in calculating the out-of-plane frequencies. The high percentage of error in mode $(1, 1)$ indicates that the results produced by researchers who use the closed form solution in which the in-plane inertia is neglected [107] or the eigen-frequencies produced by past researchers based on neglect of in-plane inertia [106] [45] could result in significant errors. It is therefore dangerous to use their results especially in the dynamic analysis of doubly curved shells subjected to earthquake loading.

8.10 Energy contributions

Deriving the energy components for the natural modes of a doubly curved shell, it is possible to better understand how the contribution of each component differs for each mode. In this section the energy components of the shell, discussed in the previous section, are presented. Both conditions of neglecting and including the in-plane inertia

are considered in the derivation of the energy components of the shell. The shell geometry and material properties are chosen as follows $R_x = 141.42\ m$, $R_y = 141.42\ m$, $h = \frac{R_y}{100}$,$\rho = 2400\ kg/m^3$, $E = 24 \times 10^9 N/m^2$, $a = 100\ m$, $b = 100\ m$. The energy components of the shell are plotted for the two cases of including and neglecting inertia in the derivation of the energy and out-of-plane frequency in Figs 8.2 and 8.3 respectively.

The total energy at mode $(i, j) = (1, 1)$ is higher when the in-plane inertia is neglected in the eigenvalue problem compared with when it is included. It is as a result of the membrane energy being overestimated when in-plane inertia is neglected. Fig 8.3(b) shows that mode $(1, 1)$ has the dominant contribution from the membrane energy. Therefore the overestimation of the membrane energy as a result of neglecting the in-plane inertia, affects mode $(1, 1)$ more than other modes as shown in Table 8.2.

Looking at Fig 8.2(b) it is noticed that the contribution from N_x increases for $i < 5$ but after that N_x does not change as i increases. To understand the reason for N_x remaining unchanged for $i > 5$, N_x in eqn (8.5) is broken down into its components:

$$
\begin{aligned}
N_{x1} &= \frac{K}{2}\int_0^{R\phi_x}\int_0^{R\phi_y}[(\frac{\partial u}{\partial x})^2]dx\ dy \\
N_{x2} &= \frac{K}{2}\int_0^{R\phi_x}\int_0^{R\phi_y}[(\frac{w}{R_x})^2] \\
N_{x3} &= \frac{K}{2}\int_0^{R\phi_x}\int_0^{R\phi_y}[-2(\frac{\partial u}{\partial x})(\frac{w}{R_x})]dx\ dy \\
N_{x4} &= \frac{K}{2}\int_0^{R\phi_x}\int_0^{R\phi_y}[\nu(\frac{\partial v}{\partial y})(\frac{\partial u}{\partial x})]dx\ dy \\
N_{x5} &= \frac{K}{2}\int_0^{R\phi_x}\int_0^{R\phi_y}[-\nu(\frac{w}{R_x})(\frac{\partial v}{\partial y})]dx\ dy \\
N_{x6} &= \frac{K}{2}\int_0^{R\phi_x}\int_0^{R\phi_y}[+\nu\frac{w^2}{R_xR_y}]dx\ dy \\
N_{x7} &= \frac{K}{2}\int_0^{R\phi_x}\int_0^{R\phi_y}[-\nu(\frac{w}{R_y})(\frac{\partial u}{\partial x})]dx\ dy
\end{aligned}
\tag{8.14}
$$

The contribution of each of these components to N_x is plotted in Fig 8.4.

It is noticed that the contribution of N_{x1}, N_{x4}, and N_{x7} rapidly decreases as i increases and consequently converges to zero for $i > 4$. However, N_{x3} has a higher value than N_{x1}, N_{x4}, and N_{x7} and converges to zero at higher values of i ($i > 10$). N_{x5} and N_{x6}

almost remain unchanged but as they have different signs, the sum of their contribution to the total N_x would be little. Among these different components, N_{x2} has the highest contribution and does not change as i increases. This is the reason that the total N_x also remains unchanged for $i > 4$. Table 8.3 represents the changes in the normalised mode shapes and clarifies the reason for the difference in the contribution of each components to the total N_x. Table 8.3 shows that $\bar{u}_{ij}$ decreases more rapidly than $\bar{v}_{ij}$ as i increases. So the components that depend on $\bar{u}_{ij}$ such as N_{x1}, N_{x4}, and N_{x7} converge to zero for $i > 4$. $\bar{w}_{ij}$ almost remains constant as i varies, so N_{x2} does not change as i varies. N_{x2} also has the largest contribution to the total N_x because it only depends on $\bar{w}_{ij}$, which is higher than $\bar{u}_{ij}$ and $\bar{v}_{ij}$.

Fig 8.2 also shows that the contribution from N_x and N_y are equal for mode $(1, 1)$. It is because for equal values of $\bar{u}_{ij}$ and $\bar{v}_{ij}$ the energy contribution of N_x and N_y in eqn (8.5) would be exactly the same, and as can be seen in Table 8.3 for $(1, 1)$, $\bar{u}_{ij} = \bar{v}_{ij} = 0.2895$. But as i increases, N_x remains almost constant because, as mentioned earlier, it mostly depends on N_{x2}, which remains unchanged as i varies. However, as i increases, N_y rapidly converges to zero. This is because as shown in eqn (8.5), N_y depends on $\bar{v}_{ij}$ $(-2\frac{\partial v}{\partial y}\frac{w}{R_y})$ that has higher value than $\bar{u}_{ij}$ $((-2\frac{\partial u}{\partial y}\frac{w}{R_y})$ in U_m^x in eqn (8.5)) for $i > 1$, as can be seen in Table 8.3. So it has higher contribution of components with negative value, which cancels the positive contribution of $(\frac{w}{R_y})^2$ component.

N_{xy} also has the largest contribution to the membrane energy for $(1, 1)$. It is because, as shown in eqn (8.5), N_{xy} only depends on $\bar{u}_{ij}$ and $\bar{v}_{ij}$, which have the highest value in mode $(1, 1)$ (Table 8.3).

(i, j)	In-plane inertia neglected	In-plane inertia included	Percentage error
(1,1)	1.00061	0.84389	18.57
(1,2)	1.00488	0.93829	7.10
(2,2)	1.01303	0.97051	4.38
(1,3)	1.02100	0.98656	3.49
(2,3)	1.03573	1.00875	2.67
(1,4)	1.06231	1.04108	2.04
(3,3)	1.06943	1.04922	1.93
(2,4)	1.08635	1.06786	1.73
(3,4)	1.13552	1.12002	1.38
(1,5)	1.14756	1.13249	1.33
(2,5)	1.18359	1.16965	1.19
(4,4)	1.22331	1.21023	1.08
(3,5)	1.25274	1.24013	1.02
(1,6)	1.30080	1.28877	0.93
(2,6)	1.35154	1.33996	0.86
(4,5)	1.36848	1.35703	0.84
(3,6)	1.44514	1.43412	0.77
(5,5)	1.54961	1.53896	0.69
(1,7)	1.55149	1.54084	0.69
(4,6)	1.595098	1.58456	0.67
(2,7)	1.61960	1.60911	0.65
(3,7)	1.74214	1.73182	0.60
(5,6)	1.82023	1.80996	0.57
(1,8)	1.93441	1.92417	0.53
(4,7)	1.93259	1.92236	0.53

Table 8.2: Comparison of frequency parameter $\lambda = \rho R^2 \omega_{ij}^2 / E$ of present results with and without in-plane inertia on a simply supported doubly curved shell with $\nu = 0.3$, $a/b = 1$, $R_y/R_x = 1.0$, $Rh/a^2 = 0.005$

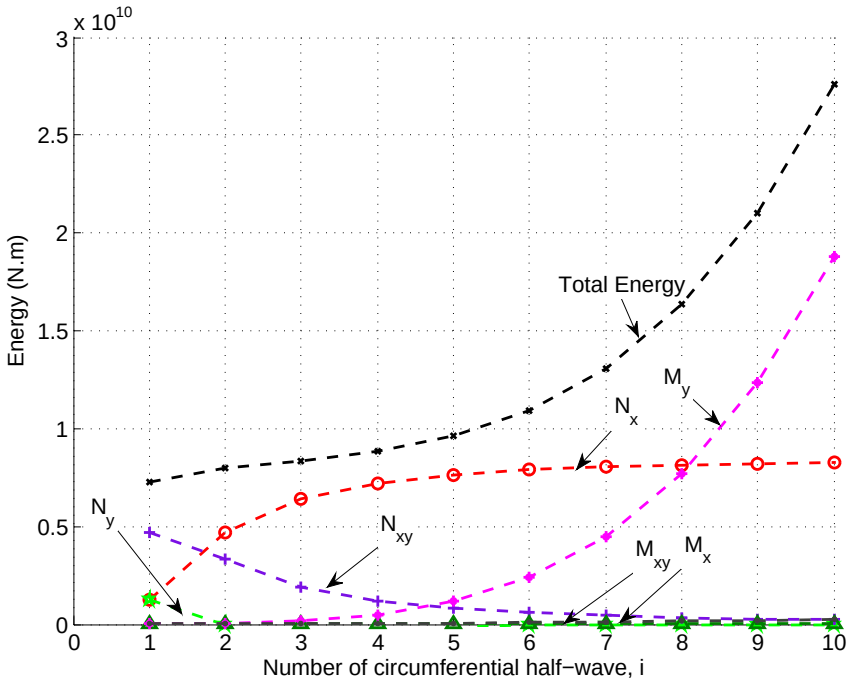

(a) In-plane inertia neglected

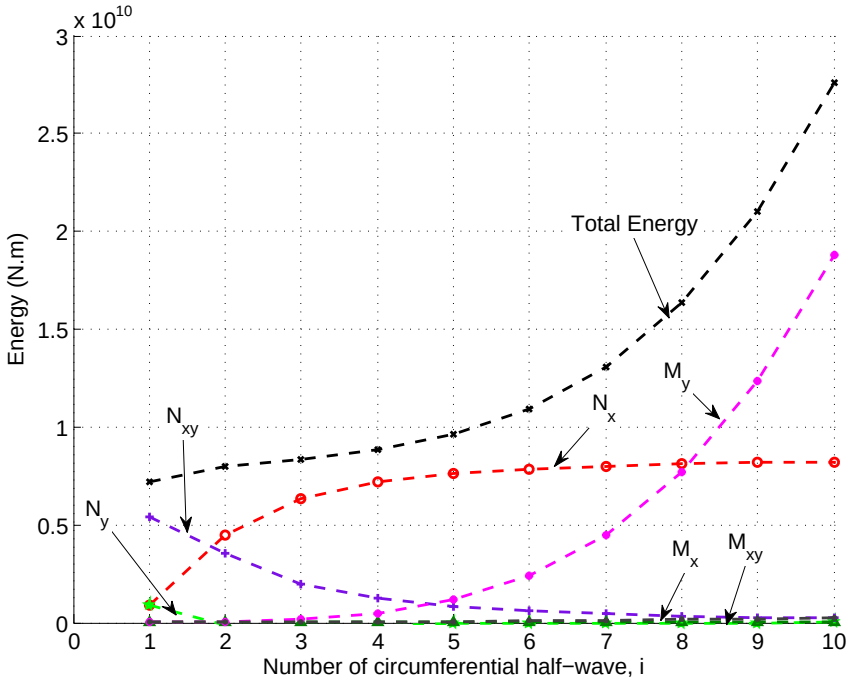

(b) In-plane inertia included

Figure 8.2: Comparisons of energy contents for shells with and without in-plane inertia in a circular doubly curved shell with $R_x = 141.42\ m$, $R_y = 141.42\ m$, $h = \frac{R_y}{100}$, $\rho = 2400\ kg/m^3$, $E = 24 \times 10^9 N/m^2$, $a = 100\ m$, $b = 100\ m$ and $j = 1$

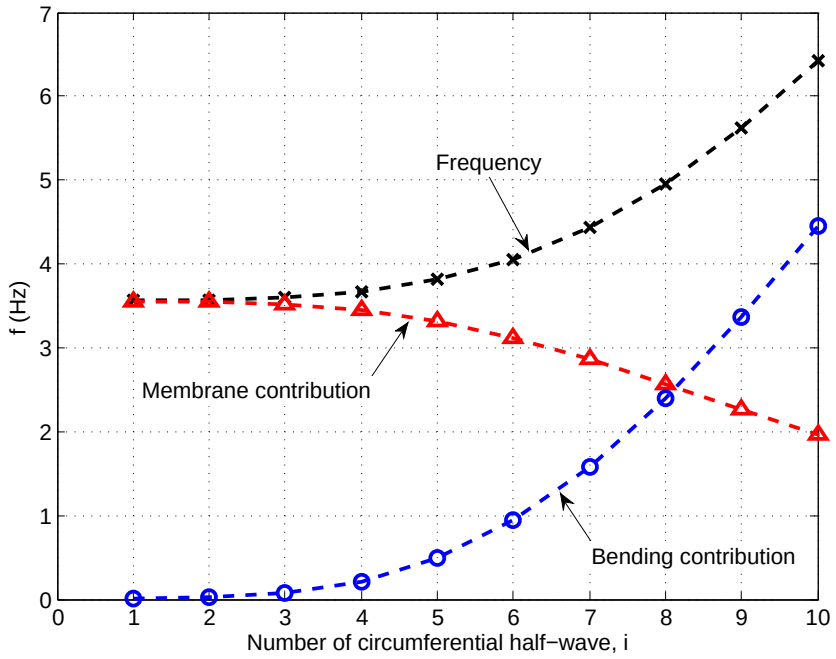

(a) In-plane inertia neglected

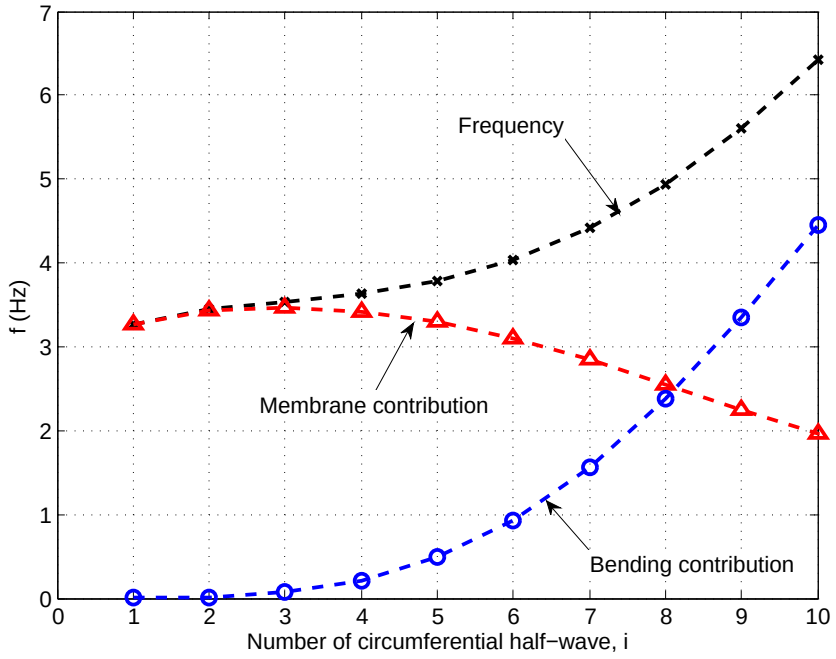

(b) In-plane inertia included

Figure 8.3: Comparisons of natural frequencies for shells with and without in-plane inertia in a circular doubly curved shell with $R_x = 141.42\ m$, $R_y = 141.42\ m$, $h = \frac{R_y}{100}$, $\rho = 2400\ kg/m^3$, $E = 24 \times 10^9 N/m^2$, $a = 100\ m$, $b = 100\ m$ and $j = 1$

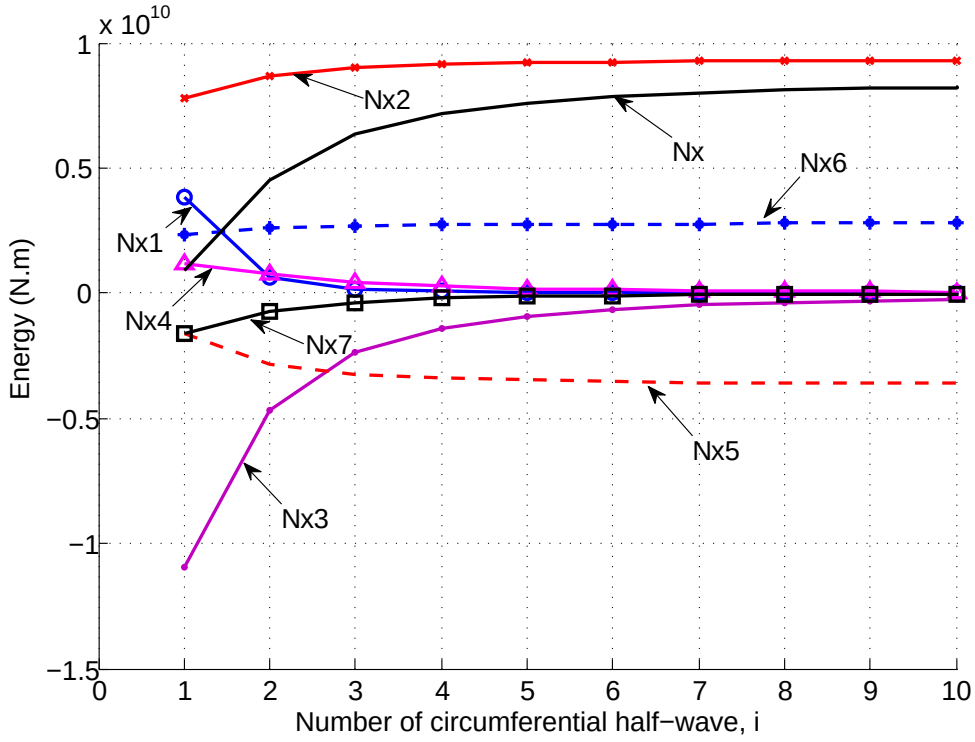

Figure 8.4: Contribution of different components of energies in N_x

i	$\bar{u}_{ij}$	$\bar{v}_{ij}$	$\bar{w}_{ij}$
1	0.2895	0.2895	0.9123
2	0.1170	0.2341	0.9652
3	0.0586	0.1758	0.9827
4	0.0345	0.1379	0.9898
5	0.0226	0.1128	0.9934
6	0.0159	0.0952	0.9953
7	0.0118	0.0822	0.9965
8	0.0091	0.0724	0.9973
9	0.0072	0.0646	0.9979
10	0.0059	0.0584	0.9983

Table 8.3: Changes in normalised mode shapes for the circular doubly curved shell having $R_x = 141.42\ m$, $R_y = 141.42\ m$, $h = \frac{R_y}{100}$,$\rho = 2400\ kg/m^3$, $E = 24 \times 10^9 N/m^2$, $a = 100\ m$, $b = 100\ m$ and $j = 1$

8.11 Comparison of frequencies of doubly curved and cylindrical shells

In order to compare the changes in the frequency content of shells as a result of adding the second curvature, a doubly curved shell with the material properties as the shell is Fig 3.4 is chosen. However, a curvature equal to the curvature of cylindrical shell in y direction is also added in x direction. The frequency content of this doubly curved shell having geometry and material properties of $R_x = R_y = 104.8m$, $\phi_x = \phi_y = \pi/3$, $h = 104.8/500$, $\rho = 4140.5\ kg/m3$, $E = 91 \times 10^9\ N/m^2$, $a = b = R\phi = 54.88\ m$ is shown in Fig 8.5. The rise to span ratio is 0.28, which does not classify this shell as a shallow shell. So in order to prevent the error the actual arc length is considered for a and b rather than their projection. This shell is only chosen to compare with the available results with a similar cylindrical shell in Fig 3.4.

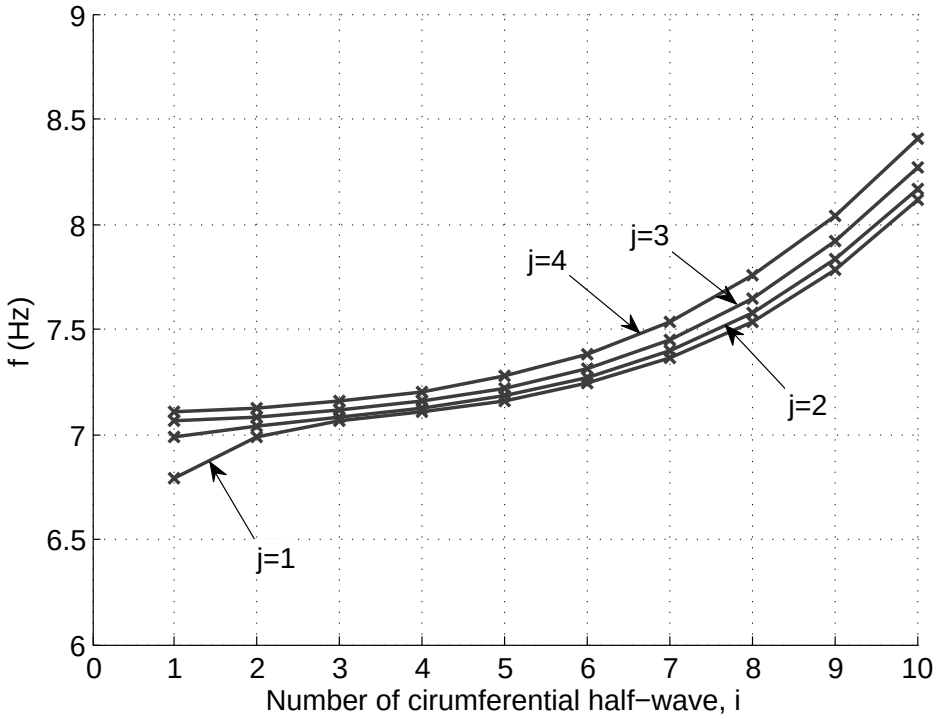

Figure 8.5: Natural frequency of a doubly curved circular shell having $R_x = R_y = 104.8\ m$, $\phi_x = \phi_y = \pi/3$, $h = 104.8/500\ m$, $\rho = 4140.5\ kg/m3$, $E = 91 \times 10^9\ N/m^2$, $a = b = R\phi = 54.88\ m$

The natural frequencies of this doubly curved shell shown in 8.5 are higher than the

cylindrical shell with the same geometry and material properties shown in Fig 3.4. The increase in the natural frequency indicates the increase in the shell stiffness. Fig 8.6(a) shows the contribution of different energy components to the total energy of the doubly curved shell. Comparing Fig 8.6(a) with Fig 3.6 shows that the total energy of the doubly curved shell is an order higher than the cylindrical shell. Also for this case of doubly curved shell the minimum energy occurs at mode $(1, 1)$, while in the cylindrical shell mode $(4, 1)$ has the minimum energy. The total energy in cylindrical shell before the point of minimum energy $(i = 4)$ is dominated by membrane energy with a higher contribution from N_{xy}, and after $i = 4$ it is dominated by bending energy (M_y), while in the doubly curved shell the relative contribution from the bending and membrane energies are different. In the doubly curved shell the contribution of the membrane energy is higher than the bending energy as it is also shown in Fig 8.6(a). It is only for $i > 14$ that the contribution of bending energy become higher than membrane energy as shown in 8.6(b).

It is now instructive to see how adding a curvature would affect the responses of shell to earthquake. Looking at the frequency content of the Landers earthquake in Fig 6.2(c) shows that adding a curvature to the shell causes the frequencies to be shifted to the region of very low displacement responses in the earthquake displacement response spectrum. For this reason it is expected that displacements would significantly reduce. In the next section the displacement, acceleration, and stress responses of the cylindrical and doubly curved shell are compared under Landers earthquake.

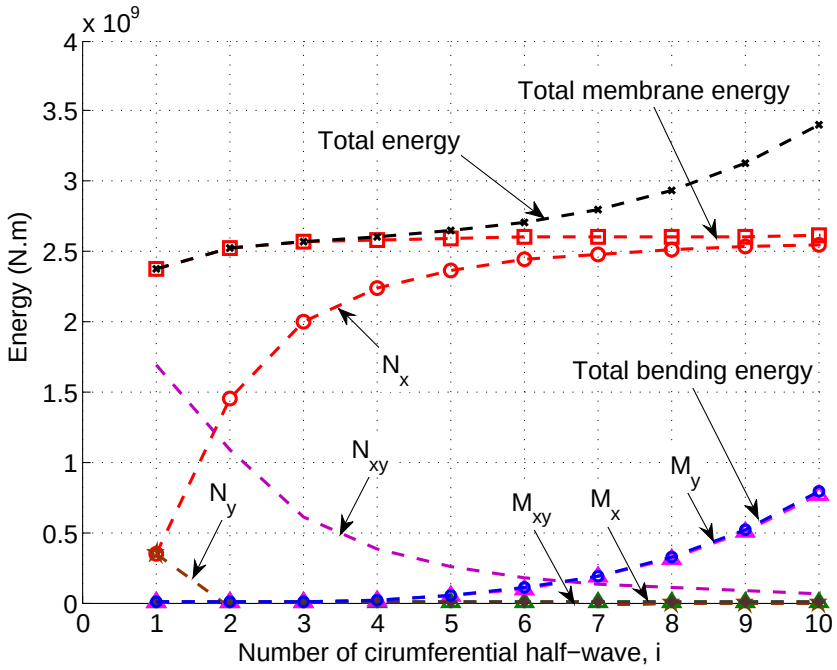

(a) Energy contribution

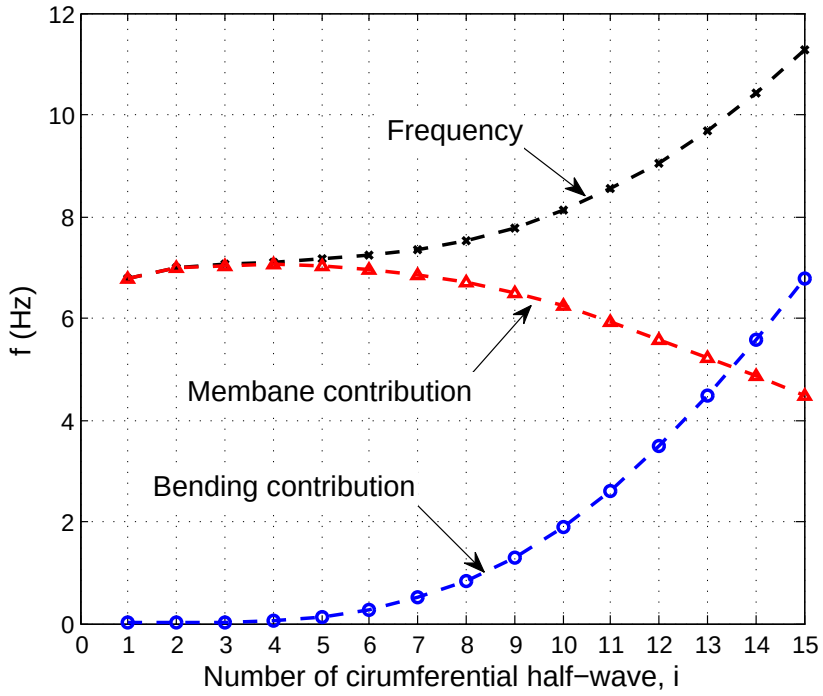

(b) Frequency

Figure 8.6: Energy contents and natural frequencies for a doubly curved circular shell having $R_x = R_y = 104.8\ m$, $\phi_x = \phi_y = \pi/3$, $h = 104.8/500\ m$, $\rho = 4140.5\ kg/m3$, $E = 91 \times 10^9\ N/m^2$, $a = b = R\phi = 54.88\ m$ and $j = 1$

8.12 Response of a doubly curved shell to a selected earthquake

In order to compare the results between a cylindrical and a doubly curved shell the same shell as in Fig 8.5 is chosen and analyzed under the vertical component of the earthquake in Fig 3.10. A convergence study is also performed using different numbers of axial and circumferential half-waves in the analysis using an analytical method. The analytical equations are solved using the time history modal analysis as explained in chapter 3. Maximum absolute displacement and acceleration responses of the shell (Fig 8.8 and 8.9) and maximum absolute stresses (Fig 8.10) over the earthquake duration are plotted along the line passing through the maximum response. The results are converged with a total number of 19 half-waves in circumferential and axial directions. Fig 8.7 shows the resulting maximum displacements and accelerations over the surface of the doubly curved shell over the duration of the earthquake. Figs 8.8 and 8.9 show the convergence of the displacements and accelerations along the line passing through the maximum displacement and acceleration as shown in Fig 8.7. Fig 4.5 shows that the displacements converged with a total of 10 lowest frequencies for a cylindrical shell. But Fig 8.8 shows that for the doubly curved shell the radial displacements are far from converged with a total of (I,J)=(4,4), which contains the lowest 10 frequencies plus an additional 6 modes. A total of $(I, J) = (19, 19)$ should be included for converged displacement results.

Similarly, for doubly curved shell more modes should be included for the convergence of stresses. The stress resultants as shown in Fig 8.10 seem to require a total of $(I, J) = (19, 19)$ for convergence, similar to Fig 4.6 for a cylindrical shell. But in order to check how many of these modes actively participate in the total responses it is helpful to find the contributions of each mode to the total response separately. Comparing the convergence study of the doubly curved shell (Fig 8.10) with the cylindrical shell in Fig 4.6 shows that they both converged with the same number of modes, but in doubly curved shell modes with a higher j contribute more significantly than in cylindrical shell. For example in M_x maximum results does not change significantly between in-

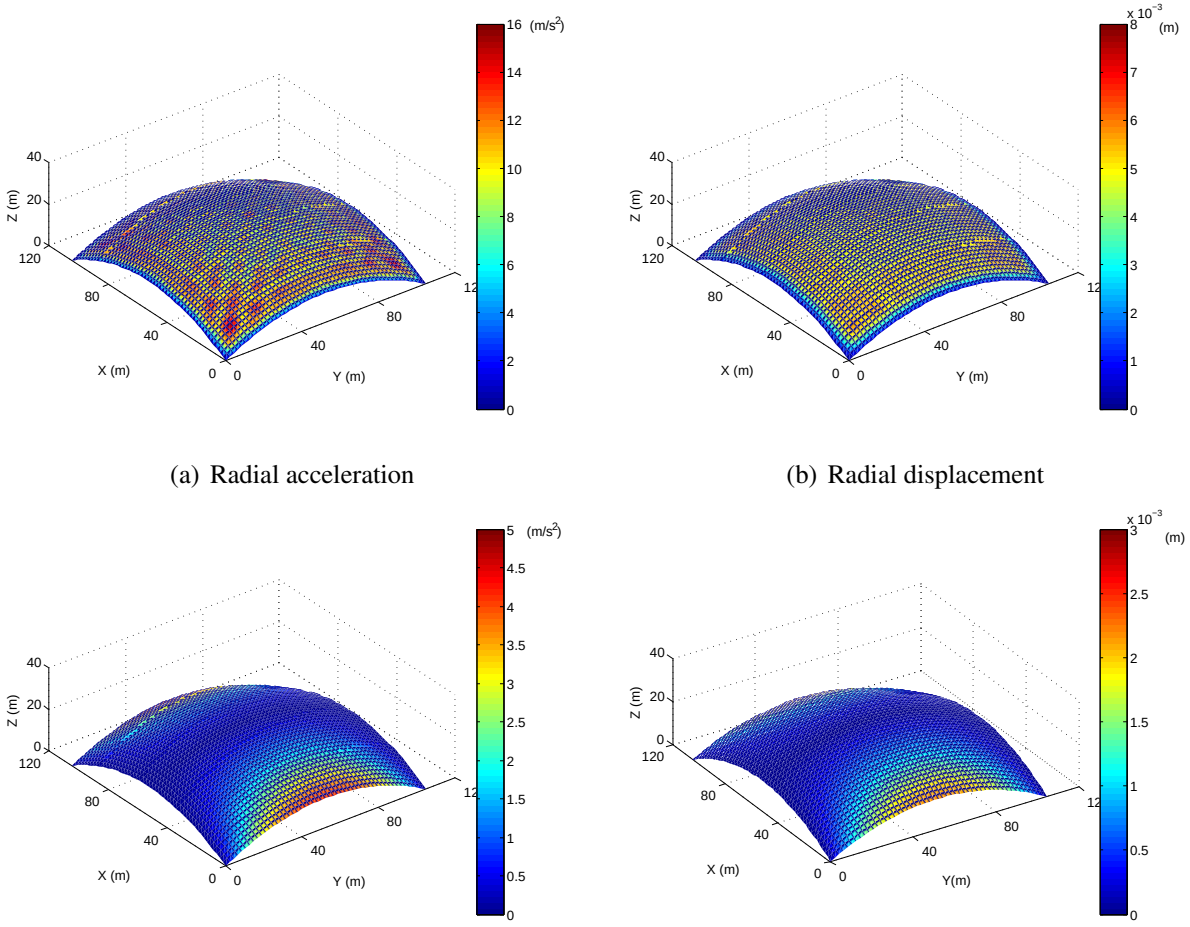

(a) Radial acceleration

(b) Radial displacement

(c) Circumferential acceleration

(d) Circumferential displacement

Figure 8.7: Maximum absolute displacement and acceleration for a total number of 19 half-waves in circumferential and axial directions

cluding a total of $(I, J) = (19, 19)$ and $(I, J) = (19, 9)$. But in the doubly curved shell (Fig 8.10) the maximum bending stress resultants in x direction resulting from including $(I, J) = (19, 19)$ are significantly higher than those resulting from including $(I, J) = (19, 9)$. This shows that in the doubly curved shell more modes are participating in the bending stress resultants in comparison with the cylindrical shell.

The maximum displacement, acceleration, and stresses responses of this shell are shown in Table 8.4. These are compared with the maximum responses of the cylindrical shell previously presented in section 3.9 with the same geometry and material properties, except for having one curvature in comparison with the two curvatures in the doubly curved shell. Table 8.4 shows that by adding a curvature in the x direction the displacement and bending stresses of the doubly curved shell becomes less

Maximum absolute result	Cylindrical Shell	Doubly curved shell
Radial acceleration m/s^2	11.3976	14.7187
Radial displacement m	0.0663	0.0057
Circumferential acceleration m/s^2	1.4641	4.0879
Circumferential displacement m	0.0049	0.0022
$M_x\ (N)$	25194	18382
$M_y\ (N)$	66627	18382
$M_{xy}\ (N)$	18188	12439
$N_x\ (N/m)$	1049400	808400
$N_y\ (N/m)$	789730	808400
$N_{xy}\ (N/m)$	934800	1609900

Table 8.4: Comparison of displacement, acceleration, and stress resultants between cylindrical and doubly curved shell with material properties of $\rho = 4041.5\ kg/m^3$, $E = 9.1 \times 10^{10}\ N/m^2$, and geometry for cylindrical shell $R = 104.8$, $h = R/500$, $\Phi = \pi/3$, $L_x = 104.8$, geometry of doubly curved shell of $R_x = 104.8\ m$, $R_y = 104.8\ m$, $h = R_x/500$, $\Phi_x = \pi/3$, $\Phi_y = \pi/3$

than the corresponding results in the cylindrical shell. It also shows an increase in N_y and N_{xy}. As shown in Fig 8.5, the natural frequencies of the shell increase by adding the curvature in the x direction. This shifts the displacement response to the area of the earthquake displacement response spectra having lower displacement responses, as shown in Fig 3.10. This might be anticipated to decrease the response of the shell when subject to the Landers earthquake. However, to understand more fully the behaviour of doubly curved shell the next section investigates the contribution of each mode to the total response.

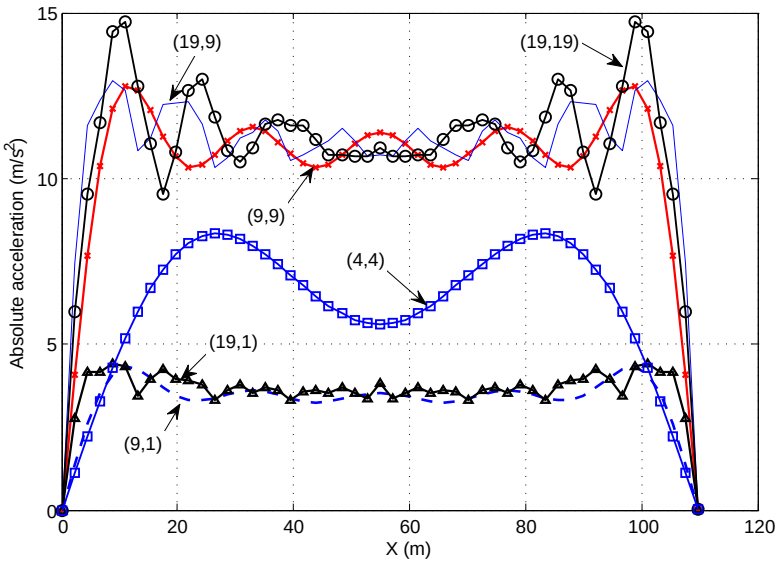

(a) Radial acceleration at $y = 8.22\ m$

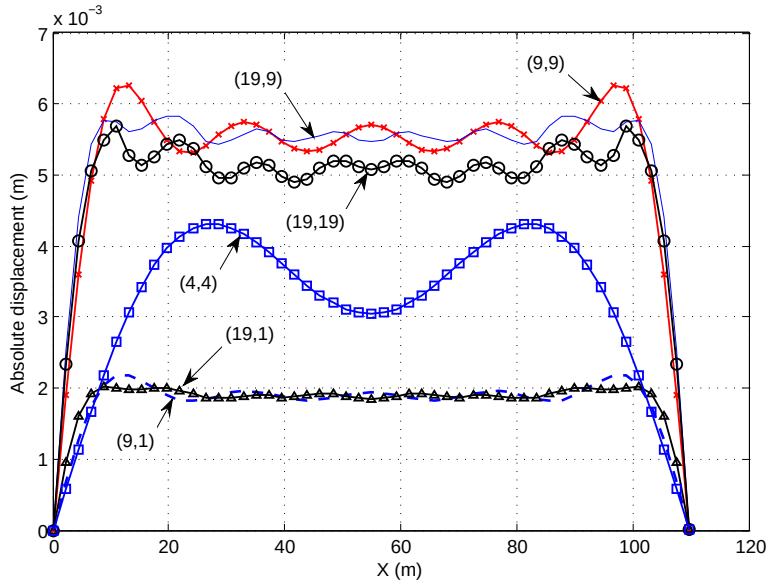

(b) Radial displacement at $y = 8.22\ m$

Figure 8.8: Maximum absolute radial displacement and acceleration along a line passing through maximum response parallel to x axis

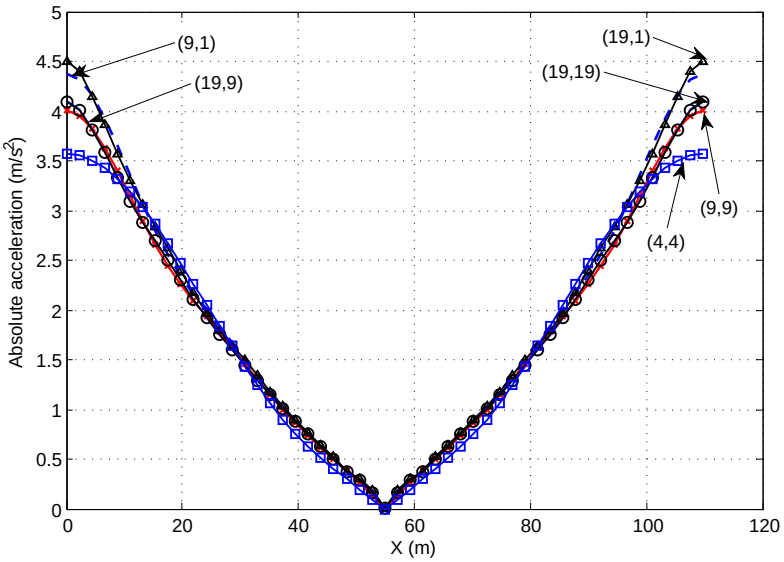

(a) Circumferential Acceleration at $y = 52.4\ m$

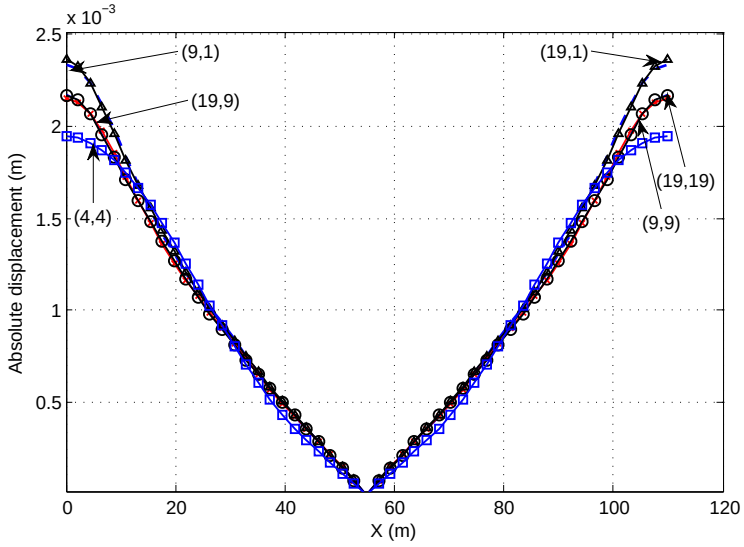

(b) Circumferential Displacement at $y = 52.4\ m$

Figure 8.9: Maximum absolute circumferential displacement and acceleration along a line passing through maximum response parallel to x axis

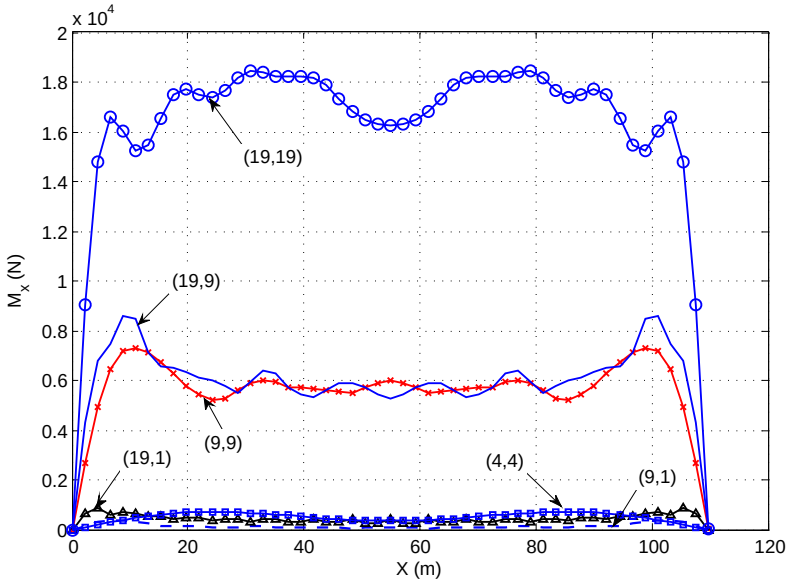

(a) M_x at $y = 100.6\ m$

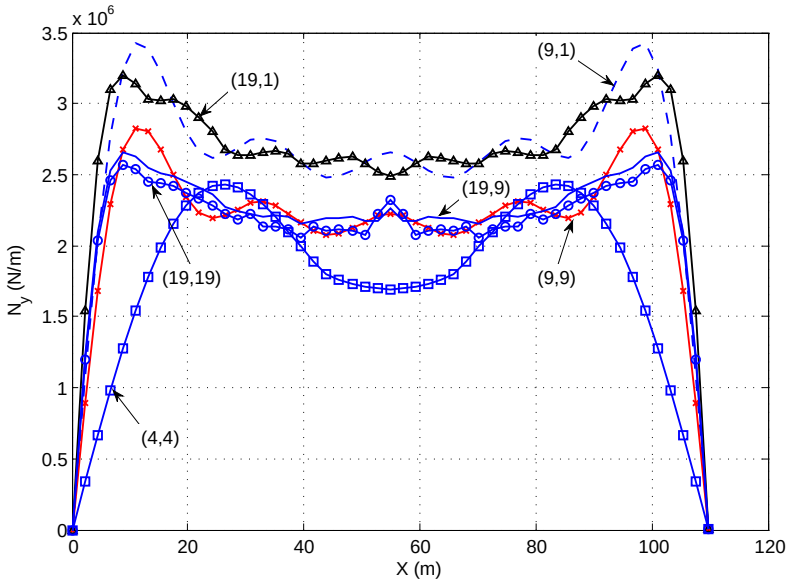

(b) N_y at $y = 52.4\ m$

Figure 8.10: Maximum stress resultants along a line passing through maximum response parallel to x axis

8.13 Participation of each mode in response

In this section the participation of different modes in the displacement response and their relationships with the modal participation in the stresses is investigated for the doubly curved shell in the previous section and compared with the modal participation of the cylindrical shell in section 3.8. For convenience, the modal damping ratio ζ_{ij} is again considered to be 0.05 for each mode. The time history modal analysis is carried out for the vertical component of the Landers earthquake as shown in Fig 3.10, using an analysis containing modes having half-wave numbers $i = 1, 2, \cdots, 19$ and $j = 1, 2, \cdots, 19$. Using the analytical method the contributions of different modes in the displacement and stress responses of the shell, at the time of maximum response, are plotted in Fig 8.11, 8.12 and 8.13 for the half-width across the line passing through the point with the maximum response; the response is symmetric about the center line aa. Like cylindrical shells the results of the analysis show that even though the maximum displacement may occur at a particular time and location, this would not necessarily relate to the most severe stresses. Stresses have a very different modal participation, as can be seen in Fig 8.11, 8.12 and 8.13 where it is more clear that the participation of different modes is not the same for displacements and stresses.

Comparing the displacement response of the doubly curved shell in Fig 8.11 and 8.12 with the displacement response of the cylindrical shell in Fig 3.16(a),(c) it is seen that although the total displacements of the cylindrical shell are much higher than those of the doubly curved shell, more modes contribute to the maximum displacement response of the doubly curved shell. For example, the radial displacement of the cylindrical shell in Fig 3.16 is dominated by the contribution of modes $(3, 1)$, $(5, 1)$, $(1, 3)$, which are all having long wavelengths. However, in the doubly curved shell (Fig 8.11), beside more modes contributing to the radial displacement, it can be seen that modes having shorter wavelengths such as $(1, 7)$ and $(1, 17)$ significantly contribute to the radial displacement.

The bending stresses in the doubly curved shell (Fig 8.13), on the other hand, have a similar effect on the stresses in cylindrical shell in Fig 3.16(c),(f); they both have significant contribution from the modes having shorter wavelengths. For clarity, Fig

8.13(a) shows only some of the modes contributing to the bending stress. However, more modes contributing to the bending stress are shown in Table 8.5, which indicate the participation of modes having shorter wavelength in the doubly curved shell. As mentioned in section 3.8 the bending stress resultants depend on i^2 and j^2, which consequently make the contribution of shorter wavelengths higher than in displacements.

The membrane stress (N_x) in the doubly curved shell (Fig 8.13(b)) is also compared with the membrane stress in the cylindrical shell in Fig 3.16(d). The comparison shows that unlike in the cylindrical shell that only modes having longer wavelength such as $(1,1)$, $(3,1)$, $(5,1)$, and $(5,3)$ contribute to the stress response, in doubly curved shell shorter wavelengths such as $(9,1)$ and $(13,1)$ contribute to the membrane stress resultant. Again for clarity, only some of the participating modes are shown in Fig 8.13(b) and other participating modes in the membrane stress in x direction are shown in Table 8.6.

The reason for participation of modes having short wavelength in N_x in doubly curved shell is that adding a curvature in x direction causes the term $\frac{w}{R_x}$ to be added in the ϵ'_x in eqn (8.2) and consequently in N_x in eqn (2.13). So N_x would have also a behaviour such as N_y in the cylindrical shell, which has significant contribution from modes having shorter wavelengths.

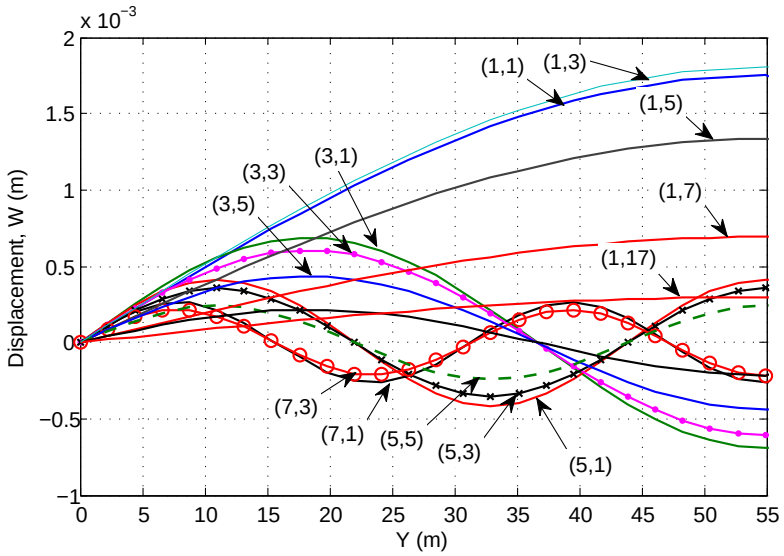

(a) Radial displacement at $y = 8.22\ m$

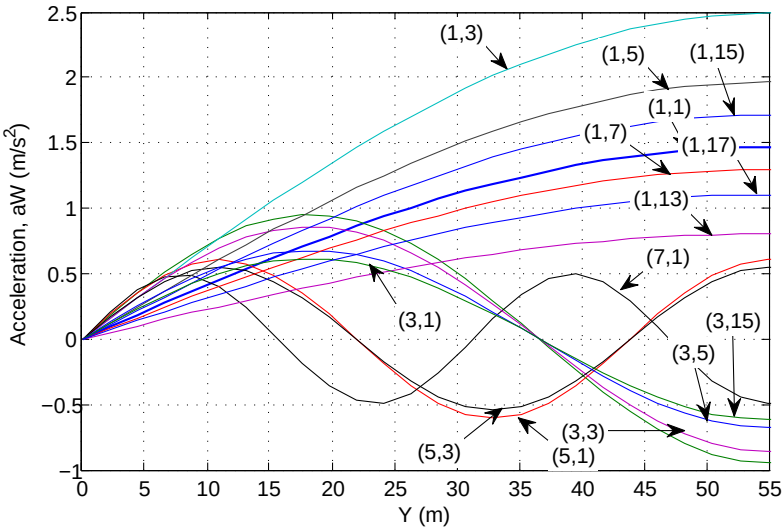

(b) Radial acceleration at $y = 8.22\ m$

Figure 8.11: Modal contribution of radial displacement and acceleration along a line passing through maximum response parallel to x axis

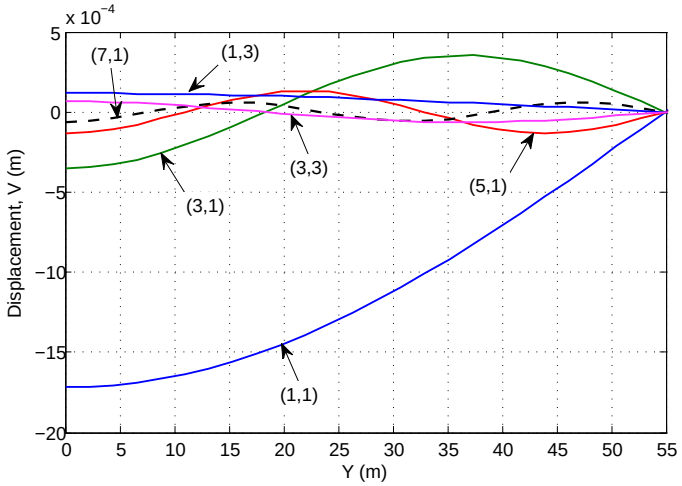

(a) Circumferential displacement at $y = 52.4\ m$

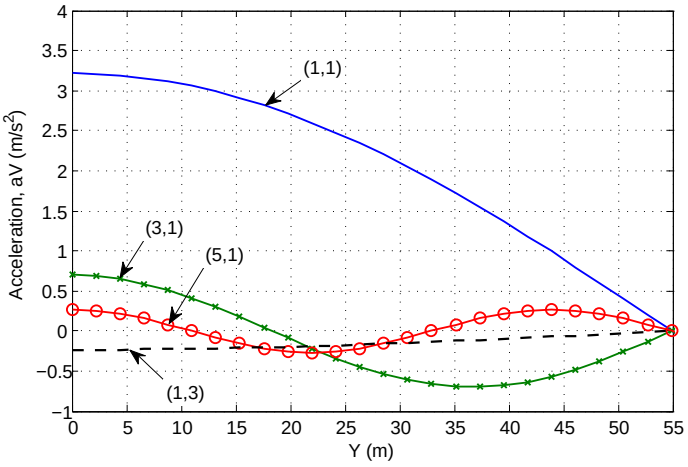

(b) Circumferential acceleration at $y = 52.4\ m$

Figure 8.12: Modal contribution of circumferential displacement and acceleration along a line passing through maximum response parallel to x axis

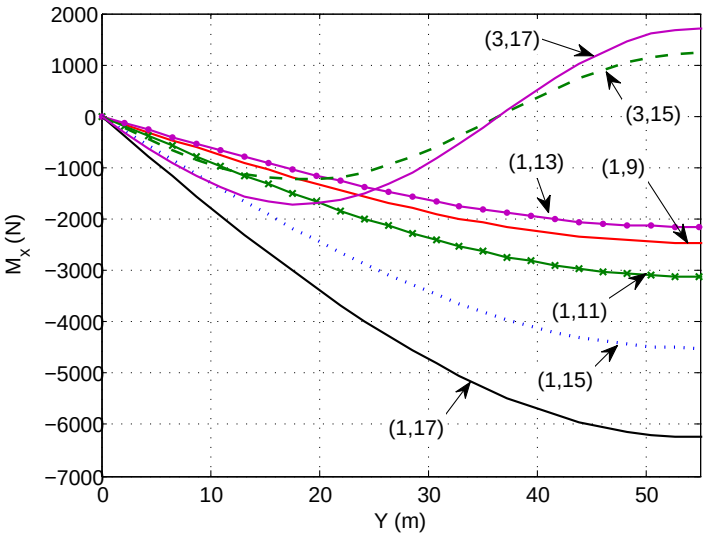

(a) M_x at $y = 100.6353\ m$

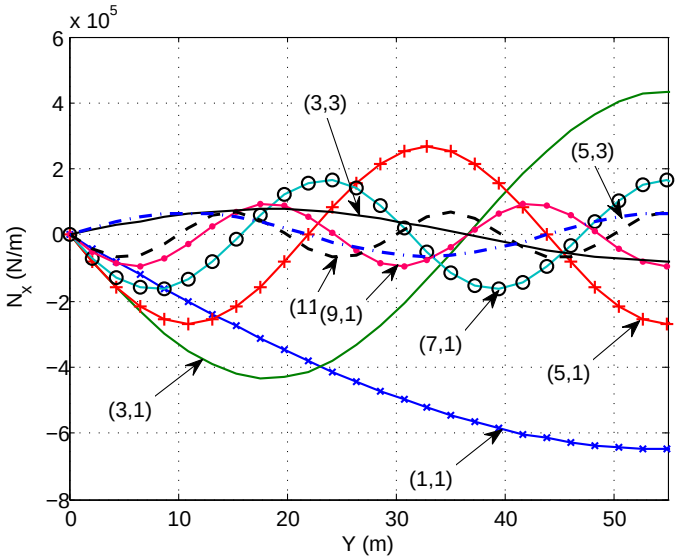

(b) N_x at $y = 8.7821\ m$

Figure 8.13: Modal contribution of stress resultant along a line passing through maximum response parallel to x axis

Mode (i,j)	Max abs value of M_x $(N.m/m)$	Mode (i,j)	Max abs value of M_x $(N.m/m)$
$(11,13)$	618.5	$(7,15)$	794.5
$(3,13)$	876.8	$(3,9)$	791.1
$(3,7)$	724.1	$(1,19)$	532.8
$(5,13)$	545.4	$(5,9)$	481.7
$(5,11)$	428.8	$(5,7)$	404.2
$(9,15)$	402.6	$(7,13)$	579.4
$(13,11)$	513.2	$(5,15)$	153
$(3,5)$	471.7	$(1,3)$	492.5

Table 8.5: Maximum absolute modal participation in M_x for modes having maximum stress resultants between 400 and 1000 along the line having the maximum total M_x in a doubly curved shell with material properties of $\rho = 4041.5\ kg/m^3$, $E = 9.1 \times 10^{10}$, and geometry of $h = R/500$, $R_x = 104.8\ m$, $R_y = 104.8\ m$, $h = R_x/500$, $\Phi_x = \pi/3$, $\Phi_y = \pi/3$

Mode (i,j)	Max abs value of N_x	Mode (i,j)	Max abs value of N_x
$(1,3)$	4.199×10^4	$(15,1)$	3.338×10^4
$(9,3)$	2.708×10^4	$(5,5)$	2.359×10^4
$(3,5)$	2.336×10^4	$(13,1)$	4.374×10^4
$(1,3)$	4.199×10^4	$(7,3)$	4.369×10^4

Table 8.6: Maximum absolute modal participation in N_x for modes having maximum stress resultants between 2×10^4 and 5×10^4 along the line having the maximum total N_x in a doubly curved shell with material properties of $\rho = 4041.5\ kg/m^3$, $E = 9.1\times10^{10}$, and geometry of $h = R/500$, $R_x = 104.8\ m$, $R_y = 104.8\ m$, $h = R_x/500$, $\Phi_x = \pi/3$, $\Phi_y = \pi/3$

The frequencies and mode numbers corresponding to some selected modes having short wavelength are shown in Table 8.7. Table 8.7 shows that these modes correspond

(i,j)	$f(hz)$	$ModeNumber$
$(5,13)$	10.35	139
$(7,13)$	11.04	156
$(15,1)$	11.28	164
$(5,15)$	12.02	183
$(7,15)$	12.78	201
$(11,13)$	13.3	211
$(13,11)$	13.3	212
$(9,15)$	13.82	226
$(1,19)$	15.73	265

Table 8.7: Short wavelength modes participating in stresses

to high mode numbers in the rank order such as mode $(9,15)$ being mode 226^{th} in rank order or mode $(1,19)$ the 265^{th} mode in rank order. This is similar to the cylindrical shell (Table 3.5) that also have the contributions from modes corresponding to high mode numbers in terms of the rank order. This indicates the need for considering about 300 modes for convergence of results in doubly curved shell.

8.14 Summary

In this chapter first the equation of motion was derived for a doubly curved shell with simply supports at four ends. The accuracy of the method was verified by comparing the governing natural frequencies with the available literature. Further investigation showed that the in-plane inertia that is usually neglected for simplification purposes in deriving the out-of-plane frequencies by researchers [45] [106] could lead to high error percentages in estimating the natural frequencies. This might consequently cause the underestimation of displacements and stress resultants when the shell is subjected to a typical earthquake loading.

The main purpose of this chapter was to compare the frequencies, displacements, and stress resultant of a doubly curved shell with a cylindrical shell. The comparison study was performed on a doubly curved shell having the same geometry and material prop-

erties as a cylindrical shell in chapter 3 by adding another curvature to the cylindrical shell. The governing natural frequencies in doubly curved shell were higher than those of the cylindrical shell. This shows that the doubly curved shell has a higher stiffness than the cylindrical shell.

The comparison of the energy content showed that the doubly curved shell has higher membrane energy than the cylindrical shell.

For a typical earthquake the displacements in the doubly curved shell were significantly lower than those in the cylindrical shell. However, unlike the cylindrical shell, shorter wavelengths contribute to the displacement responses of the doubly curved shell. The stress resultants in the doubly curved shell also reduced compared with the cylindrical shell except for N_y and N_{xy}. However, again more modes with shorter wavelengths contributed to the membrane stress resultants in the doubly curved shell.

Chapter 9

Conclusions and Recommendation for Future Work

Roof shells seem to be increasingly used to span large spaces. The increase in use of once neglected structure is suggested to be due to introducing new material and innovative ways of construction. However, there seems to be insufficient systematic research on the dynamic behaviour of roof shells. The literature review showed that the little research on the performance of roof shells has not been cross-checked. The main purpose of the present research is to tackle some aspects of behaviour of roof shells subjected to earthquake loading that have been neglected in previous research. It includes verification with available research and could then act as a basis for further investigations. However, it should be mentioned that most findings in this research are also applicable to the response of roof shells under other dynamic loading conditions.

9.1 Conclusions

A literature review was first performed to find the gaps in understanding of the dynamic analysis of roof shells. The equations of motion for a complete cylindrical shell were derived based on two methods; first, using the equilibrium equations, strain compatibility and constitutive relationships based on thin shell theory; second, the energy formulation was used to find the equation of motion in roof shells. The latter method is based on the stationary of total potential energy for providing the equilibrium in the

structure. It should be noted that all findings in this research is based on a constant damping ratio for all modes. Therefore, modes with higher frequencies would have higher damping forces. However, using different damping models may lead to different results.

9.1.1 Validation of shell theory

Using simply supported boundary conditions allowed the establishment of an exact solution to the eigenvalue problem using the aforementioned methods. The resulting natural frequencies were compared with some available natural frequencies obtained using different shell theories based on Love's first approximations. The comparison study showed that the resulting natural frequencies found from different shell theories were in good agreement for thin shells. From this comparison, the shell theory based on those of Love-Timoshenko was chosen for this research together with the equation of motion formulated on energy equations similar to those of the Goldenveizer-Novozhilov and Arnold-Warburton equations.

9.1.2 Effects of in-plane inertia in out-of-plane frequencies

The effects of including in-plane inertia in the eigenvalue problem and consequently on the out-of-plane frequencies was examined. The results showed an increase up to 46% in the out-of-plane frequencies for some modes. This indicates the poor accuracy of the results in some research that neglects the in-plane inertia only for simplification reason.

The study on the comparison of the energy contributions in thin and thick cylindrical shells showed that the thinner shells have more significant contributions from the membrane energies, while bending energies are dominant in thicker shells.

9.1.3 Confirmation of analysis

After selecting the shell theory, the investigation was extended to simply support open cylindrical roof shells. An analytical method was developed to investigate different aspects of the response of cylindrical roof shells under a typical earthquake that are not easy to explore using a general purpose FE program. The analytical method also could be used to provide confidence in the use of FE program. The accuracy of the analytical method was verified with the available literature and FE program for the case of natural frequencies. However, as there were not enough data on the controlling parameters of the response of shell to earthquake available in the literature, the validity of the response of shells to a typical earthquake loading was verified with ABAQUS, a commercially available FE program. The appropriate shell element and mesh size were chosen using a convergence study. The frequencies found using a linear eigenvalue analysis have been shown to be in practically good agreement with the analytical eigenvalue analysis. The displacements, acceleration and stress resultants using the FE program were also in convincing agreement with the results using analytical method. The very close agreement between the results using the analytical and FE methods gave confidence in use of either method.

9.1.4 Convergence with increasing number of modes

The convergence study with increasing number of modes showed that, unlike the response of ordinary buildings that converged by considering a small number of modes, cylindrical roof shells require the inclusion of a large number of modes for a converged response. In this regard, the study on the importance of the individual modes on the total response showed that modes with shorter wavelengths contribute significantly to the stress resultants. This is due to the fact that stresses have the contribution from the second order of i and j, which increase the involvements of modes having shorter wavelengths. In this context, bending stress resultants and hoop membrane resultants are shown to have the most important contribution from modes having shorter wavelengths. In a FE analysis these modes having shorter wavelengths correspond to modes having high numbers in a rank order starting from mode having the lowest frequency.

So this explains the need for including a large number of modes for converged results. For a selected shell, the required number of modes for a converged result was compared with the requirement of the UBC and Eurocode 8. UBC requires the number of modes in the modal analysis to be selected in such a way that their participating mass is at least 90% of the total effective mass. Eurocode 8 demands either the number of modes to be at least 90% of the total effective mass or all modes with effective mass greater than 5% of the total mass to be included in the modal analysis. This study showed that for the selected shell the 90% of the total effective mass was satisfied by including 98 modes in rank order. However, the stress resultants needed a total number of 300 modes to be included for converged responses. This indicates that the requirement of the code may no longer be sufficient for the case of roof shells.

9.1.5 Importance of in-plane modes

Using the analytical method, the effects of the in-plane modes in the response of cylindrical shells were investigated. The in-plane modes are those for which the in-plane deformations are dominant. Most researchers only considered the contributions from the out-of-plane deformations. However, it was shown that for some cases of shells the frequencies corresponding to the in-plane modes are in the range of the frequency spectrum of the earthquake and their inclusion could significantly affect the responses. The analysis of some cases of shells showed that including in-plane modes did not change the displacements significantly. However, significant changes were noticed in the acceleration and stress responses with, for example, up to 43% increase in hoop membrane stress in one case of shell as a result of including in-plane modes in the analysis. It should be noted that the extent of the effects of ignoring in-plane mode are strongly dependent upon the relationship between the frequency spectrum of the earthquake and the natural frequencies of the shell.

9.1.6 Relative importance of horizontal and vertical components of earthquake motion

In addition, the relative importance of horizontal and vertical components of an earthquake on the response of the shell was examined for the Landers earthquake, since

many studies are performed for the horizontal component of an earthquake while the vertical component is usually neglected. It was observed that the displacements, accelerations, and stress resultants were increased when shells were subjected to the vertical component of an earthquake. It should be noted that as one of the objectives of this research was to highlight the conditions that vertical component of earthquakes could produce higher responses compared to the horizontal component of earthquake, Landers earthquake was chosen. This earthquake had a high ratio of vertical to horizontal ground peak acceleration. However, it should be noted that this earthquake is not a typical earthquake. Again it is worth noting that the relative importance of the horizontal and vertical components of earthquake depends on the frequency spectrum of the selected earthquake and the natural frequencies of the shell.

9.1.7 Effects of pre-loading

Having shown some of the factors influencing the results, the analysis was extended to include the effects of pre-loading on the dynamic responses of cylindrical shells, a consideration often neglected in the past analysis. The equations of motion including the pre-loading were derived using the energy method for the case of roof shell when subjected to a uniform pressure loading and assumed to develop a pure membrane fundamental state. First, the classical buckling loads were derived and compared with the shell self-weight. It was shown that for some cases of shells selected for this research, the classical buckling loads are less than the shell self-weight. This shows the importance of finding the classical buckling loads before any dynamic analysis. The effect of pre-loading was then only investigated for those cases of shells having a classical buckling load higher than the shell self-weight.

Including the pre-loading, which is comprised of self-weight and additional loading such as snow loading, was shown to have significant effect on natural frequencies of the shell. The natural frequencies were decreased as a result of including pre-loadings. However, it was shown that the extent of decrease depends on the closeness of the lowest critical load and self-weight of the structure. For those cases of shells where the

lowest critical load is very close to self-weight, the inclusion of pre-loading significantly reduced the natural frequencies of the shell. The decrease in the natural frequencies was shown to cause a significant increase in the displacements, accelerations, and stress resultants responses.

A detailed study on the changes in modal contributions to the total response of shells due to pre-loading showed that the changes in the individual modes are very dependent on the changes in natural frequencies and the response spectra of the earthquake. For the modes having a significant decrease in natural frequencies as the result of including pre-loadings, if the frequencies fall into the region of the earthquake response spectrum with large changes, the modal response would significantly change.

9.1.8 Mode superposition methods

This study led to an investigation to find a simple relationship between the modal participation factor, earthquake response spectrum and maximum displacement and stress resultant responses of the shells without going through the extensive time consuming time history analysis. The aim was to examine the accuracy of the modal contribution methods to find the maximum responses of a shell. These methods are conveniently used for frame buildings and result in practically accurate results.

Using the equation of the modal participation factor helps to identify the modes with higher contributions. The maximum modal displacements were then found by multiplying the mode participation factor (MPF) by the displacement response spectrum of the earthquake corresponding to the natural frequency of the shell in that mode. This showed that the mode having the highest MPF does not necessarily have the highest contribution to the total response. This is because the contribution of the mode to the total response also depends on the response spectrum of the earthquake at the natural frequency of the shell corresponding to that mode.

The maximum stress responses were also derived by multiplying the maximum displacement response by the stress factor given by the equations of stress resultants. These were the same as the maximum modal responses using the time history analysis. The investigation on the accuracy of modal combination methods using the two

methods of square-root-of-sum-of-squares (SRSS) and complete quadratic combination (CQC) showed that both methods estimated the maximum displacement and axial membrane stresses within the practically acceptable percentage of error. However, the percentages of errors were different for various geometries of shells. Also, the stress resultants other than axial membrane stress cannot be accurately estimated using these modal combination methods.

9.1.9 Effects of pre-buckling nonlinearities

As mentioned earlier, the classical critical load was estimated using analytical method. Having established the classical critical load using the analytical method, detailed FE analysis was performed to verify the analytical predictions. Both the FE and analytical methods determined the critical loads using a linear analysis. The analytical method was based on a geometrically linear analysis using the idealized membrane theory, while the FE method considered the real boundary conditions that introduced geometric nonlinearities to the system. The lowest FE critical load was convincingly in good agreement with those found using the analytical method. The resulting critical loads were also in practically good agreement. However, the critical load using the FE analysis was noticed to produce lower critical loads in comparison with the analytical results. This is mainly because the FE analysis is based on a bending and membrane fundamental state for a shell with realistic boundary conditions, which introduced imperfection to the system. Unlike the mode shapes in analytical method that were sinusoidal waves, in FE they involved coupling between the equivalent analytical modes. This could again be due to introducing the nonlinearities into the system as a result of boundary conditions.

Next, the nonlinear snap buckling analysis of perfect open cylindrical shell was performed. The snap buckling loads were found to be much lower than the classical critical loads. It showed that the classical buckling analysis provided unsafe upper bound to the snap buckling of open cylindrical shells and for pre-loading near the snap buckling a nonlinear dynamic analysis should be performed. Furthermore, the deformations during the snap buckling analysis were found to be a localised form of the mode shape

associated with the lowest critical load rather than the overall periodic buckling as assumed in the classical analysis using the analytical method. This localisation is due to the imperfections caused by the boundary constrains.

The frequencies based on the idealized membrane state and bending nonlinear state were shown to be in good agreement. However, the frequency based on bending nonlinear state using FE analysis drop to zero unexpectedly at snap buckling, while in analytical method the frequencies reduced smoothly until it reached to zero at lowest critical load. As previously mentioned the mode shapes using these two methods were not the same.

9.1.10 Influence of double curvature

Finally, the analysis of cylindrical roof shells was extended to doubly curved shells by adding a curvature to the previously examined cylindrical shells. This was only to compare some of the basic behaviours of these two kinds of shell. However, the full investigation on the doubly curved shell requires a separate research program.

The resulting frequencies were verified with the results reported by previous researches. Most researchers neglect the in-plane inertia in the eigenvalue analysis to reduce the calculation time. However, the present research showed that including the in-plane inertia in the eigenvalue analysis could significantly reduce the out-of-plane frequencies especially those with longer wavelengths. This could lead to a significant underestimation of the dynamic responses when the doubly curved shell is subjected to earthquake loadings.

The natural frequencies and the linear dynamic responses of a cylindrical shell were compared with a doubly curved shell having the same material and geometry as cylindrical shell with added curvature in the second direction. The natural frequencies of the doubly curved shell were shown to be higher than the cylindrical shell. The displacements and stress resultants except for N_y and N_{xy} were shown to be significantly reduced in the doubly curved shell when subjected to a typical earthquake loading. However, unlike the cylindrical shell, in the doubly curved shell the axial membrane stress resultants had a significant contribution from modes with shorter wave lengths;

this was due to the added curvature in the axial direction.

9.2 Recommendations for future work

The present research has identified the following as being worthy of future investigation:

- The cylindrical roof shell in practice can have different type of boundary conditions. Hence, it is important to examine the effects of various boundary conditions, including the effects of substructure on the dynamic response of roof shells.

- The research is suggested to be continued for the cylindrical and doubly curved shell with different opening angles and shallowness.

- The effects of nonsynchronised corner or edge support motions on the response of the shells are worthy of examination and comparison with the responses of shells to synchronised support motion in the present research.

- Although the selected earthquake loading in this study satisfied the aim of this study, namely to identify the important aspects of the behaviour of roof shell that have been neglected so far, it would be beneficial to analyse shells considering earthquakes with a wider range of frequency contents. Typically, a carefully-selected suite of between six to thirty records is required for a more reliable analysis. This could lead to the identification of optimized shapes and materials for the shells subjected to a range of earthquakes having different frequency content. This can be done by choosing a shell for which the frequencies corresponding to the most significant modes fall into the low response spectrum region of the earthquake.

- In the absence of accurate damping information a constant damping ratio was considered for the structures including roof shells, throughout this study. It is

expected that different available damping models could significantly change the responses of the shell. There is a need to examine the effects of different damping models on the displacement and stress responses of roof shells. This might lead to the suggestion of a new damping model, which is more suitable for roof shells. Obviously, the research on the damping model could not be completed without experimental research on the realistic levels of damping experienced in different classes of shell and different modes.

- The nonlinear snap buckling has been shown to be much lower than the classical critical load. The deformations at buckling are also shown to be more in the form of a localised deformation rather than the periodic deformation of the linear eigenvalue analysis. It is suggested to continue the research using a complete nonlinear dynamic analysis and compare the displacements and stress resultants. This comparison study would enable us to check the difference between the level of responses for a practical loading. It might also lead to a simple procedure for finding the nonlinear dynamic response without going through the difficult and time consuming geometrically-nonlinear dynamic analysis.

- Having analysed the perfect cylindrical shell, it is important to find the changes in the snap buckling due to the influence of initial geometric imperfection.

- Finally, the buckling and nonlinear snap buckling analysis can be performed for the doubly curved shell to compare the nonlinear load carrying capacity of this class of shells compared with the cylindrical roof shells.

Bibliography

[1] A.W. Leissa. *Vibration of shells*. NASA, 1973.

[2] T. Moan. Development of accidental collapse limit state criteria for offshore structures. *Structural Safety*, 31(2):124–135, 2009.

[3] I Ortega. Simultaneous engineering in shell design and construction. In *IASS 2005 International symposium on Shell and Spatial Structures, Theory, Technique, Valuation, Maintainance*, pages 553–560, 2005.

[4] P. Ballesteros. Nonlinear dynamic and creep buckling of elliptical paraboloidal shell. *Bulletin of the Int. Association for Shell and Spatial Structures*, 66:39–60, 1978.

[5] A.C. Scordelis. Analysis of thin roof shells. *Bulletin of the Int. Association for Shell and Spatial Structures*, 87:5–19, 1985.

[6] M.S. Qatu. Recent research advances in the dynamic behavior of shells: 1989-2000, Part 1: Laminated composite shells. *Applied Mechanics Reviews*, 55:325, 2002.

[7] H. Kunieda. Earthquake response of roof shells. *International Journal of Space Structures*, 12:149–160, 1997.

[8] S. Yamada. Vibration behaviour of single-layer latticed cylindrical roofs. *International Journal of Space Structures*, 12:181–190, 1997.

[9] S. Yamada, Y. Matsumoto, and E. Saito. Seismic response behaviour of single layer latticed cylindrical roofs and the load modeling for seismic design. In

IASS 2005 International symposium on Shell and Spatial Structures, Theory, Technique, Valuation, Maintainance, pages 399–406, 2005.

[10] E.M. Hines, D.P. Billington, et al. Anton Tedesko and the introduction of thin shell concrete roofs in the United States. *Journal of Structural Engineering*, 130:1639, 2004.

[11] E.P. Saliklis and D.P. Billington. Hershey arena: Anton Tedesko's pioneering form. *Edmond P. Saliklis*, page 5, 2003.

[12] C. Meyer and M. Sheer. Do concrete shells deserve another look? *Concrete International*, 27:43–50, 2005.

[13] R. Bradshaw, D. Campbell, M. Gargari, A. Mirmiran, and P. Tripeny. Special structures: past, present, and future. *Journal of Structural Engineering*, 128:691, 2002.

[14] N. Burger and D.P. Billington. Felix Candela, elegance and endurance: An examination of the xochimilco Shell. *Journal International Association for Shell and Spatial Structures*, 152:271, 2006.

[15] T. Iori and S. Poretti. Pier Luigi Nervis Works for the 1960 Rome Olympics. *Congreso Nacional de Historia de la Construccin*, 152:605–613, 2005.

[16] V.V. Shugaev. Experience of application of reinforced concrete spatial structures in Russia, Proceedings of the IASS International Symposium, Romania', 2005.

[17] SR Roessler and D. Birtî. Thin shell concrete domes. *Concrete International*, page 49, 1986.

[18] X. Liu. New developments in the spatial structures field in China. In *IASS 2005 International symposium on Shell and Spatial Structures, Theory, Technique, Valuation, Maintainance*, pages 853–858, 2005.

[19] S. Zama, M. Yamada, H. Nishi, M. Hirokawa, K. Hatayama, T. Yanagisawa, and R. Inoue. Damage of oil storage tanks due to the 2003 Tokachi-oki earthquake. *Geophysical Exploration*, 59(4):353–362, 2006.

[20] K. Koketsu, K. Hatayama, T. Furumura, Y. Ikegami, and S. Akiyama. Damaging Long-period Ground Motions from the 2003 MW 8. 3 Tokachi-oki, Japan Earthquake. *Seismological Research Letters*, 76(1):67–73, 2005.

[21] H. Sezen, M. ASCE, and A.S. Whittaker. Seismic performance of industrial facilities affected by the 1999 Turkey earthquake. *Journal of Performance of Constructed Facilities*, 20:28, 2006.

[22] S. Kilic. Evaluation of effect of August 17, 1999, Marmara earthquake on two tall reinforced concrete chimneys. *ACI Structural Journal*, 100(3):357–364, 2003.

[23] K. Kawaguchi. a report on large roof structures damaged by the great Hanshin-Awaji earthquake. *International Journal of Space Structures*, 12:135–147, 1997.

[24] T. Saka and Y. Taniguchi. damage to spatial structures by the 1995 Hyogoken-Nanbu earthquake in Japan. *International Journal of Space Structures*, 12:125–133, 1997.

[25] K. Kawaguchi and Y. Suzuki. Damage investigations of public halls in Nagaoka city after Niigata-Chuetsu earthquake 2004 in Japan, Proceedings of the IASS International Symposium, Romania', 2005.

[26] I. Talemichi and S. Kato. A study on the seismic performance of shell and spatial structures, Proceedings of the IASS International Symposium, Romania', 2005.

[27] RN Arnold and GB Warburton. Flexural vibrations of the walls of thin cylindrical shells having freely supported ends. *Proceedings of the Royal Society of London. Series A, Mathematical and Physical Sciences*, 197(1049):238–256, 1949.

[28] RN Arnold and GB Warburton. The flexural vibrations of thin cylinders. *Proceedings of the Institution of Mechanical Engineers*, 167:62–74, 1953.

[29] DS Houghton and DJ Johns. A comparison of the characteristic equations in the theory of circular cylindrical shells. *Aeronautical Quarterly*, pages 228–36, 1961.

[30] PS Epstein. On the theory of elastic vibrations in plates and shells. *Journal of Mathematics and Physics*, 21(3):198–209, 1942.

[31] EH Kennard. The new approach to shell theory: circular cylinders. *Journal of Applied Mechanics*, 20(1), 1953.

[32] EH Kennard. Cylindrical shells: Energy, equilibrium addenda and erratum. *Journal of Applied Mechanics*, pages 111–116, 1955.

[33] GI Mikhasev. Free and parametric vibrations of cylindrical shells under static and periodic axial loads. *Technische Mechanik*, 17(3):209–216, 1997.

[34] F. Auslender and A. Combescure. Spherical elastic–plastic structures under internal explosion Approximate analytical solutions and applications. *Engineering Structures*, 22(8):984–992, 2000.

[35] R.L. Martineau, C.A. Anderson, and F.W. Smith. Expansion of cylindrical shells subjected to internal explosive detonations. *Experimental Mechanics*, 40(2):219–225, 2000.

[36] VC De Souza and JG Croll. Free vibrations of orthotropic spherical shells. *Engineering Structures*, 3(2):71–84, 1981.

[37] JGA Croll. Coupled vibration modes(two degrees of freedom mechanical model). *Journal of Sound and Vibration*, 38:27–37, 1975.

[38] VCM De Souza and JG Croll. Vibration tests on spherical shell caps. *Journal of Strain Analysis*, 18:27–36, 1983.

[39] VZ Vlasov. General shell theory and its application in Engineering. *Gostekhizdat, Moscow–Leningrad*, 1949.

[40] MS Qatu. Literature review analysis of the shock and vibration literature: Review of shallow shell vibration research. *The Shock and Vibration Digest*, 24(9):3, 1992.

[41] KM Liew, CW Lim, and S. Kitipornchai. Vibration of shallow shells: A review with bibliography. *Applied Mechanics Reviews*, 50:431–444, 1997.

[42] H. Lamb. On the vibrations of a spherical shell. *Proceedings of the London Mathematical Society*, 1(1):50, 1882.

[43] A. Leissa. *Vibration of shells*. Acoustical Society of America, New York, 1993.

[44] GR Cowper, GM Lindberg, and MD Olson. A shallow shell finite element of triangular shape(Shallow shell finite element of triangular shape, noting application to static problems). *International Journal of Solids and Structures*, 6:1133–1156, 1970.

[45] MD Olson and GM Lindberg. Dynamic analysis of shallow shells with a doubly curved triangular finite element. *Journal of Sound and Vibration*, 19(3):299–318, 1971.

[46] K.M. Liew and C.W. Lim. Vibration of doubly-curved shallow shells. *Acta Mechanica*, 114(1):95–119, 1996.

[47] RA Chaudhuri and H Kabir. Static and dynamic Fourier analysis of finite cross-ply doubly curved panels using classical shallow shell theories. *Composite structures*, 28(1):73–91, 1994.

[48] RA Chaudhuri and H Kabir. A boundary-continuous-displacement based Fourier analysis of laminated doubly-curved panels using classical shallow shell theories. *International Journal of Engineering Science*, 30(11):1647–1664, 1992.

[49] D. Chakravorty, JN Bandyopadhyay, and PK Sinha. Finite element free vibration analysis of doubly curved laminated composite shells. *Journal of Sound and Vibration*, 191(4):491–504, 1996.

[50] AV Singh and V. Kumar. Vibration of laminated shallow shells on quadrangular boundary. *Journal of Aerospace Engineering*, 9(2):52, 1999.

[51] Y. Narita, M. Itoh, and X. Zhao. Optimal design by genetic algorithm for maximum fundamental frequency of laminated shallow shells. *Advanced Composites Letters*, 5:21–24, 1996.

[52] M.S. Qatu. Recent research advances in the dynamic behavior of shells: 1989–2000, Part 2: Homogeneous shells. *Applied Mechanics Reviews*, 55:415, 2002.

[53] K.A. Alhazza and A.A. Alhazza. A review of the vibrations of plates and shells. *The Shock and Vibration Digest*, 36(5):377, 2004.

[54] F. Jiashen and F. Lei. Closed form solution for nonlinear dynamic response in shallow shells. *Applied Mathematical Modelling*, 15(8):416–424, 1991.

[55] S. Yamada and A. Takeuchi. Simple estimates of the effects of pre-stresses on the vibration behaviour of shell-like space frames. *Proceedings of the IASS International Symposium, Milano*, 2:1109–1117, 1995.

[56] S. Yamada. Estimation on the effects of initial stresses on the vibration behavior of cured shell-like structures. *Theoretical and Applied Mechanics-Science Council of Japan*, 44:21–28, 1995.

[57] S. Yamada and A. Takeuchi. A simple estimation of free vibration behaviour of latticed cylindrical panel structures, in 'Space Structures 4', 1993.

[58] S. Yamada, Y. Matsumoto, and E. Saito. Static load modeling using continuum shell analogy for single layer latticed cylindrical shell structures. In *CD-ROM Proceedings of International Symposium on New Olympic, New Shell and Spatial Structures, IASS-APCS2006, Beijing*, 20056.

[59] YB Chen, QS Li, and JM Chen. Dynamic characteristics of single-layer cylindrical lattice shells. *Structures & Buildings*, 158(1):41–51, 2005.

[60] QS Li and JM Chen. Nonlinear elastoplastic dynamic analysis of single-layer reticulated shells subjected to earthquake excitation. *Computers and Structures*, 81(4):177–188, 2003.

[61] S. Shen, J. Xing, and F. Fan. Dynamic behavior of single-layer latticed cylindrical shells subjected to seismic loading. *Earthquake Engineering and Engineering Vibration*, 2(2):269–279, 2003.

[62] S. Kato, T. Ueki, and Y. Mukaiyama. Study of dynamic collapse of single layer reticular domes subjected to earthquake motion and the estimation of statically equivalent seismic forces. *International Journal of Space Structures*, 12(3):191–204, 1997.

[63] L. Su, S.L. Dong, and S. Kato. A new average response spectrum method for linear response analysis of structures to spatial earthquake ground motions. *Engineering Structures*, 28(13):1835–1842, 2006.

[64] S. Germain and J.T. Graves. *Recherches sur la théorie des surfaces élastiques*. Mme. Ve. Courcier, 1821.

[65] S. Timoshenko. *History of strength of materials*. Dover Publications New York, 1983.

[66] H. Aron. Das Gleichgewicht und die Bewegung einer Unendlich Dunnen. *beliebig gekrummten elastischen Schale, Journal of Mathematics (Crelle*, 78:23–34, 1874.

[67] T. Koga. Free vibrations of circular cylindrical shells. *JSME International Journal, Series I*, 32:311–319, 1989.

[68] L. Rayleigh. On the infinitesimal bending of surfaces of revolution. *Proceedings of the London Mathematical Society*, 1(1):4, 1881.

[69] AEH Love. The small free vibrations and deformation of a thin elastic shell. *Philosophical Transactions of the Royal Society of London*, 179:491–546, 1888.

[70] BG Galerkin. Theory of elastic cylindrical shells. In *Doklady Akad. Nauk. SSSR*, volume 4, page 230, 1934.

[71] BG Galerkin. Equilibrium of the elastic spherical shell. *Russian) Prikl. Mat. Mekh. 6*, pages 487–511, 1942.

[72] AI Lur'ye. General theory of elastic shells. *Prikladnaya Matematika i Mekhanika*, pages 7–34, 1940.

[73] VZ Vlasov. *General theory of shells and its application in Engineering*. National Aeronautics and Space Administration, 1964.

[74] VV Novozhilov. Foundations of the nonlinear theory of elasticity, chapter 3, 1953.

[75] II Vorovich. About Bubnov–Galerkins method in the non-linear theory of vibrations of shallow shells. *Rep. USSR Acad. Sci*, 110(5):723–726, 1956.

[76] HM Mushtari and IG Teregulov. A theory of shallow orthotropic shells of medium thickness. *Trans. USSR Acad. Sci., Department of Technical Sciences. Mechanics and Mechanical Engineering*, pages 60–67, 1959.

[77] K.M. Mushtari and KZ Galimov. *Non-linear theory of thin elastic shells*. Published for the National Science Foundation by the Israel Program for the Scientific Translations; available from the Office of Technical Services, US Dept. of Commerce, 1961.

[78] AL Goldenveizer and G. Herrmann. *Theory of elastic thin shells*. Pergamon Press, 1961.

[79] AL Goldenveiser. A theory of elastic thin-wall shells, 1979.

[80] W. Flugge. Statik und dynamik der schalen. *Julius Springer, Berlin*, 1934.

[81] JK Knowles and E. Reissner. A Derivation of the Equations of Shell Theory for General Orthogonal Coordinates. *Journal of Mathematics and Physics*, 35:351–358, 1957.

[82] J.L. Sanders. An improved first-approximation theory for thin shells. *NASA*, 1959.

[83] V.V. Novozhilov and J.R.M. Radok. *Thin Shell Theory: Teoría de Estructuras Laminares*. P. Noordhoff, 1964.

[84] B. Budiansky and JL Sanders. On the best first order linear shell theory, Progress in Applied Mechanics, The Prager Anniversary Volume, 1963.

[85] R. Byrne. *Theory of small deformations of the thin elastic shell.* University of California Press, 1944.

[86] W. Flugge. Stress in shells.

[87] VV Novozhilov. The theory of thin elastic shells. *Noordhoff, Groningen*, 1959.

[88] A.E. Love. *Treatise on the mathematical theory of elasticity*. Dover Publications, 1944.

[89] S.P. Timoshenko and S. Woinowsky-Krieger. Theory of plates and shells. *Engineering Societies Monographs, New York: McGraw-Hill, 1959, 2nd ed.*, 1959.

[90] E. Reissner. A new derivation of the equations for the deformation of elastic shells. *American Journal of Mathematics*, 63(1):177–184, 1941.

[91] PM Naghdi and JG Berry. On the equations of motion of cylindrical shells. *Journal of Applied Mechanics*, 21(2):160–166, 1964.

[92] VS Vlasov. Basic differential equations in general theory of elastic shells. *English translation), NACA-TM 1241*, 1951.

[93] LH Donnell. A discussion of thin shell theory. *Proceedings of the 5th International Congress of Applied Mechanics*, pages 66–70, 1938.

[94] MS Qatu. Review of shallow shell vibration research. *The Shock and Vibration Digest*, 24(9):3–15, 1992.

[95] H Kunieda, K Kitamura, and T Ohya. Free vibration and JMA-earthquake responses of cylindrical roofs. *Annual Disaster prevention research institute*, (39):B–1, 1996.

[96] R.W. Clough and J. Penzien. *Dynamics of structures*. McGraw-Hill New York, 1975.

[97] A.K. Chopra. *Dynamics of structures*. Tsinghua University Press, 2005.

[98] B. Budiansky and JL Sanders. On the best first-order linear shell theory. *Progress in Applied Mechanics–The Prager Anniversary Volume*, pages 129–140, 1963.

[99] A. Documentation. ABAQUS theory manual. c 2006 ABAQUS.

[100] U.B.C. UBC. Uniform Building Code. In *International Conf. of Building Officials*, 1997.

[101] C.E. de Normalisation. Eurocode 8: Design of structures for earthquake resistancepart 1: general rules, seismic actions and rules for buildings. *European Standard NF EN 1998*, 1, 2005.

[102] JGA Croll. Explicit lower bounds for the buckling of axially loaded cylinders. *Int. J. Mech. Sci.*, 23(6):331–343, 1981.

[103] E. Rosenblueth. *A basis for aseismic design*. PhD thesis, Univ. of Illinois, Urbana, Ill, 1951.

[104] N.M. Newmark and E. Rosenblueth. *Fundamentals of earthquake engineering*. Prentice-Hall Englewood Cliffs, NJ, 1971.

[105] S. Shen, J. Xing, and F. Fan. Dynamic behavior of single-layer latticed cylindrical shells subjected to seismic loading. *Earthquake Engineering and Engineering Vibration*, 2(2):269–279, 2003.

[106] KM Liew and CW Lim. Vibration of doubly-curved shallow shells. *Acta Mechanica*, 1996.

[107] H. Kraus. *Thin elastic shells*. Wiley New York, 1967.

Appendix A

Modal Combination Methods

Tables A.1 to A.14 present the comparison study of the maximum response using two modal combination methods (SRSS and CQC) with the exact results using time history modal analysis. The maximum response in Tables A.1 to A.7 are found based on the assumption that the maximum response in each mode occur at different instants of time but find the maximum response for each specific spatial location over the surface of the shell. This is the same method as explained by Chopra [97]. In section 6.2 the comparison study using this method is performed for three cases of shells and shown in Table 6.2. However Tables A.1 to A.7 show the maximum responses for the 24 cases of the shells that are sued throughout the present research.

In Tables A.8 to A.14 the maximum responses for 24 cases of shells are derived regardless of the time that they occur and their location over the surface of the shell. The result for the three cases of shells are presented in Table 6.3.

L_y/L_x	B	THA	SRSS	CQC	% error SRSS	% error CQC
	2	0.1141	0.1028	0.1009	9.90	11.57
	1.75	0.1065	0.099	0.1059	7.04	0.56
	1.5	0.0953	0.0914	0.0974	4.09	2.20
1	1.25	0.0836	0.076	0.081	9.09	3.11
	1	0.0663	0.0593	0.0585	10.56	11.76
	0.75	0.0468	0.0434	0.0423	7.26	9.62
	0.74	0.0453	0.0415	0.0404	8.39	10.82
	0.5	0.0299	0.0263	0.0253	12.04	15.38
	2	0.1648	0.1593	0.1585	3.34	3.82
	1.75	0.1447	0.1459	0.1449	0.83	0.14
	1.5	0.1302	0.1303	0.1306	0.08	0.31
0.5	1.25	0.1362	0.122	0.1223	10.43	10.21
	1	0.104	0.1097	0.1105	5.48	6.25
	0.75	0.1081	0.1004	0.0999	7.12	7.59
	0.74	0.1072	0.098	0.0974	8.58	9.14
	0.5	0.0973	0.0935	0.093	3.91	4.42
	2	0.0318	0.0274	0.0282	13.84	11.32
	1.75	0.024	0.0221	0.0199	7.92	17.08
	1.5	0.0183	0.0201	0.0191	9.84	4.37
2	1.25	0.0188	0.0172	0.0157	8.51	16.49
	1	0.018	0.0173	0.0176	3.89	2.22
	0.75	0.0136	0.0132	0.0141	2.94	3.68
	0.74	0.0128	0.0132	0.0141	3.12	10.16
	0.5	0.0123	0.0112	0.0115	8.94	6.50

Table A.1: Comparison of W between modal time history analysis, CQC, and SRSS for a total number of 19 axial and circumferential half waves including effect of location

L_y/L_x	B	THA ($\times 10^6$)	SRSS ($\times 10^6$)	CQC ($\times 10^6$)	SRSS % error	CQC % error
1	2	0.5948	0.4947	0.4885	16.83	17.87
	1.75	0.7939	0.6724	0.7040	15.31	11.32
	1.5	0.8741	0.9016	0.9419	3.16	7.77
	1.25	1.1128	1.0344	1.0767	7.05	3.24
	1	1.0494	0.9820	0.9935	6.43	5.33
	0.75	1.1648	1.0304	1.0253	11.54	11.98
	0.74	1.3168	1.1649	1.2032	11.53	8.63
	0.5	1.6127	1.3929	1.3961	13.63	13.43
0.5	2	0.9406	0.8458	0.8749	10.08	6.97
	1.75	1.0824	0.9833	1.0130	9.15	6.40
	1.5	1.1718	1.0634	1.1049	9.25	5.70
	1.25	1.4218	1.3006	1.3521	8.52	4.90
	1	1.7869	0.2217	0.1914	87.59	89.29
	0.75	1.9815	1.7591	1.6776	11.22	15.34
	0.74	2.0901	1.8599	1.7626	11.01	15.67
	0.5	2.9972	3.0500	2.9064	1.76	3.03
2	2	0.2212	0.1743	0.1831	21.20	17.20
	1.75	0.2211	0.1756	0.1637	20.60	25.98
	1.5	0.2607	0.2943	0.2936	12.91	12.63
	1.25	0.3891	0.2938	0.2886	24.50	25.83
	1	0.5113	0.4127	0.4281	19.29	16.28
	0.75	0.5403	0.4248	0.4203	83.15	22.22
	0.74	0.6319	0.6592	0.6961	4.31	10.15
	0.5	1.1387	1.0268	1.0140	9.83	10.95

Table A.2: Comparison of N_x between modal time history analysis, CQC, and SRSS for a total number of 19 axial and circumferential half waves at the point where the maximum N_x occurs using THA

L_y/L_x	B	THA ($\times 10^6$)	SRSS ($\times 10^6$)	CQC ($\times 10^6$)	SRSS % error	CQC % error
1	2	0.3420	0.2805	0.2826	17.99	17.39
	1.75	0.4561	0.4119	0.4157	9.69	8.85
	1.5	0.5737	0.5918	0.5825	3.15	1.54
	1.25	0.6688	0.6571	0.6348	1.76	5.09
	1	0.7897	0.4707	0.6623	40.39	16.14
	0.75	0.9022	0.6256	0.8033	30.66	10.96
	0.74	1.1135	0.6921	0.5744	37.84	48.42
	0.5	1.9812	1.4572	1.3260	26.45	33.07
0.5	2	0.2960	0.2521	0.2518	14.83	14.92
	1.75	0.3328	0.2974	0.2770	10.64	16.77
	1.5	0.4070	0.1774	0.3434	56.41	15.64
	1.25	0.6031	0.2574	0.4228	57.32	29.89
	1	0.7474	0.3314	0.6236	55.66	16.57
	0.75	0.8432	0.4162	0.6276	50.64	25.57
	0.74	1.0151	0.4866	0.9646	52.07	4.98
	0.5	1.8209	1.0203	0.7066	43.97	61.19
2	2	0.2979	0.3419	0.3668	14.75	23.12
	1.75	0.4457	0.5031	0.4622	12.86	3.70
	1.5	0.5835	0.4294	0.4170	26.41	28.54
	1.25	0.7502	0.4920	0.5100	34.41	32.02
	1	0.9640	1.1725	1.1245	21.62	16.64
	0.75	1.3301	1.5686	1.4690	74.80	10.44
	0.74	1.5824	1.8079	1.8086	14.25	14.30
	0.5	3.5437	3.3163	3.2994	6.42	6.89

Table A.3: Comparison of N_y between modal time history analysis, CQC, and SRSS for a total number of 19 axial and circumferential half waves at the point where the maximum N_y occurs using THA

L_y/L_x	B	THA ($\times 10^6$)	SRSS ($\times 10^6$)	CQC ($\times 10^6$)	SRSS % error	CQC % error
1	2	0.3859	0.3004	0.3300	22.16	14.49
	1.75	0.5541	0.4121	0.4477	25.63	19.20
	1.5	0.6176	0.5902	0.6374	4.43	3.21
	1.25	0.9202	0.6504	0.7088	29.32	22.97
	1	0.9348	0.6042	0.6745	35.36	27.85
	0.75	1.0259	0.7530	0.8226	26.60	19.82
	0.74	1.1970	0.8983	0.8687	24.95	27.42
	0.5	1.7513	1.2681	1.3843	27.59	20.96
0.5	2	0.5611	0.4350	0.4670	22.47	16.76
	1.75	0.6696	0.5037	0.5415	24.78	19.13
	1.5	0.7204	0.5427	0.5920	24.66	17.82
	1.25	0.8972	0.6617	0.7148	26.25	20.34
	1	1.1915	0.8114	0.9028	31.90	24.23
	0.75	1.2126	0.8860	0.9182	26.93	24.28
	0.74	1.3498	0.9369	0.9903	30.59	26.63
	0.5	2.0044	1.4952	1.4244	25.40	28.94
2	2	0.3304	0.2007	0.2183	39.25	33.93
	1.75	0.3862	0.2518	0.2385	34.80	38.24
	1.5	0.4131	0.3253	0.3482	21.25	15.71
	1.25	0.4859	0.3691	0.4118	24.03	15.24
	1	0.7455	0.5742	0.6526	22.98	12.46
	0.75	0.9496	0.7300	0.8383	11.84	11.71
	0.74	1.1023	0.8600	0.9561	21.98	13.26
	0.5	1.6437	1.4750	1.4141	10.26	13.96

Table A.4: Comparison of N_{xy} between modal time history analysis, CQC, and SRSS for a total number of 19 axial and circumferential half waves at the point where the maximum N_{xy} occurs using THA

L_y/L_x	B	THA ($\times 10^4$)	SRSS ($\times 10^4$)	CQC ($\times 10^4$)	SRSS % error	CQC % error
1	2	1.2548	0.8578	0.9709	31.64	22.62
	1.75	1.5947	1.0839	1.1072	32.03	30.57
	1.5	1.7751	1.3679	1.3648	22.94	23.12
	1.25	2.3846	1.6537	1.7766	30.65	25.50
	1	2.5194	1.6260	1.9647	35.46	22.02
	0.75	2.8119	1.9158	2.3240	31.87	17.35
	0.74	3.0937	2.1872	2.8237	29.30	8.73
	0.5	4.7114	3.4554	4.9162	26.66	4.35
0.5	2	1.0734	0.9427	0.9126	12.18	14.98
	1.75	1.3576	1.1663	1.1369	14.09	16.25
	1.5	1.6760	1.4760	1.3769	11.94	17.85
	1.25	2.1605	1.9488	1.8097	9.80	16.24
	1	2.7435	2.3584	2.2323	14.04	18.63
	0.75	3.1532	2.8982	2.7573	8.09	12.56
	0.74	3.4980	3.3532	3.1424	4.14	10.17
	0.5	6.8881	5.9149	5.7001	14.13	17.25
2	2	0.9467	0.5993	0.7058	36.69	25.44
	1.75	1.1990	1.2871	1.1755	7.34	1.97
	1.5	1.5797	1.7111	1.4289	8.32	9.55
	1.25	1.8240	1.7708	1.5703	2.92	13.91
	1	2.5672	1.5138	1.5891	41.03	38.10
	0.75	3.1931	3.5540	3.2800	55.71	2.72
	0.74	3.5356	3.9887	4.4031	12.82	24.54
	0.5	6.0961	6.9094	5.4253	13.34	11.00

Table A.5: Comparison of M_x between modal time history analysis, CQC, and SRSS for a total number of 19 axial and circumferential half waves at the point where the maximum M_x occurs using THA

L_y/L_x	B	THA ($\times 10^5$)	SRSS ($\times 10^5$)	CQC ($\times 10^5$)	SRSS % error	CQC % error
1	2	0.2905	0.2284	0.2430	21.38	16.35
	1.75	0.3551	0.2792	0.2567	21.38	27.72
	1.5	0.4483	0.3444	0.3163	23.16	29.44
	1.25	0.5503	0.3953	0.3546	28.15	35.56
	1	0.6663	0.4302	0.4619	35.43	30.67
	0.75	0.5932	0.4542	0.4753	23.43	19.88
	0.74	0.6475	0.4856	0.5128	25.00	20.80
0.5	0.5	0.9690	0.8215	0.9014	15.23	6.98
	2	0.3394	0.2901	0.2854	14.55	15.93
	1.75	0.4226	0.3669	0.3594	13.18	14.96
	1.5	0.5220	0.4637	0.4347	11.17	16.72
	1.25	0.6586	0.5920	0.5661	10.10	14.05
	1	0.8491	0.7129	0.6895	16.04	18.79
	0.75	0.9572	0.8664	0.8412	9.49	12.12
	0.74	1.0452	0.9989	0.9661	4.43	7.57
	0.5	2.0760	1.8405	1.7886	11.34	13.84
2	2	0.1606	0.1076	0.1146	32.99	28.68
	1.75	0.1729	0.1204	0.1222	30.36	29.34
	1.5	0.1698	0.1560	0.1575	8.18	7.26
	1.25	0.2643	0.2059	0.1957	22.08	25.93
	1	0.3805	0.2478	0.2669	34.87	29.85
	0.75	0.3522	0.2534	0.2785	55.33	20.91
	0.74	0.4097	0.2875	0.3112	29.83	24.05
	0.5	0.7479	0.6824	0.6507	8.75	12.99

Table A.6: Comparison of M_y between modal time history analysis, CQC, and SRSS for a total number of 19 axial and circumferential half waves at the point where the maximum M_y occurs using THA

L_y/L_x	B	THA ($\times 10^4$)	SRSS ($\times 10^4$)	CQC ($\times 10^4$)	SRSS % error	CQC % error
1	2	0.7876	0.4453	0.5348	43.47	32.10
	1.75	0.9486	0.5712	0.6040	39.79	36.33
	1.5	1.1770	0.7249	0.8038	38.42	31.71
	1.25	1.4845	0.8582	0.9919	42.19	33.18
	1	1.8188	0.9580	1.2093	47.33	33.51
	0.75	2.0614	0.9838	1.3277	52.27	35.59
	0.74	2.3682	1.1148	1.5092	52.93	36.27
	0.5	3.6513	1.5691	2.2854	57.03	37.41
0.5	2	0.4931	0.2957	0.3554	40.03	27.91
	1.75	0.6200	0.3773	0.4580	39.15	26.12
	1.5	0.8243	0.4833	0.6165	41.36	25.20
	1.25	1.0465	0.6268	0.7735	40.11	26.09
	1	1.2470	0.7751	0.9637	37.85	22.72
	0.75	1.2658	0.9801	1.1375	22.58	10.14
	0.74	1.4241	1.1410	1.3721	19.88	3.65
	0.5	2.5271	2.1594	2.3858	14.55	5.59
2	2	0.6572	0.3223	0.4228	50.97	35.67
	1.75	0.7590	0.3621	0.4852	52.29	36.07
	1.5	0.8906	0.4386	0.6233	50.75	30.01
	1.25	1.1436	0.5642	0.7364	50.67	35.61
	1	1.4675	0.7400	1.0214	49.58	30.40
	0.75	1.4827	0.7582	1.2519	28.25	15.56
	0.74	1.6753	0.8788	1.2819	47.54	23.48
	0.5	2.7658	1.5758	2.0551	43.03	25.70

Table A.7: Comparison of M_{xy} between modal time history analysis, CQC, and SRSS for a total number of 19 axial and circumferential half waves at the point where the maximum M_{xy} occurs using THA

L_y/L_x	B	THA	SRSS	CQC	% error SRSS	% error CQC
	2	0.1141	0.1028	0.1112	9.90	2.54
	1.75	0.1065	0.099	0.093	7.04	12.68
	1.5	0.0953	0.0914	0.0864	4.09	9.34
1	1.25	0.0836	0.076	0.0721	9.09	13.76
	1	0.0663	0.0593	0.0638	10.56	3.77
	0.75	0.0468	0.0434	0.0467	7.26	0.21
	0.74	0.0453	0.0415	0.0442	8.39	2.43
	0.5	0.0299	0.0263	0.0287	12.04	4.01
	2	0.1648	0.1593	0.164	3.34	0.49
	1.75	0.1447	0.1459	0.1495	0.83	3.32
	1.5	0.1302	0.1303	0.1374	0.08	5.53
0.5	1.25	0.1362	0.122	0.1271	10.43	6.68
	1	0.104	0.1097	0.1132	5.48	8.85
	0.75	0.1081	0.1004	0.1006	7.12	6.94
	0.74	0.1072	0.098	0.0982	8.58	8.40
	0.5	0.0973	0.0935	0.0928	3.91	4.62
	2	0.0318	0.0274	0.0312	13.84	1.89
	1.75	0.024	0.0221	0.0208	7.92	13.33
	1.5	0.0183	0.0201	0.02	9.84	9.29
2	1.25	0.0188	0.0172	0.0174	8.51	7.45
	1	0.018	0.0173	0.0201	3.89	11.67
	0.75	0.0136	0.0132	0.0156	2.94	14.71
	0.74	0.0128	0.0132	0.0149	3.12	16.41
	0.5	0.0123	0.0112	0.0121	8.94	1.63

Table A.8: Comparison of W between modal time history analysis, CQC, and SRSS for a total number of 19 axial and circumferential half waves with neglect of the effect of location

L_y/L_x	B	THA ($\times 10^6$)	SRSS ($\times 10^6$)	CQC ($\times 10^6$)	SRSS % error	CQC % error
1	2	0.5948	0.4947	0.5248	16.83	11.77
	1.75	0.7939	0.6724	0.679	15.30	14.47
	1.5	0.8741	0.9016	0.9121	3.15	4.35
	1.25	1.1128	1.0344	1.0442	7.05	6.16
	1	1.0494	1.074	1.135	2.34	8.16
	0.75	1.1648	1.1744	1.2343	0.82	5.97
	0.74	1.3168	1.3477	1.3517	2.35	2.65
	0.5	1.6127	1.7029	1.8263	5.59	13.24
0.5	2	0.9406	0.8458	0.9044	10.08	3.85
	1.75	1.0824	0.9833	1.0487	9.16	3.11
	1.5	1.1718	1.0634	1.149	9.25	1.95
	1.25	1.4218	1.3006	1.3973	8.52	1.72
	1	1.7869	1.5994	1.715	10.49	4.02
	0.75	1.9815	1.7591	1.7209	11.22	13.15
	0.74	2.0901	1.8599	1.8156	11.01	13.13
	0.5	2.9972	3.05	2.8858	1.76	3.72
2	2	0.2212	0.2036	0.2257	7.96	2.03
	1.75	0.2211	0.2204	0.2057	0.32	6.97
	1.5	0.2607	0.2943	0.2813	12.89	7.90
	1.25	0.3891	0.3486	0.3487	10.41	10.38
	1	0.5113	0.5004	0.5501	2.13	7.59
	0.75	0.5403	0.5487	0.5977	1.55	10.62
	0.74	0.6319	0.6592	0.7057	4.32	11.68
	0.5	1.1387	1.0268	1.0877	9.83	4.48

Table A.9: Comparison of N_x between modal time history analysis, CQC, and SRSS for a total number of 19 axial and circumferential half waves with neglect of the effect of location

L_y/L_x	B	THA ($\times 10^6$)	SRSS ($\times 10^6$)	CQC ($\times 10^6$)	SRSS % error	CQC % error
1	2	0.342	0.3104	0.3803	9.24	11.20
	1.75	0.4561	0.4119	0.4771	9.69	4.60
	1.5	0.5737	0.5918	0.7737	3.15	34.86
	1.25	0.6688	0.7187	0.9927	7.46	48.43
	1	0.7897	0.7552	1.0775	4.37	36.44
	0.75	0.9022	0.9613	1.2944	6.55	43.47
	0.74	1.1135	1.1622	1.2464	4.37	11.94
	0.5	1.9812	2.14	2.1625	8.02	9.15
0.5	2	0.296	0.2521	0.3066	14.83	3.58
	1.75	0.3328	0.2974	0.4174	10.64	25.42
	1.5	0.407	0.3541	0.5433	13.00	33.49
	1.25	0.6031	0.4673	0.6993	22.52	15.95
	1	0.7474	0.5925	1.0604	20.73	41.88
	0.75	0.8432	0.7166	1.1692	15.01	38.66
	0.74	1.0151	0.8216	1.5037	19.06	48.13
	0.5	1.8209	1.5423	1.3256	15.30	27.20
2	2	0.2979	0.3786	0.4033	27.09	35.38
	1.75	0.4457	0.5031	0.4992	12.88	12.00
	1.5	0.5835	0.6646	0.8167	13.90	39.97
	1.25	0.7502	0.7645	0.9378	1.91	25.01
	1	0.964	1.1725	1.4135	21.63	46.63
	0.75	1.3301	1.5686	1.9798	17.93	48.85
	0.74	1.5824	1.8079	2.0198	14.25	27.64
	0.5	3.5437	3.3163	3.0193	6.42	14.80

Table A.10: Comparison of N_y between modal time history analysis, CQC, and SRSS for a total number of 19 axial and circumferential half waves with neglect of the effect of location

L_y/L_x	B	THA ($\times 10^6$)	SRSS ($\times 10^6$)	CQC ($\times 10^6$)	SRSS % error	CQC % error
1	2	0.3859	0.3004	0.33	22.16	14.49
	1.75	0.5541	0.4121	0.4477	25.63	19.20
	1.5	0.6176	0.5902	0.6374	4.44	3.21
	1.25	0.9202	0.6504	0.7088	29.32	22.97
	1	0.9348	0.6042	0.6745	35.37	27.85
	0.75	1.0259	0.753	0.8226	26.60	19.82
	0.74	1.197	0.8983	0.8687	24.95	27.43
	0.5	1.7513	1.2681	1.3843	27.59	20.96
0.5	2	0.5611	0.435	0.467	22.47	16.77
	1.75	0.6696	0.5037	0.5415	24.78	19.13
	1.5	0.7204	0.5427	0.592	24.67	17.82
	1.25	0.8972	0.6617	0.7148	26.25	20.33
	1	1.1915	0.8114	0.9028	31.90	24.23
	0.75	1.2126	0.886	0.9182	26.93	24.28
	0.74	1.3498	0.9369	0.9903	30.59	26.63
	0.5	2.0044	1.4952	1.4244	25.40	28.94
2	2	0.3304	0.2007	0.2183	39.26	33.93
	1.75	0.3862	0.2518	0.2385	34.80	38.24
	1.5	0.4131	0.3253	0.3482	21.25	15.71
	1.25	0.4859	0.3691	0.4118	24.04	15.25
	1	0.7455	0.5742	0.6526	22.98	12.46
	0.75	0.9496	0.73	0.8383	23.13	11.72
	0.74	1.1023	0.86	0.9561	21.98	13.26
	0.5	1.6437	1.475	1.4141	10.26	13.97

Table A.11: Comparison of N_{xy} between modal time history analysis, CQC, and SRSS for a total number of 19 axial and circumferential half waves with neglect of the effect of location

L_y/L_x	B	THA ($\times 10^4$)	SRSS ($\times 10^4$)	CQC ($\times 10^4$)	SRSS % error	CQC % error
1	2	1.2548	1.0965	1.5171	12.62	20.90
	1.75	1.5947	1.4117	1.8699	11.48	17.26
	1.5	1.7751	1.8441	2.9145	3.89	64.19
	1.25	2.3846	2.2499	3.3044	5.65	38.57
	1	2.5194	2.6736	3.9476	6.12	56.69
	0.75	2.8119	3.0222	4.7017	7.48	67.21
	0.74	3.0937	3.4818	5.1557	12.54	66.65
	0.5	4.7114	5.5658	8.4966	18.13	80.34
0.5	2	1.0734	0.9427	1.1283	12.18	5.11
	1.75	1.3576	1.1974	1.4683	11.80	8.15
	1.5	1.676	1.5218	2.0088	9.20	19.86
	1.25	2.1605	1.9488	2.5724	9.80	19.07
	1	2.7435	2.3584	3.0877	14.04	12.55
	0.75	3.1532	2.8982	3.481	8.09	10.40
	0.74	3.498	3.3532	4.3633	4.14	24.74
	0.5	6.8881	6.3364	6.9823	8.01	1.37
2	2	0.9467	1.0825	1.491	14.34	57.49
	1.75	1.199	1.515	2.3703	26.36	97.69
	1.5	1.5797	1.9659	3.2205	24.45	103.87
	1.25	1.824	2.2753	3.4045	24.74	86.65
	1	2.5672	2.8461	3.4781	10.86	35.48
	0.75	3.1931	3.9258	6.3851	22.95	99.97
	0.74	3.5356	4.3011	5.8945	21.65	66.72
	0.5	6.0961	6.9094	8.9724	13.34	47.18

Table A.12: Comparison of M_x between modal time history analysis, CQC, and SRSS for a total number of 19 axial and circumferential half waves with neglect of the effect of location

L_y/L_x	B	THA ($\times 10^5$)	SRSS ($\times 10^5$)	CQC ($\times 10^5$)	SRSS % error	CQC % error
1	2	0.2905	0.2527	0.2848	13.01	1.96
	1.75	0.3551	0.3137	0.3098	11.66	12.76
	1.5	0.4483	0.3951	0.412	11.87	8.10
	1.25	0.5503	0.4681	0.4922	14.94	10.56
	1	0.6663	0.5267	0.6015	20.95	9.73
	0.75	0.5932	0.5287	0.6563	10.87	10.64
	0.74	0.6475	0.602	0.7428	7.03	14.72
	0.5	0.969	0.9378	1.1734	3.22	21.09
0.5	2	0.3394	0.2901	0.3086	14.53	9.07
	1.75	0.4226	0.3669	0.3901	13.18	7.69
	1.5	0.522	0.4637	0.5276	11.17	1.07
	1.25	0.6586	0.592	0.6509	10.11	1.17
	1	0.8491	0.7129	0.7635	16.04	10.08
	0.75	0.9572	0.8664	0.9292	9.49	2.93
	0.74	1.0452	0.9989	1.0804	4.43	3.37
	0.5	2.076	1.8607	1.9968	10.37	3.82
2	2	0.1606	0.1304	0.1616	18.80	0.62
	1.75	0.1729	0.1504	0.1729	13.01	0.00
	1.5	0.1698	0.1837	0.2509	8.19	47.76
	1.25	0.2643	0.2446	0.2965	7.45	12.18
	1	0.3805	0.305	0.3862	19.84	1.50
	0.75	0.3522	0.3221	0.4501	8.55	27.80
	0.74	0.4097	0.372	0.4741	9.20	15.72
	0.5	0.7479	0.6824	0.9098	8.76	21.65

Table A.13: Comparison of M_y between modal time history analysis, CQC, and SRSS for a total number of 19 axial and circumferential half waves with neglect of the effect of location

L_y/L_x	B	THA ($\times 10^4$)	SRSS ($\times 10^4$)	CQC ($\times 10^4$)	SRSS % error	CQC % error
1	2	0.7876	0.4453	0.5348	43.46	32.10
	1.75	0.9486	0.5712	0.604	39.78	36.33
	1.5	1.177	0.7249	0.8038	38.41	31.71
	1.25	1.4845	0.8582	0.9919	42.19	33.18
	1	1.8188	0.958	1.2093	47.33	33.51
	0.75	2.0614	0.9839	1.3277	52.27	35.59
	0.74	2.3682	1.1148	1.5092	52.93	36.27
	0.5	3.6513	1.5691	2.2854	57.03	37.41
0.5	2	0.4931	0.2957	0.3554	40.03	27.93
	1.75	0.62	0.3773	0.458	39.15	26.13
	1.5	0.8243	0.4833	0.6165	41.37	25.21
	1.25	1.0465	0.6268	0.7735	40.11	26.09
	1	1.247	0.7751	0.9637	37.84	22.72
	0.75	1.2658	0.9801	1.1375	22.57	10.14
	0.74	1.4241	1.141	1.3721	19.88	3.65
	0.5	2.5271	2.1594	2.3858	14.55	5.59
2	2	0.6572	0.3223	0.4228	50.96	35.67
	1.75	0.759	0.3621	0.4852	52.29	36.07
	1.5	0.8906	0.4386	0.6233	50.75	30.01
	1.25	1.1436	0.5642	0.7364	50.66	35.61
	1	1.4675	0.74	1.0214	49.57	30.40
	0.75	1.4827	0.7582	1.2519	48.86	15.57
	0.74	1.6753	0.8788	1.2819	47.54	23.48
	0.5	2.7658	1.5758	2.0551	43.03	25.70

Table A.14: Comparison of M_{xy} between modal time history analysis, CQC, and SRSS for a total number of 19 axial and circumferential half waves with neglect of the effect of location